UNIVERSITÉ DE GRENOBLE

THÈSE

Pour obtenir le grade de

DOCTEUR DE L'UNIVERSITÉ DE GRENOBLE

Spécialité : **Sciences de la Terre, de l'Univers et de l'Environnement**

Arrêté ministériel : 7 août 2006

Présentée par

Julie RICHARD

Thèse dirigée par **Jean-Pierre GRATIER** et **Mai-Linh DOAN**

préparée au sein de l'**ISTerre (Institut des Sciences de la Terre)** dans **l'École Doctorale Terre, Univers, Environnement**

Mécanismes de fluage des failles actives : apport des grands forages et expérimentations de laboratoire

Thèse soutenue publiquement le **18 Décembre 2013** devant le jury composé de :

Prof. Andrea BILLI
Università di Roma, CNR Roma, Rome, Italy, Rapporteur
Prof. Olivier LACOMBE
Université Pierre et Marie Curie – Paris VI – ISTeP, Paris, France, Rapporteur
Dr. Roger SOLIVA
Université de Montpellier, Géosciences Montpellier, Montpellier, France, Examinateur
Dr. Anne-Marie BOULLIER
Université de Grenoble Alpes, ISTerre, Grenoble, France, Présidente du Jury
Prof. Jean-Pierre GRATIER
Université de Grenoble Alpes, ISTerre, Grenoble, France, Directeur de thèse
Dr. Mai-Linh DOAN
Université de Grenoble Alpes, ISTerre, Grenoble, France, Co-directrice de thèse

Université Joseph Fourier / Université Pierre Mendès France / Université Stendhal / Université de Savoie / Grenoble INP

À mon père…

REMERCIEMENTS

Il est toujours difficile de n'oublier personne, surtout lorsque l'aventure s'étire ainsi sur trois années et que les rencontres sont aussi nombreuses que riches. Je vais essayer de faire au mieux et m'excuse par avance auprès des éventuels laissés pour comptes…

Je remercie tout d'abord le jury d'avoir accepté d'évaluer ce manuscrit et de m'avoir autorisée à soutenir. Je ne m'attendais pas à des retours aussi positifs et j'ai beaucoup apprécié la discussion que nous avons eue. Merci à eux de s'être déplacés et pour leurs encouragements quant à ma poursuite en recherche.

Je ne saurai rendre justice à mes directeurs de thèse avec de simples remerciements. Sans eux, c'est évident que je ne serais jamais parvenue à terminer ces travaux. Leur grande disponibilité, leur compréhension, leur incroyable patience et surtout, leur bonne humeur et leur motivation contagieuse ont été un véritable moteur pour moi. J'ai un grand respect pour eux et je les remercie du fond du cœur de m'avoir ainsi donné leur confiance. Ils m'auront beaucoup aidée à développer la mienne, que ce soit en moi-même et en mes propres choix. Merci Jean-Pierre pour ces trois ans de thèse et les deux stages de master, je pense que je n'aurais pas pu trouver meilleur directeur. Merci Mai-Linh pour ces trois années et honnêtement, pour un premier encadrement avec en plus, une extension familiale à gérer dans la foulée, tu t'en es sortie parfaitement ! Je ne doute pas que tu continueras à être une excellente directrice !

Je tiens également à remercier toute l'équipe Mécanique des Failles, dans laquelle j'ai certes trouvé des gens extrêmement compétents mais aussi très humains et très accessibles. Ils m'ont offert une seconde famille et un soutien infaillible au moment où j'en ai eu le plus besoin. C'était absolument génial de pouvoir travailler avec des gens aussi passionnés et aussi de partager tous ces bons moments culinaires ! Merci à vous tous de m'avoir ainsi intégré et surtout, ne changez rien ! Je tiens quand même à remercier plus particulièrement certains d'entre vous à qui j'ai volé plus de temps que de raison. Merci beaucoup à François et ses retours si rapides sur les articles (presque troisième directeur à la fin !), merci à Anne-Marie pour ses précieux conseils, son aide inconditionnelle et son soutien, merci à Benjamin pour toutes ces heures de bataille avec

les cellules de percolation (on les a eues !), j'espère qu'on aura l'occasion de se recroiser sur les pistes ! Merci à Virginie pour son soutien et ses conseils, même depuis la Californie ! Et merci à Michel, pour son attention et son soutien.

Je remercie chaleureusement les autres thésards d'ISTerre, avec une mention particulière pour la petite communauté internationale dans laquelle je me sentais vraiment bien. J'ai apprécié ces "lunch break" parmi vous et je regrette de ne pas avoir eu plus de temps pour les soirées et les randos ! Merci infiniment à Selda pour son initiation au Yoga, qui m'a aidée à gérer mon stress de façon efficace dans la dernière ligne droite ! Encore une fois, une mention spéciale pour mes co-bureaux, ou plutôt mes amis Anne et Karim, qui ont eu la patience de supporter mes plaintes et mes humeurs, toujours avec le sourire.

D'une façon générale, je remercie tous les gens travaillant à ISTerre avec qui j'ai eu à interagir et à travailler et qui m'ont toujours très bien accueillie.

Dans la catégorie "extérieur", je remercie Pascal Charrier de 3SR et Jean-Luc Devidal de Clermont-Ferrand, pour leur aide technique et les discussions intéressantes que nous avons eues et qui m'ont aidée à avancer. Discussions et débats que j'ai pu aussi partager avec de nombreuses personnes en congrès et qui m'ont permis de prendre du recul sur mes travaux et d'envisager les problèmes sous des angles nouveaux. Merci à tous ces gens pour le temps qu'ils m'ont consacrée.

Je ne saurais conclure sans remercier ma famille, qui même à distance, m'a beaucoup soutenue. Merci à ma maman pour sa compréhension, sa patience et les heures passées au téléphone (et devant les fourneaux !). Merci à Julien pour son patient soutien durant ces trois années, je sais que les choses n'ont pas toujours été faciles, mais on s'en est finalement pas si mal sorti ! Enfin, merci à mon papa pour sa confiance et son écoute…

RESUME

Le fluage est une déformation ductile affectant certaines failles actives, voire toutes. Il existe en effet deux types de fluage. Le premier, le fluage permanent, concerne certaines failles. La déformation s'effectue de façon continue et constante dans le temps. Le second, plus ponctuel, est fréquemment enregistré à la suite d'un séisme. On peut alors parler de déformation post-sismique. La compréhension des mécanismes à l'origine de ces deux types de fluage apparaît étroitement liée à celle de la succession des différentes phases du cycle sismique.

Notre étude, basée à la fois sur des observations naturelles et sur des expérimentations de laboratoire, a démontré que le fluage résultait d'une combinaison de processus interagissant les uns avec les autres et favorisant la mise en place d'un mécanisme dominant. Nous avons mis en évidence que les deux paramètres les plus importants à l'établissement de cette dominance étaient la composition minéralogique de la roche et son état d'endommagement. Dans une zone de faille, ces deux paramètres varient avec le temps, la profondeur et avec l'éloignement à la zone de glissement. Par conséquent, les mécanismes de fluage évoluent eux aussi en fonction de ces données. Notre approche microstructurale d'échantillons provenant de la zone en fluage actif de la faille de San Andreas, fournis par le forage SAFOD, nous a permis d'établir une chronologie des déformations subies par les roches de cette zone. Un modèle d'évolution des mécanismes de fluage a ainsi émergé. Cette évolution est capable d'entretenir le fluage au cours du temps de façon permanente, soit par un enrichissement de la zone en minéraux à faible coefficient de friction, comme révélé par les échantillons de la Faille de San Andreas, soit par un équilibre entre processus de fracturation et de cicatrisation, maintenant la résistance de la roche à un seuil trop faible pour un fort chargement. Dans ce dernier cas, nos expérimentations de laboratoire ont montré que si les processus de cicatrisation devenaient dominants, il y avait création d'hétérogénéités de résistance à l'intérieur de la roche. A l'échelle d'une zone de faille, ces hétérogénéités peuvent être suffisamment importantes pour mener à l'initiation d'une rupture conséquente. Ces expériences sont analogues au cas de la Faille de San Andreas, où dans un contexte de fluage permanent, des microaspérités locales génèrent de la sismicité.

ABSTRACT

Creep is a ductile deformation mechanism affecting many, if not all, active faults. This mechanism is twofold. First, creep may be permanent, *i.e.* the deformation takes place through time in a continuous and constant manner. Creep may also appear in a more discontinuous manner, commonly associated with post-seismic deformation. Understanding the origin of both types of creep appears closely connected to understanding the succession of the various stages of the seismic cycle.

Our approach is based both on the investigation of natural samples and on laboratory experiments. By doing so, we demonstrate that creep results from a combination of several processes themselves interacting with one another, until the promotion of one particular mechanism. We have established that the most important driving parameters to this convergence were the mineralogical composition of the host rock and its damage state. Within the fault, these parameters change with time, depth and distance from the slip zone. Therefore, the creep mechanisms themselves may change according to the parameters above-mentioned.

Our micro-structural approach using SAFOD drill core samples from the San Andreas Fault (California) allowed us to unveil a time-lapsed picture of the deformation sequence in this area. Based on these observations, we suggest a conceptual model for the evolution of creep mechanisms. According to this model, creep is maintained within the fault zone either by the crystallization of low-friction minerals (as shown by the SAFOD samples) or by reaching equilibrium between fracturing and healing, thereby maintaining rock strength below the threshold for important stress loading. In the first scenario, our laboratory experiments showed that if the healing processes become dominant, strength heterogeneities appear within the rock. At the fault scale, these heterogeneities would become numerous enough to lead to a major rupture. These experiments are reasonably similar to what is expected for the San Andreas Fault where permanent creep occurs whereas local asperities are seismic.

TABLE DES MATIERES

INTRODUCTION

L'étude des failles actives soulève de nombreuses questions dont l'importance est directement reliée à la problématique générale de la compréhension du cycle sismique. De façon très simplifiée, une faille active doit se déformer pour accommoder les contraintes accumulées dans la croûte. Nous savons qu'elle peut effectuer cette déformation de deux façons : au cours d'un évènement court et violent représenté par une rupture sismique, mais aussi par des processus de déformation lents et asismiques que l'on peut regrouper sous le nom de fluage. L'alternance de ces deux phases de déformation est liée à des paramètres généraux tels que le contexte tectonique de la faille, sa minéralogie et sa géométrie. Ces paramètres jouent à leur tour des rôles d'importance variable dans l'activation de processus physiques et chimiques au sein de la zone de faille. C'est de ces processus que dépendra la réponse mécanique de la faille. Actuellement, la prise en compte de tous ces paramètres, leur variabilité au cours du temps et la façon dont ils interagissent entre eux, est trop conséquente pour nous permettre de prévoir avec exactitude la date, la localisation et la magnitude de la prochaine rupture sismique. Cependant, grâce à la multiplication et l'amélioration des outils d'études géodésiques et grâce à la surveillance en continue des grandes failles actives majeures, l'importance des déformations asismiques dans la dynamique du cycle sismique a été mise en évidence.

Pendant de longues années, le fluage n'était que peu, voire pas pris en compte dans les études sismiques. Désormais, il apparait comme un mécanisme clé dans l'alternance des phases de déformation de la faille et deux types de fluage ont été distingués. Le premier, intrinsèque à la faille, pourrait être qualifié de fluage permanent. La déformation s'effectue alors de façon continue et constante dans le temps. Il est présent durant les différentes phases tectoniques de l'évolution d'une faille et on le retrouve notamment au niveau des failles actives asismiques. Le second type, plus ponctuel, est enregistré spécifiquement à la suite d'un séisme. On peut alors parler de déformation post-sismique.

Suite à la multiplication des observations de cas de fluage sur les grandes failles actives,

son étude s'est peu à peu approfondie pour se concentrer sur les paramètres et les mécanismes à l'origine de ce comportement. En effet, qu'il soit permanent ou post-sismique, le fluage peut être accommodé par différents mécanismes identifiables à une échelle bien plus réduite que celle de la faille : l'échelle de la microstructure. L'étude des processus de faille ayant lieu *in situ* à cette petite échelle, est longtemps restée théorique et expérimentale du fait de la difficulté d'accès aux matériels et au manque de données physiques à plusieurs kilomètres de profondeur. En cela, les grands forages géologiques mis en place sur des failles majeures comme la Faille de San Andreas, en Californie, ont été d'une importance capitale. Ils ont fourni de nombreuses données géophysiques permettant de mieux contraindre les paramètres les plus déterminants et ils ont enfin permis de remonter des échantillons de roches prélevés en profondeur.

Les microstructures observables en lames minces permettent d'identifier quels types de déformations (ductile ou cassante) a subi la roche. Les zones de failles étant des endroits très complexes, pour un contexte donné, comme celui de la Faille de San Andreas, plusieurs mécanismes participent à l'accommodation des déformations et notamment, à l'accommodation de façon ductile et asismique. Ces mécanismes peuvent être en compétition les uns avec les autres ou s'activer mutuellement. L'observation et l'identification de marqueurs chimiques et structuraux, permettent de comprendre quels sont les processus dominants dans cette accommodation. Néanmoins, il apparait clairement que cette dominance est fortement influencée par la composition minéralogique et l'état d'endommagement de la roche. Ces deux paramètres varient avec le temps, la profondeur et avec l'éloignement à la zone active de fluage de la faille. Ceci nous a amené à considérer le problème sous un angle nouveau : comment évoluent les mécanismes de fluage au cours du temps ? Et quelles sont les répercussions de cette évolution sur le comportement de la faille ?

Pour répondre à ces questions, nous avons procédé en deux étapes. Des études microstructurales provenant d'échantillons prélevés au cœur des zones en fluage actif de la Faille de San Andreas ont constitué une première étape. Ces observations nous ont permis de déterminer quel pouvait être le processus de fluage dominant à l'œuvre dans ces zones et de construire un modèle d'évolution en fonction du temps et des données spatiales de profondeur et d'éloignement à la zone de fluage. Au cours d'une seconde

étape, nous avons mis en place des expérimentations de laboratoire pour mieux contraindre l'influence des microstructures et de l'état d'endommagement initial des roches sur leur réponse mécanique, dans le cas de fracturation dynamique et de cicatrisation par circulation fluide.

Les deux premiers chapitres ont pour but de rappeler des notions générales sur les failles actives, leur étude et les processus qui leur sont associés. Ils insisteront sur l'aspect microstructural des mécanismes, abordés en détails dans les chapitres 3 et 4. Ces deux chapitres présenteront les résultats de ces trois ans d'études et tenteront de répondre à la problématique soulevée plus haut. Enfin, une conclusion générale résumera les éléments importants révélés au cours de ce travail, ainsi que les perspectives qui lui sont associées.

CHAPITRE 1
Contexte général

Introduction

Ce premier chapitre introduit quelques définitions très générales concernant les failles et les processus qui leurs sont associés, en insistant particulièrement sur le fluage. Il traite également de l'intérêt des forages scientifiques, voire de leur nécessité, pour avancer sur les grandes problématiques liées à l'étude des failles actives et du cycle sismique. Enfin, il introduira l'objet d'étude principale de cette première partie, à savoir, la faille de San Andreas, ainsi que le forage SAFOD réalisé sur cette faille et qui a fourni les échantillons auxquels les résultats du Chapitre 3 sont dédiés.

1.1 Qu'est-ce qu'une faille active ?

1.1.1 Quelques définitions

Une faille est une zone de rupture dans la croûte terrestre aboutissant à l'individualisation de deux compartiments. Ces zones de faiblesse permettent de relaxer les contraintes mécaniques accumulées par le mouvement continu des plaques tectoniques les unes par rapport aux autres. Généralement, le glissement capable d'accommoder les contraintes tectoniques se fait sur des failles déjà existantes car la création d'une nouvelle faille nécessite beaucoup plus d'énergie que la réactivation d'un plan de faille préexistant.

On distingue trois types de failles, correspondant à différents contextes tectoniques. On trouve des failles normales dans les contextes d'extension. L'un des compartiments s'affaisse par rapport à l'autre, créant un escarpement (Figure 1.1a). Les

failles inverses, ou chevauchements, caractérisent les contextes de compression. Dans ce cas, l'un des compartiments vient chevaucher le second (Figure 1.1b). Enfin, les failles décrochantes ou décrochements, accompagnent les mouvements latéraux de coulissement. Elles peuvent être dextre ou senestre, en fonction du sens de la direction de déplacement du compartiment opposé à l'observateur (Figure 1.1c). Ces failles peuvent ou non avoir une composante de mouvement vertical. De même, les failles normales ou les chevauchements peuvent avoir une composante décrochante occasionnant un mouvement dans le plan horizontal.

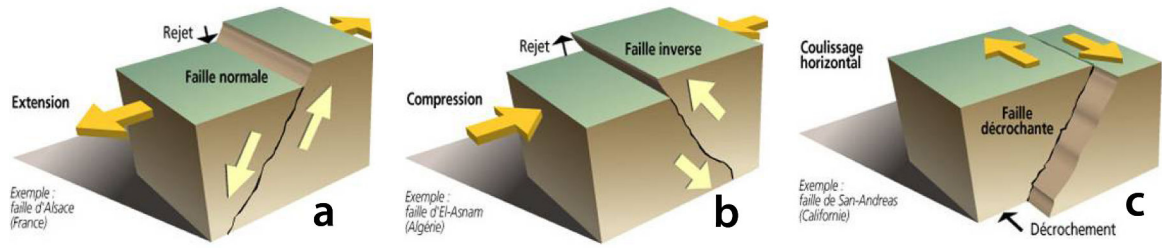

Figure 1.1 : Les différents types de failles. (a) Faille normale, (b) faille inverse, (c) faille décrochante dextre (source : Prim.net)

Une faille est considérée comme active si elle est sujette à un déplacement, ou si elle peut subir un déplacement à une échelle de temps pouvant concerner l'homme (Grant, 2007). Les failles actives peuvent être divisées en deux catégories : les failles sismiques, qui vont glisser de façon brutale en produisant des séismes et les failles asismiques, qui vont avoir un glissement très lent appelé fluage, capable d'accommoder la déformation sans produire de séisme. Enfin, une faille est dite inactive lorsqu'aucun déplacement n'y est enregistré. Evidemment, ces failles inactives ont été actives dans le passé et pourraient être réactivées.

La géométrie d'une zone de faille est souvent complexe, notamment pour les failles décrochantes dites "matures", qui sont des failles de plusieurs centaines de kilomètres de long, âgées de plusieurs millions d'années et divisées en plusieurs segments dont les comportements mécaniques diffèrent les uns par rapport aux autres.

On appelle gouge de faille la partie constituée d'une matrice très fine, souvent argileuse et englobant des éléments très altérés provenant des roches de faille, qui résulte de processus d'altérations mécaniques et chimiques variés. Cette zone, généralement très étroite et très localisée au niveau du plan de glissement (là où se produit le mouvement,

qu'il soit sismique ou asismique), fait souvent montre de propriétés physiques bien particulières. La gouge de faille est généralement située au sein d'une zone plus large, caractérisée par l'état très endommagé de ses roches. Cette zone est appelée zone endommagée (en anglais, *damage zone*) et on y trouve une fracturation intense du matériau, qui peut aller jusqu'à la pulvérisation de celui-ci. L'ensemble gouge de faille et zone endommagée peut présenter différentes géométries concernant son organisation (Faulkner et al., 2010) qui auront un impact sur le comportement mécanique global de la faille. Nous reviendrons longuement sur les propriétés et les mécanismes se produisant dans ces zones dans les chapitres suivants.

Enfin, les failles sont sujettes à de nombreux mécanismes appelés "processus de faille", qui se produisent de préférence à l'intérieur de la zone endommagée et de la gouge. Ce sont ces processus qui font évoluer les propriétés minérales et rhéologiques de la zone de faille au cours du temps. Nous voyons ci-dessous plus en détails en quoi consistent ces processus.

1.1.2 Les processus de faille

Il existe de nombreux processus physico-chimique agissant sur les propriétés minérales et rhéologiques des failles. Le comportement d'une faille est directement dépendant de ces processus. En d'autres termes, ce sont eux qui vont déterminer si celle-ci va se comporter de façon sismique ou asismique. Ils vont également donner de précieuses informations sur son cycle de déformation. Il apparait donc évident qu'une meilleure compréhension de ces processus est une étape clé dans l'étude de la mécanique des failles (Scholz, 2002; Mittempergher, 2012). Ils peuvent être séparés en deux groupes : les processus à courts termes intervenant durant les périodes co-sismique et post-sismique et les processus à longs termes intervenant durant la période inter-sismique.

Parmi les différents processus de faille, longs ou courts termes, certains contribueront à affaiblir la roche, comme les processus de déformations cassantes ou processus cataclastiques, telles la fracturation et la comminution (processus conduisant à la fragmentation d'une roche et à la réduction de la taille générale des grains). Parmi les processus affaiblissant les roches de faille, on compte aussi des mécanismes appartenant

aux déformations avec transferts de matière sous contrainte, comme la dissolution-cristallisation (voir Chapitre 2), qui peut conduire à enrichir la composition minérale en minéraux peu résistants (comme les phyllosilicates ou les argiles). D'autres processus restaureront pour leur part les propriétés rhéologiques des roches de faille après un séisme, ou même durciront ces roches, comme les processus de cicatrisation et de colmatage des fractures par cristallisation, conduisant à un nouveau chargement tectonique et l'initiation d'une nouvelle rupture sismique. Ces processus dépendent à leur tour de différents paramètres dont les plus généraux sont la composition minérale initiale des roches de la zone de faille, le type et la géométrie de la faille, qui vont déterminer des conditions de pression et de température, sans oublier le contexte tectonique qui va fixer le taux de déformation générale et les contraintes subies par la zone de faille. Enfin, la présence de fluides de compositions variables dans les zones de failles influence fortement la mise en place et la cinétique de la plupart de ces processus physico-chimique (Scholz, 2002; Mittempergher, 2012).

Dans un premier temps, ces processus peuvent être étudiés par l'intermédiaire de mesures géophysiques (mesure de résistivité, de perméabilité, variation des vitesses des ondes sismiques P et S, etc.), puis dans un second temps, par l'observation au microscope d'échantillons naturels provenant de zones de failles. La transformation et l'altération des minéraux, ainsi que les microstructures observables en lames minces réalisées dans les roches des zones de failles, correspondent à de véritables enregistrements des déformations qu'elles ont subies suite à ces processus physico-chimique (Figure 1.2). L'étude de ces roches permet donc d'une part, d'identifier et de déterminer la nature de ces processus et d'une autre part, de reconstituer une chronologie relative des déformations subies par la zone de faille.

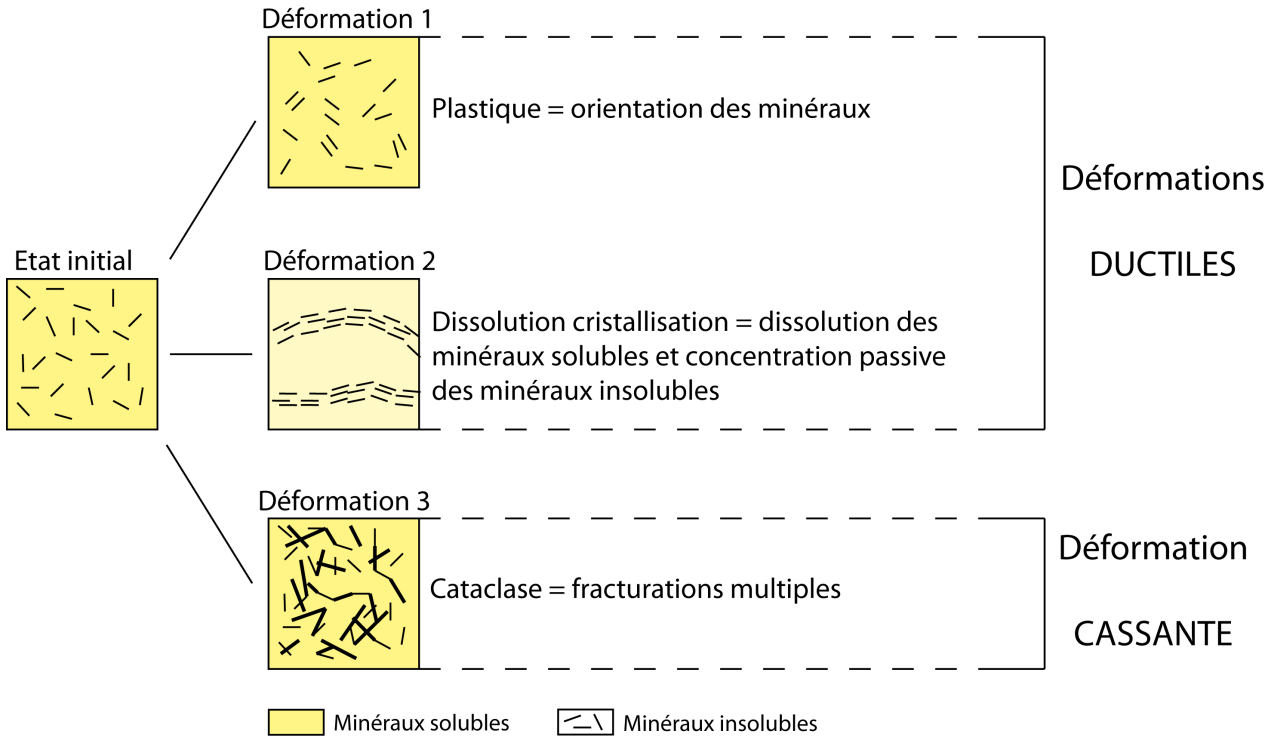

Figure 1.2 : Schématisation simple des différents marqueurs des déformations les plus générales, observables à l'échelle microstructurale de la lame mince, au microscope optique.

1.1.3 Le système de failles de San Andreas

Le système de failles de San Andreas est un réseau complexe de failles qui s'étend sur plus de 1300 km le long de la côte ouest de l'Amérique du Nord, pour plus de 100 km de large (Wallace, 1990). Ce réseau de failles constitue la frontière entre la plaque Pacifique et la plaque Nord Américaine. La Faille de San Andreas (SAF) est la plus importante de ce réseau (Figure 1.3) et l'une des plus actives au monde parmi les grandes failles continentales. Etant donné sa proximité avec deux grandes villes de Californie (San Francisco et Los Angeles) et ses antécédents sismiques (séisme de Fort Tejon en 1857 (M=7.9) et séisme de San Francisco en 1906 (M=8.2)), c'est l'une des failles les plus étudiées et les plus surveillées au monde.

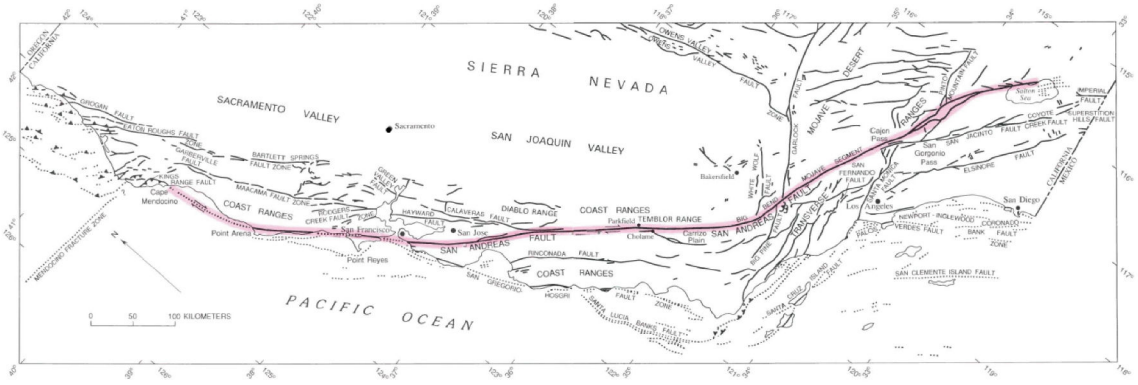

Figure 1.3 : Le réseau de failles de San Andreas en Californie. La faille de San Andreas est mise en évidence en rose (Wallace, 1990).

La faille de San Andreas est de type décrochante dextre et c'est une faille à l'échelle lithosphérique, c'est à dire qu'elle se poursuit à des profondeurs importantes (séismes jusqu'à plus de 10 km et cisaillement en profondeur). Elle recoupe des terrains géologiques variés qui présentent une asymétrie de part et d'autre de la faille (voir carte géologique en Annexe A1). Elle est divisée en différents segments présentant des comportements mécaniques variés (Figure 1.4) (Steinbrugge and Zacher, 1960; Allen, 1968; Wallace, 1970; Irwin and Barnes, 1975).

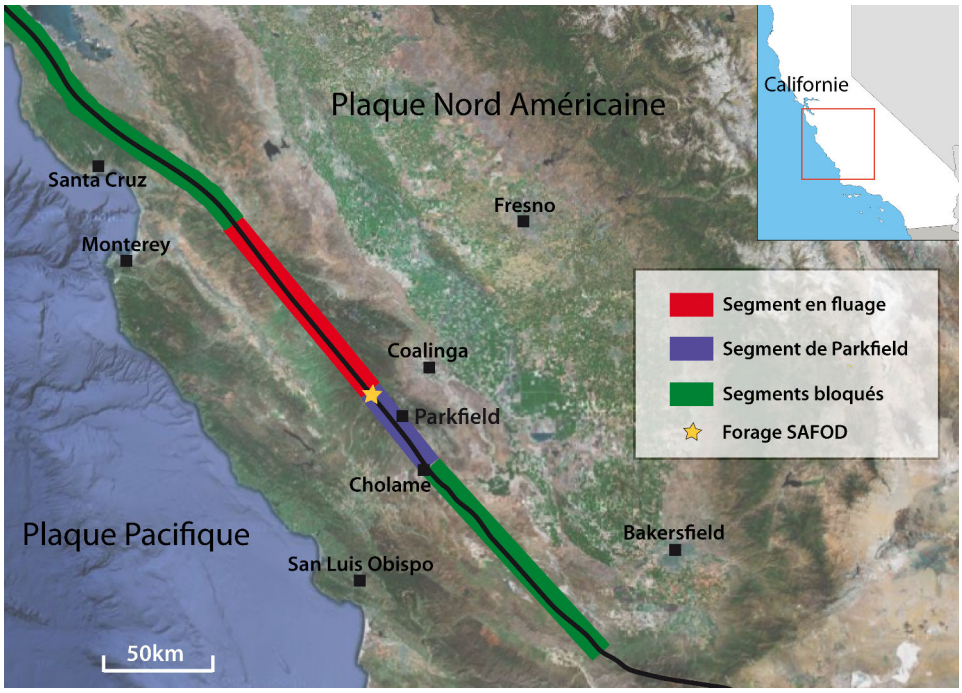

Figure 1.4 : Les différents segments de la faille de San Andreas en Californie centrale et leur comportement.

Le segment de Parkfield (Figure 1.4) est sans doute un des mieux connus car il est sujet à des séismes récurrents de magnitude 6 (7 depuis 1857 tous les 15 à 30 ans) dont le dernier s'est produit en 2004. Un taux de fluage relativement constant et une forte activé microsismique y sont également enregistrés. La réunion de ces différents phénomènes est probablement due à sa localisation. En effet, ce segment fait office de transition entre un segment en fluage permanent au Nord et un segment verrouillé au Sud, qui ne bouge que lors d'importants séismes (Fort Tejon en 1857). Cette position particulière en fait un environnement d'étude unique et particulièrement intéressant pour tenter de comprendre les interactions entre les différents processus de faille, la transition entre déformation sismique et déformation asismique, ainsi que son partitionnement.

De très nombreuses études ont été menées et sont toujours en cours sur la faille de San Andreas, dans des domaines variés, offrant une bibliographie riche et abondante. En ce qui concerne cette étude, nous nous sommes attachés à comprendre les mécanismes de fluage à l'œuvre dans la zone de fluage permanent près de Parkfield. Mais qu'entend-t-on réellement par fluage ?

1.2 Le fluage : une déformation asismique

1.2.1 Les types de fluage

Le fluage est une déformation asismique lente et irréversible qui permet de relaxer des contraintes sans provoquer de rupture majeure au sein du matériel. Dans le cas d'une faille expérimentant du fluage, cela lui permet d'accommoder une partie des contraintes tectoniques auxquelles elle est soumise, sans produire de séismes.

Au niveau des failles, on peut faire la distinction entre deux types de fluage. Premièrement, le fluage de type post-sismique qui va se développer durant des périodes pouvant aller du mois à des dizaines d'années à la suite d'un séisme et qui va donc agir de façon relativement ponctuelle. Ce type de fluage peut aussi bien être localisé dans la croûte inférieure sous la partie sismique de la faille, que dans la croûte supérieure, au niveau des zones de sismicité (Gao et al., 2000; Johanson et al., 2006; Murray and Langbein, 2006; Barbot et al., 2009). Deuxièmement, le fluage dit permanent, qui est associé à des propriétés spécifiques liées aux roches de la zone de faille ainsi qu'à leur

environnement. Pour ce type de fluage, le taux de déformation aura tendance à rester relativement constant au cours du temps (Burford and Harsh, 1980; Azzaro et al., 2001; Titus et al., 2006). Ce second type de fluage est souvent associé à une intense activité microsismique (Rubin et al., 1999; Nadeau et al. 2004).

1.2.2 Où trouve-t-on des failles qui fluent ?

Comme nous l'avons vu un peu plus haut, la faille de San Andreas est sujette au fluage et elle en présente les deux types. L'un de ses segments expérimente un fluage permanent et constant à 2,5 cm/an (Titus et al., 2006; Burford and Harsh, 1980), tandis qu'un autre, le segment de Parkfield, subit du fluage post-sismique suite aux séismes récurrents dits de type Parkfield. Ce fluage post-sismique a d'ailleurs pu être mieux étudié à la suite du dernier séisme qui s'est produit sur ce segment en 2004 (Johanson et al, 2006; Freed, 2007). Etant donné sa proximité avec le segment en fluage permanent, le segment de Parkfield subit également une partie du taux de fluage permanent (Titus et al., 2006). Il y a d'autres failles dans le réseau de San Andreas qui expérimentent du fluage. Parmi les plus connus on peut citer la faille de Calaveras (Rogers and Nason, 1971) et la faille de Hayward (Lienkaemper et al., 2001).

On trouve bien évidemment des failles qui fluent dans le reste du monde. Pour exemple, nous pouvons citer la faille en chevauchement de Chihshang (4,5 cm/an) qui est l'un des segment de la grande faille de la Longitudinal Valley à Taiwan (Yu and Liu, 1989; Lee et al., 2003). Le fluage permanent sur le segment Est de la faille Pernicana en Italie (Mt. Etna) a également fait l'objet d'une étude suivie pour estimer si ce taux de fluage variait dans le temps (Azzaro et al., 2001). Celui-ci s'est révélé relativement constant, avec un taux d'environ 2,8 mm/an.

De nombreuses failles actives dans le monde peuvent subir du fluage post-sismique ou du fluage permanent, avec des taux de déformation plus ou moins importants. L'étude du fluage sur les failles actives s'est considérablement développée ces trente dernières années. Ceci est dû au fait qu'il était difficile de l'observer sans quelques outils géodésiques sur de longues périodes de temps, pour pouvoir bien le caractériser. Ce qui nous amène maintenant à introduire la façon dont le fluage peut être détecté, notamment à l'échelle générale de la faille.

1.2.3 Comment observe-t-on le fluage ?

Puisque le fluage est une déformation asismique, il est impossible de l'observer sur les enregistrements sismiques, mise à part son association fréquente avec une certaine microsismicité. C'est d'abord sur le terrain qu'il sera le plus visible. Les déformations dans le paysage, escarpements, bombements et décalages (Figure 1.5), sont les marqueurs les plus visibles de la présence d'une faille active. Lorsque celle-ci est asismique ces marqueurs sont les principales évidences attestant d'une déformation par fluage.

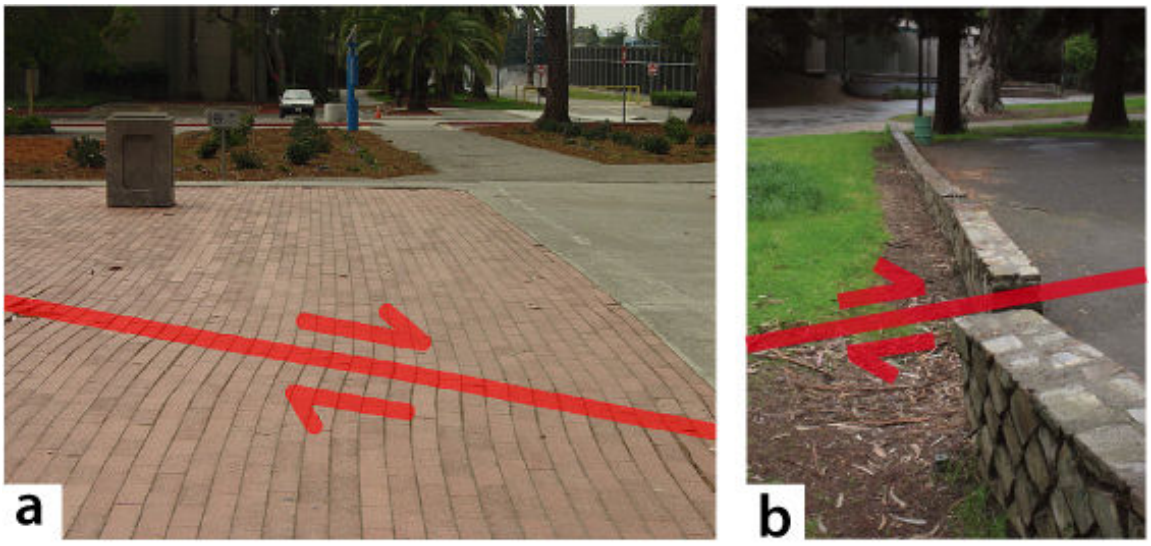

Figure 1.5 : Evidences de failles en fluage. (a) Décalage dans un sol pavé dans la partie nord du campus de Contra Costa Community College, Californie (source : USGS). (b) Décalage dans un muret datant de 1930 dans le Hayward's Memorial Park, témoin du fluage sur la faille d'Hayward (Photo de John Karachewski).

Actuellement, le fluage s'observe principalement à l'aide de mesures GPS (Global Positioning System) et INSAR (Interferometric Synthetic Aperture Radar) qui permettent de détecter le fluage sur une faille à une échelle globale et de déterminer un taux de déformation général. L'INSAR permet de délimiter précisément la ou les surfaces des zones en fluage y compris dans le cas où la déformation est répartie sur plusieurs zones. Enfin, ces méthodes sont capables de mettre en évidence des hétérogénéités spatiales et temporelles de vitesse de déformation. Plus localement, on utilise des extensomètres qui permettent d'estimer le taux de déplacement avec plus de précision, directement sur la faille et d'assurer le suivi et la surveillance continue de zones

sensibles. Ils peuvent aussi être installés dans des endroits où les mesures GPS ou INSAR sont malcommodes voire impossibles.

Ainsi, l'étude du fluage peut se faire à l'échelle de la faille en surveillant l'évolution du taux de déformation sur le long terme (Titus et al., 2006) ou encore en estimant l'importance des contraintes relaxées par un fluage post-sismique suite à un séisme important (Beeler et al., 2001; Johanson et al., 2006; Murray and Langbein, 2006). Ce type d'étude a révélé l'importance de ce mécanisme au sein du cycle sismique.

1.2.4 Limites et difficultés posées par l'étude des failles

L'étude des failles s'est longtemps basée sur les observations de terrain faites sur des éléments de failles exhumées. Ces travaux constituent la plupart de nos connaissances en termes de structures, de compositions et de mécanismes de déformations des failles. Cette méthode permet d'appréhender les différents types de failles et d'en étudier une très vaste population. Néanmoins, cette méthode est indirecte et peut être sujette à de nombreuses interprétations différentes. L'étude des mécanismes ayant lieu en profondeur à partir des observations effectuées sur les surfaces exhumées peut vite devenir délicate. En effet, lorsqu'une surface est ainsi exhumée, elle peut subir de nombreuses altérations, que ce soit au cours même de son exhumation ou par érosion, une fois à l'air libre (Zoback et al., 2007). A partir des études de failles exhumées, ce sont surtout les informations sur l'état des fluides en profondeur qui sont difficiles à appréhender. Les études sur les processus de faille via les expérimentations de laboratoire sont souvent difficiles à mettre en place sans connaître précisément les différents paramètres physiques des mécanismes ayant lieu en profondeur. De plus, étant donné la lenteur de certains de ces processus, le facteur temps devient vite, au laboratoire, un problème important dans ce genre d'expérimentation. Ceci étant, des développements récents permettant de générer au laboratoire d'une part des glissements à vitesse sismique (par des machines en rotation : Shimamoto and Tsutsumi, 1994; Di Toro et al., 2011), et d'autre part du fluage très lent avec transferts de matière (Niemeijer and Spiers, 2006; Gratier et al., 2009), ont permis de faire progresser nos connaissances notamment sur l'abaissement de friction lors des séismes et sur la cinétique des réactions fluides-roches sous contraintes. Ces travaux expérimentaux ouvrent de nouvelles perspectives, en particulier sur les

interactions entre processus sismique et asismique et entre friction et transfert de matière. Les systèmes étudiés restent cependant encore très simples par rapport à la complexité des systèmes naturels.

Les outils d'étude géophysique tels que les profils sismiques ou la tomographie ont permis une première approche de la complexité des failles en profondeur en donnant des informations sur leur géométrie, ou sur la répartition de la déformation au cours d'un séisme. Mais si ces outils sont capables de déterminer avec plus ou moins de fiabilité la géométrie de la faille en profondeur, ils ne donnent que peu de renseignements sur les processus physico-chimique ayant lieu à ces profondeurs. Les modélisations numériques ont été un bon substitut aux expérimentations de laboratoire car elles permettent de passer outre le facteur temps souvent trop conséquent. Mais ces modélisations requièrent à leur tour la connaissance des conditions in situ pour établir des modèles les plus proches possibles de la réalité.

1.3 L'apport des forages

1.3.1 La problématique de l'étude des faille

Comme nous venons de le voir, la plupart des moyens d'études nous permettant d'appréhender les processus de faille en profondeur sont très approximatifs. Ce qui nous amène à la problématique générale que tout chercheur travaillant sur les failles a probablement retourné dans son esprit un jour ou l'autre : mais que se passe-t-il réellement en profondeur ? Cette inaptitude a pouvoir accéder à la majeure partie de son objet d'étude est pour le moins frustrante… et génératrice d'une foule de questions plus pertinentes les unes que les autres. Quels sont les mécanismes qui amènent à la nucléation d'un séisme ? Quels sont ceux qui donneront un glissement asismique ? Quels sont les paramètres in situ qui favorisent ces mécanismes et qui déterminent le comportement de la faille ? Ces questions générales soulignent le problème majeur dans l'étude des faille : nous ne pouvons pas nous rendre sur place et accéder au matériel in situ pour savoir ce qui se passe vraiment en profondeur. La multiplication des observations et des expérimentations de laboratoire n'a cessé d'allonger la liste des questions majeures relatives à l'étude de la mécanique des failles (Zoback et al., 2007;

2011) : comment varient les contraintes à travers la zone de faille, que ce soit au niveau de leur orientation ou de leur magnitude ? Comment évoluent la pression fluide et la perméabilité dans la zone de faille et dans son environnement ? D'où viennent les fluides présents dans les zones de faille et quelle est leur composition ? Les gouges de faille sont des zones très particulières qui soulèvent toute une série de questions à elles seules : quelles sont les propriétés inhérentes aux gouges de failles ? Comment influent-elles sur le comportement de la faille ? Quelle est leur minéralogie et comment évolue-t-elle au cours du temps ? Quels sont les mécanismes de déformations aboutissant à leur formation ? Cette dernière question entraine à son tour celles relatives à la localisation des déformations. Quels sont les processus contrôlant la localisation du glissement et de la déformation ? Comment la rupture sismique se propage-t-elle (Zoback et al., 2007; Brodsky et al., 2009) ? Toutes ces questions sont venues étayer la nécessité de trouver un moyen d'aller recueillir des données directement au cœur des failles. Actuellement, la seule façon de faire des mesures *in situ* et de prélever du matériel en profondeur est de réaliser un forage.

1.3.2 Les apports des grands forages d'étude

Différents forages d'études ont été réalisés à travers le monde sur de grandes failles actives sensibles, souvent sujettes à des séismes de fortes magnitudes, ou présentant un contexte particulièrement intéressant pour répondre aux questions majeures vues précédemment. Parmi ces grands forages, nous pouvons citer :

- le forage Taiwan Chelungpu fault Drilling Project (TCDP), qui a débuté en 2002 sur la faille de Chelungpu (Taiwan) et s'est terminé en 2005. Il a été initié pour comprendre les mécanismes responsables du séisme de Chi-Chi de 1999 (M=7.6), étudier les mécanismes de nucléation et de rupture des grands séismes et identifier le rôle joué par la faille inverse de Chelungpu dans la tectonique régionale (Tanaka et al., 2002; Ma et al., 2003; Zoback et al., 2007; Boullier, 2011).

- le forage du Corinth Rift Laboratory project (CRL), s'est déroulé sur la faille Aigion (localisée du côté sud du golf) en Grèce en 2002. Ce forage a été réalisé pour étudier la déformation in situ d'une faille normale ainsi que les processus de rifting et enfin, pour surveiller les interactions fluide/faille (Cornet et al., 2004; Zoback et al.,

2007).

- les forages du Nankai Trough Seismogenic Zone Experiment (NanTroSEIZE), dans la zone de subduction de Nankai située au large de l'île d'Honshu (Japon), ont commencé en 2004. Cette zone est sujette a des séismes de magnitude 8 se produisant à des intervalles de 100 à 200 ans (Lin et al., 2010). Ce projet a été découpé en plusieurs expéditions, chacune devant répondre à un but précis. Les objectifs principaux de ce grand projet étaient de caractériser les propriétés des matériaux et l'état du système de faille, étudier le partitionnement entre processus sismique et asismique, évaluer les changements dans l'état du système durant la période intersismique et récolter des échantillons *in situ* (Zoback et al., 2007).

- les forages dans la faille de Nojima, au Japon, ont été réalisés un an après le séisme qui a frappé Kobé en 1995 (M7.2). Ce fut un projet pionnier pour l'étude des failles actives. Il a permis une étude détaillée de la minéralogie de la faille grâce aux échantillons prélevés durant le forage (Boullier, 2011).

- les forages du Natural Earthquake Laboratory in South African Mines (NELSAM), basés sur la faille de Pretorius en Afrique du Sud, ont été réalisés dans les mines d'or profondes situées à environ 80 km à l'ouest de Johannesburg. L'environnement des mines dont les processus d'extraction génèrent des milliers de séismes par jour offrait un cadre d'étude unique. Ce forage aura permis la cartographie 3D de la zone de rupture d'un séisme, ainsi que l'enregistrement de nombreuses données. Il a également fourni des informations sur la structure et la composition de la faille en profondeur.

Cette liste est évidemment non exhaustive et l'utilité des forages ayant fait ses preuves, d'autres projets sont en cours sur diverses grandes failles dans le monde. Mais il reste évidemment un grand forage d'étude dont nous n'avons pas parlé et que nous allons à présent voir plus en détail : le forage de la faille de San Andreas.

1.3.3 Le forage SAFOD

Le forage du San Andreas Fault Observatory at Depth drilling project (SAFOD) est localisé en Californie, sur la faille de San Andreas, près de la ville de Parkfield, sur le segment éponyme. Il se trouve également à la transition avec le segment en fluage

permanent (Figure 1.4). Cet emplacement stratégique offre un contexte d'étude unique puisqu'il est à la fois dans une zone sismique à laquelle s'ajoute un taux de fluage permanent d'environ 21 mm/an (Titus et al., 2006), du fluage post-sismique et une microsismicité permanente depuis au moins vingt ans (Nadeau et al., 1994; 1995). La plupart de ces petits séismes ont été localisés entre 2 et 12 km (Zoback et al., 2007). Les sources de certains de ces séismes récurrents de magnitude 2 se trouvant donc à une profondeur atteignable par forage, elles constituaient une cible parfaite. Par conséquent, l'un des but majeur de ce forage était de forer aussi près que possible de l'un de ces foyers de séismes récurrents, afin d'en étudier tous les paramètres possibles : construction des contraintes, type de relaxation, cicatrisation et restauration de la zone, et ce, sur plusieurs cycles. Les autres buts visaient l'étude des mécanismes physiques et chimiques à l'origine des processus de faille et de la génération de séismes (Zoback et al., 2007, 2011).

Le forage a été effectué en plusieurs phases (Figure 1.6). La toute première, le trou pilote (Pilote Hole) est un trou vertical pour reconnaître la géologie locale et effectuer une première batterie de mesures, notamment à mesurer le champ de contraintes. Cela a permis de mettre en évidence la singularité de l'orientation des contraintes principales dans la faille et de considérer cette dernière comme une faille faible (voir Chapitre 3). Il a aussi servi à confirmer que la localisation du site était bien la plus appropriée et a apporté des réponses à certaines questions de premier ordre concernant l'outillage et l'instrumentation. Le forage du puits principal (mainhole), a ensuite commencé avec la première phase. Celle-ci avait pour but de s'arrêter juste avant l'endroit où était supposée commencer la zone de faille proprement dite et d'être consolidée, pour ensuite faciliter la seconde phase, où de nombreux problèmes allaient probablement être rencontrés. Elle a également servi à établir différents paramètres importants pour le forage en lui-même, relatif par exemple, à la densité de la boue de forage. La phase 2 a servi à effectuer une seconde campagne de mesures qui a permis de localiser précisément la zone de faille et d'identifier des zones de cisaillement actif dont nous allons reparler un peu plus loin. Elle a également fourni de nombreux éléments de roche broyée (cuttings) sur lesquels se sont initiées les premières études d'échantillons *in situ* pour cette faille. Enfin, la phase 3 a consisté en différents puits de forages latéraux, qui ont surtout été utilisés pour remonter des carottes dans lesquelles ont été découpés de

nombreux échantillons et où d'autres mesures ont été effectuées.

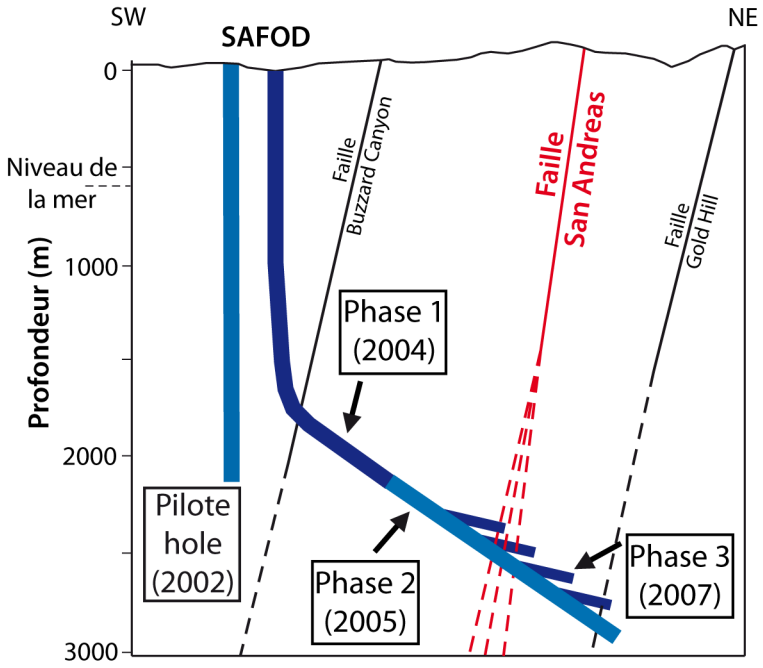

Figure 1.6 : schéma en coupe montrant les différentes phases du forage SAFOD (modifié d'après Zoback et al., 2006; 2010).

Le programme d'étude des échantillons ramenés par le forage SAFOD a été ouvert à la communauté scientifique du monde entier. Un projet international associant les universités de Grenoble (France), Padoue (Italie), Louisville (Etats-Unis), Oslo (Norvège) et Aix la Chapelle (Allemagne) nous a permis d'obtenir plusieurs dizaines d'échantillons issus des carottes, nous fournissant ainsi l'opportunité de pouvoir travailler sur des échantillons prélevés au cœur d'une faille, à plus de 2 km de profondeur.

A l'échelle du forage, des zones de faibles vitesses dans les profils des ondes P et S, ainsi que des anomalies dans les mesures de résistivité ont révélé une zone d'environ 200 mètres de large, dans laquelle les roches étaient fortement endommagées. Cette zone, appelée zone endommagée (damage zone), a à son tour présenté d'autres anomalies encore plus prononcées au niveau des vitesses sismiques et de la résistivité, en deux endroits très localisés (Figure 1.7). Des déformations du tube d'acier installé dans le puits de forage au niveau de ces deux zones ont montré qu'elles subissaient un fluage actif. La première, la SDZ (Southern Deforming Zone), est située entre 3196 m et 3198 m et la seconde, la CDZ (Central Deforming Zone), qui est aussi la plus active, est localisée

entre 3296,5 m et 3299 m (toutes les profondeurs se rapportant à la localisation des échantillons ou de zones particulières dans les puits de forage ne correspondent pas à des profondeurs réelles, mais des mesures de profondeurs relatives le long du forage (pour plus de précision sur les différents systèmes de mesures, voir Chapitre 3, Table 1)). Ces zones ne dépassent pas les 2-3 mètres de large et sont données comme étant les traces actives de la faille de San Andreas. C'est principalement au cours de la Phase 3 que ces zones ont été échantillonnées et qu'elles ont rendu possible l'étude de zones en fluage actif à partir d'échantillons naturels. C'est dans ces zones que nous avons réalisé notre étude sur les processus de fluage, dont les résultats sont présentés Chapitre 3.

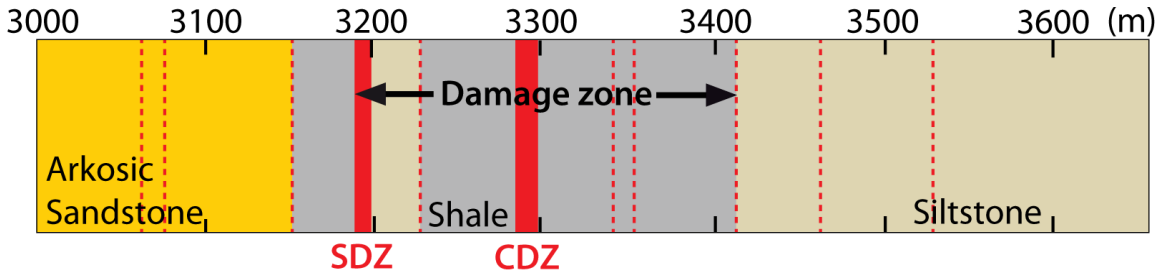

Figure 1.7 : Coupe présentant la géologie globale le long du forage (entre 3000 m et 3700 m) et la localisation des deux zones en fluage actif (en rouge). Les traits en pointillés rouges représentent les failles mineures recoupées par le forage à cet endroit (profondeurs relative à la Phase 3, voir Chapitre 3 Table 1) (après Zoback et al., 2010).

Conclusion

L'un des enjeux majeurs de ces dernières années a été d'élargir notre champ de compréhension du cycle sismique en tentant d'identifier tous les processus qui façonnent et régissent le comportement des failles, déterminant le moment et la localisation de la rupture tant redoutée. Un instant et un lieu, voilà les grandes finalités de l'étude des failles. Pouvoir déterminer exactement où et quand aura lieu le prochain grand séisme relève pourtant encore de la science fiction… Comme nous venons de le voir, les paramètres à prendre en compte sont légions et nos connaissances des différents processus de faille sont encore très parcellaires. Néanmoins, avec l'avènement des forages d'études, de nombreuses avancées ont pu être réalisées dans l'étude des failles, notamment en donnant accès aux mesures physiques et aux échantillons *in situ*. Ces derniers ont ouvert le champ aux études microstructurales des processus de faille que nous venons d'aborder. Et parmi tous ces processus, les candidats potentiels pouvant entrainer un comportement en fluage sont nombreux. Leur recherche et leur identification alimentent de nombreux débats encore d'actualité. Dans le chapitre qui suit, nous proposons de voir un peu plus en détails ces mécanismes de fluage.

Références

Allen, C.R., 1968. The tectonic environments of seismically active and inactive areas along the San Andreas fault system. In W.R. Dickinson and A. Grantz, eds., Proceedings of conference on geologic problems of San Andreas fault system: Stanford, California, Stanford Univ. Pubs. Geol. Sci., 11: 70-82.

Azzaro, R., Mattia, M., and Puglisi, G., 2001. Fault creep and kinematics of the eastern segment of the Pernicana Fault (Mt. Etna, Italy) derived from geodetic observations and their tectonic significance. Tectonophysics 333: 401-415.

Barbot, S., Fialko, Y., and Bock, Y., 2009. Postseismic deformation due to the M_w 6.0 2004 Parkfield earthquake: stress-driven creep on a fault with spatially variable rate-and-state friction parameters. Journal of Geophysical Research, 114, B07405.

Beeler, N.M., Lockner, D.L., and Hickman, H., 2001. A simple stick-slip and creep-slip model for repeating earthquakes and its implications for microearthquakes at Parkfield. Bulletin of the Seismological Society of America, 91: 1797-1804.

Boullier, A.-M, 2011. Fault-zone geology: lessons from drilling through the Nojima and Chelungpu faults. From: Fagereng, A., Toy, V.G. & Rowland, J.V. (eds) Geology of the Earthquake Source: A Volume in Honour of Rick Sibson. Geological Society, London, Special Publications, 359: 17-37.

Brodsky, E.E., Ma, K.-F., Mori, J., Saffer, D.M., and the participants of the ICDP/SCEC International Workshop, 2009. Rapid Response Fault Zone Drilling Past, Present, and Future. Scientific Drilling, 8: 66-74, doi:10.2204/iodp.sd.8.11.2009.

Burford, R.O., and Harsh, P.W., 1980. Slip on the San Andreas Fault in Central California from alignment array surveys. Bulletin of the Seismological Society of America, 70: 1233-1261.

Cornet, F.H., Bernard, P., and Moretti, I., 2004. The Corinth Rift Laboratory. Comptes Rendus Geosciences, 336: 235-241.

Di Toro, G., Han, R., Hirose, T., De Paola, N., Nielsen S., Mizoguchi, K., Ferri F., Cocco, M., and Shimamoto T., 2011. Fault lubrication during earthquakes, Nature 471: 494-498, doi:10.1038/nature09838.

Faulkner, D.R., Jackson, C.A.L., Lunn., R.J., Schlische, R.W., Shipton, Z.K., Wibberley, C.A.J., and Withjack, M.O., 2010. A review of recent developments concerning the structure, mechanics and fluid flow properties of fault zones. Journal of Structural Geology, 32: 1557-1575.

Freed, A.M., 2007. Afterslip (and only afterslip) following the 2004 Parkfield, California,

earthquake. Geophysical Research Letters, 34, L06312.

Gao, S.S., Silver, P.G, and Linde, A.T., 2000. Analysis of deformation data at Parkfield, California: detection of a long-term strain transient. Journal of Geophysical Research, 105: 2955-2967.

Grant, L., 2007. Historical seismicity — Paleoseismology. In Kanamori, H., and Schubert, G., (Eds.), Earthquake Seismology—Treatise on Geophysics Vol.4: Amsterdam (Elsevier), 567-585.

Gratier, J-P., Guiguet, R., Renard, F., Jenatton, L., and Bernard, D., 2009. A pressure solution creep law for quartz from indentation experiments. Journal of Geophysical Research, 114, B03403, doi:10.1029/2008JB005652.

Irwin, P.W., and Barnes, I., 1975. Effect of geologic structure and metamorphic fluids on seismic behavior of the San Andreas fault system in central and northern California. Geology, 3: 713-716.

Johanson, I.A., Fielding, E.J., Rolandone, F., and Bürgmann, R., 2006. Coseismic and postseismic slip of the 2004 Parkfield earthquake from space-geodetic data. Bulletin of Seismological Society of America, 96: S269-S282, doi:10.1785/0120050818.

Lee, J.-C., Angelier, J., Chu, H.-T., Hu, J.-C., Jeng, F.-S., and Rau, R.-J., 2003. Active fault creep variations at Chihshang, Taiwan, revealed by creep meter monitoring, 1998–2001. Journal of Geophysical Research, 108, 2528, doi:10.1029/2003JB002394.

Lienkaemper, J.J., Galehouse, J.S., and Simpson, R.W., 2001. Long-term monitoring of creep rate along the Hayward Fault and evidence for a lasting creep response to 1989 Loma Prieta Earthquake. Geophysical Research Letters, 28: 2265–2268.

Lin, W., Doan, M.-L., Moore, J.C., McNeill, L., Byrne, T.B., et al., 2010. Present-day principal horizontal stress orientations in the Kumano forearc basin of the southwest Japan subduction zone determined from IODP NanTroSEIZE drilling Site C0009. Geophysical Research Letters, 37, L13303, doi:10.1029/2010GL043158.

Ma, K.-F., Brodsky, E.E, Mori, J., Song, C., Ji, T.R., and Kanamori, H., 2003. Evidence for fault lubrication during the 1999 Chi-Chi, Taiwan, earthquake (Mw 7.6). Geophysical Research Letters 30: 1244, doi:10.1029/2002GL015380.

Mittempergher, S., 2012. Physico-chemical processes in seismogenic faults: active and exhumed examples. Thèse de doctorat, Université de Grenoble.

Murray, J., and Langbein, J., 2006. Slip on the San Andreas Fault at Parkfield, California, over two earthquake cycles, and the implications for seismic hazard. Bulletin of Seismological Society of America, 96, S283-S303, doi:10.1785/0120050820.

Nadeau, R.M., Michelini, A., Uhrhammer, R.A., Dolenc, D., and McEvilly, T.V., 2004. Detailed kinematics, structure and recurrence of micro-seismicity in the SAFOD target region. Geophysical Research Letters, 31, L12S08, doi:10.1029/2003GL019409.

Nadeau, R.M., Foxall, W., and McEvilly, T.V., 1995. Clustering and periodic recurrence of microearthquakes on the San Andreas fault at Parkfield, California. Science 267: 503-507.

Nadeau, R., Antolik, M., Johnson, P., Foxall, W., and McEvilly, T.V., 1994. Seismological studies at Parkfield III: Microearthquake clusters in the study of fault-zone dynamics. Bulletin of the Seismological Society of America 87: 1463-1472.

Niemeijer, A.R., and Spiers, C.J., 2006. Velocity dependence of strength and healing behaviour in simulated phyllosilicate-bearing fault gouge. Tectonophysics, 427: 231-253.

Rogers, T.H., and Nason, R.D., 1971, Active fault displacement on the Calaveras fault zone at Hollister, California. Seismological Society of America Bulletin, 61: 399-416.

Rubin, A.M., Gillard, D., and Got, J.L., 1999. Streaks of microearthquakes along creeping faults. Nature, 400: 635-641.

Scholz, C., 2002. The mechanics of earthquakes and faulting. Cambridge University Press, 2 mai 2002, 471p.

Shimamoto, T., and Tsutsumi, A., 1994. A new rotary-shear high-speed frictional testing machine: its basic design and scope of research [in Japanese with English abstract]. Journal of the Tectonic Research Group of Japan, 39: 65–78.

Steinbrugge, K.V., and Zacher, E.G., 1960. Creep on the San Andreas fault. Fault creep and property damage. Seismological Society of America Bulletin, 50: 389-396.

Tanaka H., Wang, C.Y., Chen W.M., et al., 2002. Initial science report of shallow drilling penetrating into the Chelungpu fault zone, Taiwan. Terrestrial, Atmospheric and Oceanic Sciences 13: 227-251.

Titus, S.J., DeMets, C., and Tikoff, B., 2006. Thirty-five-year creep rates for the creeping segment of the San Andreas Fault and the effects of the 2004 Parkfield earthquake: constraints from alignment arrays, continuous global positioning system and creepmeters. Bulletin of the Seismological Society of America, 96: S250-S268.

Wallace, R.E., 1990. General features. In: R.E. Wallace, The San Andreas Fault System, California. USGS Professional Paper 1515, Washington, 283p.

Wallace, R.E., 1970. Earthquake recurrence intervals on the San Andreas fault. Geological Society of America Bulletin, 81: 2875-2890.

Yu, S.-B., and Liu, C.-C., 1989. Fault creep on the central segment of the longitudinal valley fault, eastern Taiwan. Proceedings of the geological society of China, 32: 209-231.

Zoback, M.D., Hickman, S., Ellsworth, W., and the SAFOD Science Team, 2011. Scientific drilling into the San Andreas fault zone — An overview of SAFOD's first five years. Scientific Drilling, 11: 14-28, doi:10.2204/iodp.sd.11.02.2011.

Zoback, M., Hickman, S., and Ellsworth, W., 2010. Scientific drilling into the San Andreas fault zone. Eos (Transactions, American Geophysical Union), 91: 197–199.

Zoback, M.D., Hickman, S., and Ellsworth, W., 2007. The role of fault zone drilling. In Kanamori, H., and Schubert, G., (Eds.), Earthquake Seismology—Treatise on Geophysics Vol.4: Amsterdam (Elsevier), 649-674.

Zoback, M.D., 2006. SAFOD penetrates the San Andreas Fault. Scientific Drilling, Special Issue 2: 32-33.

CHAPITRE 2
Les mécanismes de fluage

Introduction

Nous avons vu qu'il existait des outils pour détecter et surveiller le fluage à l'échelle de la faille, mais qu'en est-il des mécanismes responsables de ce comportement ? Comment étudie-t-on ces mécanismes à l'échelle de l'échantillon et du microscope ? Quels sont les marqueurs qui permettent de les distinguer et de les identifier ? Comment fonctionnent-ils et dans quel contexte peuvent-ils être actifs ? Comment quantifier les déformations qu'ils accommodent ? Ce chapitre a pour but de fournir une première approche des deux grands mécanismes de fluage abordés en détails dans le Chapitre 3. Il se propose également de donner un aperçu de la diversité des mécanismes pouvant conduire à ce type de déformation asismique.

2.1 Le fluage par dissolution cristallisation

2.1.1 Principes

Le fluage par dissolution-cristallisation sous contraintes est un mécanisme de déformation ductile largement répandu dans les roches de la croûte terrestre (Rutter 1983; Gratier, 1987). Il consiste en un transfert de matière, assisté par l'intermédiaire de fluides. Ces fluides peuvent être piégés (cas des films fluides très fins aux contacts inter-grains, Renard et Ortoleva, 1997). Ils peuvent également être libres (dans le réseau de pores ou dans des fractures). La taille du système clos est la taille pour laquelle la quantité de matière dissoute est égale à la quantité de matière recristallisée. Cette taille peut varier de l'échelle du grain (avec un transfert par diffusion) jusqu'à celle d'un massif (des

transferts advectifs sont alors requis). A une échelle donnée, celle des grains par exemple, on peut ainsi avoir un système clos (quantités dissoutes et re-précipitées égales) ou ouvert (dissolution sans dépôt par exemple).

Le principe de base est simple : sous l'effet des contraintes, les espèces solubles (comme le quartz, la calcite, le feldspath, la serpentine, etc.), vont se dissoudre progressivement et quitter la zone de contrainte maximum dite de dissolution, via une diffusion dans la phase fluide piégée sous contrainte (Paterson, 1973; Weyl, 1959). Selon la taille du système clos, ces espèces solubles vont précipiter dans une zone de dépôt qui sera très proche de la zone de dissolution, ou plus ou moins éloignée. Cette migration des espèces solubles conduit alors, dans la zone de dissolution, à une concentration passive des espèces dites insolubles (phyllosilicates, oxydes métalliques, etc.) (Figure 2.1).

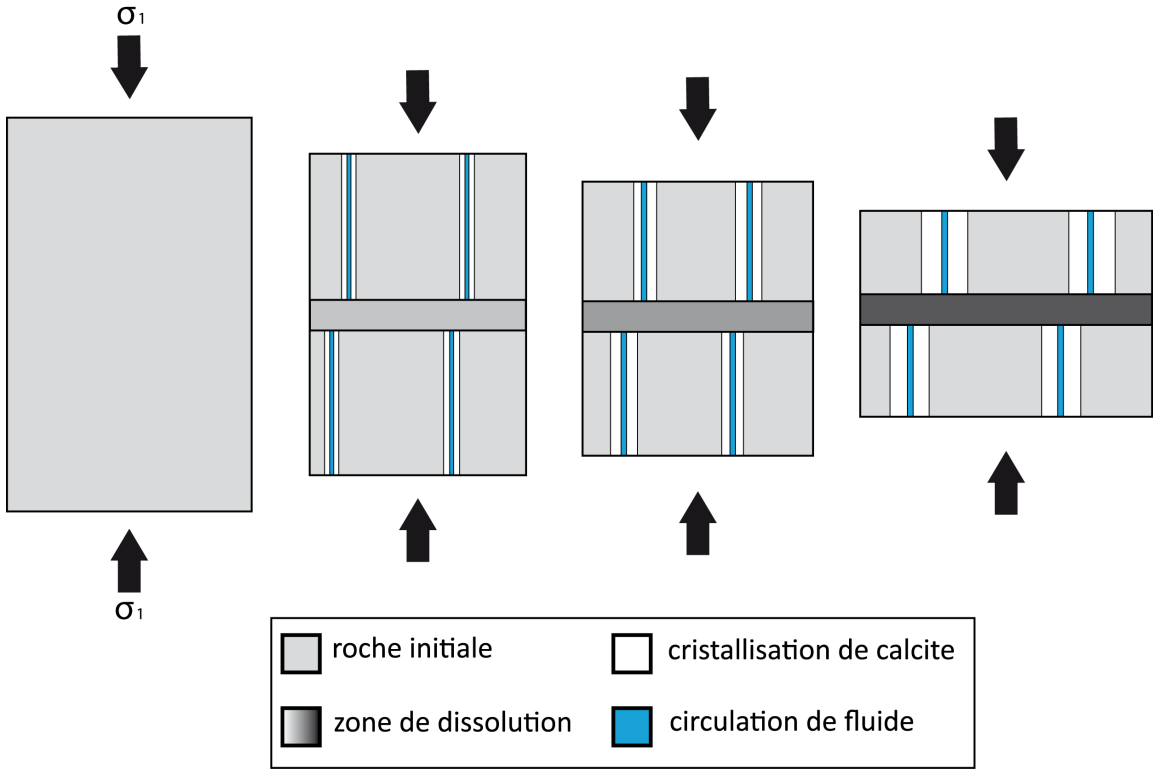

Figure 2.1 : schéma illustrant les principes de base du mécanisme de dissolution cristallisation. Au fur et à mesure du temps, la zone de dissolution présente une concentration en minéraux insolubles de plus en plus marquée (en gris foncé), tandis que les zones de recristallisation s'étendent au détriment des zones initiales.

Le mécanisme de dissolution-cristallisation sous contrainte se résume ainsi à trois étapes : une étape de dissolution, une étape de transfert, par diffusion le long de la phase

fluide piégée puis transfert éventuellement par advection de fluides libres, et enfin, une étape de dépôt/cristallisation. Par conséquent, la vitesse de ce mécanisme sera limitée par l'étape comprenant le processus le plus lent. Celui-ci étant variable selon le contexte et les conditions initiales, on va donc trouver différentes lois pouvant décrire le fluage par dissolution-cristallisation (Raj, 1982; Lehner, 1995; Zhang et al., 2002; Gratier et al., 2013). Cependant, dans la majorité des cas, la phase la plus lente est celle du transfert par diffusion le long d'un film fluide piégé, qui est requise même en cas d'advection. Dans ce cas, ce processus de diffusion est très lent, ce qui explique la difficulté à reproduire ce mécanisme au laboratoire. La vitesse de déformation la plus rapide possible ne peut guère dépasser 10^{-10} s^{-1} (Niemeijer and Spiers, 2006; Rutter, 1976; Gratier et al., 2013).

Il existe différentes conditions initiales qui influent fortement sur la mise en place et l'efficacité du mécanisme de dissolution-cristallisation. Parmi les plus importantes on peut citer la minéralogie ainsi que la composition du fluide, ce sont elles qui vont influencer la solubilité des minéraux, très important pour ce mécanisme. Il faut également noter qu'il est plus aisé de dissoudre une roche contenant à la fois des espèces solubles et insolubles, qu'une roche constituée d'un seul et même minéral (Gratier et al., 2013; Hickman and Evans, 1991; Zubtsov et al., 2004). La quantité de fluide disponible et l'état d'endommagement de la roche jouent également un rôle important. Nous avons vu qu'une phase fluide plus abondante pouvait accélérer la phase de diffusion et emporter le matériel dissous plus loin (jusqu'à plusieurs kilomètres, Gratier et al., 2013). Si la roche est très fracturée, la distance entre les fractures sera donc très courte, ce qui réduit notablement la distance sur laquelle la matière doit être diffusée et accélère le mécanisme (Figure 2.2a). Ce qui permet d'avoir au final, un taux de déformation plus rapide. Une roche dont la taille moyenne des grains est très petite produira le même effet. Dans ce cas, le mécanisme de dissolution cristallisation se produit à l'interface entre les grains, ce qui leur permet d'accommoder des taux de déformation importants en glissant les uns sur les autres (Paterson, 1995) comme dans les processus de superplasticité (Ashby and Verrall, 1973; Boullier and Gueguen, 1975), mais à plus faible température (Figure 2.2b et Figure 2.10a,b,c).

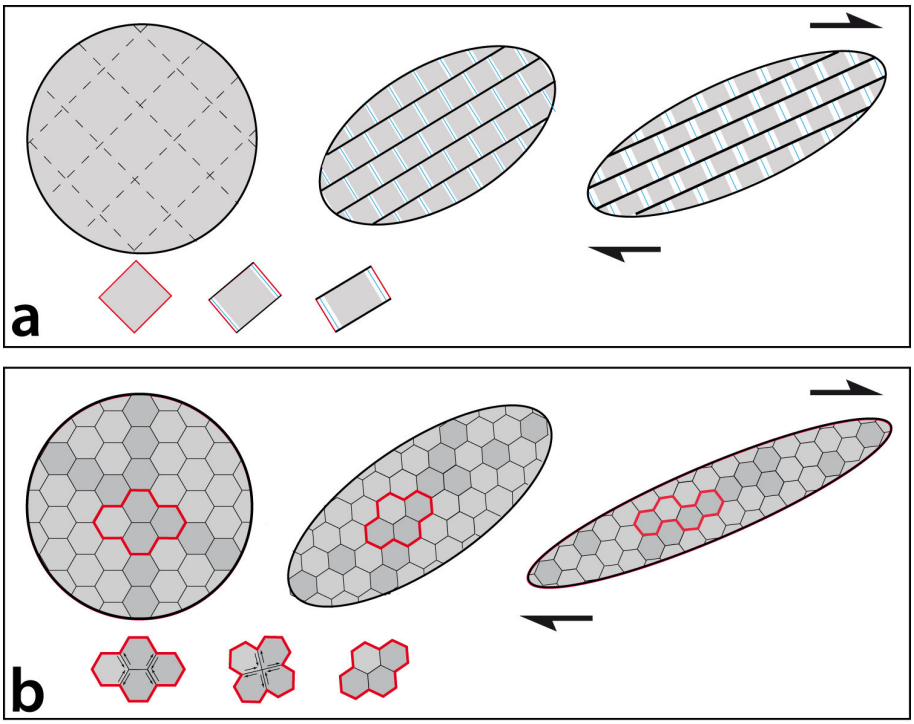

Figure 2.2 : Schéma représentant les deux cas de figure qui permettent d'accélérer la cinétique du fluage par dissolution cristallisation. a. Cas où la distance entre les fractures est la plus petite possible. b. Cas où il n'y a pas ou trop peu de fracturation et où la taille des grains doit être la plus petite possible (modifié d'après Gratier et al., 2011 et Ashby and Verrall, 1973).

Les processus de fracturation et de comminution contribuent donc à activer et à accélérer le fluage par dissolution cristallisation. En revanche, la recristallisation associée à ce mécanisme contribue, au cours du temps, à cicatriser et à colmater les zones de fractures ainsi qu'à réduire la porosité. Ce qui va aboutir à un ralentissement de la vitesse de fluage en raison de l'allongement de la distance sur laquelle doit être transférée la matière. Dans une zone de microsismicité récurrente, comme c'est le cas sur la faille de San Andreas au niveau du segment de Parkfield ou celui en fluage permanent, ce type de fluage peut devenir particulièrement efficace car il s'effectue selon un cycle qui est alors capable de s'auto-entretenir (Figure 2.3).

Le fluage par dissolution cristallisation entraîne une ségrégation chimique de la roche (Gratier, 1987), conduisant à la migration de certains minéraux et à la concentration passive des autres. Ce phénomène favorise le développement d'une foliation, qui est l'un des marqueurs les plus évidents de ce mécanisme, à l'échelle de la microstructure. Nous allons maintenant voir ces marqueurs plus en détails.

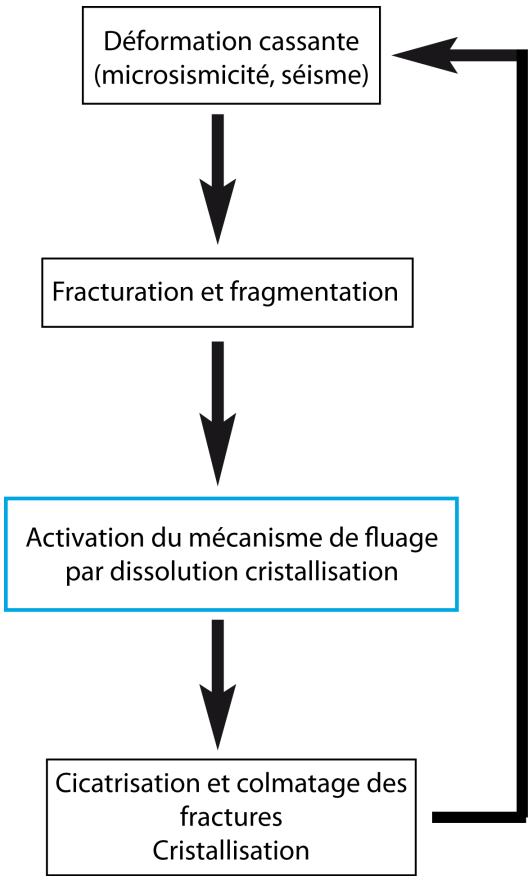

Figure 2.3 : Schéma récapitulatif du cycle du fluage par dissolution cristallisation.

2.1.2 Les marqueurs microstructuraux du fluage par dissolution cristallisation

Comme nous venons de le souligner, le mécanisme de fluage par dissolution cristallisation développe une foliation, dans le cas d'une roche composée à la fois de minéraux solubles et de minéraux insolubles. Ce marqueur évident qui s'observe en lames minces au microscope optique (Figure 2.4a), sera par conséquent introuvable dans le cas d'une roche composée uniquement d'espèces solubles. Et dans ce cas, sauf à trouver des évidences de dissolutions de structures préexistantes (grains, fossiles, veines), il sera difficile de trouver des preuves de ce mécanisme.

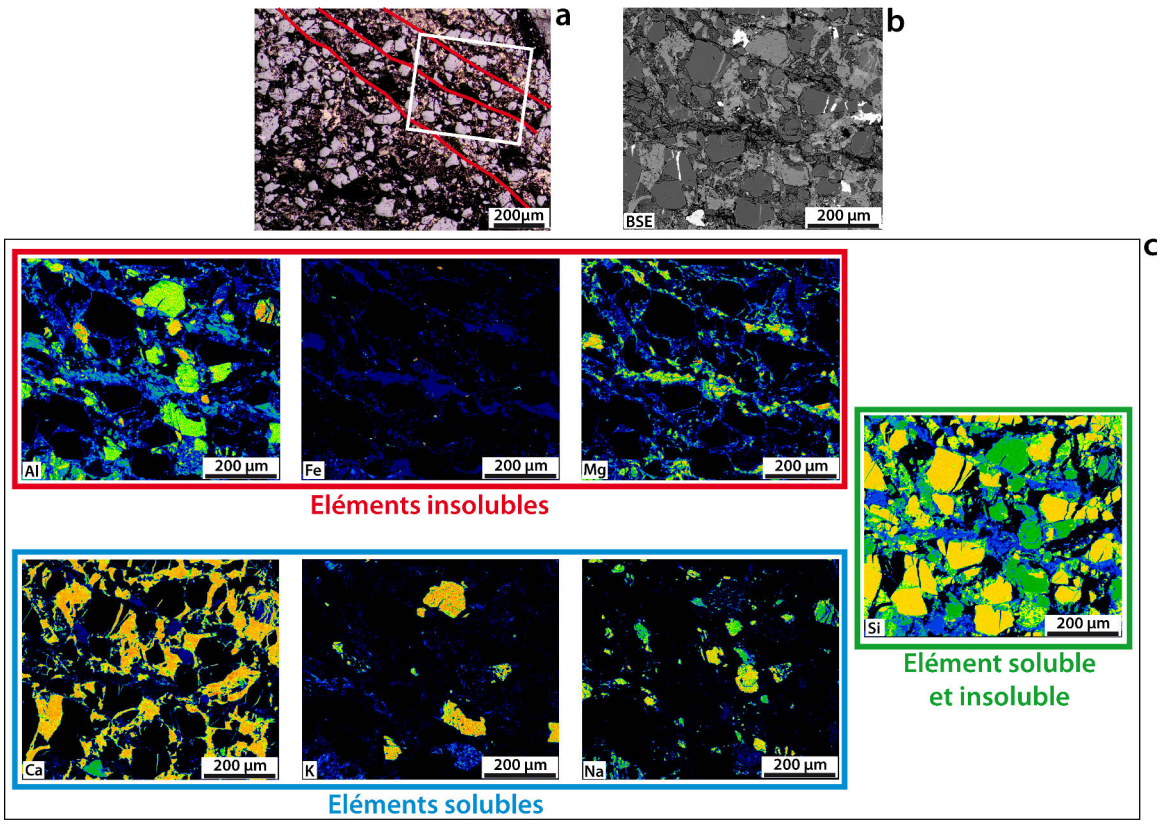

Figure 2.4 : Evidences de foliation développée par dissolution cristallisation dans une lame mince réalisée dans un échantillon provenant de la faille de San Andreas. (a) Photo prise au microscope optique, certains plans de foliation sont représentés en rouge, le cadre blanc correspond aux zooms présentés en b et c. (b) Image BSE réalisée à la microsonde présentant la zone dans laquelle a été réalisé les cartographies chimiques de c. (c) Cartographies chimique réalisées à la microsonde. Les couleurs donnent l'intensité de la présence de l'élément : bleu représentant une présence faible et orange une présence forte.

Cette foliation devient particulièrement évidente en cartographie chimique (Figure 2.4c), où l'on voit bien la concentration des éléments insolubles comme l'aluminium, le fer ou le magnésium, dans les plans de foliation. Ces plans se développent perpendiculairement à la contrainte normale principale en compression (Figure 2.1) dans les zones dites exposées, par opposition aux zones protégées, qui conservent la structure et la composition de la roche initiale. Ces zones protégées se trouvent souvent au voisinage d'un objet dur faisant office de barrière à la déformation (Figure 2.5). Cette foliation par différenciation chimique est le marqueur principal permettant d'identifier de façon fiable le fluage par dissolution cristallisation.

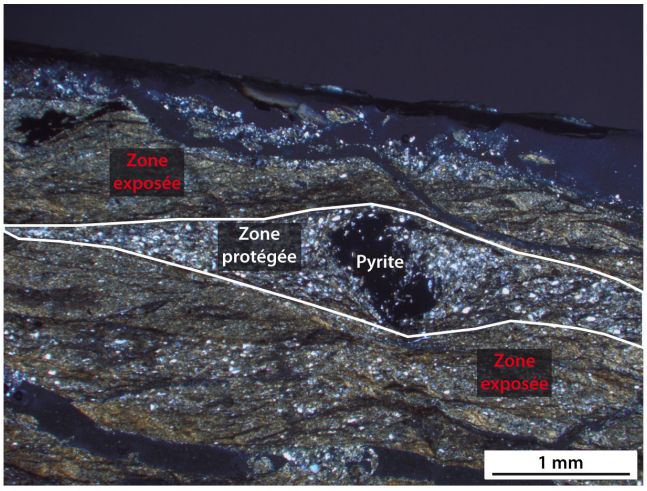

Figure 2.5 : Photo de lame mince au microscope optique montrant un exemple de zone protégée (délimitée par les lignes blanches), au voisinage d'une pyrite et le développement d'une foliation dans les zones exposées de part et d'autres. Echantillon provenant de la faille de San Andreas.

Il existe également d'autres marqueurs, comme les indentations entre deux minéraux (Figure 2.6), souvent accompagnées de fracturation quand leur solubilité respective est très voisine (Figure 2.6a). Un milieu fortement fracturé peut également inciter à rechercher des dissolutions puisque c'est l'un des processus contribuant à activer ce mécanisme de fluage (Gratier et al., 2011) (Figure 2.6).

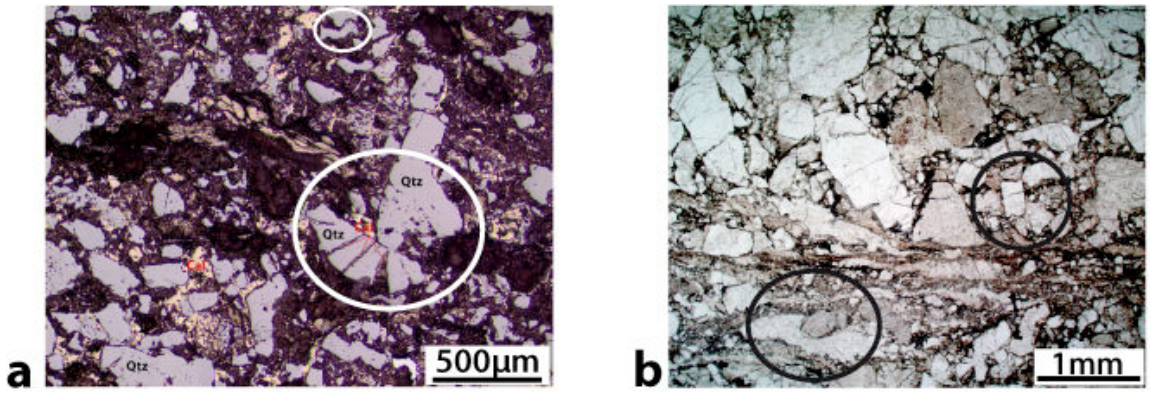

Figure 2.6 : Exemples d'indentation et de fracturation en lames minces (microscope optique). Les cercles noirs et blancs soulignent quelques indentations. (a) Indentations entre minéraux de même nature. (b) Indentations entre minéraux différents. Qtz : quartz, Cal : calcite.

Comme nous l'avons dit plus haut, ce type de fluage entraîne une cicatrisation des fractures lors du transport des espèces solubles. Des évidences de cicatrisation comme de nombreuses veines de calcite pouvant aller jusqu'à des réseaux assez denses présentant plusieurs générations de calcite (Figure 2.7), sont d'autres preuves attestant que le fluage

par dissolution cristallisation a pu être actif à un moment donné dans ces zones et qu'il pourrait encore l'être. Néanmoins, ces marqueurs ne suffisent pas à eux seuls à attester ou non de la présence et de l'activité du fluage par dissolution cristallisation. Il est donc nécessaire de recouper les différentes preuves.

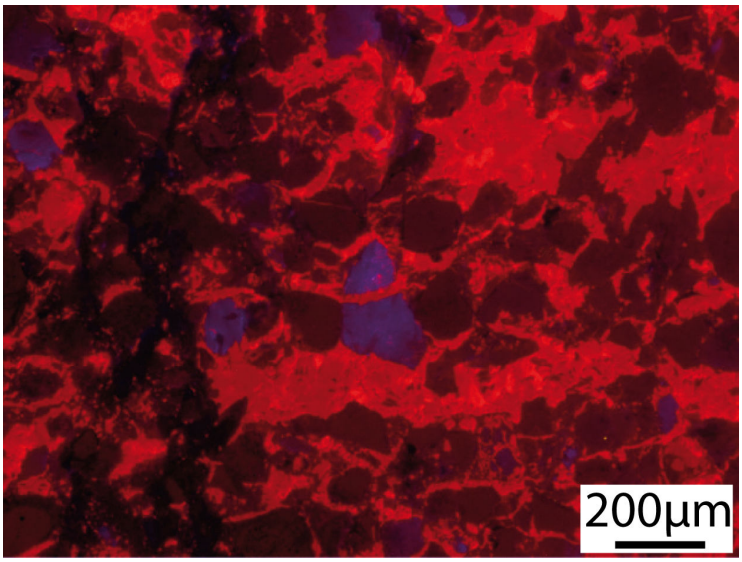

Figure 2.7 : Photo d'une lame mince en cathodoluminescence présentant différentes générations de calcite (en rouges lumineux). Les minéraux en bleu sont des feldspaths et le quartz est brun. Echantillon provenant de la faille de San Andreas.

Ce mécanisme est capable d'accommoder des déformations importantes, tout en étant actif dans de très petits volumes de roche, notamment en raison de sa grande capacité de localisation de la déformation (Gratier et al., 2011).

2.1.3 Quantification des déformations accommodées

Le processus de dissolution, de transfert de matière et de déposition, implique un changement de la composition minéralogique de la zone par rapport à son état initial, avant déformation et donc, un changement de volume. Ce changement peut par conséquent être quantifié par le biais d'un comparatif entre la composition chimique de la zone exposée (ZE) et la composition d'une zone protégée (ZP) censée refléter la composition initiale de la roche. Ce changement de masse peut s'exprimer dans un premier temps en utilisant la concentration passive des minéraux insolubles dans la ZE en la comparant avec la concentration de ces mêmes insolubles dans la ZP :

$$\Delta M/M_0 = (I_p/I_e)-1 \quad (1)$$

où $\Delta M/M_0$ représente le changement relatif de masse, I_p la concentration de tous les insolubles dans la ZP et I_e cette même concentration dans la ZE. Ce calcul peut aussi être effectué pour chaque minéral soluble suivant cette seconde formule :

$$\Delta M_m/M_{m0} = (I_p/I_e)(S_e/S_p)-1 \quad (2)$$

où S_e et S_p représentent la concentration de chaque minéral soluble dans la ZE et dans la ZP, respectivement (Gratier et al., 2013). Ces deux équations sont valables lorsque l'on considère un système ouvert. Dans le cas d'un système clos où les minéraux dissous reprécipitent dans la zone protégée, on utilisera plutôt les équations suivantes :

$$\Delta M/M_0 = ((I_p/I_e)-1)/(I_p/I_e)+1) \quad (3)$$

$$\Delta M/M_0 = ((I_p/I_e)(S_e/S_p)-1)/((I_p/I_e)(S_e/S_p)-1) \quad (4)$$

Ces méthodes peuvent fournir de bons résultats, à partir du moment où aucun autre processus de transfert de matière n'a pu intervenir dans les zones étudiées. Gratier et al., (2011) en fournissent un exemple appliqué aux échantillons provenant de la faille de San Andreas fournis par le forage SAFOD.

Il existe d'autres méthodes pour estimer le changement de volume effectué par les transferts de matière dû au processus de fluage par dissolution cristallisation. Elles peuvent être géométriques (Ramsay, 1967), ou géochimiques, en incluant la différence de densité des zones considérées (Gresens, 1967).

2.2 Le fluage avec friction (cataclastique ou granulaire)

2.2.1 Quelques notions de mécanique

En mécanique, la friction est une force de résistance s'opposant au glissement relatif de deux surfaces l'une contre l'autre (fluide ou solide). Elle est également connue sous la dénomination de force de frottements. Son action est simple, au cours du mouvement de deux surfaces l'une contre l'autre, elle convertit l'énergie cinétique en chaleur. Tous les matériaux possèdent un coefficient de friction μ, sans dimension, qui est défini par la force cisaillante F nécessaire pour produire un glissement entre les deux

surfaces considérées que divise la force normale N appliquée sur les surfaces :

$$\mu = F/N \qquad (5)$$

Plus ce coefficient de friction est faible, plus la force nécessaire à appliquer sur une surface pour la faire glisser sur une autre sera faible. Ce coefficient dépend directement de la nature des matériaux et globalement : $0 < \mu \leq 1$. En mécanique des roches, l'équation (5) peut se réécrire comme suit :

$$\mu = \tau / \sigma_n \qquad (6)$$

où τ représente la force de cisaillement et σ_n la contrainte normale (Byerlee, 1978). De nombreuses expérimentations de laboratoire ont permis de définir le coefficient de friction de la plupart des roches et minéraux (Byerlee, 1978; Scholz, 2002). Ces expérimentations ont également mis en évidence une catégorie de minéraux considérés comme faibles, étant donné leur faible coefficient de friction. Ces minéraux sont principalement des argiles, comme par exemple, la montmorillonite ou la vermiculite. On peut aussi retrouver ces minéraux faibles au niveau des gouges de faille, ce qui influe beaucoup sur le comportement de la faille et met en évidence le rôle important que joue la gouge et sa minéralogie dans la mécanique des failles.

2.2.2 Fluage et friction

Le mécanisme de fluage controlé par friction va surtout intervenir au niveau des gouges de failles. Comme nous venons de le voir, la minéralogie va jouer un rôle prépondérant dans ce mécanisme de fluage. De nombreuses expérimentations se sont attachées à caractériser l'influence de la minéralogie de la gouge sur les propriétés de friction de la zone de faille (Carpenter et al., 2009; Ikari et al., 2009, 2011; Vrolijk and van der Pluijm, 1999; Niemeijer and Spiers, 2006). Tembe et al. (2010), ont ainsi pu mettre en évidence que le coefficient de friction dépendait fortement de la quantité d'argile présente dans la gouge ainsi que de sa minéralogie. Dans plusieurs expérimentations, il a été démontré qu'il fallait en moyenne plus de 50% d'argile dans un environnement quartzo-feldspathique pour que le mécanisme de fluage puisse être efficace sans augmenter significativement la température le long de la faille comme observé dans la faille de San Andreas (Ikari et al., 2009; Tembe et al. 2010; Moore et

Lockner, 2011; Lachenbruch et Sass,1980).

Les conditions requises pour la mise en place de ce type de fluage sont donc une quantité de minéraux argileux (ou phyllosilicates) supérieur à 50% et de préférence, des types d'argiles possédant un coefficient de friction très faible ($\mu \leq 0,2$). Dans le cas des zones en fluage actif de la faille de San Andreas, le principal minéral responsable du faible coefficient de friction de ces zones est la saponite. C'est une argile appartenant à la famille des smectites, dont le comportement est très proche de celui de la montmorillonite et avec un coefficient de friction très faible (< 0,2).

Le fluage avec friction peut intervenir dans deux mécanismes de déformation :

- Le fluage granulaire, (granular flow) durant lequel les grains ou des éléments de grains vont glisser les uns sur les autres sans se déformer en interne, pour accommoder la déformation (Adam et al., 2005; Fossen et al., 2006). Pour un matériel polycristallin avec des éléments argileux, le mouvement des grains les plus durs est accommodé par les minéraux argileux glissant les uns sur les autres et entourant chaque grain. Pour la mise en place de ce processus, la quantité d'argile doit à nouveau être majoritaire par rapport aux grains plus durs, afin d'éviter toute interaction entre ces derniers susceptible de mettre en œuvre d'autres processus.

- Le fluage cataclastique (cataclastic flow) est un processus de déformation courant dans les roches de la croûte terrestre et capable d'accommoder d'importantes déformations (Hadizadeh et Rutter, 1983; Zhu and Wong, 2012). Les processus de cataclase vont fragmenter la roche et même en fracturer les grains. Par la suite, la rotation de ces fragments va permettre de continuer à accommoder la déformation en faisant intervenir des processus de friction aux limites de ces fragments (Sibson, 1977). Dans le cas où la zone s'enrichit en argile, la rotation et le glissement des fragments pourra être assumé de la même façon que dans le fluage granulaire par des glissements privilégiés sur les minéraux argileux. Il est à noter que le développement de foliation avec des lits riches en argiles facilite encore plus le glissement (Collettini et al., 2009). Si la quantité d'argile n'est pas assez importante pour accommoder le mouvement, alors la résistance aux processus de friction peut entraîner d'autres mécanismes, tels que des transferts sous contrainte ou des déformations plastiques.

2.2.3 Evidences en lames minces

A l'échelle de la lame mince, les évidences de ces mécanismes peuvent être difficiles à identifier si plusieurs processus se sont succédés dans la zone. Il est parfois malaisé de déterminer si l'état final observé en lame mince correspond uniquement au dernier épisode de déformation enregistré par la roche, ou si ce résultat est le fruit d'une succession de mécanismes dont on peut remonter la chronologie car chaque étape a laissé ses propres marques.

Néanmoins, dans le cas du fluage granulaire, on pourra observer une quantité d'argile très majoritaire par rapport au pourcentage de grains de minéralogies différentes et ayant un coefficient de friction plus élevé (Figure 2.8). Cette évidence à elle seule témoigne de la forte possibilité d'avoir une zone fluant par faible friction puisque la condition critique à la mise en place de ce mécanisme est satisfaite.

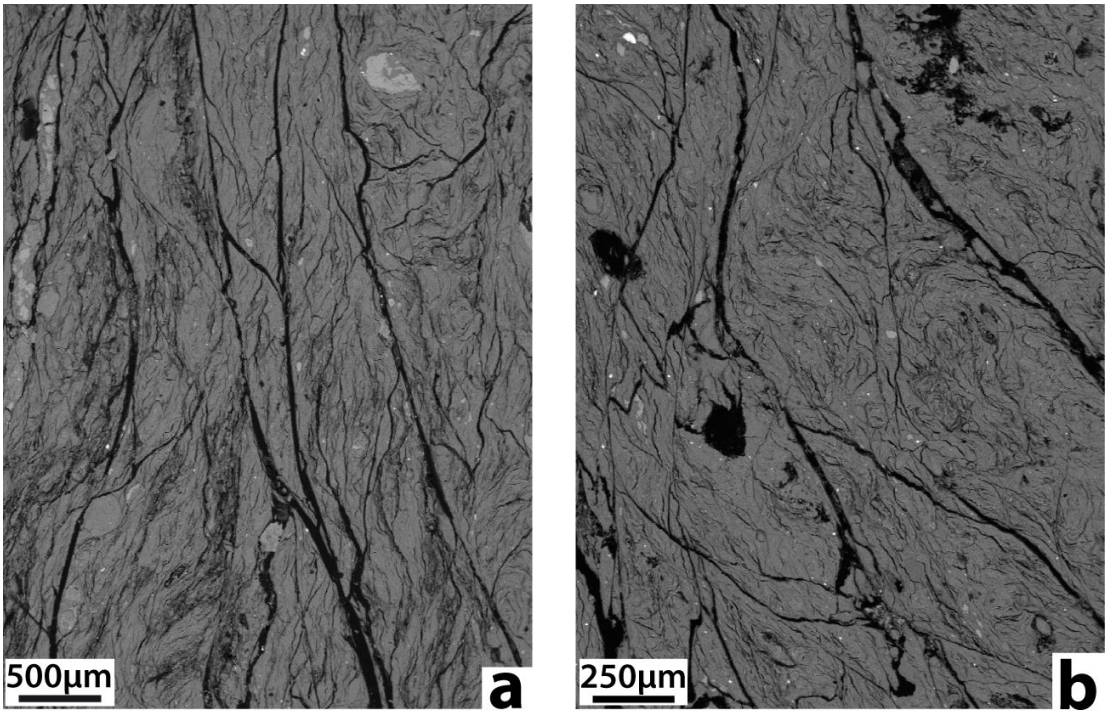

Figure 2.8 : Images BSE prises au MEB montrant des lames minces majoritairement composées d'argile (saponite), par opposition aux petits grains plus durs d'un contraste différent. Echantillons provenant de la zone de fluage actif CDZ de la faille de San Andreas.

On pourra alors observer, au niveau de la structure des argiles une possible orientation préférentielle de la foliation dans les feuillets, si la quantité de grains n'est pas trop

importante. Dans le cas inverse, la rotation des grains entrainée par le mouvement des feuillets d'argiles pourra perturber la mise en place de cette orientation préférentielle et donner naissance aux microstructures chaotiques observées dans les zones de fluage actif de la faille de San Andreas (voir Chapitre 3, Figure 9). Si aucun autre mécanisme n'a joué dans la zone, alors les grains ne seront effectivement ni fracturés, ni déformés et aucune évidence en faveur d'un processus de cicatrisation ne pourra être trouvé. Le cas échéant, étant donné la prépondérance des argiles, cette évidence indiquera que le dernier mécanisme de déformation a été le fluage par faible friction dans le cas du fluage granulaire.

Dans le cas du fluage cataclastique, les fragments de roche et leurs grains vont présenter des microfracturations et leur forme aura subi des transformations suites aux processus de cataclase. Les bordures des fragments et des grains pourront donc présenter un aspect très irrégulier, voir des indentations, ainsi que des évidences de cicatrisation au niveau du colmatage des fractures. Différentes compositions de calcite révélées par des analyses en cathodoluminescence dans les fractures colmatées peuvent indiquer plusieurs cycles de fracturation et de cicatrisation. Des minéraux néoformés peuvent également être observés. Ces évidences sont caractéristiques des roches mylonitiques (Sibson, 1977) que l'on peut notamment retrouver au niveau des gouges de failles. Que le milieu s'enrichisse ensuite en argile par le biais de processus de dissolution cristallisation pouvant être activés lors du fluage cataclastique, ces marqueurs seront néanmoins toujours visibles sur les grains et permettront ainsi d'établir une chronologie dans les différents épisodes de déformation.

2.3 Les autre mécanismes de fluage

2.3.1 La corrosion sous contraintes (stress corrosion)

Ce mécanisme permet le développement de cracks dits sous-critiques au niveau des joints de grains (intergranulaire) ou à travers les grains (transgranulaire). Il est considéré comme le mécanisme le plus important favorisant la croissance de crack sous-critique dans la croûte terrestre (Atkinson, 1984). La croissance de crack sous-critique par corrosion sous contraintes se met en place dans des environnements particuliers du point

de vue chimique, comportant un ou plusieurs agents agressifs pour le matériel considéré. Généralement, l'eau est le principal agent qui va réagir avec le matériel et l'affaiblir. L'action conjuguée de cet affaiblissement liée aux réactions chimiques et des contraintes (résiduelles ou inhérentes), va favoriser le développement de cracks sous-critiques, parallèles à la direction de contrainte principale en compression et perpendiculairement à la direction de la contrainte maximale en traction. La cinétique de ce mécanisme est déterminée par des processus à l'échelle atomique qui se produisent à l'extrémité du crack (Anderson and Grew, 1977). Ce mécanisme est particulièrement redouté dans les constructions en génie civile ou en aéronautique. Dans la nature, le mécanisme de corrosion sous contraintes pourrait jouer un rôle important dans les intrusions magmatiques et les processus de remontée du magma à travers la lithosphère (Anderson and Grew, 1977). Différentes expérimentations sur des grès et des basaltes ont permis de montrer que le mécanisme de fluage par croissance de crack sous-critique dans le cadre du mécanisme de corrosion sous contraintes était fortement lié à la pression et à la température (Heap, 2009), qui sont des paramètres qui contrôlent la cinétique des réactions (avec la nature du fluide). Malgré son efficacité, ce mécanisme resterait associé à de faibles valeurs de déformations finies (Atkinson, 1984).

2.3.2 Fluage par dislocation (dislocation creep) et superplasticité

Le fluage par dislocation se met en place au niveau du réseau cristallin d'un cristal. C'est aussi un mécanisme agissant à l'échelle atomique (Poirier, 1985; Hirth and Tullis, 1992). Il implique des mouvements de dislocation dans le réseau cristallin qui aboutissent à la déformation plastique du cristal considéré. Le principe est simple : une dislocation va se déplacer selon un plan de glissement (glide plan) et entraîner dans son mouvement une partie du réseau cristallin en cassant les liaisons les unes après les autres et en les reformant (Figure 2.9). Ce mouvement du réseau cristallin va entraîner ce que l'on appelle un défaut du réseau, de part et d'autre du plan du glissement, qui sera ici une dislocation (Twiss and Moores, 2000).

Les dislocations se forment suite aux contraintes exercées sur le cristal. Ce mécanisme est donc fortement dépendant des contraintes exercées et de la température. Ce mécanisme est aisé à identifier parce qu'il se traduit par des réorientations cristallines facilement

mesurables au niveau des minéraux (Poirier, 1985).

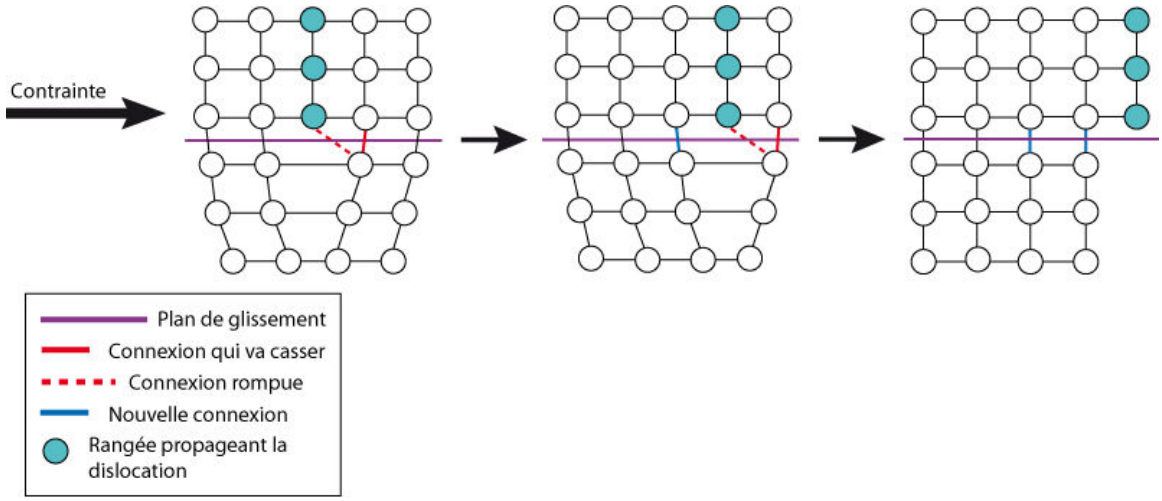

Figure 2.9 : Propagation d'une dislocation dans un réseau cristallin dans le mécanisme de fluage par dislocation.

Nous avons rapidement évoqué le mécanisme de fluage par glissement aux joints de grains précédemment. C'est sur ce principe qu'est basé le mécanisme de fluage par superplasticité avec accommodation par diffusion (Ashby et Verrall, 1973; Boullier et Guéguen, 1975). Le principe de ce mécanisme repose sur le glissement des grains les uns sur les autres au niveau des joints de grain (grain boundary sliding). Ce glissement donne lieu à une légère réorganisation de la position des grains les uns par rapport aux autres, échangeant ainsi leurs plus proches voisins (Figure 2.10a,b,c). Le glissement des grains est accommodé par diffusion dans le solide en bordure de grain ce qui permet d'accommoder de très grandes déformations sans avoir besoin de déformer significativement les grains, comme c'est le cas des fluages de Coble ou de Nabarro-Herring (Figure 2.10d,e,f), qui sont eux associés à des changements de forme des grains par diffusion aux joints de grains ou dans les grains respectivement. Ce glissement des grains peut également être accommodé par d'autres mécanismes qui permettent d'accélérer sa cinétique (Ashby and Verrall, 1973). Ce mécanisme est très efficace pour accommoder les grandes déformations mais il nécessite une température relativement haute, qui ne peut être trouvée, en règle générale, qu'à des profondeurs supérieures à 10 km dans les roches de la croûte terrestre.

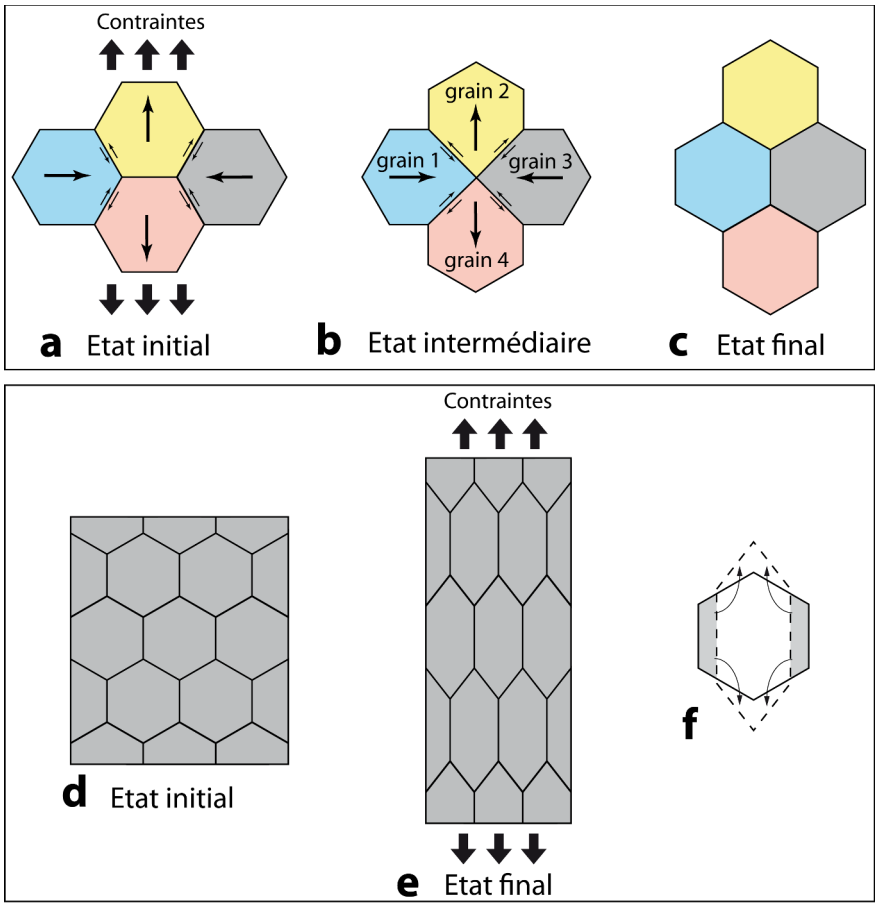

Figure 2.10 : Schémas illustrant différents mécanismes de fluage. (a), (b) et (c) illustrations des différentes étapes du mécanisme de fluage par glissement aux joins de grain accommodé par diffusion. Les grains subissent une déformation minime entre l'état initial et l'état final qui sont thermodynamiquement identiques. (d), (e) et (f) accommodation des contraintes par déformation (allongement) des grains lors des mécanismes de fluage de type fluage par dislocation, Nabarro-Herring ou Coble (modifié d'après Ashby and Verrall, 1973).

2.3.3 Fluage par maclage (twinning)

Le mécanisme de déformation plastique par maclage est très répandu dans la calcite et ceci, pour plusieurs raisons. La première, c'est que ce mécanisme peut se mettre en place dans un environnement où les contraintes de cisaillement sont relativement faibles et la seconde, c'est qu'il peut également se produire à basses températures (<100°C) (Burkhard, 1993; Groshong, 1972). Sous l'effet de contraintes de cisaillement, le maclage permet de développer des déformations au sein des réseaux cristallins (Rowe and Rutter, 1990). Ce type de déformation peut-être trouvé dans des environnements tectoniques variés puisqu'il peut affecter n'importe quel type de roche calcaire, quelque

soit son origine. Néanmoins, le mécanisme de déformation par maclage ne peut pas aboutir à de grandes valeurs de déformation lorsqu'il agit de façon isolée et qu'il n'est couplé à aucun autre mécanisme. Cette limitation réside dans le fait qu'il ne dispose que d'une seule façon d'accommoder les déformations : en glissant par cisaillement individuel des grains, de façon discontinue (Burkhard, 1993). En revanche, on le trouve souvent couplé aux processus de dissolution cristallisation.

Conclusion

Il existe encore d'autres mécanismes de fluage, plus ou moins connus, mais qui ne s'appliquent que peu au contexte des failles. Nous venons de voir que les deux mécanismes les plus influents dans ce domaine sont le fluage par dissolution cristallisation et le fluage avec friction (cataclastique ou granulaire). Ces deux mécanismes jouent un rôle très important au niveau des zones de gouge et par conséquent, des zones de fluage actif. Les évidences que laissent ces deux processus à l'échelle de la lame mince modifient la structure et la minéralogie des roches de la zone de faille, conduisant à une évolution des propriétés mécaniques de ces zones au cours du temps. C'est l'étude et la compréhension des différentes étapes de cette évolution que traite le chapitre suivant.

Référence

Adam, J., Urai, J.L., Wieneke, B., Oncken, O., Pfeiffer, K., Kukowski, N., Lohrmann, J., Hoth, S., van der Zee, W., and Schmatz, J., 2005. Shear localisation and strain distribution during tectonic faulting : new insights from granular-flow experiments and high-resolution optical image correlation techniques. Journal of Structural Geology, 27: 283-301.

Anderson, O.L., and Grew, P.C., 1977. Stress corrosion theory of crack propagation with applications to geophysics. Reviews of Geophysics, 15: 77-104.

Ashby, M., and Verrall, R., 1973. Diffusion-accommodated flow and superplasticity. Acta Metallurgica, 21: 149-163.

Atkinson, B.K., 1984. Subcritical crack growth in geological materials. Journal of Geophysical Research, 89: 4077-4114.

Boullier, A.M., and Guéguen, Y., 1975. SP-mylonites: origin of some mylonites by superplastic flow, Contributions to Mineralogy and Petrology, 50: 93-104.

Burkhard, M., 1993. Calcite twins, their geometry, appearance and significance as stress-strain markers and indicators of tectonic regime: a review. Journal of Structural Geology, 15: 351-368.

Byerlee, J., 1978. Friction of rocks: Pure and Applied Geophysics, 116: 615–626.

Carpenter, B.M., Marone, C., and Saffer, D.M., 2009. Frictional behavior of materials in the 3D SAFOD volume. Geophysical Research letters, 36, L05302.

Collettini, C., Viti, C., Smith, S.A.F., and Holdsworth, R.E., 2009. Development of interconnected talc networks and weakening of continental low-angle normal faults. Geology, 37: 567-570.

Fossen, H., Schultz, R.A., Shipton, Z.K., and Mair, K., 2006. Deformation bands in sandstone: a review. Journal of the Geological Society of London, 164: 755-769.

Gratier, J.-P., Dysthe, D.K., and Renard, F., 2013. The role of pressure solution creep in the ductility of the Earth's upper crust. Advances in Geophysics, 54: 47-179.

Gratier, J.-P., Richard, J., Renard, F., Mittempergher, S., Doan, M.L., Di Toro, G., Hadizadeh, J., and Boullier, A.M., 2011. Aseismic sliding of active faults by pressure solution creep: Evidence from the San Andreas Fault Observatory at Depth. Geology, 39: 1131-1134.

Gratier, J.-P., 1987. Pressure solution-deposition creep and associated tectonic

differentiation in sedimentary rocks. In: Jones, M.E., and Preston, R.M.F., (Eds), Deformation of Sedimentary Rocks. Geological Society Special Publication, 29: 25-38.

Gresens, R.L., 1967. Composition volume relations of metasomatism. Chemical Geology, 2: 47-65.

Groshong, R.H., 1972. Strain calculated from twinnig in calcite. Bulletin of Geological Society of America, 83: 2025- 2038.

Hadizadeh, J., and Rutter, E.H., 1983. The low température brittle ductiel transition in a quartzite and the occurrence of cataclastic flow. Geologische Rundschau, 72: 493-509.

Heap, M.J., 2009. Creep: Time-dependent brittle deformation in rocks. Thèse de doctorat, UCL (University College London).

Hickman, S.H., and Evans, B., 1991. Experimental pressure solution in halite: the effect of grain/interphase boundary structure. Journal of the Geophysical Society, London, 148: 549-560.

Hirth, G., and Tullis, J., 1992. Dislocation creep regimes in quartz aggregates. Journal of Structural Geology, 14: 145-159.

Ikari, M.J., Marone, C., and Saffer, D.M., 2011. On the relation between fault strength and frictional stability. Geology, 39: 83-86.

Ikari, M.J., Saffer, D.M., and Marone, C., 2009. Frictional and hydrologic properties of clay-rich fault gouge. Journal of Geophysical Research, 114, B05409.

Lachenbruch, A.H., and Sass, J.H., 1980. Heat flow and energetics of the San Andreas Fault Zone. Journal of Geophysical Research, 85: 6185-6222.

Lehner, F.K., 1995. A model for intergranular pressure solution in open systems. Tectonophysics, 245: 153-170.

Moore, D.E., and Lockner, D.A., 2011. Frictional strengths of talc-serpentine and talc-quartz mixtures. Journal of Geophysical Research, 116, B01403, doi: 10.1029/2010JB007881.

Niemeijer, A.R., and Spiers, C.J., 2006. Velocity dependence of strength and healing behaviour in simulated phyllosilicate-bearing fault gouge. Tectonophysics, 427: 231-253.

Paterson, M.S., 1995. A theory for granular flow accommodated by material transfer via an intergranular fluid. Tectonophysics, 246: 135-161.

Paterson, M.S., 1973. Nonhydrostatic thermodynamics and its geologic applications. Reviews of Geophysics and Space Physics, 11: 355-389.

Poirier, J.-P., 1985. Creep of Crystals. Ed. Cambridge University Press.

Raj, R., 1982. Creep in polycrystalline aggregates by matter transport through a liquid phase. Journal of Geophysical Research - Solid Earth, 87: 4731-4739.

Ramsay, J.G., 1967. Folding and fracturing of rocks. MacGraw-Hill Book Company, New York, 568p.

Renard, F., and Ortoleva, P., 1997. Water films at grain-grain contacts: Debye-Huckel, osmotic model of stress, salinity, and mineralogy dependence. Geochimica et Cosmochimica Acta, 61: 1963-1970.

Rowe, K.J., and Rutter, E.H., 1990. Paleostress estimation using calcite twinning expérimental calibration and application to nature. Journal of Structural Geology, 12: 1-17.

Rutter, E.H., 1983. Pressure solution in nature, theory and experiment. Journal of the geological Society of London, 140: 725-740.

Rutter, E.H., 1976. The kinetics of rock deformation by pressure solution. Philosophical Transactions of the Royal Society of London, 283: 203-219.

Scholz, C., 2002. The mechanics of earthquakes and faulting. Cambridge University Press, 2 mai 2002, 471p.

Sibson, R.H., 1977. Fault rocks and fault mechanisms. Journal of the Geological Society, 133: 191–213.

Tembe, S., Lockner, D.A., and Wong, T.-F., 2010. Effect of clay content and mineralogy on frictional sliding behavior of simulated gouges: Binary and ternary mixtures of quartz, illite, and montmorillonite. Journal of Geophysical Research, 115, B03416 doi:10.1029/2009JB006383.

Twiss, R.J., and Moores, E.M., 2000. Structural Geology. Freeman W.H., and co., (6th ed.).

Vrolijk, P., and van der Pluijm, B.A., 1999. Clay gouge. Journal of Structural Geology, 21: 1039-1048.

Weyl, P.K., 1959. Pressure solution and the force of crystallization: a phenomenological theory. Journal of Geophysical Research, 64: 2001-2025.

Zhang, X.M., Salemans, J., Peach, C.J., and Spiers, C.J., 2002. Compaction experiments on wet calcite powder at room temperature: evidence for operation of intergranular pressure solution. Geological Society of London, Special Publication, 200: 29-40.

Zhu, W., and Wong, T.F., 2012. The transition from brittle faulting to cataclastic flow: Permeability evolution. Journal of Geophysical Research - Solid Earth, 102: 3027-3041.

Zubtsov, S., Renard, F., Gratier, J.-P., Guiguet, R., Dysthe, D.K., and Traskine, V., 2004. Experimental pressure solution compaction of synthetic halite/calcite aggregates. Tectonophysics, 385: 45-57.

CHAPITRE 3

Etude des mécanismes de fluage dans la faille de San Andreas, Californie

---

Introduction

Après avoir introduit toutes les notions de base relatives aux failles actives et aux différents mécanismes de fluage, nous allons maintenant nous attacher à un cas d'étude particulier : le fluage sur la faille de San Andreas. Par le biais d'une approche microstructurale basée sur l'étude d'échantillons naturels provenant d'une zone en fluage actif fournis par le forage SAFOD, nous avons pu identifier les principaux mécanismes de fluage à l'œuvre dans cette zone, ainsi qu'une chronologie des déformations. De cette étude, nous avons pu élaborer un modèle 3-Dimensions (temps, distance à la zone de fluage et profondeur) de l'évolution d'une zone de fluage.

Temporal and spatial variation in an active creeping fault zone: insights from the brittle and ductile microstructures in the San Andreas Fault Observatory at Depth

Julie Richard[1], Jean-Pierre Gratier[1], Mai-Linh Doan[1], Anne-Marie Boullier[1], François Renard[1,2]

[1] ISTerre, University Grenoble 1 & CNRS, BP 53, 38041, Grenoble, France

[2] Physics of Geological Processes, University of Oslo, 0316 Oslo, Norway

(Soumis à Journal of Geophysical Research)

Abstract

Creep processes relax a major part of the tectonic stresses in active faults, either by permanent or episodic processes, also known as afterslip. The aim of this study is to obtain a better understanding of these creep mechanisms and their evolution in time and space. Results are presented from microstructural studies of natural samples collected from the SAFOD drilling site through the San Andreas Fault, California. Fault microstructures give a record of the chronology of the deformation which started with a thick, 200 m wide deformed zone – corresponding to the present-day damaged zone – mostly accommodated by pressure solution creep and developed into a weak metre-size creeping zone, with the dissolution of soluble minerals and the concentration of phyllosilicates leading to a high soft matrix content. In this process, the foliation changes from a texture with cleavages and veins with parallel orientation to foliation without any coherent orientation in the present-day creeping zone. Pressure solution creep is promoted by the presence of fluids and phyllosilicates and by fracturing and comminuting processes. Conversely, fracture sealing, making pressure solution creep less efficient, tends to strengthen the rocks leading to tectonic differentiation. Within the first 3-4 km depth of the crust the creeping mechanism is controlled by the very low friction

of the saponite and by diffusive sliding of polymineral clasts embedded in the clay matrix. At greater depths (4-12 km), where the saponite is transformed into corrensite and subsequently chlorite with much higher friction coefficients, pressure solution diffusive grain boundary sliding is likely to be the controlling creeping mechanism.

1 – Introduction

Active continental faults relax stress during short seismic events generating earthquakes. They can also accommodate a major part of the deformation during periods of slow, aseismic sliding by creep. Two types of creep can be distinguished. The first is a permanent steady-state creep associated with specific properties of the fault rocks and their environment. The deformation stays constant with time and the strain rate remains fairly constant (Burford and Harsh, 1980; Azzaro et al., 2001; Titus et al., 2006). The second type of creep is recorded over periods ranging from months to decades after an earthquake; it can be considered as a post-seismic creep process and occurs either in the lower crust below the seismic fault or in the upper crust around seismic patches (Gao et al., 2000; Johanson et al., 2006; Murray and Langbein, 2006; Barbot et al., 2009). In the latter case it is also called afterslip process (Freed, 2007). Both steady-state creep and post-seismic (afterslip) creep seem to be linked to two important deformation mechanisms: (micro)fracturing on one hand, and healing and sealing processes on the other (Rubin et al., 1999; Gratier et al., 1999; Perfettini and Avouac, 2004; Nadeau et al., 2004; Li et al., 2006; Zoback et al., 2010; Gratier et al., 2011). Those two mechanisms are in competition. Fracturing reduces the strength of the fault rocks and could enhance aseismic deformation whereas sealing processes strengthen the rocks, increasing their cohesion (Gratier, 2011). More generally, such processes of coupled dissolution-precipitation reactions create or destroy porosity and are responsible for slow deformation in the mid- to upper-crustal rocks (Wintsch and Yi, 2002; Putnis, 2002).

Considering the relationships between aseismic deformation and fault processes, creep mechanisms need to be identified in order to gain a better understanding of the seismic cycle. Numerous observations have been made on creep in major active continental faults (Steinbrugge and Zacher, 1960; Yu and Liu, 1989; Lee et al., 2005;

Titus et al., 2006) and questions are now focused on the mechanisms responsible for such behaviour.

The San Andreas Fault (SAF) is one of the most active continental faults in the world and one of the best surveyed. It is a mature fault divided into segments, some of which experience steady-state and/or post-seismic creep. The San Andreas Fault Observatory at Depth (SAFOD) drilling project has given the unique opportunity to study samples taken from the fault core at depth. Numerous studies on creep based on the material provided by this drilling project have been performed (d'Alessio et al., 2006; Moore and Rymer, 2007; Solum et al., 2007; Schleicher et al., 2009a; Schleicher et al., 2010; Janssen et al., 2010; Zoback et al., 2010; Gratier et al., 2011; Holdsworth et al., 2011; Janssen et al., 2012; Hadizadeh et al., 2012). A key discovery in the SAF creeping segment is the observation that the creeping process, and more generally sliding along the entire San Andreas Fault, does not lead to a local increase in heat, as would be the case if it were linked to a friction process (Lachenbruch et Sass, 1980). Consequently, the fault is said to be weak (see below for more details). At least three major mechanisms have been investigated that could weaken the fault and enhance creep deformations. The first is linked to pore fluid overpressure (Rice, 1992; Chester et al., 1993), and some studies have provided evidence of episodic fluid overpressure in the fault core (Mittempergher et al., 2011), but they also showed that this mechanism alone is not enough to explain the weakness of the fault and the observed creep rate. Moreover, the potential sources of fluid in the fault do not provide a sufficiently high flux (Fulton and Saffer, 2009; Fulton et al., 2009). Such high fluid pressure events must be episodic and related to earthquake activity (Mittempergher et al., 2011) since, at the present time, no evidence of high fluid pressure was found in the borehole (Zoback et al., 2011). The second deformation mechanism is frictional sliding. In order to fit the observed low heat flow along the creeping zone, a large amount of very weak minerals is required, such as talc, smectite and clay. Consequently this mechanism depends both on rock composition and on temperature and pressure conditions (Moore and Lockner, 2007; Moore and Rymer, 2007; Carpenter et al., 2009; Collettini et al., 2009; Carpenter et al., 2011; Lockner et al., 2011). Laboratory experiments also suggest that low friction is correlated to velocity-strengthening behaviour that inhibits the nucleation of earthquakes (Ikari et al., 2011).

Finally, the last creeping process that could accommodate large aseismic deformation without heat production is pressure solution creep (Rutter and Mainprice, 1979; Schleicher et al., 2009b; Gratier et al., 2011). This deformation mechanism is a stress-driven fluid-assisted mass transfer process, widely spread in the rocks of the upper crust (Gratier et al., 2013a). Due to local variations in chemical potential related to local stress heterogeneities, soluble species (such as quartz, feldspar, serpentine, etc.) are progressively dissolved, transferred along a fluid phase trapped under stress and either precipitated or washed away when reaching open pores (Weyl, 1959; Paterson, 1973). This leads to a passive concentration of insoluble species (such as phyllosilicates, oxides, etc.) in the dissolution zones. Such chemical segregation develops a foliation perpendicular to the direction of the maximum normal stress and consequently leads to ductile deformation of the rock by spaced or slatey cleavage (Hobbs et al., 1974; Ramsay, 1967; Siddans, 1972; Wood, 1974).

The present study analyzes rock microstructures that have recorded creep, in twelve samples collected from the Phase 3 core of the SAFOD, located in the damaged zone (about 3200 m to 3400 m measured depth) (Zoback et al., 2010), in order to identify the main creep mechanism that currently takes place in the SAF. Optical microscopy, cathodoluminescence (CL), Scanning Electron Microscopy (SEM), Field Emission Gun Scanning Electron Microscopy (FEG-SEM), Back-Scattered Electron imaging (BSE) and Electron Probe Micro–Analysis (EPMA) on thin sections were used. Additional X-Ray Powder Diffraction (XRPD) analyses on fragments were collected.

Eight samples were taken directly from the most active shear zone detected in the main hole: the Central Deforming Zone (CDZ), which experiences active creep today. Two types of microstructure can be distinguished in the thin sections: (i) foliated zones with a foliation orientation consistent with (i.e., parallel) fault displacement, (ii) foliated zones without any coherent orientation, very rich in clays and with very small grain size. Those observations indicate that pressure solution is the main creep mechanism but raise several questions: Are these two types of microstructure characteristic steps in the changes taking place in the pressure solution creep mechanism? Did they develop in parallel or in series, depending on the initial conditions prevailing in the area? Is there a spatial and temporal variation in these microstructures? This raises a more general question: how do the

creeping zone microstructures evolve in time and space? Finally, a model is proposed to show how these active creeping zones are formed and change in space and time, based on microstructural observations of natural samples.

2 – San Andreas Fault and SAFOD borehole

2-1 Geological setting and general features

The San Andreas Fault System, California, is a complex network of faults extending over 1300 km in length and 100 km width (Wallace, 1990), forming the junction between the subducting Pacific plate and the North American plate. The San Andreas Fault is the major continental fault of this network, and one of the most active in the world. It is a lithospheric mature dextral strike-slip fault divided into different segments with varying mechanical behaviour (Figure 1a) (Steinbrugge and Zacher, 1960; Allen, 1968; Wallace, 1970; Irwin and Barnes, 1975). The creeping segment is experiencing a continuous aseismic slip at a rate ranging between about 28 mm/yr and 33 mm/yr (Burford and Harsh, 1980; Titus et al., 2006), close to the 34 mm/yr long-term estimated geological slip rate (Sieh and Jahns, 1984) and exhibiting a high microseismic activity (Provost and Houston, 2001). The creeping zone is bounded by locked segments that have experienced some infrequent earthquakes of high magnitude, such as the Fort Tejon earthquake in 1857 (M=7.9) (Sieh, 1978) on the southern locked segment, and the San Francisco earthquake in 1906 (M=8.2) on the northern locked segment. The locked segments are also characterized by negligible or nonexistent creep (Ellsworth, 1990). Finally, the Parkfield segment forming the junction between the creeping segment and the southern locked segment has a transitional behaviour. This segment has been experienced seven repeating earthquakes of magnitude close to 6 since 1857 (Bakun and McEvilly, 1984; Jackson and Kagan, 2006), a transitory postseismic creep episode after the last 2004 event (Titus et al., 2006) and microseismic activity (Thurber et al., 2004).

The fault crosses different geological formations and, given the tectonic setting of subduction, the geographical distribution of these formations is not symmetrical on both sides of the fault, especially in the Parkfield area (Figure 1b), where the present study is

focused. The structure of the fault itself is complex and presents major heterogeneities at depth, with some formations intensively deformed like the Franciscan Complex, and the presence of a large body of serpentine close to the Parkfield segment (McPhee et al., 2004, Li et al., 2004).

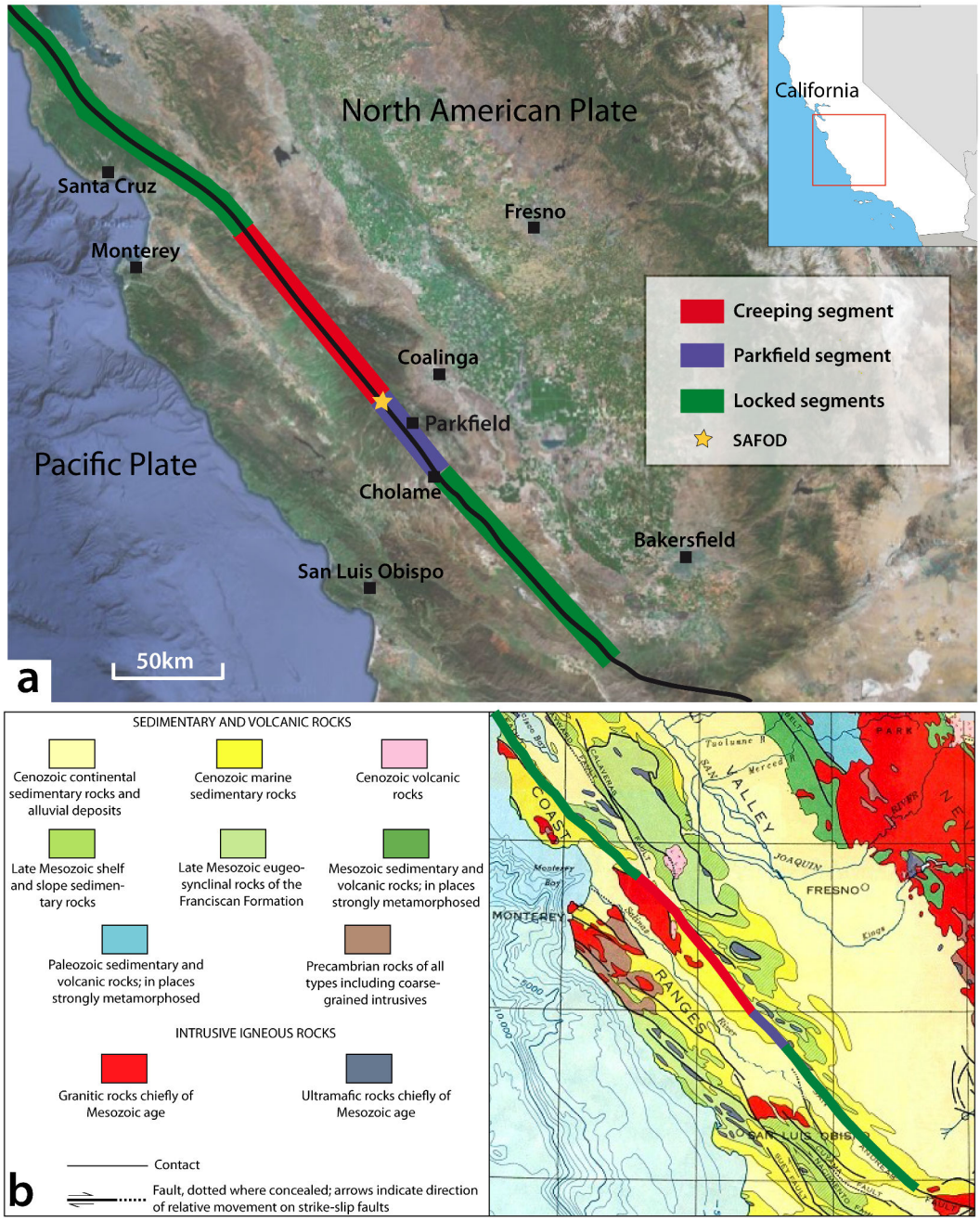

Figure 1: (a) Location map of the San Andreas Fault (SAF) and SAFOD borehole in central California, displaying also the different fault segments. (b) Simplified geological map of central California, matching the area shown in (a) (modified from the Simplified Geological Map of California – California Geological Survey).

Studies have also revealed some very specific features in the geophysical and mechanical properties of the SAF. Brune et al., (1969) showed that this fault slides with a much lower shear stress than that predicted by laboratory friction experiments (Byerlee, 1978). This property was confirmed by other studies (Chéry et al., 2004; Boness and Zoback, 2004; Townend and Zoback, 2004; Zoback et al., 2010). Moreover, there is no heat flux anomaly across the creeping segment (Brune et al., 1969; Lachenbruch et Sass, 1980). This latter discovery, well-known as the San Andreas stress-heat flow paradox (Hanks and Raleigh, 1980; Zoback et al., 1988; Lachenbruch and Sass, 1992), has raised, at a very early stage, the question of potential mechanisms that can produce creep, without heat production. Finally, Mount and Suppe, (1987) and Zoback et al., (1987) provided evidence showing that the orientation of the maximum horizontal compressive stress is at a high angle to the fault. This angle increases with depth and ranges from 25° to 69° between 1000 m to 2200 m depth (Hickman and Zoback, 2004). All those observations point to a weak fault embedded in a strong crust (Zoback et al., 1987; Rice, 1992; Zoback, 2000; Fulton et al., 2004; Zoback et al., 2010). Despite some other studies claiming the possibility of a strong fault in a strong crust (Scholz, 1992; 2000), the model of a weak fault is now widely adopted for the SAF.

When considering the morphology of such a strike-slip fault, a major difficulty is to access the fault core material. Given that exhumed portions have lost much information on the physical and chemical mechanisms acting at depth, drilling at depth directly through the fault was considered to be a better way of studying the fault processes *in situ* (Zoback et al., 2010).

2-2 SAFOD borehole

The San Andreas Fault Observatory at Depth (SAFOD) drilling project aimed to provide *in situ* geophysical borehole data and fault core samples to obtain a more accurate idea of the fault rock properties at depth, the conditions for earthquake nucleation, and to find an explanation for the San Andreas stress/heat flow paradox (Zoback, 2006; Hickman et al., 2007; Zoback et al., 2011). The borehole was drilled close to the town of Parkfield (Figure 1), on the eponym fault segment and reached 3 km vertical depth (Figure 2). This site was chosen because of its location at the transition

between two segments having different mechanical behaviour and the presence of patches of repeating microearthquakes located between 2 km and 12 km depth within an aseismic creeping zone (Nadeau et al., 2004; Zoback et al., 2010). The main borehole was drilled in three phases between summer 2004 and summer 2007 (Zoback et al., 2011).

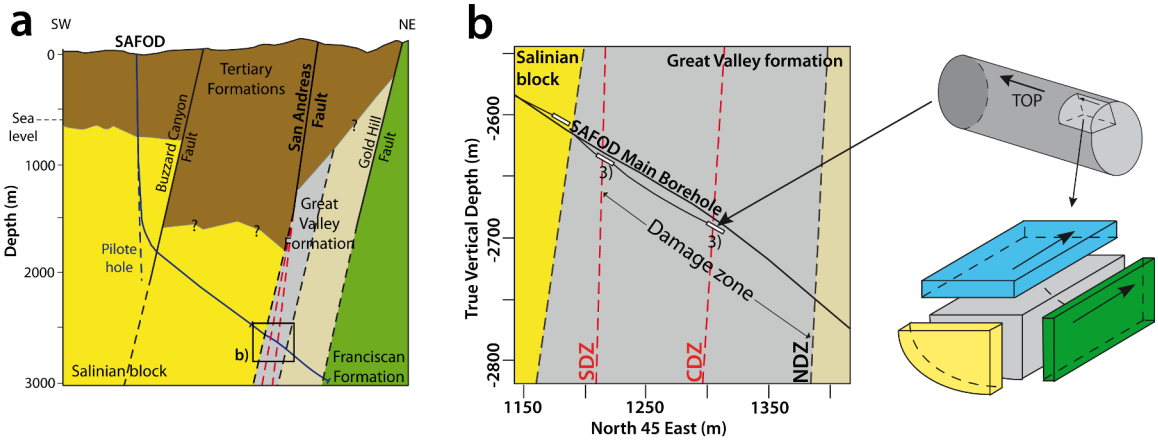

Figure 2: (a) Simplified NW-SE geological cross-section of the SAFOD borehole area and its intersection with the depth division of the SAF into three main strands. Dashed red lines indicate the two active creeping zones (SDZ and CDZ) (after Zoback et al., 2010). A black square delineates the area focused in b). (b) Simplified cross-section of the SAFOD main borehole and location of the sidetrack boreholes used to obtain core samples during Phase 3, in the damaged zone area (after Zoback et al., 2011), and sketch representing the orientation and position of the samples studied relative to the oriented core. Thin sections of those samples were cut according to the three directions represented by the coloured sections (blue, green and yellow). The blue and green sections are parallel to the hole and perpendicular to the fault and consequently to the foliation, while the yellow section is perpendicular to the hole and parallel to the foliation.

The SAFOD borehole has provided accurate information on the fault geometry and geophysical properties of the fault rocks at depth (Solum et al., 2006; Bradbury et al., 2007; Solum et al., 2007; Jeppson et al., 2010; Zoback et al., 2011), and evidence supporting the model of a weak fault in an otherwise strong crust (Tembe et al., 2006; Tembe et al., 2009, Zoback et al., 2010; Mittempergher et al., 2011). It was possible to locate at depth the boundaries between different geological formations, (Figure 2a) and at least seven relatively large fault zones were crossed by the borehole (Bradbury et al., 2007). A 200-m wide damaged zone (Figure 2b and Figure 3) has been detected by the decrease in the velocity of P and S waves and by its low resistivity, compared to the other sections of the borehole (Zoback et al., 2011). Inside this damaged zone, two specific areas were distinguished by their localized active deformation: the South Deforming

Zone (SDZ) and the Central Deforming Zone (CDZ). These zones are characterized by on-going deformation of the steel casing around the borehole, and anomalies in the velocity of P and S waves and in the resistivity were also detected.

Those two shear zones experience active creep deformation and are presented as the active trace of the SAF (Hickman et al., 2007; Zoback et al., 2011). Both of them are less than 3 m wide (Figure 3). The first zone, the SDZ, is located between 3196 m and 3198 m depth (depths are given here relative to Phase 3 Core, see Table 1 for the equivalence between the different depth location systems). This is the less active zone. The CDZ, located between 3296.5 m and 3299 m depth (relative to Phase 3 Core) is the more active deforming zone. Their mineral composition is different from the rocks outside the active deforming areas (Holdsworth et al., 2011). They are found to contain large amounts of clays, serpentine clasts and a very small amount of talc (Solum et al., 2006; Hickman et al., 2007; Moore and Rymer, 2007; Holdsworth et al., 2011).

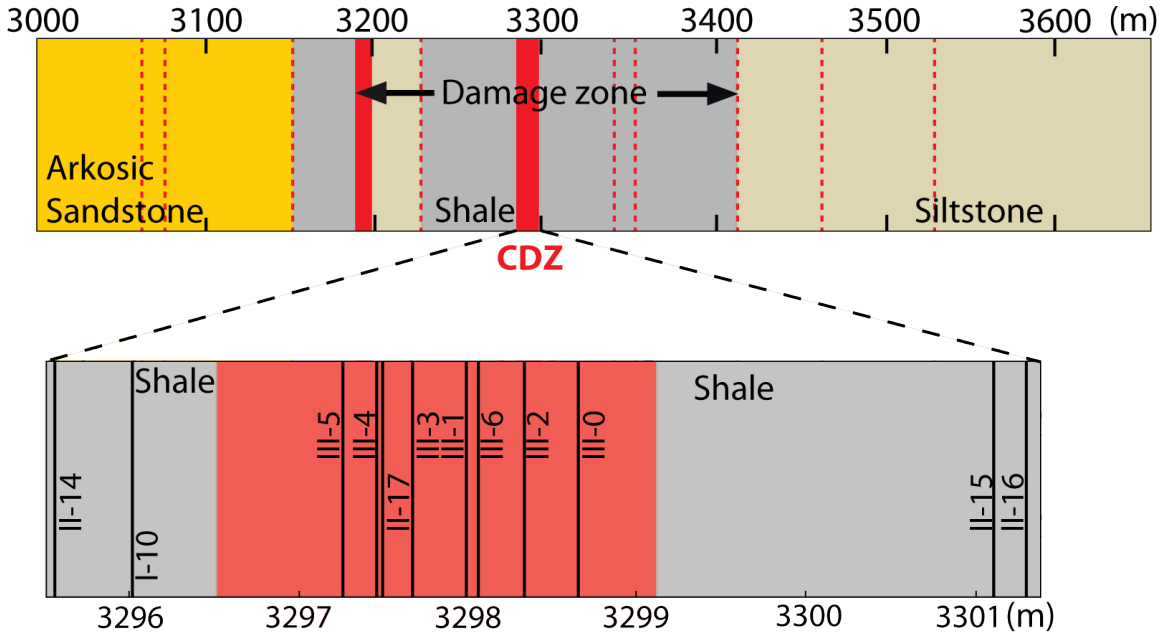

Figure 3: Location of the samples studied in a schematically-represented part of the main hole. The measured depth values are relative to Phase 3 Core. Colours show the different rock formations, vertical red bars indicate the places where the steel casing is actively deforming and dotted red lines mark the faults crossed by the borehole.

3 – Microstructures in the San Andreas Fault zone

3-1 Location and preparation of the samples

During the three rounds of sample requests, several samples were collected to characterize the typical microstructures found in the SAFOD fault zone. Here, the focus was placed on twelve samples collected close to or inside the active creeping zone of the CDZ, in order to study the deformation microstructures and the mineral composition in this area and to characterize its spatial variations along the CDZ and at its boundaries. Based on these observations, a model is proposed to predict the spatial microstructural change in a creeping zone, and to determine the main deformation processes, defining limits on the time-dependent change in the fault by using cross-cutting geological relationships.

Figure 3 shows the location of the samples studied. The measured depths are relative to Phase 3 Core (see Table 1). Each of these samples, except sample III-2 and part of sample I-10, was impregnated with epoxy resin and cut into thin sections. At least three thin sections of each sample were made along three perpendicular directions relative to the core top (Figure 2b). In the first stage, an optical microscope was used to determine the general features inside and outside the creeping zone. These observations provided an initial compilation of the most representative thin sections for each sample, on which SEM observations and chemical mapping studies were carried out. A second selection based on this analysis was then made in order to focus on four main thin sections on which microprobe analyses and chemical mapping studies were performed: three samples inside the creeping zone, and a fourth located outside the creeping zone but within the damaged zone.

Core Section	MD Phase 2 (m)	MD Phase 3 (m)	Samples
G41	3299,518	3295,558	II-14
G42	3299,997	3296,037	I-10
CDZ top	3300,524	3296,564	
G43	3301,23	3297,27	III-5
G43	3301,44	3297,476	III-4
G43	3301,448	3297,488	II-17
G44	3301,64	3297,68	III-3
G44	3301,96	3297,99	III-1
G44	3302,04	3298,06	III-6
G44	3302,3	3298,34	III-2
G45	3302,61	3298,65	III-0
CDZ bottom	3303,084	3299,124	
G51	3305,126	3301,166	II-15
G52	3305,279	3301,319	II-16

Table 1: Overview of the location of the samples studied listed with increasing depth along the borehole (MD) in SAFOD. The Core Section column gives information on sidetrack boreholes (G43 stands for hole G, Run 4, Section 3). All the samples presented here come from Phase 3. In the denomination of samples (Column Samples), the first number indicates the Round of sample requests (II-14 stands for Round II, sample n°14 of the sample set received from this Round). As the Phase 3 core consists of a series of boreholes sidetracking the Phase 2 hole, the measured depths can vary depending on the hole considered. Zoback et al. (2010) give the methodology for correlating the values of the measured depths of Phase 3 with those of Phase 2. Here, for the values of the core section of Hole G, Runs 4-6, a value of 3.96 m needs to be added to the Phase 3 measured depths to obtain the corresponding depth with Phase 2. The two columns, MD Phase 2 and MD Phase 3, give the corresponding values in metres of measured depth of our samples, taking into account this correction, as well as the location of the top and bottom of the CDZ.

3-2 Sample observations

Previous mineralogy studies have revealed that the damaged zone is mainly composed of siltstones, mudstones, shales (Solum et al., 2007; Bradbury et al., 2007; Schleicher et al., 2009a), and very fine grey sandstones of the Great Valley sequence (Holdsworth et al., 2011). Concerning the two active creeping zones, they are mainly composed of phyllosilicate minerals (mainly clays) with serpentine clasts as well as lithic clasts from siltstone and mudstone rocks, similar to those composing the fault rocks at the boundaries of the creeping zone. These clasts have a wide size range and are embedded in the clay-rich matrix (Holdsworth et al., 2011; Moore and Rymer, 2012).

3-2-1 Outside the creeping zone – the damaged zone

The damaged zone appears to be both foliated and fractured. Most of the grains, and more specifically quartz and feldspar grains, are highly fractured (Figure 4a,b). The minerals are generally very altered, especially at their boundaries, with irregular shapes. Widespread indentations between grains of different or similar nature can also be observed (Figure 4c,d,f). Networks of numerous calcite veins are easily identifiable (Figure 4d,e,f) and are another typical feature of the damaged zone. They were found in every thin section of samples taken outside the creeping zone. The different red colours of the calcite in cathodoluminescence imaging underline the variations in minor element content (Fe, Mg, …). Just like the other minerals, calcite grains are highly fractured in some areas (Figure 4). Finally, pervasive foliation is the main deformation pattern in this damaged zone. Such foliation may be observed at different scales, from the grain scale to the thin section scale.

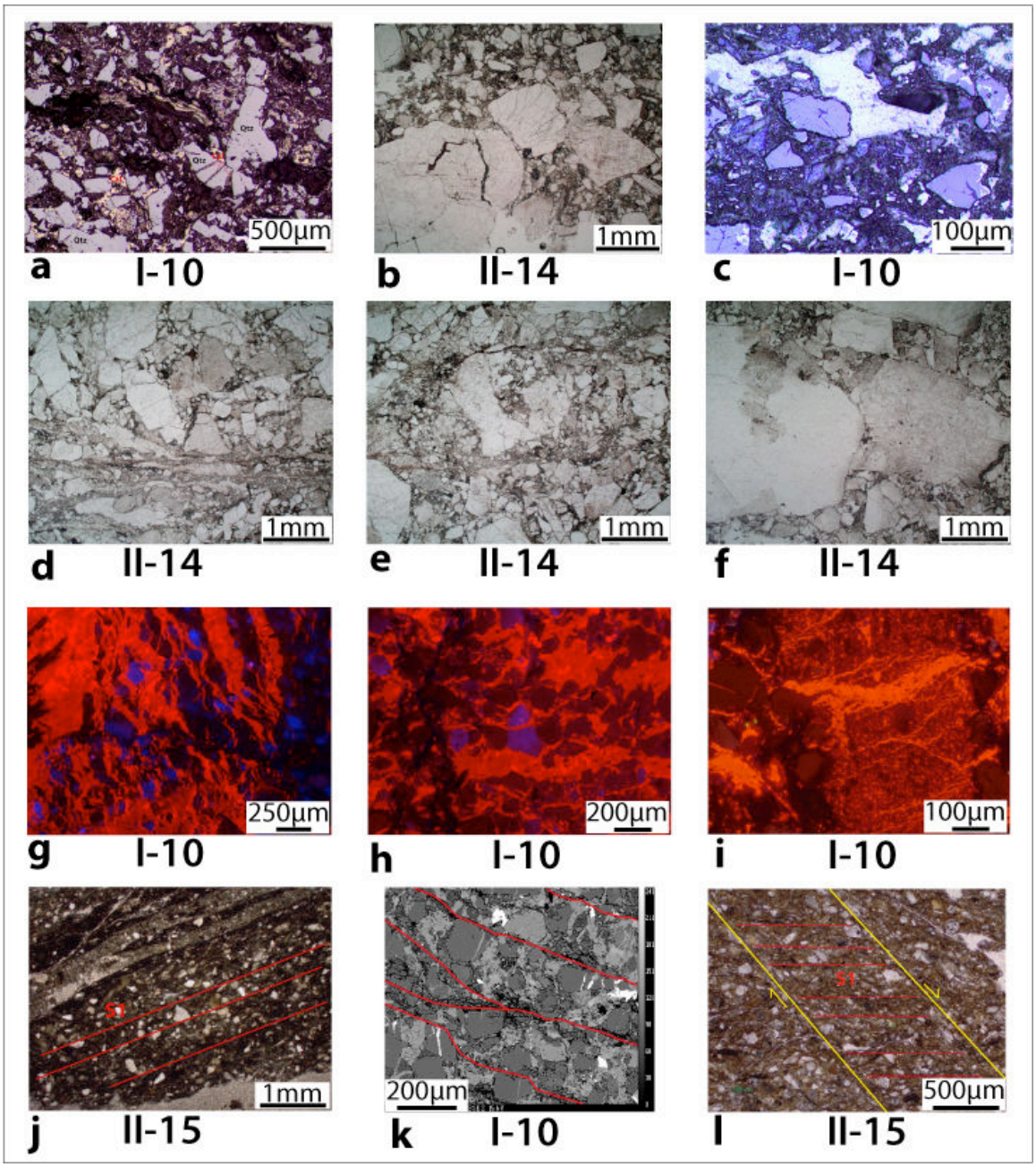

Figure 4: Main microstructural features observed in thin sections in the samples located outside the creeping zone. (a) Optical microscope picture showing dynamic fracturing with radial cracks. (b) (c) (d) (e) Optical microscope pictures showing the general intense fracturing of the material as well as the indentations. (f) Optical microscope picture with an example of the numerous indentations between quartz and feldspar grains. (g) (h) (i) Cathodoluminescence images showing the well-developed calcite vein network in bright red, at different scales. The minerals in blue and green are feldspars and the dark brown ones are quartz. (j) Optical microscope picture presenting an example of foliation developed by pressure solution mechanism. (k) Microprobe BSE image showing solution cleavages at the grain scale. (l) Another example of foliation, developed between shear planes also by a pressure solution creep process.

3-2-2 Inside the creeping zone

For samples taken inside the creeping zone, a notable difference is the composition of the rock. X-ray diffraction analyses performed on all samples from the creeping zone indicated a clay content ranging from 50% to 70%, well above the phyllosilicate content in the damaged zone. XRD analyses reveal that these clays belong to the smectite group (saponite). These results are confirmed by SEM and microprobe chemical analysis. Another typical feature of the rock inside the creeping zone is the presence of polymineral clasts of various sizes, ranging from 10 µm to 15 mm (Figure 5). Their composition is very close to that of the rocks outside the creeping zone (the damaged zone), except for the serpentine clasts (Figure 5a), which are not very widespread in the damaged zone. This is the second main difference with the mineral composition of the rock outside the creeping zone. The amount of serpentine in the creeping zone ranges between 10% and 15%. XRD and microprobe analyses indicate two kinds of serpentine, chrysotile and lizardite, which were imaged using a FEG-SEM (Figure 6). Many polymineral clasts are composed of fractured serpentine with calcite veins. Other clasts are made of quartz and feldspar that are the most common minerals forming the polymineral clasts. It should be noted that most of those polymineral clasts are fractured. Small amounts of chlorite, iron and titanium oxides as well as very rare talc grains can be found in some aggregates. Most of the polymineral clasts have a typical almond shape and their boundaries present evidence of dissolution indenting by pressure solution creep (Figure 5). Pressure solution cleavages, with almond shapes, may be seen around aggregates (Figure 5c). These are characterized by both concentrations of dark minerals inside the cleavage planes and pressure shadows on the ends of the almond shapes. Calcite growth is most often observed in some pressure shadows of the polymineral clasts (Figure 5c). The presence of large quantities of very small grains (<10µm) was also noted, dispersed within the clay matrix (saponite), usually made of serpentine, calcite, quartz, feldspar and iron oxide. The shapes of their edges are often very irregular (Figure 6d,e,f and Figure 8). The last noticeable feature is the very thin shear planes in different directions and different scales, observed in all thin sections (Figure 5g,h). It is really difficult to determine any coherency from all these planes and almost impossible to find a main shear sense.

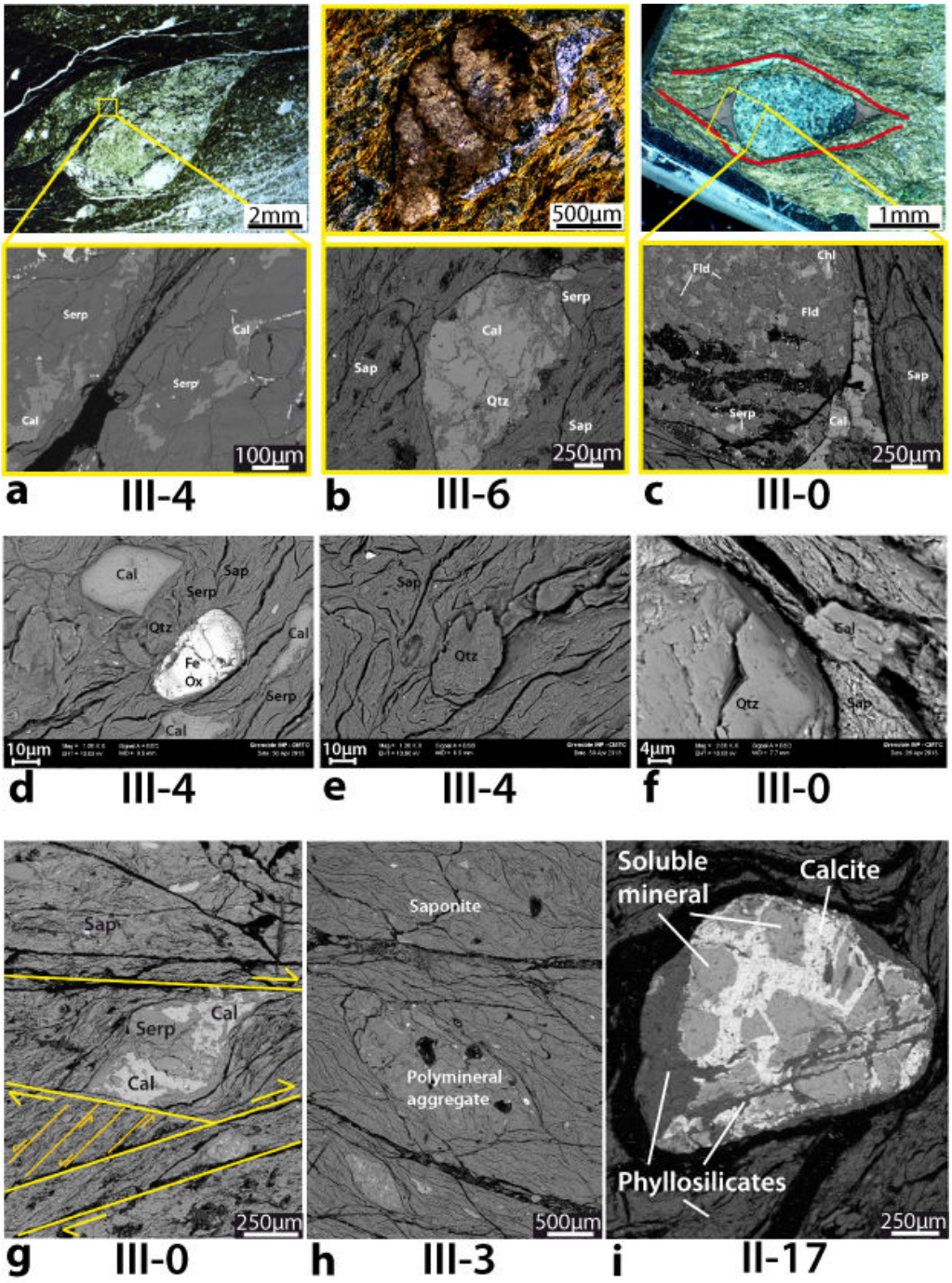

Figure 5: Main microstructural features observed in thin sections of samples located inside the creeping zone. (a-c) Top: colour optical microscope pictures presenting some examples of polymineral clasts. Bottom: Microprobe BSE images (in black and white) show the differences in mineral composition between these aggregates. (d-f) FEG-SEM BSE images showing examples of small grains presenting evidence of pressure solution at their edges. They also show the abundance of very small grains (<10µm) inside the clay matrix, forming the creeping zone material. (g, h) SEM BSE images displaying the multiple shear planes and their various orientations (yellow lines), as well as the very disturbed foliation inside the thin shear planes. Qtz: quartz, Cal: calcite, Serp: serpentine, Fld: feldspar, Chl: chlorite, Sap: saponite, Fe ox: iron oxide.

However, the thin sections cut perpendicularly to the foliation were relatively less chaotic than those cut parallel. Inside the different shear planes, oblique and highly folded foliation can be seen, with absolutely no coherent orientation (Figure 5). Just like the shear planes, the foliation has different scales and orientations. The rotation of the foliation and the shear planes is correlated to the presence of polymineral clasts at all scales and the small rigid grains.

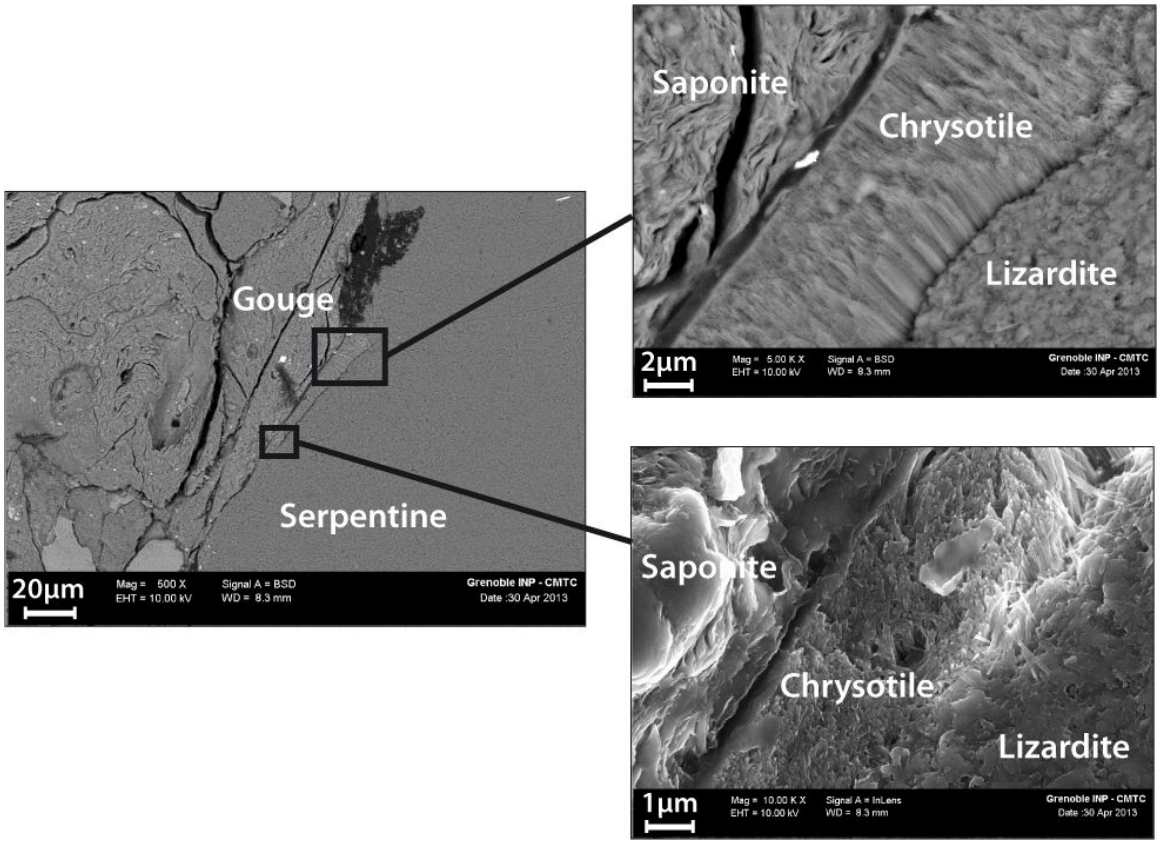

Figure 6: Examples of two different serpentines. The three pictures are FEG-SEM images, taken from sample III-0 at the boundary between an aggregate mainly composed of serpentine and saponite clay. Most of the serpentine forming clasts or present in the aggregates is lizardite. Chrysotile is located mainly along the boundaries of the serpentine aggregates or clasts, as here.

3-3 Interpretations

All the above observations provide evidence for identifying the mechanisms leading to these microstructures.

3-3-1 Outside the creeping zone – the damaged zone

The fractured grains may show multiple radial fracturing along their contact planes that is indicative of dynamic fracturing processes (Sagy et al., 2001). The alteration of the minerals reflects the episodic fluid flow through the damaged zone at least during early times, and the multiple grain indentations are evidence of grain boundary dissolution under stress and sliding. The extensive calcite vein networks indicate that many fractures have been sealed. Their abundance underlines the importance of the healing and sealing processes that were active here. The different red colours of calcite in cathodoluminescence show that several sealing episodes were probably connected to successive fluid flow episodes (Mittempergher et al., 2011). Moreover, given that the calcite grains are more fractured than the other minerals, this supports the idea of multiple deformation episodes associating fracturing, sealing and fluid flow through the damaged zone. Several micro- to meso-faults may be identified in the damaged zone (Mittempergher et al., 2011; Holdsworth et al., 2011; Hadizadeh et al., 2012; Solum et al., 2006; Schleicher et al., 2009b), with a µm to cm displacement range, which could be the markers of the present-day microseismicity.

The tectonic layering, associated with the pervasive foliation, is indicative of a pressure solution process, with passive concentration of insoluble minerals, such as phyllosilicates, in pressure solution seams (Figure 4g,h,i and Figure 7). Deposition veins may or may not occur between the spaced cleavages (Figure 7). This typical microstructure leads to localized deformation. The decrease in total mass at the level of each pressure solution cleavage seam may be estimated at about −88% in these foliated areas, based on the measured proportional decrease in mass of each mineral (Gratier al., 2011). Mass transfer has modified the mechanical properties of the deformed rocks in different ways, according to two end-member zones with different rheologies: the dissolution zone and the deposition zone.

In the dissolution zone, the passive concentration of insoluble species, such as

phyllosilicates, activates the kinetics of mass transfer because diffusion along the interface between phyllosilicates and soluble minerals is faster than along healed cracks within soluble mineral grains. This is demonstrated by natural observations (Gratier, 2011) and by experiments (Zubtsov, 2004; Niemeijer and Spiers, 2005). This leads to a positive feedback process that makes it easier to localize the dissolution. Local weakening is therefore linked both to mechanical and chemical processes: decrease in friction and activation of the dissolution respectively, due to phyllosilicate concentration. Conversely, in the deposition zone, the presence of a large amount of calcite-filled veins tends to strengthen the rocks as it is more difficult to dissolve monomineralic rocks than a mixture of soluble and insoluble grains (Gratier et al., 2013b).

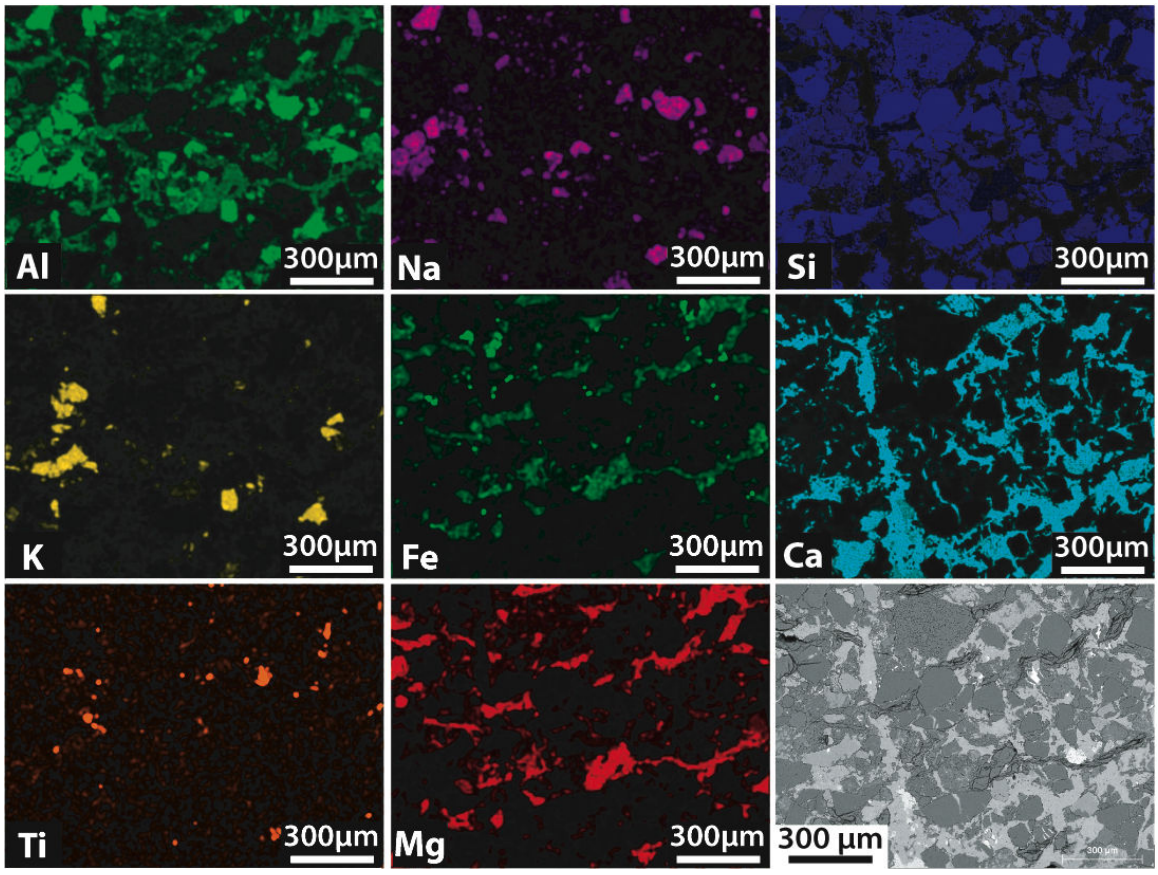

Figure 7: Element distribution from Scanning Electron Microscopy (SEM) analyses. Brighter colours indicate higher concentrations. The passive concentration of several elements (Fe, Mg, Ti) that belong to insoluble minerals (phyllosilicates and oxides) underlines pressure solution cleavage that contributes to a tectonic layering process.

Dissolution cannot be observed at grain scale in the veins, but only at the boundary of such veins (Figure 4), where the thin fluid phase is located. All these features provide strong evidence that pressure solution creep may represent the main creep mechanism in the damaged zone, outside the localized creeping zones associated with fracturing and sealing processes.

3-2-2 Inside the creeping zone

The observations revealed that polymineral clasts are mainly composed of fractured serpentine with calcite veins. This observation contradicts the common belief that serpentine is always a soft mineral. When serpentine minerals are sealed together in clasts, they behave as rigid, soluble bodies that can acquire a brittle property. However, like quartz, feldspar and calcite, serpentines are soluble under stress (Andreani et al., 2004) and may deform slowly by pressure solution creep in the presence of a trapped fluid phase, especially in mixtures of soluble and insoluble grains.

It was found that most of the polymineralic clasts were fractured, although the size of rupture area (cm at most) and the amount of displacement (a few μm to several mm) are indicative of very low-magnitude seismic events in the creeping zone. Concerning the other material present in the creeping zone, i.e. small grains of various minerals, the irregular shapes of their boundaries are interpreted as evidence of indentation by pressure solution creep.

The different features found inside the creeping zone suggest that the pressure solution creep process has been active and has helped weaken this zone by passive clay concentration. Remnants of the initial state are still trapped in the creeping zone in the form of polymineral clasts of variable dimensions (Figure 5). To summarize, two deformation mechanisms compete: sliding along very low friction coefficient saponite grains, and stress-driven mass transfer processes that help accommodate sliding of the polymineral clasts embedded in the clay-rich matrix.

3-4 Microstructures reveal two different deformation mechanisms

Based on these observations, for both the creeping zone and the damaged zone, two broad microstructural groups can be identified: (i) foliated domains with clear orientation in the damaged zone, and (ii) foliated domains without preferential orientation in the CDZ.

In the first case, the foliation has developed by a pressure solution creep mechanism in a general context of volume decrease but with local redeposition in calcite veins. This foliation is due to massive dissolution of soluble material, and partial redeposition that may also come from advective fluid flow (Gratier et al 2011), leading to tectonic layering. The typical characteristics of this microstructure are: (1) intense fracturing of the material, (2) numerous indentations between the grains and (3) localized redeposition of calcite evidenced by thick and extensive vein networks. This microstructure is widespread in the damaged zone, outside the active creeping zones. But it was also observed in some large polymineral clasts (several cm) inside the CDZ as remnants of an initial state.

The second type of microstructure – foliation without preferential orientation – is associated with both sliding on clay minerals along numerous micro-shear planes and rotation of the polymineral clasts. This microstructure is observed in the active creeping zone only; its main features are: (1) an abundance of soft clay minerals (>50% in the entire composition), (2) a grain size generally smaller than that found outside the creeping zone, (3) the presence of polymineral clasts of various sizes and compositions (mainly quartz, feldspars and serpentine minerals with calcite veins) embedded in the clay-rich matrix.

4 – Discussion

All those natural microstructural observations have implications on the rheological and mechanical behaviour of the fault, at different scales. To better understand the mechanisms of aseismic fault creep processes, the parameters responsible for the onset of creep mechanisms, as well as the interactions between these mechanisms are described in detail below. Again based on these observations, it may be argued that

the microstructures underline a chronology that can be used as a basis for proposing a 3D model of time-dependent changes in the creeping zone that could be extrapolated at depth.

4-1 Parameters controlling the creeping mechanisms

Based on the sample observations, two different creep mechanisms were found. Inside the damaged zone, there is extensive evidence of pressure solution creep (Figure 7), linked to the development of foliation (Schleicher et al 2009b, Holdsworth et al 2011, Gratier et al 2011, Hadizadeth et al 2013). Inside the creeping zone, the main creep mechanisms are grain sliding, with a crucial role being played by the low friction of clay minerals (Lockner et al 2011, Carpenter et al 2011), and locally indenting and sliding of pressure solution clasts (Figure 5 and Figure 8). Both mechanisms - pressure solution and low friction - require some specific parameters to be activated and efficient, as discussed below.

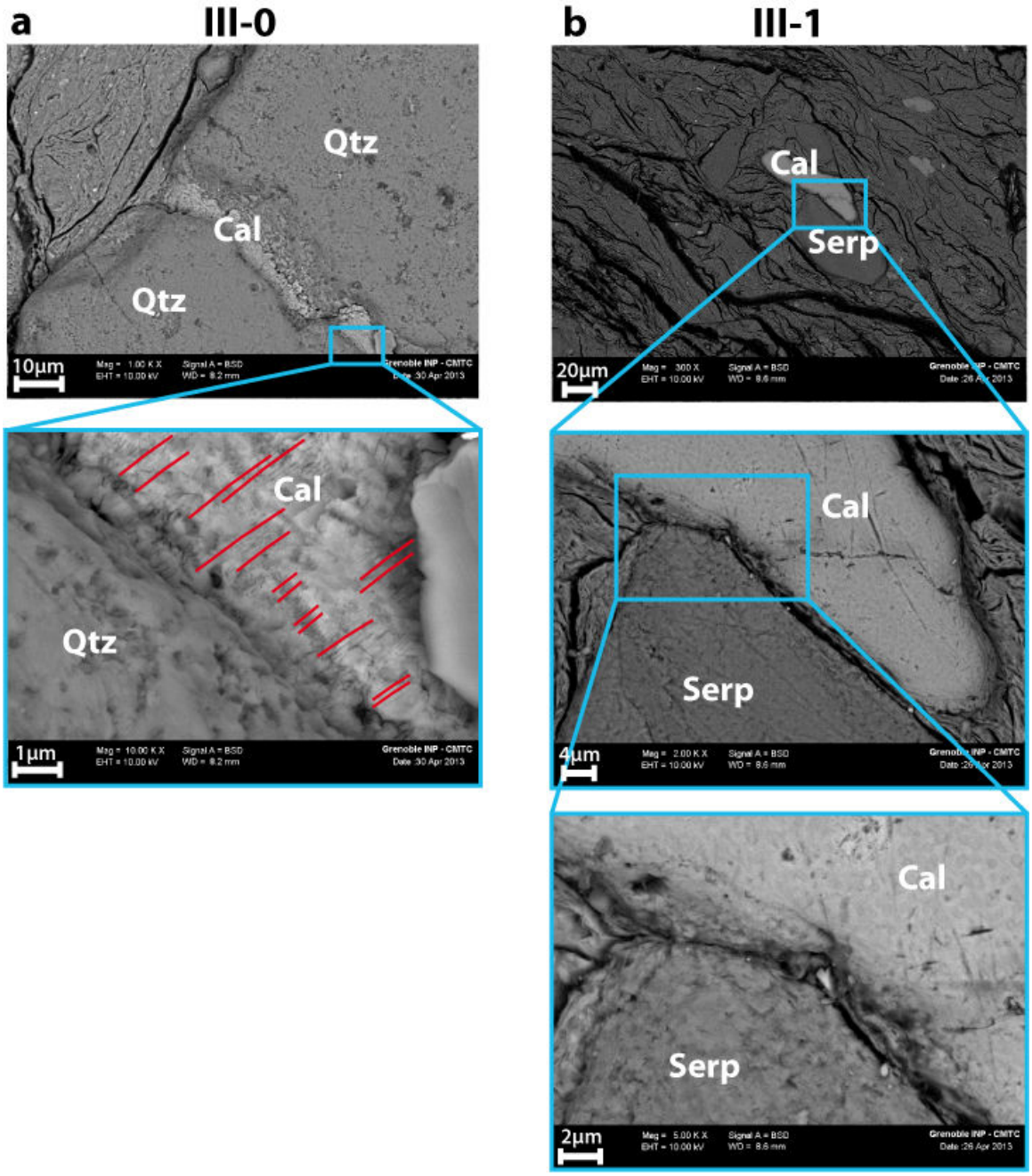

Figure 8: FEG-SEM images showing evidence of a pressure solution process at the grain contacts. (a) Striated calcite between two quartz grains. The quartz grain boundaries are also striated and show evidence of indentations. (b) Contact between a calcite grain and a serpentine grain. The boundaries of the grains are striated and indented, especially in the area of contact.

4-1-1 Pressure solution creep

The pressure solution mechanism requires certain specific conditions to occur at the relatively fast strain rate observed in the creeping zone (10^{-10} to 10^{-11} s^{-1}) (Titus et al., 2006). Firstly, the mechanism is activated by the presence of fluids that must act as a solvent for at least one of the minerals contained in the rock (Weyl, 1959; Rutter, 1976; Paterson, 1973). Secondly, all conditions being the same, a mixture of insoluble and soluble species deforms more easily by pressure solution than a monomineralic rock composed of only soluble species. This is because the kinetics of diffusive mass transfer along phyllosilicate/soluble mineral boundaries is much faster than along the boundaries of soluble minerals that can heal (Zubtsov et al., 2004). Thirdly, pressure solution is activated by fracturing or by comminution processes, because the strain rate in pressure solution creep rate laws is inversely proportional to the mass transfer distance d (Weyl, 1959; Rutter, 1976; Raj, 1982). The strain rate is proportional to $1/d^3$ for diffusion-controlled pressure solution, and to $1/d^2$ for reaction-controlled pressure solution. In nature, pressure solution is often controlled by diffusion at depth, and is therefore much more efficient with the smallest possible mass transfer distance. This mass transfer distance is commonly considered to be the grain size, but it could also be the distance between fractures because fractures can act as shortcuts for diffusion (Gratier et al., 1999). However, because fracturing is only transitory, as fractures are most often healed or sealed, this effect eliminates the diffusion shortcut effect of the fractures. With time, fracturing accelerates creep by decreasing d, thus weakening the deformed rocks; whereas healing and sealing processes slow down creep by increasing d, thus strengthening the rocks. Hence, stress could build-up in the creeping area, leading to new brittle deformation that will accelerate the rate of pressure solution creep and repeat the deformation as a cycle (Gratier et al., 1999; Gratier and Gueydan, 2007).

Finally, at regional scale, a distinction must be made between two end-member cases. Firstly, pressure solution may occur in a closed system, with diffusive mass transfer through an almost immobile fluid phase: all the dissolved materials are recrystallized inside a given volume, at dm scale, leading to both cleavage development with tectonic layering and sealing of fractures with growth of veins (mainly calcite veins in the SAF context). This case is found in places where there is not enough fluid flow to

take out (or bring in) the dissolved materials. Alternatively, in open systems, pressure solution may occur with high fluid flow through the deformed rock, which washes away all the dissolved species or which brings new solute minerals that can precipitate in veins or voids. In this case, either all soluble species are removed from the deformed zone without any deposition, or extensive deposition is seen in open spaces (Gratier et al 2013a).

4-1-2 Low friction processes

Laboratory experiments have highlighted the importance of gouge mineralogy on the fault zone frictional properties (Carpenter et al., 2009; Ikari et al., 2009; Ikari et al., 2011a) and especially for phyllosilicate-rich fault gouges (Vrolijk and van der Pluijm, 1999; Niemeijer and Spiers, 2006). An important question raised by those observations is the following: what amount of clay is sufficient to induce low frictional sliding? Tembe et al. (2010) performed friction experiments on synthetic gouge mixtures and showed that the friction coefficient depends on the amount of clay as well as the clay mineralogy. Their results are in agreement with the three-regime model of Lupini et al. (1981) that describes the degradation of frictional strength with clay content in three sequential phases. Tembe et al. (2010) imaged the *post-mortem* microstructures and showed that a considerable decrease in friction coefficient occurs when clay forms a connected matrix that separates the remaining grains. This kind of result is also supported by the study of Colletini et al. (2009). In this context, all the deformation is supported and accommodated by the clay structure. According to the experiments of Tembe et al., (2010), the clay content must be greater than 50% in the case of a montmorillonite/quartz mixture to reach a friction coefficient lower than 0.2 (the average friction coefficient of the CDZ determined by laboratory friction experiments is in the range 0.16 – 0.21) (Carpenter et al., 2011; Lockner et al., 2011). Montmorillonite belongs to the smectite group, like saponite, and its mechanical behaviour is close to that of saponite (friction coefficient of montmorillonite < 0.2). Such results, indicating that a quite large quantity of weak grains in a gouge is necessary to reduce significantly the overall friction, have also been simulated using a discrete elements method developed to reproduce the frictional properties of fault gouges (Rathbun et al., 2013).

Consequently, making a low frictional sliding process efficient requires a rock composition with more than 50% clay content if mixed with quartzo-feldspathic materials (Ikari et al., 2009; Tembe et al. 2010; Moore and Lockner, 2011), as is the case for the SAF creeping zone. Therefore, the most important parameter to activate the low friction creep mechanism is the mineral composition of the fault core: there should be high a sufficient concentration of low friction minerals. Different processes may lead to the concentration of low friction clay inside the creeping zone:

(i) The mineral composition of the creeping zone was already different from that of the surrounding rocks. In this case, certain minerals should be observed in the creeping zone that are not seen in the damaged zone and that cannot develop from metamorphic reactions. This is the case for the SAF creeping zone: serpentine polymineral clasts are mainly observed in the creeping zones. These clasts embedded in the clay matrix show solution cleavage and associated veined structures that have been rotated during the shear creeping process, reflecting the early development of such structures. The Mg-rich content of such serpentine minerals is evidence of a generally high Mg content in other minerals, especially phyllosilicates that could have produced the Mg-rich saponite by alteration, in a similar manner to the Mg-rich chlorites produced through corrensite transition.

(ii) Low-friction clay minerals were initially present and their proportion has changed over time because of the passive concentration of the phyllosilicate minerals associated with the pressure solution process in an open system. In such case, soluble minerals such as quartz, feldspars, calcite, and serpentines are removed from the deformed zone, leading to the passive concentration of insoluble species like phyllosilicates. If this process is acting alone, the relative increase in concentration of all insoluble minerals should be the same.

(iii) The mineral composition has changed because of the growth and/or precipitation of new minerals by metasomatic reactions. For example, saponite is the product of the reaction between quartzo-feldspathic minerals at low temperature. These minerals come from the wall rocks and the serpentine clasts (Lockner et al., 2011; Moore and Rymer, 2007). Such an assumption relies on fluid flow through the creeping zone, possibly episodic and related to earthquakes.

As seen above, in all these cases, ultimately the low friction mineral content needs to reach a high level (>60%) to be efficient enough to become the main creep mechanism. None of these three assumptions alone can explain our observations. The mineral composition was probably slightly different in the creeping zones than in the surrounding rocks, since it is the only place where serpentinites are so abundant. Serpentinites were deformed in an early stage, because of the extensive calcite veins associated with a lot of serpentine clasts, but would not be capable of accommodating the present large creep rate. Indicators of pressure solution are found in the creeping zone. Passive concentration of phyllosilicates probably occurred at first, but it is only when the initial phyllosilicates were sufficiently rich in Mg that the saponite-rich gouge could be generated. If this were not the case, the missing magnesium may have been brought in by fluid advection.

In summary, the findings are as follows: (i) a difference in initial state, for example a higher initial Mg content in both serpentines and Mg-rich chlorites in the proto-creeping zone; (ii) the observation of early pressure solution creep supports passive concentration of such Mg-rich phyllosilicates; (iii) a part of the increased clay content may be the result of metasomatic reactions, considering the large amount of Mg-rich phyllosilicates required to obtain this clay concentration.

4-2 From the damaged zone to the creeping zone: time-dependent change

These observations and interpretations document a time-dependent change in the mineral composition and a spatial change of the microstructure from the damaged zone to the creeping zone. This chronology is deduced both from the foliation development and its change with time, and from the observations of the interactions between friction and pressure solution.

4-2-1 How did the foliation develop?

4-2-1-a In the damaged zone

Pressure solution creep is the main deformation mechanism known to develop foliation characterized by tectonic layering (Figure 7) with or without associated calcite deposition in veins. Such cleavage or cleavage-and-vein structures develop in an open system with two structural end members: (i) zones where the dissolution of soluble

species washed away by fluid flow led to the passive concentration of phyllosilicates (Figure 4j,k,l), and (ii) zones where calcite precipitation occurred in veins oriented perpendicular to the cleavage (Figure 7). Both end-members may be seen as parallel layers in the damaged zone, amplifying tectonic layering. Both processes accommodate aseismic deformation leading to an agreement between the orientation of the foliation and that of the fault. The strain reached by such a pressure solution cleavage or cleavage-and-vein structures may theoretically be quite large, up to 60% shortening in some SAFOD samples (Gratier et al., 2011). However, the actual strain never exceeds such a value for two reasons that are related to the processes at work in the two end-member zones: (i) if most of the soluble species are washed away and if they do not bear a significant differential stress (being dispersed in a soft matrix), pressure solution cannot continue; (ii) if calcite precipitates in veins, the dissolution of such veins is much slower than the dissolution of a mixture of soluble and insoluble species (see § 4-1-1 above). Sixty per cent of shortening in a shear zone is the strain that is associated with a shear strain value (g) of 1 (Ramsay, 1967). In the SAF case, g is much higher: several km of displacement lead to g values exceeding 1000, and the actual displacement on the SAF is even higher. Consequently, mechanisms other than cleavage and cleavage-and-vein deformation must be at work in the creeping zone.

4-2-1-b In the CDZ

Evidence of pressure solution creep is seen within the polymineral clasts (Figure 5): most of these closely healed clasts of serpentine, quartz and feldspar are deformed by cleavage-and-vein process, the veins being most often sealed by calcite, as observed in the damaged zone. If there were only quartz and feldspar clast aggregates, it might be assumed that they could have been ripped from the damaged zone. However, there are very few, if any, serpentine clasts in the damaged zone so the only explanation to the presence of such serpentine clasts is that they are the remnants of an initial state of the now creeping zone. They are evidence of an early stage that is now only seen in the damaged zone. On the another hand, the main structure of the present-day creeping zone is the foliation without preferential orientation, already described by various authors (Schleicher et al., 2009a; 2010; Holdsworth et al., 2011). There are two theories to

explain such a specific foliation. First, the sliding of clay minerals may be associated with the development of micro shear planes and the rotation of the polymineralic clasts whether it be the mineral aggregates or the smaller grains (Figure 9b). The rotations of all those rigid objects drag the foliation and contribute to the chaotic microstructure observed (Figure 9c). Alternatively, if the clasts cannot rotate between two shear planes, the system is locked, and the only way to continue deforming is to develop constantly new foliations, superimposed on the previous ones (Figure 9d). The possible rotation of the polymineral clasts may be linked to their shape ratio and to their interaction with the matrix. Indenting by pressure solution at the boundary of such polymineral clasts suggests that pressure solution accommodated by diffusion contributes to the general grain-clast boundary sliding of all the minerals of the creeping zone. This process can accommodate almost infinite shear values. However, the internal deformation of some clasts (Figure 5) is much more complex that what is seen in the damaged zone (Figure 4). Such a structure, with veins of calcite oriented in almost all directions may indicate that at least part of the clast fracturing occurs within the creeping zone and is associated with rotation of the clasts.

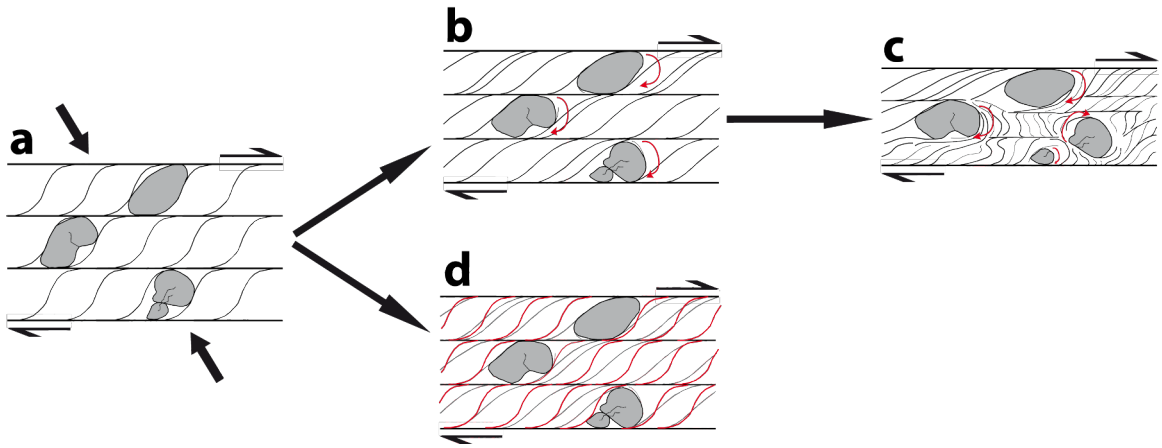

Figure 9: Model of clay deformation leading to foliation without preferential orientation. (a) Initial state, with a normal foliation oriented at about 45° to the shear plane. (b) The foliation follows a normal trend, tending to become parallel with the shear planes. But the presence of hard bodies (aggregates and all-size grains) hinders this parallelization and stops the development of the foliation. (c) The grains start to rotate, continuing to accommodate the deformation. This rotation is controlled by the sliding of the clay minerals one against the other or by pressure solution creep at grain boundaries, when soluble grains are in contact or under stress. (d) If the grains do not rotate, the system is locked. To continue deformation, the only way is to develop a new foliation, superimposed on the previous one. This process can be repeated every time the grains lock the system.

4-2-2 How do friction, fracturing and mass transfer interact in the creeping processes?

Figure 10 shows two possible developments in a deformed rock undergoing pressure solution creep. They both start in the same manner: pressure solution concentrates phyllosilicates in the solution cleavage seams and deposition and crystallization of calcite occurs inside the fractures that are formed by stress concentration at the grain contacts (Figure 7). Starting from this step, two scenarios of microstructure development can be proposed:

(i) In the initially stronger rocks, large fractures develop that become sealed with a large amount of calcite (or other soluble minerals) (Figure 4g,h,i and Figure 5b,g,i). These monomineralic regions will become stronger, and consequently break, and be sealed again, which will harden them even more (Figure 10f). Repeated fractures that are seen both in the damaged zone and in the creeping zone could explain the well-known microseismicity associated with the creeping process along the SAF (Hadizadeh et al., 2012). This process, localized near the creeping zone, needs to be studied in more detail, since some of the faults seen in the damaged zone are not necessarily related to the creeping process. Conversely, the multi-fractured clasts trapped and embedded in the clay matrix (Figure 5i) are deformed during the creeping process.

(ii) Conversely, in the initially weaker rocks or at least in the zones were little redeposition occurred, dissolution of soluble minerals washed out by fluid flow led to the passive concentration of phyllosilicates. Such zones are mostly open systems with very little soluble mineral redeposition (Figure 10d,e). Some calcite mineral growth may be seen in pressure shadows of the mineral aggregate patches (Figure 5c). Moreover, it has been proposed (Schleicher et al., 2009b; Schleicher et al., 2010; Holdsworth et al., 2011) that at least part of the clay minerals may result from precipitation, or alteration of pre-existing phyllosilicates or mafic rocks, with more or less episodic fluid flow that could bring Mg-rich fluid from serpentine massifs. This would be an example of dissolution-precipitation reactions that would induce creep (Wintsch and Yi, 2002). Alternatively, the creeping zone may have had a slightly different composition from pre-existing serpentine – as reflected by the presence of serpentine clasts only in the creeping zone – and Mg-rich chlorites. These two cases – i.e., concentration by pressure solution process and

transformation of pre-existing phyllosilicates – lead to an increase in clay amount, promoting the same type of behaviour: a decrease in the friction value in the creeping zone thanks to the low friction of the saponite and enhancement of stress-driven reactions, both facilitating pressure solution diffusion-controlled grain sliding. Pre-existing phyllosilicates were then progressively transformed into a soft mineral (at least down to 3-4 km depth, which corresponds to the field of stability of saponite), thanks to fluid-rock interactions and possible metasomatic reactions linked to episodic fluid flow through the creeping zone.

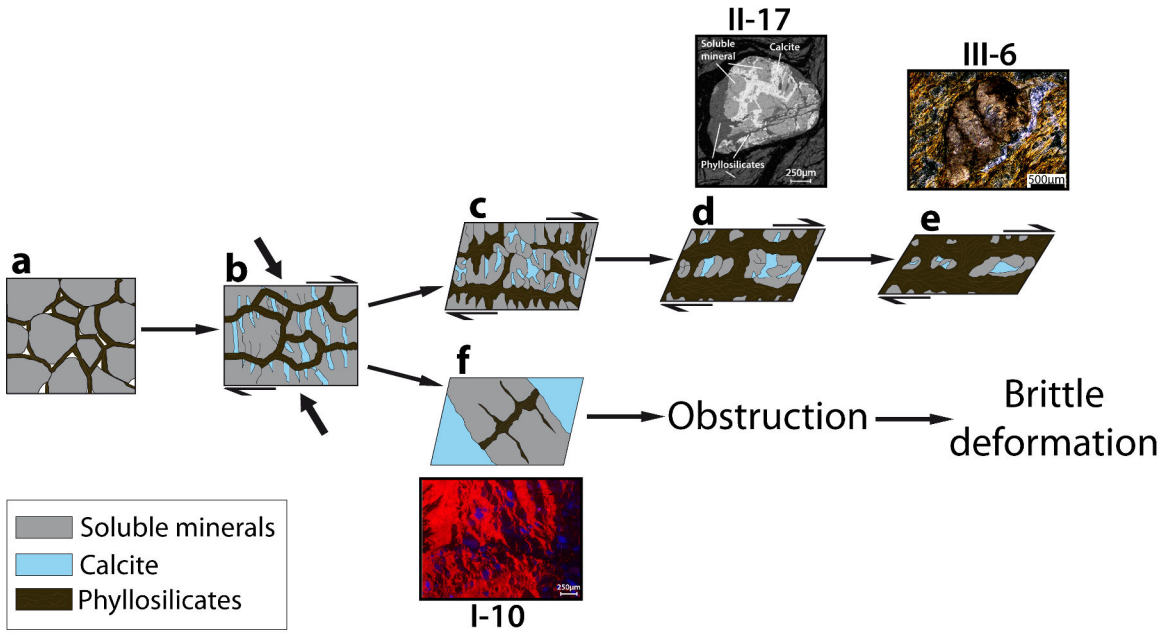

Figure 10: Model of mineral change inside the damaged zone. (a) Initial state: the grey grains are soluble minerals such as quartz, feldspars, serpentine, etc. (b) Deformation starts with compression and shearing, which leads to fracturing at indenting contacts and activation of pressure solution creep. Soluble minerals start dissolving, calcite (in blue) is precipitated into the fractures and phyllosilicates (in brown) begin to be passively concentrated. (c) A foliation is developed with the passive concentration of phyllosilicates. The opening of veins becomes wider. (d) With time, the soluble minerals continue to dissolve. Because of fluid circulation, the main part of the dissolved material is transported away. Phyllosilicate concentration increases with the growth and crystallization of clay. Polymineral clasts start to be formed and act as hard objects. (e) Final state: rotation of the hard objects. Initially, they were the aggregates protected by the calcite or the monomineralic aggregates, harder to dissolve. (f) The large calcite veins wedge the system and stop the ductile deformation.

4-3 From the damaged zone to the creeping zone: the localization process

Interactions between friction, fracturing and pressure solution in the creeping zone also lead to a localization process. There is good evidence that at the beginning of the process, the whole damaged zone was creeping mostly by pressure solution cleavage (Figure 11), as has been observed in other faults (Faulkner et al., 2003; Gratier et al 2013b). However, interactions between fracturing and sealing lead to mechanical differentiation. In the initially stronger rock, fracturing and associated sealing strengthen the rocks: the stronger the rock, the more likely it may break and be sealed by new calcite that renders the rock even stronger. Only a failure in the sealing process can end this feedback process. Conversely, in the zone with minimum deposition and maximum fluid flow, rocks soften progressively thanks to effects of both the progressive concentration of phyllosilicates activating pressure solution and the progressive transformation of phyllosilicates into soft clays (at least in the upper part of the crust). This progressive weakening may have been initially induced by the occurrence of successive earthquakes (Figure 11) that could have contributed to opening the system, promoting episodic fluid flow (Mittempergher et al., 2011), and to reducing the grain size, promoting pressure solution. The end-member of such a change is a zone without any soluble species or with dispersed clasts that do are not subjected to significant differential stress. In such a case, the low friction of clay minerals mostly controls shear strength. It is not clear whether the present creeping zone has already reached this stage in the first 3-4 km, or if diffusive clast sliding still plays a role as a deformation mechanism.

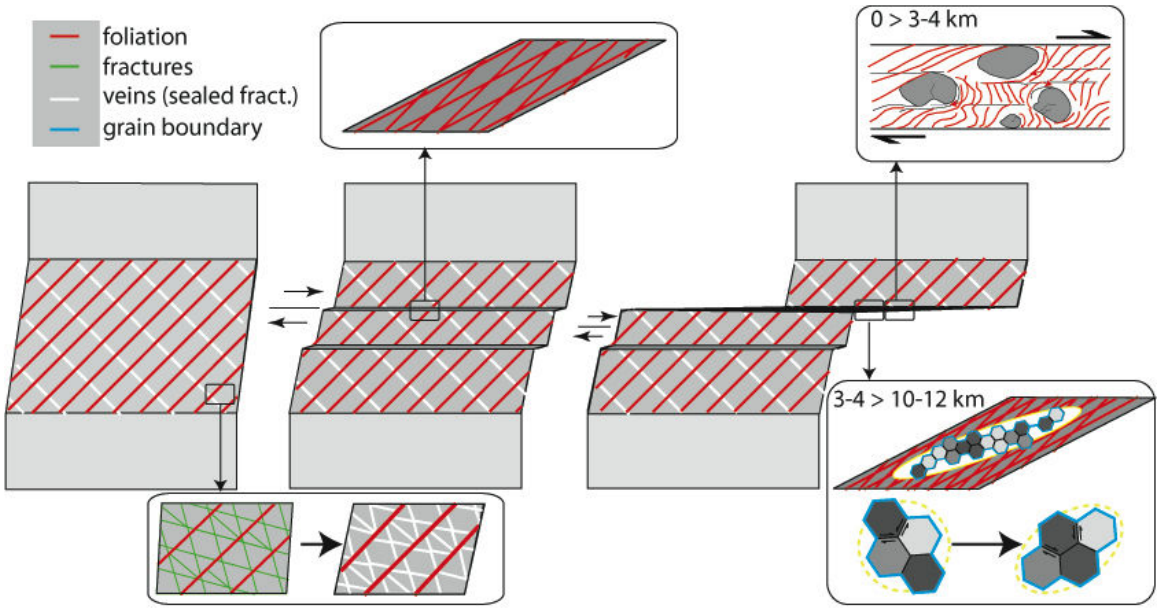

Figure 11: Schematic model of the change in a creeping zone. On the left a creeping zone, up to several hundred metres wide, initiates in a zone combining several conditions favourable to pressure solution creep: (i) presence of fluids that can dissolve at least part of the rock, (ii) mixture of soluble and insoluble minerals, (iii) small grain size or fractured grains. The creeping rate is not efficient enough to relax the stress so earthquakes occur through this zone (middle part). This has two effects: grain size reduction, which activates pressure solution creep, and fluid flow enhancement through the pre-creeping zone. These fluids evacuate the soluble species and thus concentrate phyllosilicates, also promoting pressure solution creep. On the right hand side, a metre-wide creeping zone is stable: in the upper part of the crust (0 – 3-4 km) creep is promoted both by the very low friction of the clay minerals (saponite) that derived from both the passive concentration of phyllosilicate and the metamorphic reactions linked to episodic fluid flows. In the lower part of the crust (3-4 to 10-12 km), diffusion-accommodated grain-sliding pressure solution creep is efficient enough to accommodate aseismic sliding.

4-4 Change in creeping mechanisms with depth

The change in creep mechanisms with depth is strongly dependent on rock composition and microstructure. As the temperature increases with depth, mineral composition changes, leading to dissolution-precipitation reactions (Putnis, 2002; Wintsch and Yi, 2002). In the San Andreas Fault, saponite clay, which is a stable mineral up to about 110°C, will transform at depth into corrensite that is stable up to 150°C and is likely to change into Mg-rich chlorite at greater depth (Moore and Rymer, 2012). Those mineral transformations tend to strengthen the creeping zone at depth, because the friction coefficients of these two minerals are much higher (0.6 to 0.7) than that of saponite (0.2). Therefore, the accommodation of deformation by low friction minerals is efficient near the surface (up to 3-4 km of depth, Lockner et al., 2011; Carpenter et al.,

2011), but becomes less efficient and more energy consuming with depth. On the other hand, the required conditions for efficient pressure solution creep are fulfilled if a trapped fluid phase is kept within the creeping zone and if fracturing and comminution processes have reduced the grain size, i.e., the characteristic mass transfer distance. In such a case, diffusive grain boundary sliding controlled by pressure solution is likely to be the most efficient process at depth. Such a process is comparable to superplasticity (Ashby and Verall, 1973). Only the diffusive path is different, either within a trapped fluid phase (Gratier et al., 2011), or along dry grain boundaries (Boullier and Gueguen, 1975). Such a process is able to accommodate almost infinite shear deformation (Figure 12).

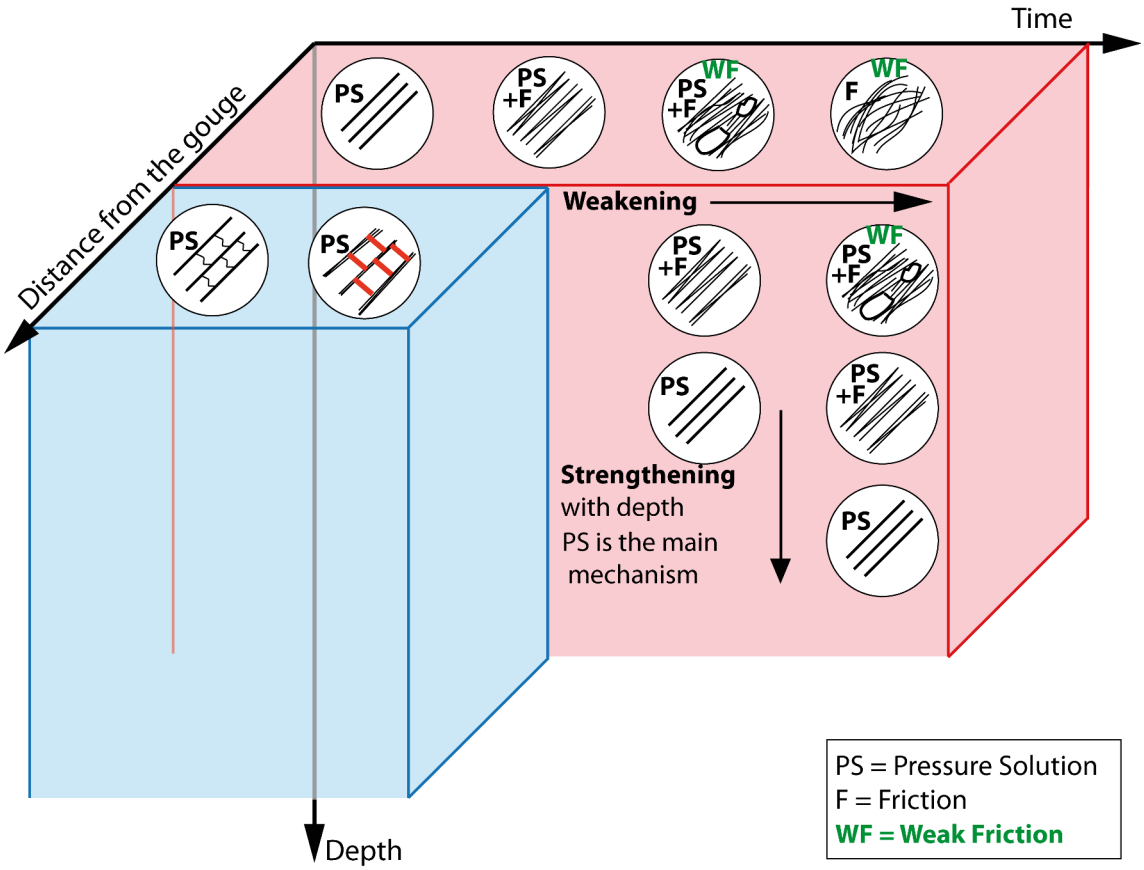

Figure 12: Model of a creeping fault zone showing the change in mineralogy as a function of time, depth and creeping zone distance. The blue domain corresponds to the creep mechanism observed in the damaged zone, in the samples outside the creeping zone. In this domain, pressure solution creep is the main creep mechanism. Healing by calcite precipitation allows this mechanism to be maintained with time as well as at depth. The red domain corresponds to the creep mechanisms observed in the active creeping zone. Pressure solution creep is very efficient at the beginning at all depths. However, because there is no or little healing in this domain because fluids drive away the dissolved materials, the mineralogical composition evolves with time leading to increasing clay content in the upper 3-4 km. The friction coefficient of the creeping domain becomes very low and the sliding of clay layers on top of each other could accommodate a substantial part of the creeping rate. It is completed by stress-driven diffusive mass transfer that accommodates the sliding of grains and clast aggregates. Low friction related to saponite is not operative below 3-4 km because of the transformation of saponite into corrensite then chlorite, which have higher friction coefficients. When saponite starts to transform into harder minerals with the increase in temperature, the entire domain becomes stronger and more difficult to deform by friction. Diffusion-accommodated grain-sliding pressure solution creep remains efficient and is the main creep mechanism at depth.

5 – Conclusion

From microstructural observations of rock samples collected at depth in the active creeping zone of the San Andreas Fault, a model is proposed for the temporal and spatial change in creep mechanism for creeping zones. It is shown that, in a first stage, the creeping zone was relatively wide, 100 m, corresponding approximately to the width of the damaged zone. Deformation was mostly controlled by pressure solution creep, as evidenced by the development of a cleavage-and-vein structure and foliation parallel to fault displacement. Subsequently, interactions between friction, fracturing and mass transfer led to very localized, metre size, creeping zones without clear parallel foliation. Localization towards such a weak creeping zone was promoted by several parameters: (i) the passive concentration of phyllosilicates in zones where other more soluble minerals such as quartz and feldspars were washed away by episodic fluid flow; (ii) fracturing and comminution processes that increased the rate of mass transfer at grain scale; (iii) the alteration of the phyllosilicates into softer minerals, such as saponite. Conversely, in zones where fractures were sealed, i.e., in the present-day damaged zone, pressure solution creep rate is lower because sealing decreases the efficiency of diffusive mass transfer and friction is much higher since phyllosilicate alteration is limited by hampered fluid flow.

Today, deformation in the creeping zone within the first 3-4 km is controlled by the very low friction of saponite and by diffusive sliding of polymineral clasts embedded in the clay matrix. At greater depths (4-12 km), saponite is transformed into corrensite, and then into chlorite, both with higher friction coefficients. Hence, pressure solution diffusive grain boundary sliding is likely to be the controlling creeping mechanism. In the damaged zone, pressure solution may still be at work but successive fracturing and sealing processes have strengthened the rocks and the strain rate is very low. Microseismicity accompanying creep may be explained by the multiple fracturing of the polymineral clasts embedded in the soft matrix of the creeping zone and by ruptures of asperities and heterogeneities at the boundaries and near the creeping zone.

References

Allen, C.R., 1968. The tectonic environments of seismically active and inactive areas along the San Andreas fault system. In W.R. Dickinson and A. Grantz, eds., Proceedings of conference on geologic problems of San Andreas fault system: Stanford, Calif., Stanford Univ. Pubs. Geol. Sci., 11: 70-82.

Andreani, M., Boullier, A.M., and Gratier, J.-P., 2005. Development of schistosity by dissolution crystallization in a Californian serpentinite gouge. Journal of Structural Geology, 27: 2256-2267.

Ashby, M., and Verall, R., 1973. Diffusion-accommodated flow and superplasticity. Acta Metallurgica, 21: 149-163.

Azzaro, R., Mattia, M., and Puglisi, G., 2001. Fault creep and kinematics of the eastern segment of the Pernicana Fault (Mt. Etna, Italy) derived from geodetic observations and their tectonic significance. Tectonophysics, 333: 401-415.

Bakun, W.H., and McEvilly, T.V., 1984. Recurrence models and Parkfield, California, earthquakes. Journal of Geophysical Research, 89: 3051-3058.

Barbot, S., Fialko, Y., and Bock, Y., 2009. Postseismic deformation due to the M_w 6.0 2004 Parkfield earthquake: stress-driven creep on a fault with spatially variable rate-and-state friction parameters. Journal of Geophysical Research, 114, B07405.

Boness, N.L., and Zoback, M.D., 2004. Stress-induced seismic velocity anisotropy and physical properties in the SAFOD Pilot Hole in Parkfield, CA. Geophysical Research Letters, 31, L15S17.

Boullier, A.M., and Guéguen, Y., 1975. SP-mylonites: origin of some mylonites by superplastic flow, Contributions to Mineralogy and Petrology, 50: 93-104.

Bradbury, K.K., Barton, D.C., Solum, J.G., Draper, S.D., and Evans, J.P., 2007. Mineralogic and textural analyses of drill cuttings from the San Andreas Fault Observatory at Depth (SAFOD) boreholes: Initial interpretations of fault zone composition and constraints on geologic models. Geosphere, 3: 299-318.

Brune, J.N., Hehnyey, T.L., and Roy, R.F., 1969. Heat flow, stress, and rate of slip along the San Andreas Fault, California. Journal of Geophysical Research, 74: 3821-3827.

Burford, R.O., and Harsh, P.W., 1980. Slip on the San Andreas Fault in Central California from alignment array surveys. Bulletin of the Seismological Society of America, 70: 1233-1261.

Byerlee, J., 1978, Friction of rocks: Pure and Applied Geophysics, 116: 615–626.

Carpenter, B.M., Marone, C., and Saffer, D.M., 2009. Frictional behavior of materials in the 3D SAFOD volume. Geophysical Research letters, 36, L05302.

Carpenter, B.M., Marone, C., and Saffer, D.M., 2011. Weakness of the San Andreas Fault revealed by samples from the active fault zone. Nature Geoscience, 4: 251-254.

Chéry, J., Zoback, M.D., and Hickman, S., 2004. A mechanical model of the San Andreas fault and SAFOD Pilot Hole stress measurements. Geophysical Research Letters, 31, L15S13.

Chester, F.M., Evans, J.P., and Biegel, R.L., 1993. Internal structure and weakening mechanisms of the San Andreas Fault. Journal of Geophysical Research, 98: 771-786.

Collettini, C., Viti, C., Smith, S.A.F., and Holdsworth, R.E., 2009. Development of interconnected talc networks and weakening of continental low-angle normal faults. Geology, 37: 567-570.

Cox, S.F., and Etheridge, M.A., 1989. Coupled grain-scale dilatancy and mass transfer during deformation at high fluid pressures: examples from Mount Lyell, Tasmania. Journal of Structural Geology 11: 147-162.

d'Alessio, M.A., Williams, C.F., and Bürgmann, R., 2006. Frictional strength heterogeneity and surface heat flow: Implications for the strength of the creeping San Andreas fault. Journal of Geophysical Research, 111, B05410.

Ellsworth, W.L., 1990. Earthquake history, 1769-1989. In: R.E. Wallace, The San Andreas Fault System, California. USGS Professional Paper 1515, Washington, 283p.

Faulkner, D.R., Lewis, A.C., and Rutter, E.H., 2003, On the internal structure and mechanics of large strike-slip fault zones: field observations of the Carboneras fault in southeastern Spain, Tectonophysics, 367: 235-251.

Freed, A.M., 2007. Afterslip (and only afterslip) following the 2004 Parkfield, California, earthquake. Geophysical Research Letters, 34, L06312.

Fulton, P.M., Saffer, D.M., Harris, R.N., and Bekins, B.A., 2004. Re-evaluation of heat flow data near Parkfield, CA: Evidence for a weak San Andreas Fault. Geophysical Research Letters, 31, L15S15.

Fulton, P.M., Saffer, D.M., and Bekins, B.A., 2009. A critical evaluation of crustal dehydration as the cause of an overpressured and weak San Andreas Fault. Earth and Planetary Science Letters, 284: 447-454.

Fulton, P.M., and Saffer, D.M., 2009. Potential role of mantle-derived fluids in weakening the San Andreas Fault. Journal of Geophysical Research, 114, B07408, doi:10.1029/2008JB006087.

Gao, S.S., Silver, P.G, and Linde, A.T., 2000. Analysis of deformation data at Parkfield, California: detection of a long-term strain transient. Journal of Geophysical Research, 105: 2955-2967.

Gratier, J.-P., Renard, F., and Labaume, P., 1999. How pressure solution creep and fracturing processes interact in the upper crust to make it behave in both a brittle and viscous manner. Journal of Structural Geology, 21: 1189-1197.

Gratier, J.-P., and Gueydan, F., 2007. Deformation in the presence of fluids and mineral reactions: effect of fracturing and fluid-rocks interaction on seismic cycle, in: Tectonic Faults, agent of change on a dynamic earth, edited by M.R. Handy, G. Hirth, N. Hovius, Dahlem Workshop, The MIT Press, Cambridge, Mass., USA. 319-356.

Gratier, J.-P., Richard, J., Renard, F., Mittempergher, S., Doan, M.L., Di Toro, G., Hadizadeh, J., and Boullier, A.M., 2011. Aseismic sliding of active faults by pressure solution creep: Evidence from the San Andreas Fault Observatory at Depth. Geology, 39: 1131-1134.

Gratier, J.-P., 2011. Fault permeability and strength evolution related to fracturing and healing episodic processes (years to millennia): the role of pressure solution. Oil & Gas Science and Technology, 3: 491-506.

Gratier, J.P., Dysthe, D.K., and Renard, F., 2013a. The role of pressure solution creep in the ductility of the Earth's upper crust. Advances in Geophysics, 54: 47-179.

Gratier, J.P., Thouvenot, F., Jenatton, L., Tourette, A., Doan, M.L., and Renard, F., 2013b. Geological control of the partitioning between seismic and aseismic sliding behaviours in active faults: evidence from the Western Alps, France. Tectonophysics, 600: 226-242.

Hadizadeh, J., Mittempergher, S., Gratier, J.-P., Renard, F., Di Toro, G., Richard, J., and Babaie, H., 2012. A microstructural study of fault rocks from the SAFOD: Implications for the deformation mechanisms and strength of the creeping segment of the San Andreas Fault. Journal of Structural Geology, 42: 246-260.

Hanks, T.C., and Raleigh, C.B., 1980. The conference on magnitude of deviatoric stresses in the Earth's crust and uppermost mantle. Journal of Geophysical Research, 85: 6083-6085.

Hickman, S., and Zoback, M., 2004. Stress orientations and magnitudes in the SAFOD pilot hole. Geophysical Research Letters, 31, L15S12, doi:10.1029/2004GL020043.

Hickman, S., Zoback, M., Ellsworth, W., Boness, N., Malin, P., Roecker, S., and Thurber, C., 2007. Structure and properties of the San Andreas Fault in Central

California: recent results from the SAFOD experiment. Scientific Drilling, Special Issue, 1: 29-32.

Hobbs, B.E., Means, W.D., and Williams, P.F., 1976. An outline of structural geology, Wiley and Sons, New York, 571p.

Holdsworth, R.E., van Diggelen, E.W.E, Spiers, C.J., de Bresser, J.H.P., Walker, R.J., and Bowen, L., 2011. Fault rocks from the SAFOD core samples: Implications for weakening at shallow depths along the San Andreas Fault, California. Journal of Structural Geology, 33: 132-144, doi:10.1016/j.jsg.2010.11.010.

Ikari, M.J., Marone, C., and Saffer, D.M., 2011. On the relation between fault strength and frictional stability. Geology, 39: 83-86.

Ikari, M.J., Saffer, D.M., and Marone, C., 2009. Frictional and hydrologic properties of clay-rich fault gouge. Journal of Geophysical Research, 114, B05409.

Irwin, P.W., and Barnes, I., 1975. Effect of geologic structure and metamorphic fluids on seismic behavior of the San Andreas fault system in central and northern California. Geology, 3: 713-716.

Jackson, D.D., and Kagan, Y.Y, 2006. The 2004 Parkfield earthquake, the 1985 prediction and characteristic earthquakes: lessons for the future. Bulletin of Seismological Society of America, 96, S397-S409, doi:10.1785/0120050821.

Janssen, C., Wirth, R., Rybacki, E., Naumann, R., Kemnitz, H., Wenk, H.R., and Dresen, G., 2010. Amorphous material in SAFOD core samples (San Andreas Fault): Evidence for crush-origin pseudotachylytes? Geophysical Research Letters, 37, L01303.

Janssen, C., Kanitpanyacharoen, W., Wenk, H.R., Wirth, R., Morales, L., Rybacki, E., Kienast, M., and Dresen, G., 2012. Clay fabrics in SAFOD core samples. Journal of Structural Geology, 43: 118-127.

Jeppson, T.N., Bradbury, K.K., and Evans, J.P., 2010. Geophysical properties within the San Andreas Fault Zone at the San Andreas Fault Observatory at Depth and their relationships to rock properties and fault zone structure. Journal of Geophysical Research, 115, B12423.

Johanson, I.A., Fielding, E.J., Rolandone, F., and Bürgmann, R., 2006. Coseismic and postseismic slip of the 2004 Parkfield earthquake from space-geodetic data. Bulletin of Seismological Society of America, 96, S269-S282, doi:10.1785/0120050818.

Lachenbruch, A.H., and Sass, J.H., 1980. Heat flow and energetics of the San Andreas Fault Zone. Journal of Geophysical Research, 85: 6185-6222.

Lachenbruch, A.H. and Sass, J.H., 1992. Heat flow from Cajon Pass, fault strength, and tectonic implications. Journal of Geophysical Research, 97: 4995-5015.

Lee, J.C., Angelier, J., Chu, H.T., Hu, J.C., and Jeng, F.S., 2005. Monitoring active fault creep as a tool in seismic hazard mitigation. Insights from creepmeter study at Chihshang, Taiwan. Comptes Rendus Geosciences, 337: 1200-1207.

Li, Y.G., Vidale, J.E., and Cochran, E.S., 2004. Low-velocity damaged structure of the San Andreas Fault at Parkfield from fault zone trapped waves. Geophysical Research Letters, 31, L12S06, doi:10.1029/2003GL019044.

Li, Y.G., Chen, P., Cochran, E.S., Vidale, J.E., and Burdette, T., 2006. Seismic evidence for rock damage and healing on the San Andreas Fault associated with the 2004 M 6.0 Parkfield earthquake. Bulletin of Seismological Society of America, 96, S349-S363.

Lockner, D.A., Morrow, C., Moore, D., and Hickman, S., 2011. Low strength of deep San Andreas fault gouge from SAFOD core. Nature, 472: 82-85, doi:10.1038/nature09927.

Lupini, J.F., Skinner, A.E, and Vaughan, P.R., 1981. The drained residual strength of cohesive soils. Geotechnique, 31: 181-213.

McPhee, D.K., Jachens, R.C., and Wentworth, C.M., 2004. Crustal structure across the San Andreas Fault at the SAFOD site from potential field and geologic studies. Geophysical Research Letters, 31, L12S03, doi:10.1029/2003GL019363.

Mittempergher, S., Di Toro, G., Gratier, J.P., Hadizadeh, J., Smith, S.A.F., and Spiess, R., 2011. Evidence of transient increases of fluid pressure in SAFOD phase III cores. Geophysical Research Letters, 38, L03301, doi:10.1029/2010GL046129.

Moore, D.E., and Lockner, D.A., 2007. Talc friction in the temperature range 25°-400°C: Relevance for fault-zone weakening. Tectonophysics, 449: 120-132.

Moore, D.E., and Rymer, M.J., 2007. Talc-bearing serpentinite and the creeping section of the San Andreas fault. Nature, 448: 795-797, doi:10.1038/nature06064.

Moore, D.E., and Lockner, D.A., 2011. Frictional strengths of talc-serpentine and talc-quartz mixtures. Journal of Geophysical Research, 116, B01403, doi: 10.1029/2010JB007881.

Moore, D.E., and Rymer, M.J., 2012. Correlation of clayey gouge in a surface exposure of serpentinite in the San Andreas Fault with gouge from the San Andreas Fault Observatory at Depth (SAFOD). Journal of Structural Geology, 38: 51-60.

Mount, V.S., and Suppe J., 1987. State of stress near the San Andreas fault: Implications for wrench tectonics. Geology, 15: 1143-1146.

Murray, J., and Langbein J., 2006. Slip on the San Andreas Fault at Parkfield, California, over two earthquake cycles, and the implications for seismic hazard. Bulletin of Seismological Society of America, 96, S283-S303, doi:10.1785/0120050820.

Nadeau, R.M., Michelini, A., Uhrhammer, R.A., Dolenc, D., and McEvilly, T.V., 2004. Detailed kinematics, structure and recurrence of micro-seismicity in the SAFOD target region. Geophysical Research Letters, 31, L12S08, doi:10.1029/2003GL019409.

Niemeijer, A.R., and Spiers, C.J., 2006. Velocity dependence of strength and healing behaviour in simulated phyllosilicate-bearing fault gouge. Tectonophysics, 427: 231-253.

Niemeijer, A.R., and Spiers, C.J., 2005. Influence of phyllosilicates on fault strength in the brittle-ductile transition: insights from rock analogue experiments. High-Strain Zones: Structure and Physical Properties, Geological Society, London, Special Publications, 245: 303-327.

Paterson, M.S., 1973. Nonhydrostatic thermodynamics and its geologic applications. Reviews of Geophysics and Space Physics, 11: 355-389.

Perfettini, H., and Avouac, J.P., 2004. Postseismic relaxation driven by brittle creep: A possible mechanism to reconcile geodetic measurements and the decay rate of aftershocks, application to the Chi-Chi earthquake, Taiwan. Journal of Geophysical Research, 109, B02304.

Provost, A.S., and Houston H., 2001. Orientation of the stress filed surrounding the creeping section of the San Andres Fault: Evidence for a narrow mechanically weak fault zone. Journal of Geophysical Research, 106: 11373-11386.

Putnis, A., 2002. Mineral replacement reactions: from macroscopic observations to microscopic mechanisms, Mineralogical Magazine, 66: 689-708.

Raj, R., 1982. Creep in polycrystalline aggregates by matter transport through a liquid phase. Journal of Geophysical Research-Solid Earth, 87: 4731-4739.

Ramsay, J.G., 1967. Folding and fracturing of rocks. MacGraw-Hill Book Company, New York, 568p.

Rathbun, A., Renard, F., and Abe, S., 2013, Numerical investigation of the interplay between wall geometry and friction in granular fault gouge, Journal of Geophysical Research, 118: 878-893.

Rice, J.R., 1992. Fault stress states, pore pressure distribution, and the weakness of the San Andreas Fault. In Evans B., Wong T.F. (Eds), Fault Mechanics and Transport Properties in Rocks, Academic Press, London.

Rubin, A.M., Gillard, D., and Got, J.L., 1999. Streaks of microearthquakes along creeping faults. Nature, 400: 635-641.

Rutter, E.H., Maddock, R.H., Hall, S.H., and White, S.H., 1986. Comparative microstructures of natural and experimentally produced clay-bearing fault gouges. Pure and Applied Geophysics, 124: 3-30.

Rutter, E.H., 1976. The kinetics of rock deformation by pressure solution. Philosophical Transactions of the Royal Society of London, 283: 203-219.

Rutter, E.H., 1983. Pressure solution in nature, theory and experiment. Journal of the geological Society of London, 140: 725-740.

Rutter, E.H., and Mainprice, D.H., 1979. On the possibility of slow fault slip controled by a diffusive mass transfer, Gerlands Beitr. Geophysik, Leipzig, 88: 154-162.

Sagy, A., Reches, Z., and Roman, I., 2001. Dynamic fracturing : field and experimental observations: Journal of Structural Geology, 23: 1223–1239.

Schleicher, A.M., Warr, L.N., van der Pluijm, B.A., 2009a. On the origin of mixed-layered clay minerals from the San Andreas Fault at 2.5–3 km vertical depth (SAFOD drillhole at Parkfield, California). Contrib. Mineral. Petrol., 157: 173-187, doi:10.1007/s00410-008-0328-7.

Schleicher, A.M., Tourscher, S.N., van der Pluijm, B.A., and Warr, L.N., 2009b. Constraints on mineralization, fluid-rock interaction, and mass transfer during faulting at 2–3 km depth from the SAFOD drill hole. Journal of Geophysical research, 114, B04202, doi:10.1029/2008JB006092.

Schleicher, A.M., van der Pluijm, B.A., and Warr, L.N., 2010. Nanocoatings of clay and creep of the San Andreas fault at Parkfield, California. Geology, 38: 667-670, doi:10.1130/G31091.1.

Scholz, C.H., 1992. Weakness amidst strength. Nature, 359: 677-678.

Scholz, C.H., 2000. Evidence for a strong San Andreas fault. Geology, 28: 163-166.

Sibson, R.H., 1990. Faulting and fluid flow. In "Fluids in tectonically active regimes of the continental crust." (B. E. Nesbitt, Ed.), pp. 93-132. Short Course Handbook. Mineralogical Association of Canada.

Siddans, A.W.B., 1972. Slaty cleavage — a review of research since 1815. Earth-Science Reviews 8: 205-232.

Sieh, K.E., 1978. Slip along the San Andreas fault associated with the great 1857 earthquake. Bulletin of the Seismological Society of America, 68: 1421-1448.

Sieh, K.E., and Jahns, R.H., 1984. Holocene activity of the San Andreas fault at Wallace Creek, California. Geological Society of America Bulletin, 95: 883–896.

Solum, J.G., Hickman, S.H., Lockner, D.A., Moore, D.E., van der Pluijm, B.A., Schleicher, A.M., and Evans, J.P., 2006. Mineralogical characterization of protolith and fault rocks from the SAFOD Main Hole. Geophysical Research Letters, 33, L21314, doi:10.1029/2006GL027285.

Solum, J.G., Hickman, S., Lockner, D.A., et al., 2007. San Andreas Fault zone mineralogy, geochemistry and physical properties from SAFOD cuttings and core. Scientific Drilling, Special Issue 1: 64-67, doi:10.2204/iodp.sd.s01.34.2007.

Steinbrugge, K.V., and Zacher, E.G., 1960. Creep on the San Andreas fault. Fault creep and property damage. Seismological Society of America Bulletin, 50: 389-396.

Tembe, S., Lockner, D.A., Solum, J.G., Morrow, C.A., Wong, T.F., and Moore, D.E., 2006. Frictional strength of cuttings and core from SAFOD drillhole phases 1 and 2. Geophysical Research Letters, 33, L23307, doi:10.1029/2006GL027626.

Tembe, S., Lockner, D., and Wong, T.F., 2009. Constraints on the stress state of the San Andreas Fault with analysis based on core and cuttings from San Andreas Fault Observatory at Depth (SAFOD) drilling phases 1 and 2. Journal of Geophysical Research, 114, B11401, doi:10.1029/2008JB005883.

Tembe, S., Lockner, D.A., and Wong, T.F., 2010. Effect of clay content and mineralogy on frictional sliding behavior of simulated gouges: Binary and ternary mixtures of quartz, illite, and montmorillonite. Journal of Geophysical Research, 115, B03416, doi:10.1029/2009JB006383.

Thurber, C., Roecker, S., Zhang, H., Baher, S., and Ellsworth, W., 2004. Fine-scale structure of the San Andreas fault zone and location of the SAFOD target earthquakes. Geophysical Research Letters, 31, L12S02, doi:10.1029/2003GL019398.

Titus, S.J., DeMets, C., and Tikoff, B., 2006. Thirty-five-year creep rates for the creeping segment of the San Andreas Fault and the effects of the 2004 Parkfield earthquake: constraints from alignment arrays, continuous global positioning system and creepmeters. Bulletin of the Seismological Society of America, 96, S250-S268, doi:10.1785/0120050811.

Townend, J., and Zoback, M.D., 2004. Regional tectonic stress near the San Andreas fault in central and southern California. Geophysical Research Letters, 31, L15S11, doi:10.1029/2003GL018918.

Vrolijk, P., and van der Pluijm, B.A., 1999. Clay gouge. Journal of Structural Geology, 21: 1039-1048.

Wallace, R.E., 1970. Earthquake recurrence intervals on the San Andreas fault. Geological Society of America Bulletin, 81: 2875-2890.

Wallace, R.E., 1990. General features. In: R.E. Wallace, The San Andreas Fault System, California. USGS Professional Paper 1515, Washington, 283p.

Weyl, P.K., 1959. Pressure solution and the force of crystallization: a phenomenological theory. Journal of Geophysical Research, 64: 2001-2025.

Wintsch, R.P., and Yi, K., 2002, Dissolution and replacement creep: a significant deformation mechanism in mid-crustal rocks, Journal of Structural Geology, 24: 1179-1193.

Wood, D.S., 1974. Current views of the development of slaty cleavage. Annual Review of Earth and Planetary Sciences, 2: 369-400.

Yu, S.B., and Liu, C.C., 1989. Fault creep on the central segment of the longitudinal valley fault, eastern Taiwan. Proceedings of the Geological Society of China, 32: 209-231.

Zoback, M.D., et al., 1987. New evidence for the state of stress on the San Andreas fault system. Science, 238: 1105-1111.

Zoback, M.D., Silver, L.T., Henyey, T., and Thatcher, W., 1988. The Cajon Pass scientific drilling experiment: Overview of phase I. Geophysical Research Letters, 15: 933-936.

Zoback, M.D., 2000. Strength of the San Andreas Fault. Nature, 405: 31-32.

Zoback, M.D., 2006. SAFOD penetrates the San Andreas Fault. Scientific Drilling, Special Issue, 2, 32-33.

Zoback, M., Hickman S., and Ellsworth W., 2010. Scientific drilling into the San Andreas fault zone. Eos (Transactions, American Geophysical Union), 91: 197–199.

Zoback, M., Hickman, S., Ellsworth, W., et al., 2011. Scientific drilling into the San Andreas Faut Zone – An Overview of SAFOD's first five years. Scientific Drilling, 11: 14-28.

Zubtsov, S., Renard, F., Gratier, J.-P., Guiguet, R., Dysthe, D.K., and Traskine, V., 2004. Experimental pressure solution compaction of synthetic halite/calcite aggregates. Tectonophysics, 385: 45-57.

Conclusion

Ce travail nous a permis de mettre en évidence l'importance du rôle des mécanismes de fluage dans l'évolution d'une zone de gouge. Il nous a permis d'identifier quels étaient les processus de fluage les plus efficaces dans le cas d'une des zones en fluage actif de la faille de San Andreas. Il serait désormais intéressant de compléter ces résultats avec une étude analogue sur la seconde zone en fluage actif, la SDZ. Sachant que cette dernière est moins active, sa comparaison avec la CDZ permettrait de compléter notre modèle 3D et de déterminer si cette zone est dans un stade plus précoce ou plus avancée que sa voisine plus active.

CHAPITRE 4

Caractérisation de l'endommagement et de son influence sur les processus de cicatrisation dans un calcaire poreux

---

Introduction

Les interactions entre les différents processus de faille sont très complexes et comme nous l'avons vu, la mise en place des différents mécanismes de fluage est fortement influencée par les conditions initiales du milieu. Nous avons également mis en évidence l'importance de la fracturation dans l'activation du processus de fluage par dissolution cristallisation et le rôle de celui-ci dans la cicatrisation des roches. Dans ce chapitre, nous présentons les résultats d'expérimentations de laboratoire sur un calcaire très poreux : le calcaire Estaillades. Les motivations de ces expérimentations étaient, dans un premier temps, la caractérisation de l'organisation de l'endommagement dynamique à l'échelle microstructurale dans un milieu hétérogène, ainsi que son influence sur la porosité. Dans un second temps, nous avons voulu mettre en évidence le rôle de cet endommagement sur la cinétique de la cicatrisation par circulation fluide et l'évolution de la perméabilité au sein de l'échantillon.

Microstructures induced by dynamic damaging and fracture healing in porous limestone: an experimental approach

Julie Richard[1,2], Mai-Linh Doan[1,2], Jean-Pierre Gratier[1,2], François Renard[1,2,3]

[1] *University Grenoble Alpes, ISTerre, F-38041 Grenoble, France*

[2] *CNRS, ISTerre, F-38041 Grenoble, France*

[3] *University of Oslo, Physics of Geological Processes, 0316 Oslo, Norway*

(Soumis à Pure and Applied Geophysics)

Abstract

Fracturing and healing are crucial processes inducing changes in permeability and mechanical behavior of fault zones. Fracturing increases the permeability of fault rocks, creating flow-channels for fluid circulation and enhancing the kinetics of fluid-rock processes, such as pressure solution creep or metamorphism. Conversely, healing processes decrease permeability by closing the fractures and lead to rock strengthening. Consequently, the timescales of these two processes play an important role in controlling the strength of fault zones and their ability to rupture during earthquakes.

This study reports on microstructural observations on porous limestone samples that experienced rapid dynamic damaging and long-term healing due to fluid percolation under laboratory conditions. Dynamic damaging was performed by impacting the samples with steel bars, inside a Split Hopkinson Pressure Bars apparatus. Healing was performed by leaving the samples for three months under triaxial and flow-through conditions.

Samples damaged at high strain rate have two kinds of fracture network: a series of radial and circular macrofractures, and an incipient pulverization zone at the center of the sample loaded at the highest strain rate. Fracture density determined microscopically

from X-ray images correlates with the dissipated energy computed from macro-mechanical data. X-ray images quantify well the damaged state of the samples.

Percolation experiments show that the main healing processes promoting closure of the fractures in the sample are a combination of mechanical compaction and chemical compaction by pressure-solution processes leading to sample deformation and porosity reduction. Microfracturing networks were found to heal faster than the largest fractures, leading to a heterogeneous strengthening of the rock, this feature may have a considerable influence on the processes of earthquake nucleation and rupture propagation.

1. Introduction

Fracturing and healing are two major mechanisms that strongly influence the mechanical behavior of active faults. They are involved in different fault processes, leading to strengthening or weakening of fault zones. Given that their dependence on different parameters varies from one fault to another, and because of the scarcity of *in situ* observations, defining the extent of these two mechanisms remains challenging.

An extreme example of off-fault damage is the pulverized rocks located next to sections of certain major strike-slip faults, such as the San Andreas Fault (Dor et al., 2006a; Wechsler et al., 2011). Such damaging processes may provide important information on rupture propagation during an earthquake (Dor et al., 2006a,b), on earthquake propagation velocity and on dynamic effects responsible for gouge formation (Reches and Dewers, 2005). They also help distinguish between damaging related to fault processes and surface-weathering (Wechsler et al., 2011).

Several experimental studies have been performed to understand the propagation of cracks (Ravi-Chandar and Knauss, 1984a,b; Sagy et al., 2001; Renard et al., 2009a) and the transition between damaged to pulverized rocks (Doan and Gary, 2009; Dor et al., 2009; Yuan et al., 2011; Doan and Billi, 2011). Such experiments highlight the dependence of fracturing mechanisms on different parameters, the most important ones being the strain rate, the total strain, and the material characteristics (Doan and Gary, 2009). They also show evidence that fracturing activates fluid-rock reaction processes,

such as pressure solution creep (Weyl, 1959; Rutter, 1976; Raj, 1982), which are involved in healing mechanisms and consequently in the processes controlling changes in fault strength (Sleep and Blanpied, 1992; Gratier et al., 1999; Gratier et al., 2003; van Noort et al., 2008; Gratier, 2011a). Healing processes take place on relatively long time scales, making it difficult to observe the mechanism *in situ* in nature. However, healing experiments enhanced by pressure solution processes can be performed under specific conditions (high solid solubility, high temperature, etc.) (Brantley et al., 1990; Hickman and Evans, 1991; Cox and Paterson, 1991; Karner et al., 1997; Bos and Spiers, 2002; Hellmann et al., 2002a,b; Nakatani and Scholz, 2004; Yasuhara et al., 2005; Tenthorey and Cox, 2006; Le Guen et al., 2007; Niemeijer et al., 2008), thus avoiding the time scale constraint. These studies show that healing processes are dependent on pressure and temperature conditions and on the fluid chemistry and mineralogical characteristics of the material. Generally, experiments are performed on monocrystals or with monomineral aggregates, both for fracturing and healing experiments. But rocks have a complex structure and are heterogeneous at different scales, especially for materials with high porosity such as some natural carbonates or fault gouge rocks. The microscale heterogeneities influence the geometry of fracture propagation (Renard et al., 2009a) and the healing rate. That is why it is crucial to characterize processes at the microstructure scale of natural materials in order to obtain a better understanding of the implications of the heterogeneities for the fracturing and healing processes. Moreover, thanks to progresses made in the *in-situ* observation of rock using X-ray computed microtomography (Raynaud et al., 1989; Géraud et al., 1998; Lenoir et al., 2007; Renard, 2012), microstructures of samples can be accessed without the disadvantages related to the preparation of thin sections, especially the destruction of the sample.

The aim of the present study is to characterize the development of fracture networks within samples that experienced dynamic damage and then healing under the controlled conditions of laboratory experiments. First, five porous limestone samples were dynamically damaged, using a Split Hopkinson Pressure Bar apparatus (SHPB). Images of the samples were taken before and after fracturing, using X-ray microtomography, to study, at the microstructure scale, the fracture networks induced by dynamic stress loading. Then, to understand healing processes, long-term percolation experiments were

carried out, under triaxial conditions, on one pre-damaged sample and on one pristine sample, with microtomography images again being taken before and after the experiments.

2. Materials and Methods

2.1 Sample material

The limestone samples were collected in the Estaillades quarry (SE France). This Cretaceous bioclastic limestone has a porosity close to 30% and a permeability of 270 mD (Le Guen et al., 2007). It was chosen because of its relatively high permeability, typical of a reservoir rock, and its heterogeneities that act as stress concentrators during deformation. This limestone contains fossil grains of algae of millimeter size, as well as broken calcitic shells, with dimensions in the range 0.6 mm to more than 1 mm, embedded in microsparitic cement (Figure 1a). Two kinds of porosity may be observed: inter-granular macro-pores, which are well connected, and intra-granular micro-pores found in some red algae fossil grains (Han et al., 2007).

Different sample sizes were used (Table 1 & 2). The diameter and height of the samples was varied to identify and minimize boundary effects related to the two deformation instruments used in this study. 3D images of each sample were taken by X-ray tomography, to characterize its initial microstructure before deformation (Figure 1b). After each experiment, another 3D image of each sample was taken in order to establish a comparison with the initial state.

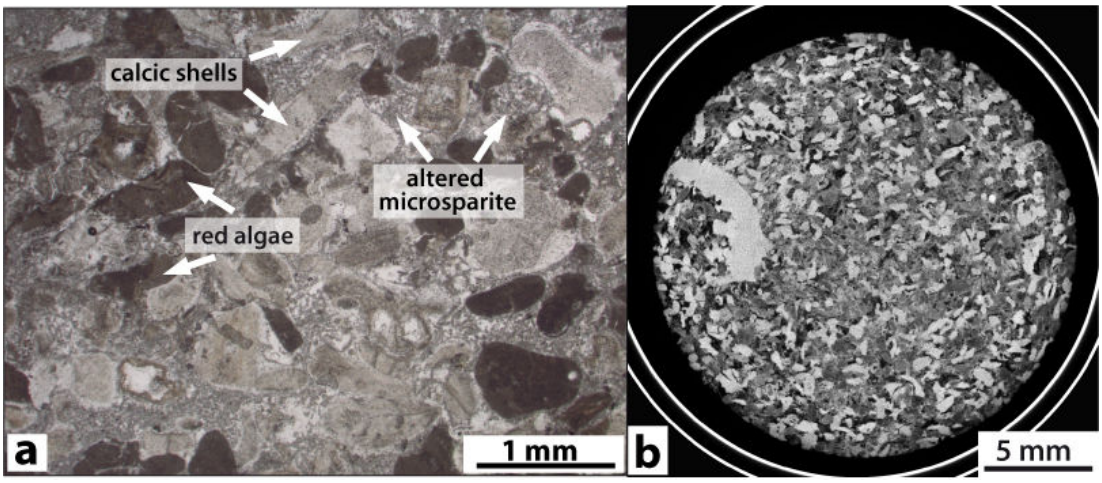

Figure 1: a) Optical microscopy image of a representative thin section of a sample of Estaillades limestone in its initial state. The dark grains correspond to red algae debris and the light grey grains correspond to calcitic shells. The grains are embedded into a microsparitic cement. b) X-ray tomography images of one slice in a sample of Estaillades limestone before deformation. Black holes are porosity, the dark grey grains correspond to the red algae debris, the white grains to calcitic shells, and the microsparitic cement is in light grey. The size distribution of the calcitic shell and red algae grains covers a range of 100 to 5000 micrometers.

2.2 Damaging and percolation experiments

2.2.1 The Hopkinson Bar apparatus for dynamic damaging

The experiments were carried out using a Split Hopkinson Pressure Bar (SHPB) apparatus that enables samples to be damaged at high strain rate (Doan and Gary, 2009; Chen and Song, 2010), at ISTerre, Grenoble, France (Figure 2a). Another sample of larger diameter (C3, see Table 1) was deformed in the Laboratoire de Mécanique des Solides of the Ecole Polytechnique, Palaiseau, France. Each sample is fixed between two steel bars. It is then loaded by a stiff striker impacting the bar assembly and launched by a spring gun. The striker velocity controls strain rate and the maximum stress level to be reached. The striker length controls the loading duration (here ~70µs, for the ISTerre bars). The bars are 2 cm diameter, 1.5 m long and are made of steel. Both bars are equipped with two strain gauges located near the input edge and the center of each bar. These strain gauges measure the incident, reflected and transmitted elastic waves that can be used to determine the stress and strain history of the sample (Chen and Song, 2010).

The aim of these experiments was to characterize the microstructures of the fracture networks and the mechanical behavior of the Estaillades limestone subjected to dynamic

damage. Five experiments were performed at different loading conditions, controlled by the speed of the striker (Table 2).

The fracture density for each sample after inducing damage with the SHPB apparatus was measured inside each sample in order to obtain an average value. For each sample, the surface area occupied by the fractures was estimated on four selected X-ray tomography slices and their proportion with respect to the total surface area of the image was calculated. An average value of the fracture density was also estimated for the initial state of the Estaillades limestone. A damage index is defined as the proportion of fracture surface area in a given tomography slice, at the pixel resolution of the tomography acquisitions; this index is dimensionless and given as a percentage. The microcrack networks below the pixel resolution are estimated and included in the error bars. The results are presented Table 2.

2.2.2 Triaxial instrument for long-term deformation and healing of the samples

Two identical triaxial instruments were used with the axial stress (σ_1), confining stress (σ_3), fluid pressure (P_f), temperature and fluid flow rate being independently controlled and monitored (Figure 2b), (Hellmann et al., 2002a; Le Guen et al., 2007). Experiments were performed under triaxial conditions with $\sigma_1 > \sigma_3 > P_f$ for a timespan of several months. The uniaxial strain of the samples was measured with high-resolution digital linear encoders (LE/12/SIP50, Solartron) at constant time-steps of 10 minutes. The sensitivity of the displacement sensors is 0.5µm. The samples were enclosed in a Viton® sleeve before mounting them in the triaxial cells. The uniaxial stress (σ_1) was imposed by nitrogen gas pressure applied on a piston, directly in contact with the sample. The horizontal confining stress (σ_3) was controlled by nitrogen gas pressure applied on the Viton® sleeve. All experiments were performed at 20°C.

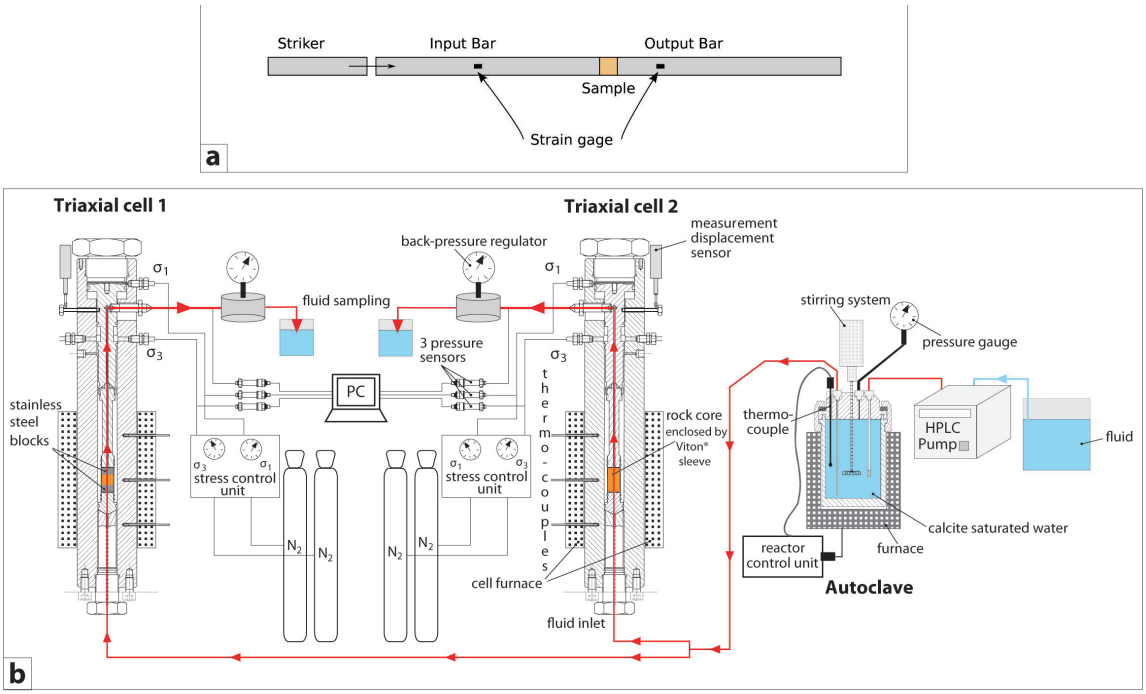

Figure 2: a) Sketch of the Split Hopkinson Pressure Bars (SHPB). b) Sketch of the triaxial cells coupled to percolation. σ_1 is the uniaxial stress, σ_3 corresponds to the confining pressure or the lateral stress and $\sigma_2 = P_f$ is the fluid pressure. These three parameters and the injection rate were all separately controlled and measured. The calcite-saturated water was prepared in a separate pressure vessel (modified after Le Guen et al., 2007).

Fluids were injected into the samples by means of a high-pressure liquid chromatography pump (Knauer K-1001 HPLC). The fluid flow rate is constant during the experiment at 0.300 ml/min. The fluid is composed of deionized water with ammonium chloride [NH_4Cl] at 53.49 g/l, that increases the solubility of the calcite in solution (Ikornikova, 1961) and manganese chloride tetrahydrate [$Cl_2Mn\ 4H_2O$] at 0.90 g/l. The manganese is added to detect any calcite that may have precipitated during the experiment, because when this element is incorporated into newly formed calcite, this calcite has different color under cathodoluminescence microscopy. Firstly, the injected fluid was prepared in a pressure vessel filled with 25 g of calcite grains (diameter 0.315 mm to 0.500 mm) in 0.3 l of double deionized water (Figure 2b) to dissolve the calcite in the injected fluid. The solution was subsequently pushed from the pressure vessel into the triaxial cells and circulated from bottom to top of the rock samples. Finally, the solution was collected at the outlet (Figure 2b). The fluid pressure in the entire system was controlled by back-pressure regulators located at the outlet of each triaxial cell (Le Guen et al. 2007). The vertical axial strain, vertical stress (σ_1), confining pressure (σ_3) and fluid pressure (P_f)

were monitored in order to determine the deformation of two samples of Estaillades limestone over a period of three months (Table 1). During the first seven weeks, no fluid circulation was imposed, but two injection tests were carried out and both uniaxial and confining stresses were slowly increased. This period is used as a reference state to compare the strain values obtained without fluid circulation with those measured in the presence of circulating fluids. During the final five weeks, a fluid was injected into the samples at a constant flow rate.

	C1 (undamaged)	**C3 (damaged)**
Diameter (mm)	24.9	24.8
Weight (g)	44.53	24.27
l_0 height (mm)	49.3	25
l (mm)	46.05	25.65
e	-0,066	0.026
$\dot{e}$ (s^{-1})	-10^{-8}	$7.1.10^{-9}$
σ_1 (Mpa)	14.6	1.5
P_f (Mpa)	1	1
σ_3 (Mpa)	2.1	2
T (°C)	20	20
Fluid flow ($m^3.s^{-1}$)	5.10^{-9}	5.10^{-9}
Tomography acquisition	- Initial - After percolation	- After damaging (Initial) - After percolation

Table 1

To compare the mechanical behavior and the microstructures in the presence of fluid circulation, one dynamically damaged sample (sample C3, 25 mm diameter, 25 mm height) and one sample without damage (sample C1, 25 mm diameter, 50 mm height) were used. The samples were installed in and removed from the two cells at the same time. The fluid flow injection rate was the same for both samples. The experimental parameters (σ_1, σ_3, P_f, T, fluid flow rate, characteristics of the samples) for both samples are summarized in Table 1.

2.2.3 Imaging of samples

A laboratory-built tomograph, installed in the 3S-R laboratory at the University of

Grenoble-Alpes, was used to characterize the microstructures of the samples using X-ray micro-tomography with a voxel resolution in the range 20-40 micrometers. Tomography acquisitions were performed twice on sample C3: after deformation in the SHPB (initial state) and after percolation (final state). Sample C1 was scanned twice as well: before the percolation experiment (initial state) and after the percolation experiment (final state). Some complementary data were provided by optical microscopy and Field Emission Gun Scanning Electron Microscopy (FEG-SEM) on thin sections produced from samples after deformation.

3. Results

3.1 Dynamic fracturing: microstructural characterization

3.1.1 Effect of loading on fracture density

Two sets of experiments were conducted separately. We first prepared a highly dynamically deformed sample for the healing experiments. This sample was 2.5cm in diameter and jacketed with a thick Viton sleeve. It was loaded at Ecole Polytechnique on a large SHPB device, able to damage intensively the sample. The strength of the sample was 56 MPa, with a large loading rate of 567/s.

The second kind of experiments was performed at ISTerre, on a smaller set of bars, designed to load at smaller strain smaller samples, only 2 cm in diameter. For the latter experiments, the strain rate achieved was almost independent on the striker speed, within the range of 70-80 /s.

The fracture densities are related to the loading conditions (see Table 2). It was found that the sample C3, struck with the larger SHPB and with the largest loading is the one with the highest fracture density, close to 19% (Figure 3b and Table 2). The sample was close to pulverization, with the presence of several crushed areas with a dense network of thin fractures, next to areas without any visible fracture (Figure 3b). This indicates a very heterogeneous damage distribution, with both large fractures and large zones of a dense network of thin microfractures.

The samples tested with the smaller testing device enable to investigate the formation of

damage at smaller strain. None of the samples were pulverized, but rather were damaged along few large fractures, either radial or circular. The sample CHB2, struck with the smallest strain, has the smallest fracture density (Figure 3a and Table 2), close to 0.7%. Samples CHB1, CHB3 and CHB4 follow this trend with damage indices ranging from 2% to 3.7%.

We now compare these microstructural descriptions with the macroscopic mechanical data provided by the sensors of the SHPB instrument (Figure 4). In order to understand the energy related to damage mechanism, we estimate dissipated energy during loading by computing the quantity $\int_0^{\infty} \sigma \dot{\varepsilon} dt$. This quantity corresponds to the area below the stress-strain curve. Despite the two datasets were collected at different scale, they appear to correlate well, both for the samples tested at ISTerre and the sample tested at École Polytechnique.

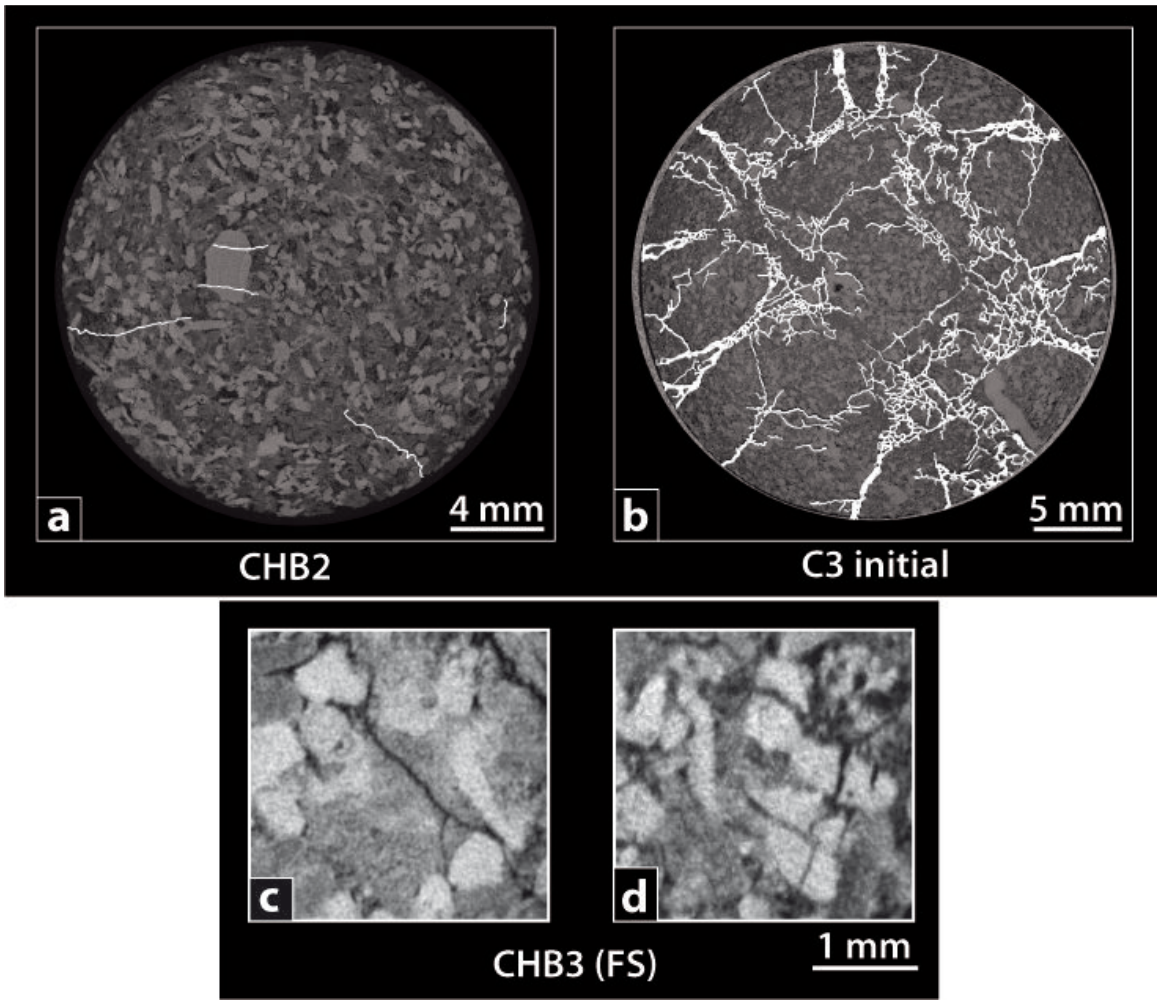

Figure 3: X-ray tomography images of dynamically damaged samples (a) Sample CHB2 with the lowest fracture density and fracture propagation towards the center of the sample. (b) Sample C3 with the highest fracture density and radial fracture propagation; see Table 2 for the experimental conditions. The fracture networks are underlined with white lines. (c & d) Zooms on slices of sample CHB3 showing the two types of fracture propagation: around the grains (c) and through the grains (d).

3.1.2. Effect of damaging on fracture geometry

In most cases, the fracture network has a specific organization. Main radial fracture zones are found close to the boundary of the sample and they propagate in thin circular fracture zones, which generally do not propagate through the center, leaving a relatively undamaged central area (e.g. samples C3, CHB1, CHB4 and part of CHB3, Figure 3b). Conversely, in some places in CHB3 and more generally in CHB2, fractures propagating mainly towards the center of the sample were observed (Figure 3a).

Two kinds of fracture propagation can be distinguished: (i) propagation bypassing

the grains and developing along grain boundaries (Figure 3c), and (ii) propagation occurring straight across the grains (Figure 3d).

	CHB1	CHB2	CHB3	CHB4	C3
Weight (g)	10.6	10.6	10.8	11	24.27
Height (mm)	20	19.7	20	19.8	25
Diameter (mm)	19.1	19.5	19.5	19.1	24.8
Impact velocity ($m.s^{-1}$)	4	3	3.5	4.5	6.7
Peak stress (MPa)	13	12	11	19	56
Maximum strain (%)	0.9	0.6	1	1.2	2.3
Maximum strain rate (s^{-1})	78	78	73	84	570
Dissipated energy (MJ/m^3)	0.072	0.028	0.059	0.12	0.77

	Slice #	Total area (mm^2)	Fracture area (mm^2)	Fracture density (%)	Density average (%)
Initial state	-	-	-	-	0.3±0.3
CHB2	216	293.7	1.3	0.4	0.7±0.4
	526	293.7	1.9	0.6	
	876	293.7	1.2	0.4	
	1331	293.7	3.8	1.3	
CHB3	152	293.7	5.2	1.8	2.0±0.8
	507	293.7	7.4	2.5	
	847	293.7	6.4	2.2	
	1232	293.7	4.9	1.6	
CHB1	179	286.5	7.6	2.6	2.9±1
	514	286.5	6.7	2.3	
	884	286.5	8.9	3.1	
	1184	286.5	9.6	3.4	
CHB4	309	286.5	8.3	2.9	3.7±1.2
	509	286.5	8.5	3	
	934	286.5	13.2	4.6	
	1193	286.5	13	4.5	
C3 Initial	214	535.3	85.4	16	18.8±10.4
	430	535.3	81.4	15.2	
	864	535.3	111.3	20.8	
	1049	535.3	123.3	23	
C3 Final	1026	451.3	35.6	7.9	7.1±3.6
	816	451.3	28.8	6.4	

Table 2

For the sample with the smallest dissipated energy (CHB2), the fractures seem to propagate easily inside the large calcitic grains (Figure 3a), which are the less porous parts of the samples (bright white grains in all the X-ray tomography images). In this case, very few fractures were observed through the smallest grains. Most of the time, when these small grains are fractured, the comparison between the initial state and the

final state revealed that they were already damaged. The samples that experienced more damage have additional fractures, less sensitive to initial heterogeneities. The fracture networks they form propagate widely through the sample. For these fractures, small grains (most of the time both calcitic shells and fossil algae) are preferentially broken rather than larger grains.

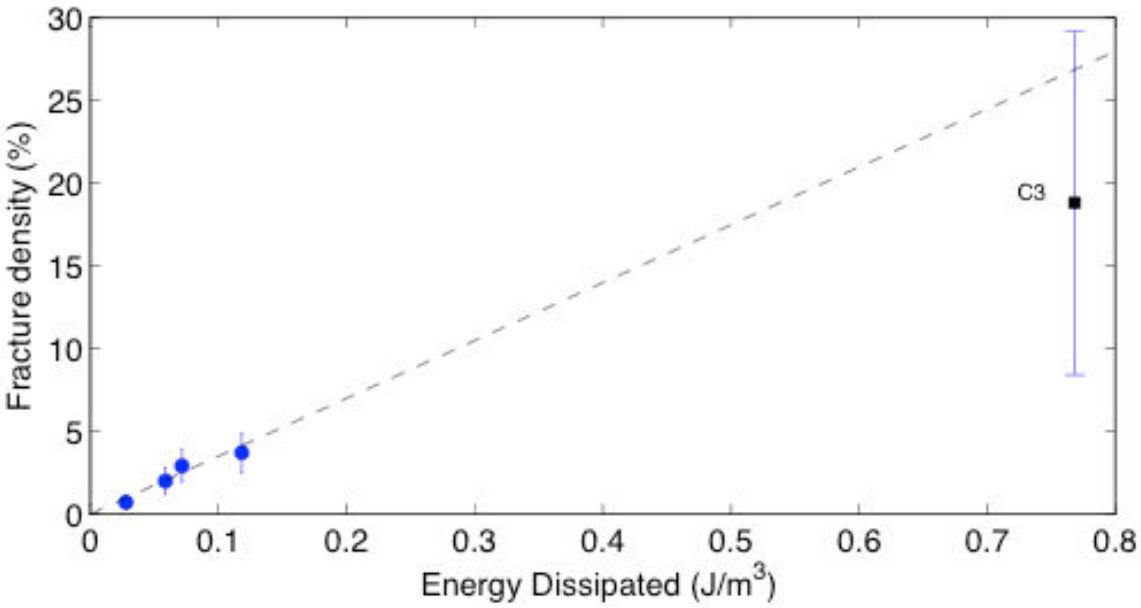

Figure 4: Cross-plot of microstructural fracture density, estimated with X-ray tomography (table 2), versus dissipated energy, estimated from macroscopic data from the SHPB instrument. The samples tested at ISTerre are marked with blue circles, the sample tested in École Polytechnique (C3) is marked with a black square. All data align along a line of slope ~35 %/(MJ/m^3).

3.1.3 Effect of damaging on connected porosity

The Estaillades limestone has a porosity close to 30%, which is mostly connected. Based on X-ray tomography images at grain scale, the structure of the pore network was compared before and after deformation (Figure 5). The porosity could not be quantified in greater detail due to the limited grayscale dynamics of the tomography data. Therefore, only qualitative information is provided here. In the initial state, the pores are not necessarily connected at the grain scale (Figure 5-IS), but it is known from permeability measurements (Le Guen et al., 2007) that they are connected at the scale of the sample as a whole. After damaging, most of the pores, which existed before the experiment, are connected at the grain scale and the overall porosity increases (Figure 5-FS). This indicates that the tortuosity of the flow path between two connected pores has decreased.

The newly formed pore networks, connected by the fracture network, are often observed in the dark matrix in the initial state. Because the pore network is directly related to fracturing in the damaged samples, it is in samples C3 and CHB4 that the largest pores are identified.

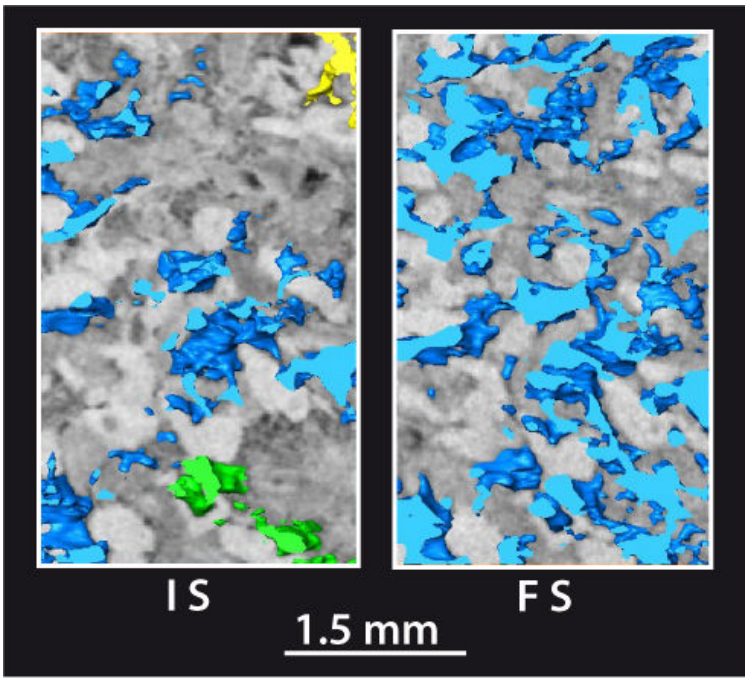

Figure 5: X-ray tomography processed images showing a detail of the porosity network in 3D for sample CHB3, in its initial state (IS) and in its final state (FS). The colors (blue, green and yellow) indicate different pores, which are not connected at the grain scale. In the final state, all the pores are connected in a single network, showing that the distance between connected pores has decreased due to damaging.

3.2 Fluid circulations: development of dissolution and healing processes

3.2.1 Total strain and creep rate

The triaxial rig was used to study the change in strength and porosity under the effect of both axial stress and reactive-fluid circulation on two samples: one widely damaged by dynamic fracturing (C3) and the other in its initial undeformed state (C1).

The uniaxial strain e of the sample was calculated from the axial vertical displacement measured on the X-ray tomography images and defined as $e = | l\text{-}l_0 | / l_0$, where l_0 is the initial sample height, and l is the sample height after deformation. The overall shortening after three months is about 6% (Figure 6). The displacement sensor gives the same result

as well. Moreover, from the displacement data and based on the previous study of Le Guen et al., (2007) using the same triaxial cells and limestone sample, the vertical axial creep rate was calculated over the entire percolation period (5 weeks) by (results in Table 1):

$$\dot{e} = |l\text{-}l_0| / l_0.\Delta t \qquad (2)$$

The creep rates are comparable for both samples (-10^{-8} s^{-1} for C1 and 7.1×10^{-9} s^{-1} for C3), although it should be noted that the stress conditions were different.

The experiments started with dry samples. The first fluid injection caused a rapid response in the strain rate for both samples, the same response was recorded for the second injection as well (Figure 6, the two injections are indicated with dotted black lines). Compaction was observed with some rapid creep events in the cumulative strain curve of sample C1 (arrows in Figure 6) during the percolation period (starting with the dotted blue line). However, the sudden transient creep events in the behavior of C1 observed during the last weeks of percolation cannot be correlated to any variation in fluid pressure and no significant variation was noted in the other control parameters (*i.e.* σ_1, σ_3) as shown on the stress curves (Figure 6). These high strain rate events occurred for periods ranging from several hours to several days, leading to an increase in the strain rate of several orders of magnitude. Moreover, after these rapid creep events, the strain curve recovered back to the same slope.

Concerning the overall strain of sample C3, the method used was the same as that for C1. However, due to the weakness of the damaged sample, a very small difference between σ_1 - σ_3 was imposed at the beginning of the experiment. The confining pressure (σ_3) was then left to increase towards a value slightly greater than σ_1 (Figure 6) in order to achieve maximum sealing of the vertical fracture network induced during the dynamic stress loading process (Figure 8-IS). Consequently, sample C3 did not actually shorten but was slightly stretched during the flow-through process. As observed on the cumulative strain curve of C3 (Figure 6), its behavior oscillated between stretching and no stretching. Those oscillations are not correlated with any pressure variations and, overall, the curve keeps the same slope throughout the percolation period.

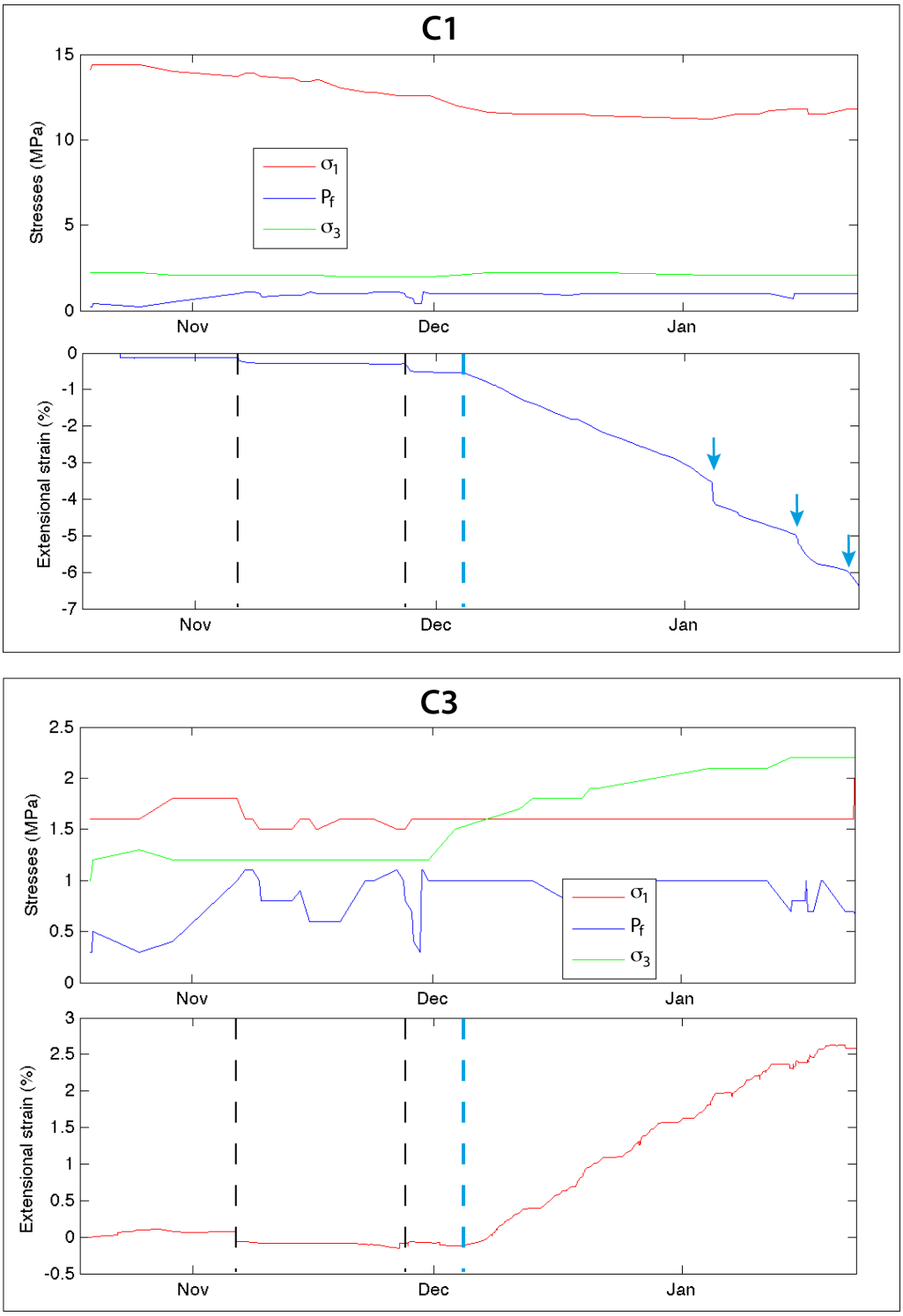

Figure 6: Stresses and cumulative extensional strain curves for sample C1 and C3 for the entire experimentation duration. The dotted black lines on the strain curves correspond to the first two very short fluid injections through the entire circuit. Dotted blue lines correspond to the start of the fluid circulation period. Blue arrows on C1 extensional strain curve underline sudden high strain events.

3.2.2 Microstructures in the undamaged sample (C1) after healing

The X-ray tomography images of sample C1 in its initial and final states after fluid circulation were analyzed. At the base of the sample, close to the fluid inlet, some porosity cavities developed over a distance of 5 mm. These large pores show a broad range of sizes, from less than 0.2 mm to 2.5 mm, and are (at the tomography scale) poorly connected to each other (Figure 7). These pores most probably formed due to dissolution of the material (i.e. karstification process), which indicates that the initial fluid was slightly undersaturated with respect to calcite. It should be noted that these pores are only located at the bottom of the sample and are not observed anywhere else in the sample. Similar features have already been observed in the same type of experiments on chalk by Hellmann et al., 2002b.

A thin layer of calcite particles forming between the sample and the sleeve near the top of the sample was also observed (Figure 7). This might be related to preferential fluid circulation between the sample and the sleeve: after percolation through the sample, the finest particles removed from the enlarged pores are carried with the flow. Consequently, when the fluid escapes, these particles are trapped between the sample and the sleeve. Optical microscopy and cathodoluminescence observations on thin sections made from sample C1 confirmed that this unconsolidated aggregate was not a calcite precipitate, but a very thin particle deposit. Indeed, under cathodoluminescence, no difference in the red shade color could be detected between the calcite grains of the sample and those deposited outside of the sample.

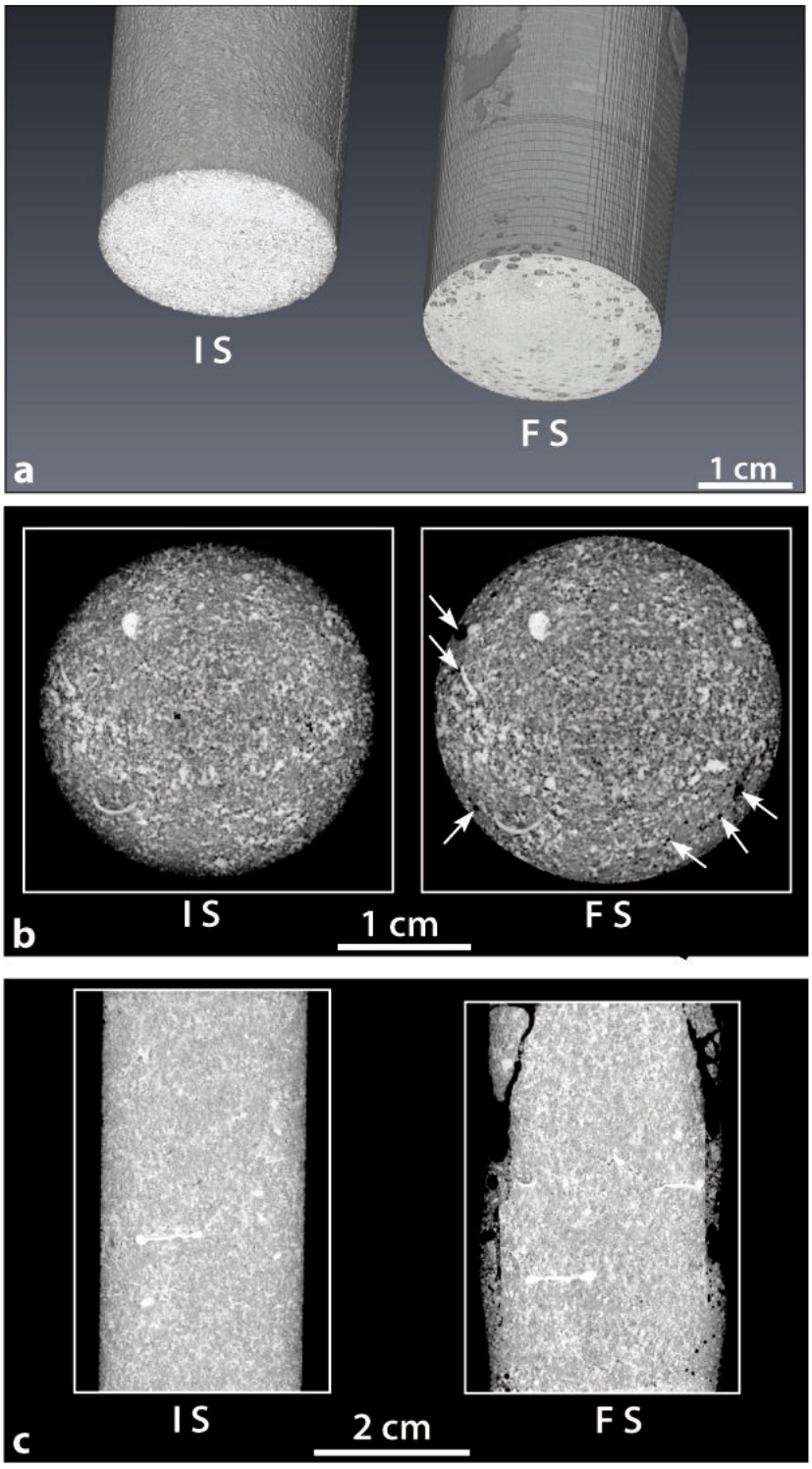

Figure 7: X-ray tomography images of sample C1 (undeformed before healing) (a) 3D images of the initial state (IS) and the final state (FS), showing the pores (black areas) that formed at the bottom of the sample. (b) Slice of the same sample as in a), the white arrows indicate the pores formed in the final state (FS). (c) 2D cross-sections showing a general comparison between the initial state and the final state, with large pores localized at the bottom, and small particles deposited between the sample and the sleeve.

3.2.3 Microstructures in the damaged sample (C3) after healing

For sample C3, the main observation is that the large fractures induced by the dynamic damaging process (Figure 8- IS) were significantly healed after three months (Figure 8-FS). The dense network of different size fractures that is characterizing the bottom and top of the damaged sample can no longer be seen on the tomographic images taken after the healing process (Figure 8 & 9).

The same dissolution pores as for C1 are observed, but in greater abundance. Some of these large pores follow the traces of the initial fractures (Figure 8b). Once again, the concentration of these large pores is higher at the base of the sample, where the fluid was injected. In this case however, the large pores spread all the way to the middle of the sample (Figure 8). These pores appear isolated from each other at this scale.

By comparing the X-ray tomography images of the damaged and healed states, some correlation was found between the main damage fractures and the largest pores (Figure 9). Nevertheless, as already mentioned above, a lot of those dissolution pores are not clearly connected to each other and they are not all connected with the fractures (Figure 10). These connections might be too thin to be detected on the X-ray tomography images at the given resolution. However, they are observed at microscopic scale in thin sections. In the thin sections of C3, the same crushed areas as those shown in Figure 9 were found and these are directly linked to the largest fractures.

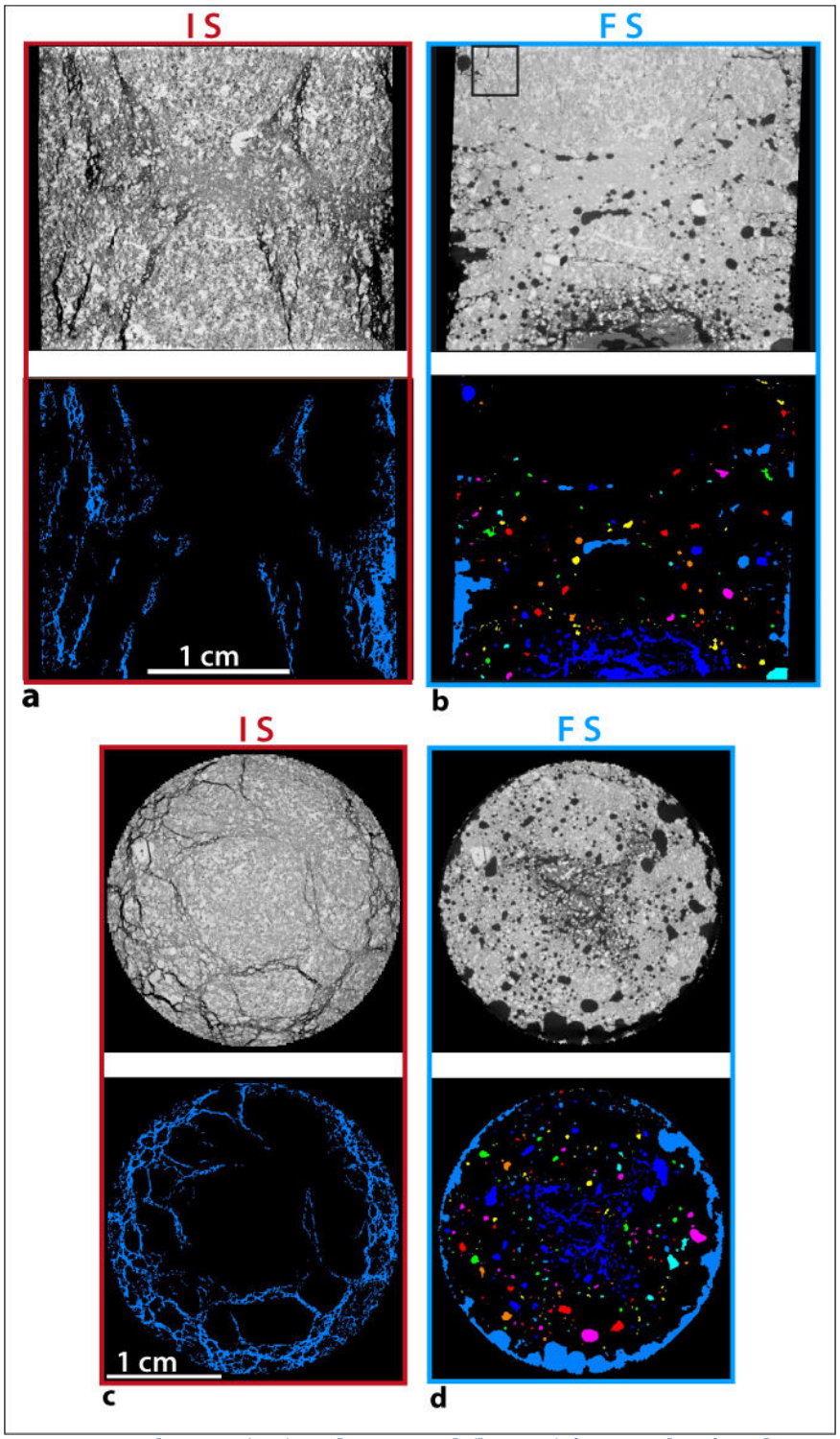

Figure 8: X-ray tomography raw (top) and processed (bottom) images showing the pattern of open fractures and newly formed porosity (in black on raw images) inside sample C3 (damaged before healing). The different colors on processed images correspond to pores that are not connected. (a) Damage fracture networks during the initial (fractured) state (IS) in cross-section. (b) Pore networks and healing of the fractures during the final state (FS) in cross-section. The black square is the area where the images of Figure 11 (g – l) were taken. (c) Same as a) but in 2D slice view. (d) Same as b) but in 2D slice view.

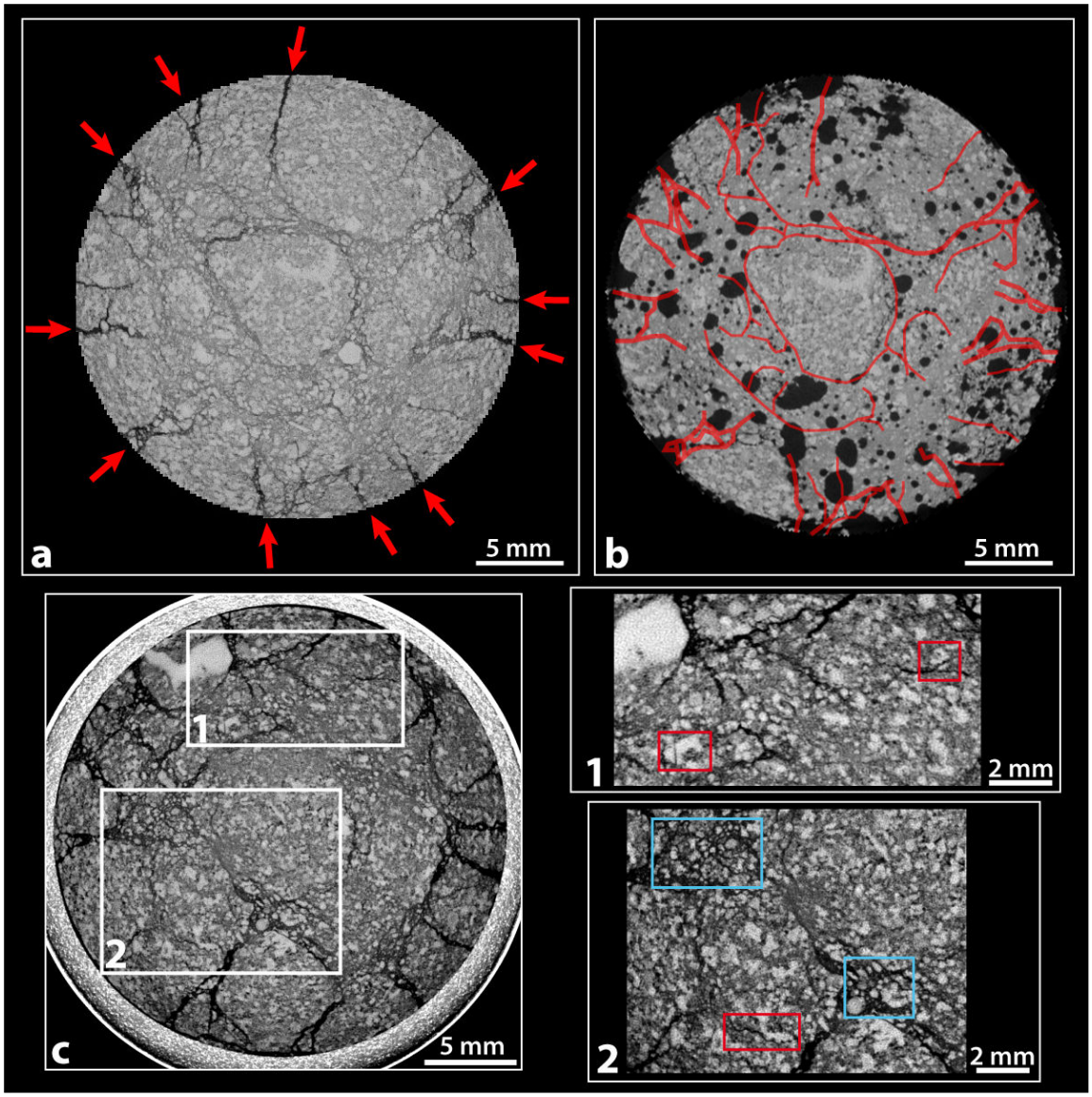

Figure 9: X-ray tomography images of sample C3. (a) Slice of the initial (fractured) state showing the fracturing network in black. The main fractures are labeled with red arrows. (b) Slice of the final state, at the same location, with red lines indicating the position of the initial main fractures that were subsequently healed. (c) Slice in C3 showing the location of the zoom 1) and 2). (1) and (2) the red squares underline fractures, which bypass or break the grains; the blue squares indicate crushed areas.

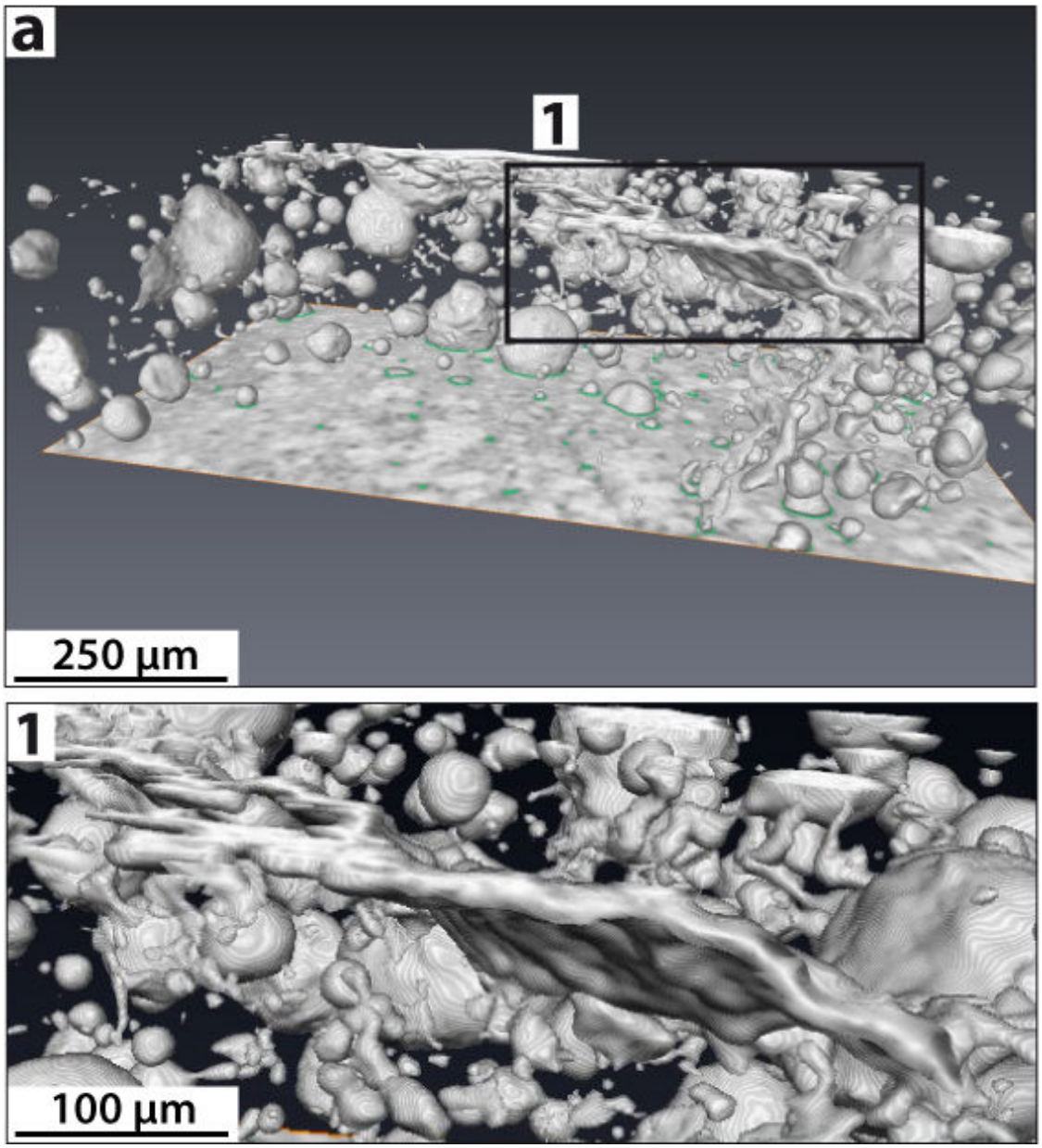

Figure 10: X-ray tomography processed image showing a 3D sub-volume at the grain scale in sample C3. The newly formed porosity (bubble) and a fracture are displayed in (1). The porosity network made by the dissolution holes is connected in 3D through thin fractures.

3.2.4. Microstructural comparison between C1 and C3

SEM-FEG observations obtained from thin sections of C1 and C3 were analyzed to investigate both the effect of dynamic damaging and the healing recovery process at microstructural scale. From the observations on the undamaged and healed sample C1, after fluid circulation, three main initial preserved grain microstructures can be distinguished: (i) large grains showing an intragranular fracture porosity, mostly healed during natural diagenetic processes (Figure 11a,d), (ii) micrograins showing grain boundaries which tend to disappear and presenting intergranular porosity and large grain indentations (Figure 11b,e,f), (iii) large fossils with internal porosity related to the fossil structure (Figure 11c). There is no clear evidence of a healing process related to the experimental fluid circulation in this undamaged sample.

The damaged sample C3 was investigated to see whether it contained the same two main types of structures in order to isolate the effect of the dynamic loading on the final microstructures. The observations showed (i) a more fractured state, with some large main fractures and a lot of small cracks (Figure 11g,j); (ii) some fan-like fracture networks developed parallel to the principal stress direction of dynamic loading, which are also observed inside the micrograined structures (Figure 11h). Most of the experimentally induced fractures with an aperture of just a few micrometers were healed (Figure 11l). Fractures with larger apertures remained open when they were horizontal (parallel to the maximum horizontal confining stress) and closed when they are vertical (perpendicular to the maximum horizontal confining stress). The intergranular porosity is more developed and the grain boundaries are more pronounced than in their initial state, leading to a clear decohesion and loose grains in some areas (Figure 11i,k,l) that are related to the dynamic damage effect. Dissolution associated with the sealing effect can be seen at grain scale only by the indenting of loosened grains (Figure 11k,l) and possibly by dissolution features (stylolite) along some fractures (red arrows Figure 11g,j).

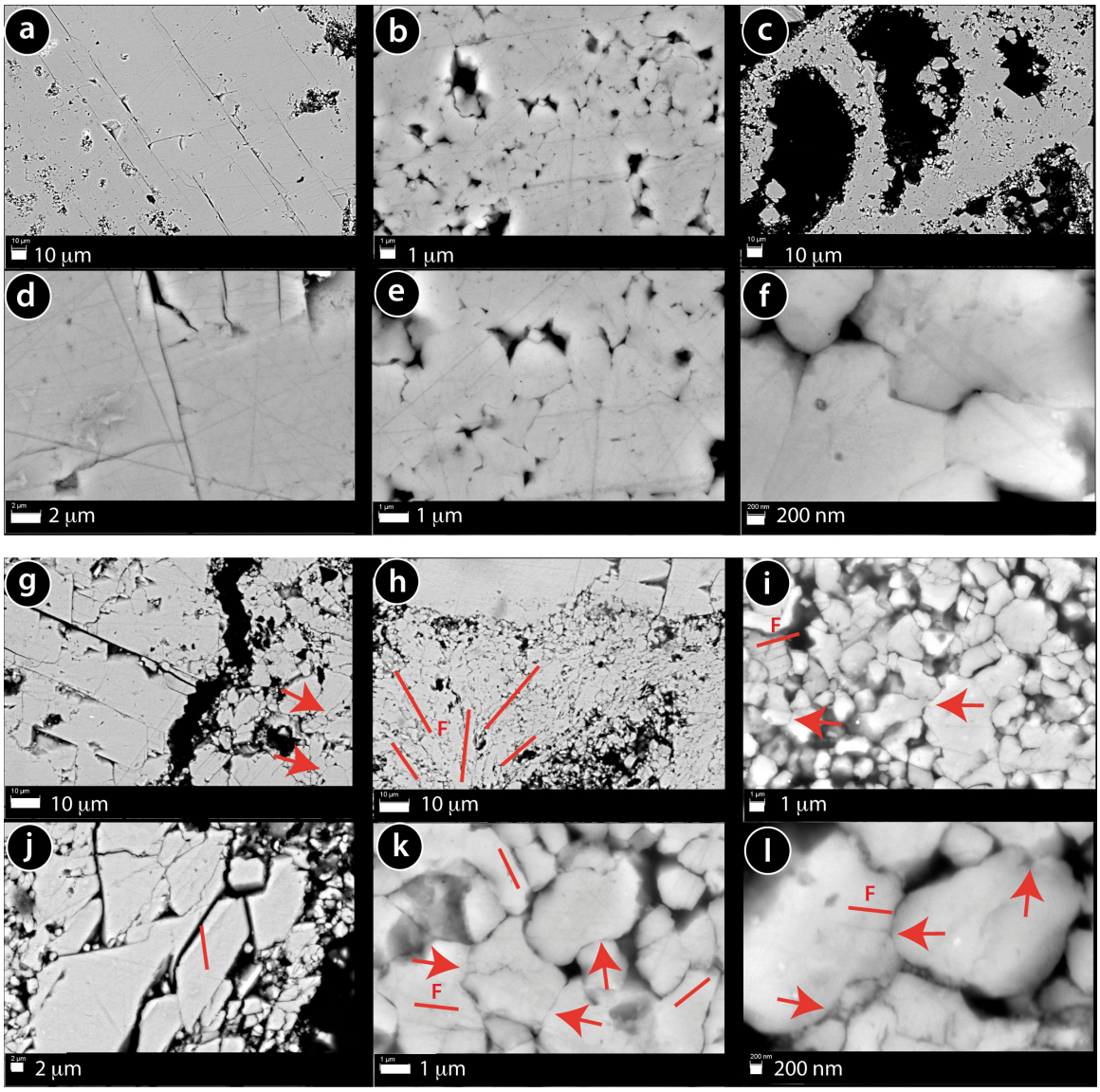

Figure 11: SEM-FEG images of Estaillades limestone showing the effect of dynamic loading and healing recovery. (a-f) and (g-l). (a - f): Initial grain microstructure of sample C1 (flow-through process under static stress on undamaged sample) with various pore densities and sizes and with diagenetic pressure solution indenting: (a & d) large grain with fracture porosity, (b & e) micrograins with intergrain porosity, (c) fossils with internal structure porosity, (f) grain indenting. (g – l): Evidence of dynamic stress loading with fractures (F), grain boundary decohesion and local dissolution of loose grains (arrow) in the C3 sample (flow-through process under static stress on sample damaged by dynamic stress loading): (g &j) fractured large grain and dissolution features (red arrows), (h & k) fan-like fracture network, (i & l) grain boundary decohesion, and dissolution indenting between loose grains (red arrows). See the black square in Figure 8 to locate the images (g – l).

4. Discussion

4.1 Characterization of the dynamic fracturing

4.1.1 Damage at the micro- and macro-scale

X-ray CT scan images document fractures of aperture greater than voxel resolution (~20 µm). On the other hand, the dissipated energy computed from mechanical data is related to the expansion of fractures at all scale within the sample. Figure 4 shows that these two independent dataset are well correlated. Even the most damaged sample, with finely crushed zones, lies on this line, if errors in fracture density is taken into account. This suggests a scale independence of damage, and that X-ray images provide good estimate of damage pattern.

The area of the fractures seen on the X-ray image can be computed as $2 \times \frac{sample\,volume \times fracture\,density}{fracture\,aperture}$. Using a fracture energy of ~0.15 J/m^2 (Røyne et al, 2011), the surface energy related to the fractures visible on the X-ray can be estimated. For instance, for CHB1, the surface energy needed for the creation of the fractures visible on the X-ray image, normalized to the sample volume, amount to 0.45 kJ/m^3. This is about 160 times less than the dissipated energy computed from mechanical data (72 kJ/m^3, see Table 2). This suggests that X-ray images at the resolution of the scanning can only depict less than 1% of the total area of the fracture created. The missing fracture area lies in fractures of smaller aperture and in small-scale roughness of the main fractures.

Sample C3, the most comminuted one, has smaller apparent fracture density than expected from the correlation of Figure 4. The additional missing percentage of fracture may lie within the finely crushed areas that start to develop at the center of the sample. Despite this contribution, the linear trend between mechanical data and X-ray images suggests that the X-ray imaging technique provides reliable data to estimate the energy dissipated by dynamic loading.

4.1.2 Microstructural markers of high strain rate damage

With the Split Hopkinson Pressure Bars, samples were loaded at strain rates higher than 50/s. At such strain rates, new fracture patterns appear. For instance, the fan-like fracture networks observed on the microstructures of the C3 sample (Figure 11h), the sample loaded at the highest strain rate, are similar to the branching system described by Sagy et al. (2001) as geometric features associated with dynamic fractures. Indeed, the fracture networks resulting from dynamic damaging are characterized by a complex geometry and rough edges (Figure 11g,h,i,j and Figure 10) (Sagy et al., 2001).

On the contrary, fractures across the largest grains in sample C1 (Figure 11a,d), the reference sample that did not experience any additional damage, display a simple straight geometry and smoother edges, which could be attributed to slow growth (i.e. subcritical rate) during diagenetic processes and/or during the percolation experiment. These pre-existing fractures could act as seeds (Sagy et al., 2001) for the fractures developed by dynamic loading.

4.1.3 Stress concentration and strain localization: role of heterogeneities

The loading by Split Hopkinson Pressure Bars is too fast to be servo-controlled. Hence, despite the different striker speeds, the strain rate experienced by the samples tested at ISTerre is similar. The loading history is rather controlled by the intrinsic properties of the samples. Samples CHB1, CHB2 and CHB3 have the same strength (Table 2) and display similar fracture patterns: fracturing is poorly developed in the sample and mainly concentrated around the largest calcitic shell grains and pores (Figure 12a). In general, the main fractures tend to initiate close to large heterogeneities (i.e. grains and pores) and then, to follow grain boundaries or small cracks already present in the sample (Figure 12b,c and Figure 3c,d).

Conversely, in the sample with the highest impact velocity (C3), localization is less efficient since the large calcitic shell grains are not damaged (Figure 12e). This type of behavior has already been noted in a previous article on pulverization (Doan and Gary, 2009) and correlates to the observation of fracture density organization.

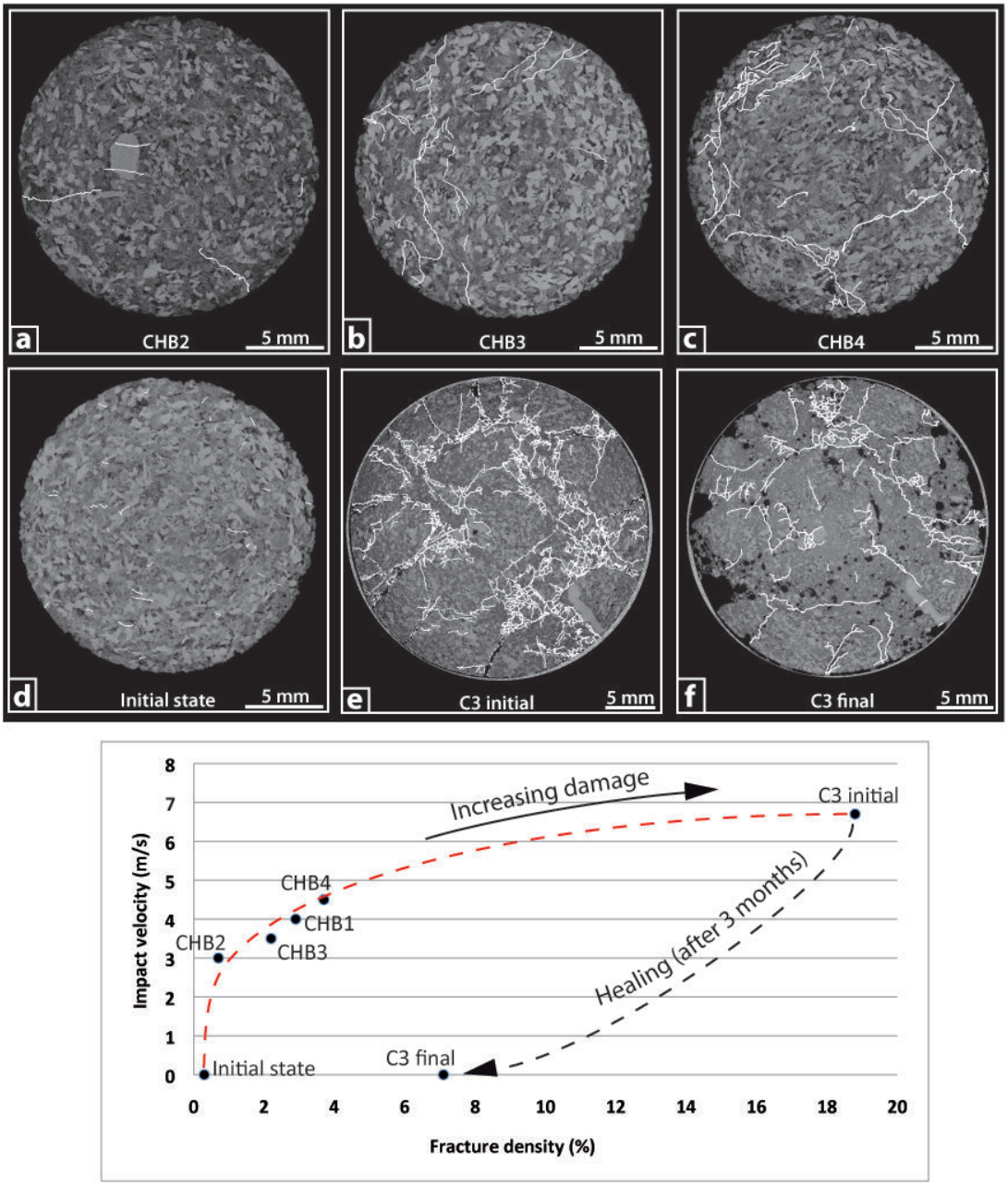

Figure 12: X-ray tomography images (a - f) illustrating the dependence of the fracture density on loading and healing history. The fracture networks are underlined by white lines.

4.2 Characterization of the healing process

4.2.1 Strain variation

The contribution of the rapid transient creep events represent about a third (2%) of the total strain of C1 (6.5%) (Figure 6). These sudden creep events could be caused by high dissolution rates producing mechanical collapses of the rock matrix rather than stick-slip behavior developed by the Viton piston O-rings on the internal wall of the triaxial cell (Figure 2b) (Le Guen et al., 2007). The oscillating behavior observed on sample C3 shows no correlation with the stresses or the fluid pressure during the percolation period, except during the last week of January 2013 (Figure 6). The cause of this chaotic oscillating behavior can be attributed to the high state of damage of the sample (i.e. the weak cohesion of the grains) and to the low effective axial pressure. In other words, it is impossible to determine if those oscillations are only due to the damage state of the sample, or controlled by experimental parameters.

Finally, it is difficult to define the exact role of the damaged state of sample C3 on the total strain value when comparing it with sample C1, as these two samples have not experienced the same stress history. However, the fractured and crushed state of some areas of C3 could allow stress rotation and pressure solution indenting of the loose grains (Figure 11k,l). This leads to grain reorganization at microstructure scale, which easily accommodates the stress on these specific areas.

4.2.2 Dissolution and healing processes

A large porosity network was found to have developed in C3 (Figure 8) compared with the few pores appearing on the 3D reconstruction inside the lower quarter of C1 (Figure 7). These large pores, formed by dissolution, are more developed in C3 because fluid circulation was facilitated by the fractures. The average flow rates estimated from the fluid output of the cells are around 300 ml/day for C3 and 240 ml/day for C1, thus the fluid circulated faster in the damaged sample (C3). The fractures act as preferential pathways for the fluid, leading to fluid circulation throughout the sample and enhancing the dissolution process (Gratier, 2011a), creating a positive feedback loop.

The amount of calcite calculated from ICP analyses at the inlet of the fluid circuit and at the outlet of both cells is not significantly different and remains constant at around

1.5g/l. From this data, it was not possible to estimate dissolution or healing rates. However, the microstructures and the measured fracture densities of the initial state (18.8%) and the final state (7.1%) of C3 imply efficient healing during fluid circulation (Figure 12e,f).

Several different healing mechanisms, with or without material supplies, were observed. They depend on the crack aperture (Gratier et al., 2003). The first mechanism, self-healing of cracks, is a widespread healing process for minerals, driven by the reduction of surface energy in the system (Brantley et al., 1990; Renard et al., 2009b). The fractures progressively heal into a thin film of pores and eventually close completely. Some very thin pore networks observed in the final state may correspond to fractures in the intermediate state (Figure 9). The second mechanism, sealing of cracks, closes fractures by deposition of minerals. This mechanism was studied using various methods on thin section (Figure 9 and Figure 12e,f). Cathodoluminescence did not show any clear evidence of calcite recrystallization in the crushed areas of sample C3, but observations made with FEG-SEM revealed the differences between the microstructure of C1 and C3. After characterizing the three main grain structures on C1 that attest of initial diagenetic processes since healing processes did not develop in this sample (Figure 11a-f, see 3.2.4), it was possible to distinguish between microstructures left by healing due to percolation and those due to diagenetic processes in sample C3. Since evidence of grain indenting inside the loose grain structures (Figure 11k,l) was found, a third healing mechanism can be invoked, pressure solution creep with compaction. Given the amount of loose-grain areas with grain boundary decohesion (around 50% of the thin section surface area), the main healing processes in sample C3 are a combination of mechanical grain sliding and chemical compaction by pressure solution creep and are responsible for radial compaction of the sample. The same combination for healing processes has already been observed with healing experiments in halite (Bos and Spiers, 2002).

Finally, heterogeneities in the rock samples play an important role in the healing process. The largest pores, located at the same place as the largest fractures, slowed down or inhibited healing in the vicinity of these heterogeneities. They are the less healed domains. Conversely, the areas protected by the large calcitic shells have experienced less strain and are very well healed. The degree of healing is of the same order as the

areas corresponding to the crushed material and fine fracturing (Figure 12e,f). The healing rate thus depends on the fracture and pore dimensions (Brantley et al., 1990; Renard et al., 2000), but also on grain boundary structures, which influence the dissolution in the pressure solution process and the subsequent healing rate (Hickman and Evans, 1991; van Noort and al., 2008).

4.3 Applications to faults

4.3.1 Fracture networks and fault damage zones

The experiments carried out here confirm that the damage state of a rock strongly influences its mechanical behavior. In nature, dynamic damaging of rock is associated with seismic deformation, either from a large earthquake or from microseismicity. The fractures networks in fault damage zones result from cumulative damage due to repeated seismic deformation and creep deformation during interseismic periods (Tenthorey and Cox, 2006). The fault damage zone structure can vary from one fault to another and the internal structure plays an important role in mechanical properties of the whole fault zone (Faulkner et al., 2003) and on the strain distribution across the fault core, which can either be localized or homogeneous (Rutter et al., 1986; De Paola et al., 2008; Faulkner et al., 2010). Moreover, Faulkner et al., (2006) showed that stress rotations in a weak fault occur inside the damage zone surrounding the fault core. Depending on the size and depth of the fracture networks, the fault can be weakened by phyllosilicates development over a wide area. Collettini et al., (2009) observed that phyllosilicates such as talc developed by fluid-assisted processes inside the fracture networks of a weak fault damage zone. Consequently, heterogeneous fracturing plays an important role in the stress distribution and orientation in the faults, and also affects fluid flow and mechanical behavior (Faulkner et al., 2003; Collettini et al., 2009; Faulkner et al., 2010; Gratier, 2011a).

In the experiments carried out here, the fluid circulates faster inside the damaged sample, because the main fractures act as preferential flow-channels. At the scale of a fault zone, this effect increases the kinetics of the fluid-rock reactions, as is the case for pressure solution creep with compaction (Gratier et al., 2011b) and, after some time, this leads to

the healing of these fractures. The permeability and thus the flow rate of the fault zone are dependent on fracture length and aperture. The largest fractures accommodate a higher fluid flux, whereas microfracturing enables the fluid to penetrate into the rock mass (Brantley et al., 1990). These two scales of fracture porosity trigger differences in healing rates.

For the entire percolation period (five weeks), a healing rate of about 0.3 % per day for sample C3 is estimated from the decrease in fracture density between the initial (damaged) state and the final state. Microfractures are nicely healed by self-healing process while the largest fractures are much slower to heal by mechanical and pressure solution compaction, at least for the timescale used in the experiments. This difference in fracture lifetimes leads to a healing process spread over two time scales (Brantley et al., 1990; Renard et al., 2000). In this particular case, the healing observed (Figure 8) is mainly due to mechanical compaction and pressure solution processes. However, inside the largest fractures, grains remain loose and not very well healed. The lack of cohesion in the loose grain areas observed inside C3 (Figure 11i,k,l) and consequently the porosity related to these structures leads to the development of large heterogeneities, inside the rock mass. Moreover, the rapid healing of the thin crack networks reduces the pore connections and tends to localize the stresses. At the fault scale, the areas strengthened by healing processes could be the places where new brittle deformation is initiated. Thus, healing processes in active faults should control the earthquake recurrence time and the initiation and localization of dynamic fracturing (Bos and Spiers, 2002).

5. Conclusion

Dynamic damage experiments were performed on five samples of porous Estaillades limestone in order to understand the role of the heterogeneities on the geometry of fracture propagation. Long-term fluid-assisted healing experiments were also carried out on two samples of the same limestone, one damaged, the other undamaged, with the aim being to assess the effect of the damaged state on fluid flow and healing rate. The following conclusions can be drawn from the results obtained:

1/ High strain rate loading of samples induced a dense network of fractures. The

sample loaded at the highest strain rate is almost pulverized.

2/ There is a strong relation between the fracture density determined from X-ray imaging and the dissipated energy computed from the macro-mechanical data, although these two parameters are characterized at different size scales. X-ray imaging is therefore a good proxy to quantify damage within the samples.

3/ Porosity networks increase and develop on two scales: small fractures enhance the formation of new pathways within the initial porosity network and large fractures increase porosity, creating flow-channels for a faster fluid circulation.

4/ Fracture aperture influences healing rate: microfractures heal faster by self-healing process than large fractures that are closed by mechanical and pressure solution compaction. This time difference creates heterogeneous domains within the rock, leading to localization of the strain and the loading stress.

5/ In fault zones, the damaged state of rocks has a strong influence on the permeability and consequently, on the kinetics of fluid-rock reactions, such as healing by pressure solution process. The microfracture networks heal faster than the large fractures and lead to heterogeneous strengthening of the rocks. As a result, these domains could act as stress concentrators where new ruptures initiate.

References

Bos, B., and Spiers, C.J., 2002. Fluid-assisted healing processes in gouge-bearing faults: insights from experiments on a rock analogue system. Pure and Applied Geophysics, 159: 2537-2566.

Brantley, S.L., Evans, B., Hickman, S.H., and Crerar, D.A., 1990. Healing of microcracks in quartz: Implications for fluid flow. Geology, 18: 136-139.

Chen, W., and Song, B., 2010. Split Hopkinson (Kolsky) Bar: Design, Testing and Application. Springer, Berlin.

Cox, S.F., and Paterson, M.S., 1991. Experimental dissolution-precipitation creep in quartz aggregates at high temperatures. Geophysical Research Letters, 18: 1401-1404.

De Paola, N., Collettini, C., Faulkner, D.R., Trippetta, F., 2008. Fault zone architecture and deformation processes within evaporitic rocks in the upper crust. Tectonics, 27, TC4017, doi:10.1029/2007TC002230.

Doan, M.-L., and Billi, A., 2011. High strain rate damage of Carrara marble. Geophysical Research Letters, 38, L19302, doi: 10.1029/2011GL049169.

Doan, M.-L., and Gary, G., 2009. Rock pulverization at high strain rate near the San Andreas fault. Nature Geoscience, 2: 709-712, doi: 10.1038/NGEO640.

Dor, O., Chester, J.S., Ben-Zion, Y., Brune, J.N., and Rockwell, T.K., 2009. Characterization of damage in sandstones along the Mojave section of the San Andreas Fault: Implications for the shallow extent of damage generation. Pure and Applied Geophysics, 166: 1747–1773, doi:10.1007/s00024-009-0516-z.

Dor, O., Ben-Zion, Y., Rockwell, T.K., and Brune, J., 2006a. Pulverized rocks in the Mojave section of the San Andreas Fault Zone. Earth and Planetary Science Letters, 245: 642-654.

Dor, O., Rockwell, T.K., and Ben-Zion, Y., 2006b. Geologic observations of damage asymmetry in the structure of the San Jacinto, San Andreas and Punchbowl faults in southern California: a possible indicator for preferred rupture propagation direction. Pure and Applied Geophysics, 163: 301-349, doi: 10.1007/s00024-005-0023-9.

Faulkner, D.R., Jackson, C.A.L., Lunn., R.J., Schlische, R.W., Shipton, Z.K., Wibberley, C.A.J., and Withjack, M.O., 2010. A review of recent developments concerning the structure, mechanics and fluid flow properties of fault zones. Journal of Structural Geology, 32: 1557-1575.

Faulkner, D.R., Mitchell, T.M., Healy, D., and Heap, M.J., 2006. Slip on 'weak' faults by the rotation of regional stress in the fracture damage zone. Nature, 444: 922-925, doi:

10.1038/nature05353.

Faulkner, D.R., Lewis, A.C., and Rutter, E.H., 2003. On the internal structure and mechanics of large strike-slip fault zones: field observations of the Carboneras fault in southeastern Spain. Tectonophysics, 367: 235-251.

Géraud, Y., Mazerolle, F., Raynaud, S., and Lebon, P., 1998. Crack location in granitic samples submitted to heating, low confining pressure and axial loading. Geophysical Journal International, 133: 553-567.

Gratier, J.-P., 2011a. Fault permeability and strength evolution related to fracturing and healing episodic processes (years to millennia): the role of pressure solution. Oil & Gas Science and Technology - Rev. IFP Energies nouvelles, 66: 491-506.

Gratier, J.-P., Richard, J., Renard, F., Mittempergher, S., Doan, M.-L., Di Toro, G., Hadizadeh, J., and Boullier, A.-M., 2011b. Aseismic sliding of active faults by pressure solution creep: Evidence from the San Andreas Fault Observatory at Depth. Geology, 39: 1131-1134.

Gratier, J.-P., Favreau, P., and Renard, F., 2003. Modeling fluid transfer along California faults when integrating pressure solution crack sealing and compaction processes. Journal of Geophysical Research, 108, B2, 2104, doi: 10.1029/2001JB000380.

Gratier, J.-P., Renard, F., and Labaume, P., 1999. How pressure solution creep and fracturing processes interact in the upper crust to make it behave in both a brittle and viscous manner. Journal of Structural Geology, 21: 1189-1197.

Han, M., Fleury, M., and Levitz, P., 2007. Effect of the pore structure on resistivity index curves. International Symposium of the Society of Core Analysts, Calgary, Canada.

Hickman, S.H., and Evans, B., 1991. Experimental pressure solution in halite: the effect of grain/interphase boundary structure. Journal of the Geophysical Society, London, 148: 549-560.

Hellmann, R., Renders, P.J.N., Gratier, J.-P., and Guiguet, R., 2002a. Experimental pressure solution compaction of chalk in aqueous solutions. Part 1. Deformation behavior and chemistry. The Geochemical Society, Special Publication, 7.

Hellmann, R., Gaviglio, P., Renders, P.J.N., Gratier, J.-P., Békri, S., and Adler, P., 2002b. Experimental pressure solution compaction of chalk in aqueous solutions. Part 2. Deformation examined by SEM, porosimetry, synthetic permeability, and X-ray computerized tomography. The Geochemical Society, Special Publication, 7.

Ikornikova, N.Y., 1961. The process of solution of calcite in aqueous solution of chlorides at high temperatures and pressures. Soviet Phys. Crystallogr., 5: 726-733.

Karner, S.L., Marone, C., and Evans, B., 1997. Laboratory study of fault healing and lithification in simulated fault gouge under hydrothermal conditions. Tectonophysics, 227: 41-55.

Le Guen, Y., Hellmann, R., Collombet, M., Gratier, J.-P., Renard, F., and Brosse, E., 2007. Enhanced deformation of limestone and sandstone in the presence of high PCO2 fluids. Journal of Geophysical Research B: Solid Earth, 112, B05421, doi: 10.1029/2006JB004637.

Nakatani, M., and Scholz, C.H., 2004. Frictional healing of quartz gouge under hydrothermal conditions: 1. Experimental evidence for solution transfer healing mechanism. Journal of Geophysical Research – Solid Earth, 109, B07201.

Niemeijer, A., Marone, C., and Elsworth, D., 2008. Healing of simulated fault gouges aided by pressure solution: results from rock analogue experiments. Journal of Geophysical Research, 113, B04204, doi: 10.1029/2007JB005376.

van Noort, R., Visser, H.J.M., and Spiers, C.J., 2008. Influence of grain boundary structure on dissolution controlled pressure solution and retarding effects of grain boundary healing. Journal of Geophysical Research, 113, B03201, doi: 10.1029/2007JB005223.

Raj, R., 1982. Creep in polycrystalline aggregates by matter transport through a liquid phase. Journal of Geophysical Research-Solid Earth, 87: 4731-4739.

Ravi-Chandar, K., and Knauss, W.G., 1984a. An experimental investigation into dynamic fracture: I. Crack initiation and arrest. International Journal of Fracture, 25: 247-262.

Ravi-Chandar, K., and Knauss, W.G., 1984b. An experimental investigation into dynamic fracture: II. Microstructural aspects. International Journal of Fracture, 26: 247-262.

Raynaud, S., Fabre, D., Mazerolle, F., Géraud, Y., and Latière, H.J., 1989. Analysis of the internal structure of rocks and characterization of mechanical deformation by a non-destructive method: X-ray tomodensitometry. Tectonophysics, 159: 149-159.

Reches., Z., and Dewers, T.A., 2005. Gouge formation by dynamic pulverization during earthquake rupture. Earth and Planetary Science Letters, 235: 361-374.

Renard, F., 2012. Microfracturation in rocks: from microtomography images to processes. European Physical Journal Applied Physics, 60: 24203, doi: 10.1051/epjap/2012120093.

Renard, F., Bernard, D., Desrues, J., and Ougier-Simonin, A., 2009a. 3D imaging of fracture propagation using synchrotron X-ray microtomography. Earth and Planetary Science Letters, 286: 285-291, doi: 10.1016/j.epsl.2009.06.040.

Renard, F., Dysthe, D.K., Feder, J.G., Meakin, P., Morris, S.J.S., and Jamtveit, B., 2009b. Pattern formation during healing of fluid-filled cracks: an analog experiment. Geofluids, 9: 365-372, doi: 10.1111/j.1468-8123.2009.00260.x.

Renard, F., Gratier, J.-P., Jamtveit, B., 2000. Kinetics of crack-sealing, intergranular pressure solution, and compaction around active fault. Journal of Structural Geology, 22: 1395-1407.

Røyne, A., Bisschop, J., Dysthe, D.K., 2011. Experimental investigation of surface energy and subcritical crack growth in calcite. Journal of Geophysical Research, 116, doi:10.1029/2010JB008033.

Rutter, E.H., Maddock, R.H., Hall, S.H., and White, S.H., 1986. Comparative microstructures of natural and experimentally produced clay-bearing fault gouges. Pure and Applied Geophysics, 124: 3-30.

Rutter, E.H., 1976. The kinetics of rock deformation by pressure solution. Philosophical Transactions of the Royal Society of London, 283: 203-219.

Sagy, A., Reches, Z., and Roman I., 2001. Dynamic fracturing: field and experimental observations. Journal of Structural Geology, 23: 1223-1239.

Sleep, N.H., and Blanpied, M.L., 1992. Creep, compaction and the weak rheology of major faults. Nature, 359: 687-692.

Tenthorey, E., and Cox, S., 2006. Cohesive strengthening of fault zones during the interseismic period: An experimental study. Journal of Geophysical Research, 111, B09202, doi: 10.1029/2005JB004122.

Wechsler, N., Allen, E.E., Rockwell, T.K., Girty, G., Chester, J.S., and Ben-Zion, Y., 2011. Characterization of pulverized granitoids in a shallow core along the San Andreas Fault, Littlerock, CA. Geophysical Journal International, 186: 401-417.

Weyl, P.K., 1959. Pressure solution and the force of crystallization: a phenomenological theory. Journal of Geophysical Research, 64: 2001-2025.

Yasuhara, H., Marone, C., and Elsworth, D., 2005. Fault zone restrengthening and frictional healing: the role of pressure solution. Journal of Geophysical Research, 110, B06310, doi: 10.1029/2004JB003327.

Yuan, F., Prakash, V., and Tullis, T., 2011. Origin of pulverized rocks during earthquake fault rupture. Journal of Geophysical Research, 116, B06309, doi: 10.1029/2010JB007721.

Conclusion

Cette approche expérimentale nous a permis de mettre en évidence le rôle de l'état d'endommagement dans l'évolution de la porosité ou de la perméabilité de l'échantillon. Elles ont montré que la fracturation ne s'organisait pas de la même façon en fonction de la vitesse de chargement et que celle-ci, selon cette vitesse de chargement, était plus ou moins influencée par les hétérogénéités déjà existantes dans la roche, comme les grains et pores de grandes tailles. Ces expérimentations ont également montré que dans une roche fortement endommagée, la cinétique et le taux de cicatrisation variaient d'une zone à l'autre. Les zones comportant un intense réseau de microfractures, proche de la pulvérisation, cicatrisaient plus vite que les zones présentant de larges fractures. Cette observation implique qu'il y a création d'hétérogénéités de résistance au sein de la roche, durant la phase de cicatrisation. A l'échelle d'une zone de faille, ce type d'hétérogénéités pourrait concentrer les contraintes. Ces zones pourraient être celles dans lesquelles peuvent s'initier de nouvelles ruptures sismiques.

CONCLUSION GENERALE ET PERSPECTIVES

L'étude des processus de faille responsables de l'alternance des différentes phases du cycle sismique est un domaine très vaste où il reste encore beaucoup à faire. Ces trois ans de travail ont fourni un aperçu de la potentialité de l'étude des microstructures pour appréhender ces processus, l'importance de leur interactions et leur évolution au cours du temps. Ils nous ont permis de dégager un modèle d'évolution du fluage dans les zones actives de la Faille de San Andreas, en prenant en compte les changements de minéralogie et donc, de résistance des roches composant ces zones.

Nous avons montré à la fois par l'observation de structures naturelles et par l'expérimentation sur roches que l'état initial de la roche jouait un rôle prépondérant dans la mise en place des différents processus de faille. L'état d'endommagement des roches est l'un des facteurs clés déterminant la perméabilité de la zone de faille et par conséquent, l'activation de nombreux processus que régissent les réactions fluides roches. Au cours du temps, et suite à la dominance de certains mécanismes tel que le fluage par dissolution cristallisation, cet état évolue. Les fractures sont comblées et refermées, la roche se cicatrise jusqu'à retrouver une partie de ses propriétés rhéologiques initiales. L'accommodation des contraintes par déformations ductiles devient plus difficile du fait de la résistance de la roche qui augmente. Ce phénomène conduit alors à une nouvelle rupture violente dans le cas des failles sismiques et le cycle peut ainsi se répéter au cours du temps. Dans le cas des failles asismiques, l'accommodation des contraintes par les mécanismes de fluage reste suffisamment efficace pour éviter cette rupture. Ceci peut s'expliquer par le fait que la résistance de la zone de faille n'atteint jamais le seuil nécessaire à la mise en place d'un chargement suffisant pour provoquer une rupture importante. L'état d'endommagement et la minéralogie particulière qui sont nécessaires à l'activation des mécanismes d'affaiblissement (comme la fracturation et la croissance de minéraux possédant un faible coefficient de friction), trouvent alors un équilibre avec les mécanismes de renforcement (comme la cicatrisation par cristallisation de calcite ou par

compaction). Cet équilibre doit être entretenu par un contexte particulier favorisant la conservation d'une faible résistance au niveau de la zone de glissement de la faille. L'activité microsismique importante généralement enregistrée au niveau des failles asismiques et des segments de failles subissant un fluage permanent sur lesquels aucun séisme important n'est observé pourrait être l'un de ces contextes particuliers qui active les transferts de matière. La présence d'une zone enrichie en minéraux à faible coefficient de friction en est une seconde. Evidemment, ces contextes peuvent se retrouver au niveau de la même zone de faille.

Il faut garder à l'esprit que notre modèle d'évolution des processus de fluage s'appuie sur un cas d'étude particulier : celui de la Faille de San Andreas. Dans le but de le généraliser, l'étude des microstructures d'autres failles montrant des comportements similaires est nécessaire. Les forages scientifiques ayant tendance à se multiplier sur les zones de failles sensibles, l'accès aux échantillons in situ pourra être possible.

Dans le même ordre d'idée, nous manquons encore de contraintes, notamment temporelles, sur la cinétique de ces différents mécanismes de renforcement et d'affaiblissement des roches en milieu naturelle. Le volet expérimental de cette étude trouve ainsi de nombreuses perspectives évidentes. L'étude de l'influence de l'endommagement dans des roches complexes, proche de celles rencontrées au niveau des zones de failles, sur les processus de cicatrisation serait intéressante à réaliser sur plusieurs cycles. Cela apporterait de nouvelles contraintes sur les durées de recouvrement de la résistance des roches, en prenant en compte son évolution microstructurale au fur et à mesure des différents cycles.

ANNEXES

Geology, published online on 21 October 2011 as doi:10.1130/G32073.1

Aseismic sliding of active faults by pressure solution creep: Evidence from the San Andreas Fault Observatory at Depth

J.-P. Gratier[1], J. Richard[1], F. Renard[1,2], S. Mittempergher[3], M.-L. Doan[1], G. Di Toro[3,4], J. Hadizadeh[5], and A.-M. Boullier[1]
[1]ISTerre (Institut des Sciences de la Terre) Observatoire, Université Joseph Fourier Grenoble, CNRS, BP 53, Grenoble 38041, France
[2]Physics of Geological Processes, University of Oslo, 0316 Oslo, Norway
[3]Università di Padova, Via Giotto 1, Padua 35137, Italy
[4]Istituto Nazionale di Geofisica e Vulcanologia, Via di Vigna Murata 605, Rome 00143, Italy
[5]Department of Geography and Geosciences, University of Louisville, Louisville, Kentucky 40292, USA

ABSTRACT

Active faults in the upper crust can either slide steadily by aseismic creep, or abruptly causing earthquakes. Creep relaxes the stress and prevents large earthquakes from occurring. Identifying the mechanisms controlling creep, and their evolution with time and depth, represents a major challenge for predicting the behavior of active faults. Based on microstructural studies of rock samples collected from the San Andreas Fault Observatory at Depth (California), we propose that pressure solution creep, a pervasive deformation mechanism, can account for aseismic creep. Experimental data on minerals such as quartz and calcite are used to demonstrate that such creep mechanism can accommodate the documented 20 mm/yr aseismic displacement rate of the San Andreas fault creeping zone. We show how the interaction between fracturing and sealing controls the pressure solution rate, and discuss how such a stress-driven mass transfer process is localized along some segments of the fault.

INTRODUCTION AND GEOLOGICAL FRAMEWORK

Aseismic deformation is observed in active fault zones, but the mechanisms of deformation are still unclear (Scholz, 2002). Samples collected from the San Andreas Fault Observatory at Depth (SAFOD, California) allow correlation of fault rock microstructures with real-time geophysical data, and therefore provide useful information for identifying such mechanisms. Here we show that a stress-driven mass transfer process, i.e., pressure solution creep (Rutter and Mainprice, 1978), can accommodate the aseismic deformation of the San Andreas fault.

The SAFOD borehole, drilled to 3 km depth, is at the southern part of a 175-km-long creeping section of the San Andreas fault (Fig. 1A). The sliding rate is 28 mm/yr in the central part of the creeping segment, and decreases toward both northern and southern ends (Fig. 1B). The creep rate near the SAFOD site is ~20 mm/yr (Fig. 1B), as measured at the surface within a 20-m-thick fault zone (Titus et al., 2006). Such a narrow creeping zone appears to extend through the entire upper crust, coinciding with a zone of observed microseismicity (Nadeau and Dolenc, 2005). The southernmost part of the creeping section, where the creeping rate gradually falls to zero (Fig. 1B), is a zone of repeating M6 earthquakes, the most recent being the 2004 M6 Parkfield earthquake.

At the SAFOD site, the right-lateral displacement of the San Andreas fault has juxtaposed arkosic sandstones and conglomerates of the Pacific plate against the shale, siltstone, and claystone of the North American plate (Fig. 1C). Microstructural observations of the core samples show evidence of deformation across the damaged zone extending to core-parallel depths of 3150–3410 m (Zoback et al., 2010): shear zones alternate with foliated rocks more or less parallel to the San Andreas fault (Solum et al., 2006). Borehole casing deformation revealed two low-seismic-velocity, actively creeping, zones of foliated rocks (Fig. 1C): a main creeping segment (central deforming zone) at 3300.07–3302.81 m and a secondary creeping segment deforming at lower shear rate (southern deforming zone) at 3191.4–3193 m; both the central and southern deforming zones contain serpentine clasts and highly sheared siltstones (Zoback et al., 2010) without clear displacement discontinuity at their boundaries.

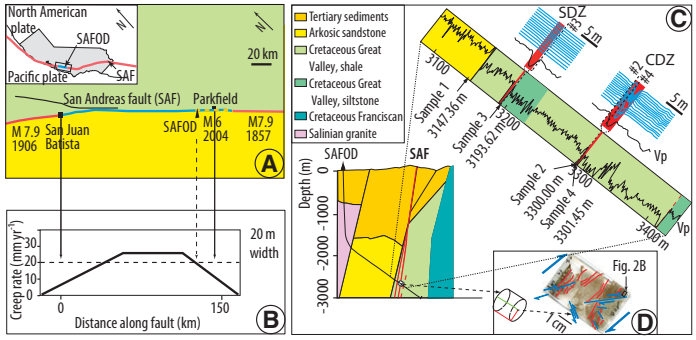

Figure 1. A: Map view of San Andreas fault system showing creeping segment (blue line) with trace of last two M 7.9 earthquakes that currently are locked segments (red lines) and transitional zone of M6 earthquakes (dotted line); coloring corresponds to contact at 3 km depth in C. SAFOD—San Andreas Fault Observatory at Depth. B: Evolution of creep rate along creeping zone (Titus et al., 2006). C: Schematic cross section of SAFOD site, perpendicular to fault; enlargement shows P wave velocity log (Zoback et al., 2010) together with location of four described samples; two creeping faults are highlighted in red; enlargement in vicinity of these creeping zones (top right) shows casing deformation (blue lines) indicating active creep and accurate location of three of the samples. SDZ—southern deforming zone; CDZ—central deforming zone. D: Sketch of thin section (sample 2) perpendicular to foliation (red), with minor faults (blue) (location of Fig. 2B is shown).

EVIDENCE OF PRESSURE SOLUTION CREEP

Based on the microstructural study of samples from the SAFOD core, we infer that an important mechanism of aseismic deformation is pressure solution creep, which induces pervasive and irreversible deformation of the whole rock. This mechanism is active both in the less deformed samples collected from the damaged zone (sample 1) and in intensely deformed foliated samples of the creeping zone (sample 2) shown in Figure 1D. We show that the most highly deformed zones have the highest amount of strain accommodated by pressure solution. Evidence of pressure solution is revealed using elemental distribution maps in sample 1 (Fig. 2A). Stress-driven dissolution associated with horizontal contraction is demonstrated by the dissolution of Ca-Na feldspars at feldspar-quartz grain impingements along a pressure solution seam, whereas K, Mg, Fe, and Ti (phyllosilicates, Fe and Ti oxides, sulfurs) are passively concentrated in the same seam (Fig. 2A). Fracturing is associated with pressure solution. Contraction perpendicular to the dissolution seam, apparent from the grain shape change (Fig. 2A), was estimated to be ~10%. Since there is no evidence of redeposition in veins nearby, it may be concluded that the soluble species have been transported away from the zone of dissolution.

In sample 2, Ca, Si, and Na are depleted within the solution seams where Mg, Fe, Ti are passively concentrated (Fig. 2B). Such a pressure

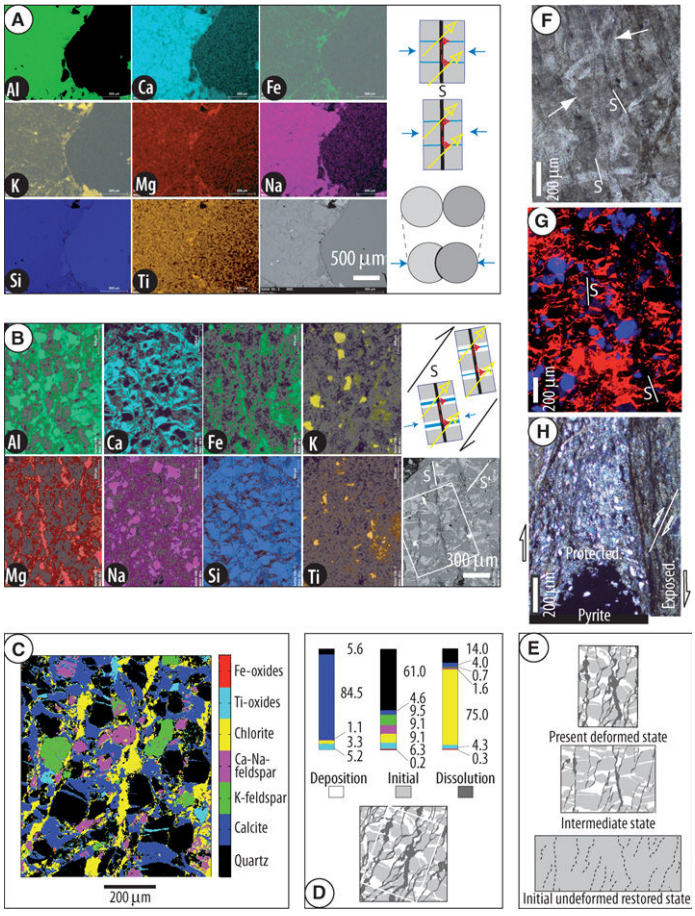

Figure 2. Pressure solution evidence. A and B: Elements distribution from scanning electron microscopy (SEM) analyses for samples 1 and 2, respectively; brighter color indicates higher content; small sketches show diffusive mass transfer path (red arrows) from solution seams (black) (S) to fluid (blue) within vein (white) and fluid flow (yellow). C: Mineralogical distribution in white rectangle area of B (bottom right), sample 2. D: Same area as C. Top—mineral composition of deposition, initial, and dissolution zones. Bottom—areas of three zones are 27%, 58%, and 15%, respectively. E: Present deformed state (top) and restored undeformed state (bottom) of area of white rectangle of D with intermediate deformed state (middle). F: Evidence of stress dissolution of calcite (arrows) within vein with pressure solution seams (S), sample 3. G: Calcite filling of fracture network (orange) perpendicular to solution cleavage (S) (cathodoluminescence, sample 3). H: Stress shadow effect showing evidence of pressure solution grain size reduction from protected to exposed zone with quartz and feldspar depletion, sample 3. (Images A, B, F, G, H can be seen in larger view in the GSA Data Repository[1].)

solution process leads to a foliation oriented at a high angle to the drillhole axis (Figs. 1C and 1D). In contrast to sample 1, calcite minerals in sample 2 fill a network of veins oriented perpendicular to the solution seams, consistent with an extension parallel to the foliation. Finite deformation can be calculated from mineral distribution (Fig. 2C). Three zones are distinguished (Fig. 2D): (1) a dissolution zone (with passively concentrated chlorites and Fe oxides), (2) a deposition zone (with precipitated calcite and occasional Ti oxides), and (3) an initial zone (predeformation zone composed of quartz, feldspars, and chlorites). Veins open and seal progressively (Mittempergher et al., 2011). Consequently, initial zones are dissolved at the beginning of the pressure solution process, then both initial and deposition zones are progressively dissolved (Figs. 2E and 2F). The relative mass change, $\Delta M/M_0$, is calculated using the passive concentration of insoluble minerals in the dissolution zone compared with the composition of the protected zone between solution seams (Figs. 2D and 2E) as:

$$\Delta M / M_0 = \left(I_p / I_d\right) - 1, \quad (1)$$

where I_p and I_d are the content in insoluble minerals in the protected and in the dissolution zone, respectively, and M_0 is the mass of a representative volume element before deformation. Two end members of mass transfer amount are obtained by comparing the composition of dissolution zones with the protected zones: either initial zones or both initial and deposition zones. The two calculations give about the same amounts of relative mass decrease for the dissolution zones (−88% to −90%). A mean value of contraction perpendicular to the foliation of ~60% can be calculated by taking into account the areas of the dissolution zones (Fig. 2D). A mean extension of ~50% perpendicular to the veins is evaluated from the ratio of deposition areas to initial areas (Figs. 2D and 2E). The mass decrease of each soluble mineral that shows no significant differential alteration between protected and dissolution zones can also be calculated (Gratier et al., 2003): quartz, −96%; K-feldspars, −99%; Ca-Na feldspars, −98%; calcite, −94%. Foliation as mineral segregation appears to be linked to the pressure solution creep, with an almost complete disappearance of the soluble minerals in the zones of dissolution. Mass conservation calculations comparing the amounts of dissolved Ca-Na feldspars and deposited minerals in veins show that a large proportion of calcite must come from outside the studied area, brought by episodic fluid flow (Mittempergher et al., 2011). Evidence of dextral shearing is found in thin sections cut normal to the foliation cleavage from both en echelon fractures (Fig. 1D) and crosscutting cleavages (S and S′, Fig. 2B). Consequently, the calcite vein network and the solution cleavage surfaces are consistent with a stress-driven mass transfer process that accommodates right-lateral strike-slip movement along the San Andreas fault (Fig. 2B). Similar solution cleavage–vein network texture (Fig. 3A) is recorded in samples collected near the creeping zone of the southern deforming zone (sample 3, Fig. 2G), but accommodating lower finite strain than in the central deforming zone. Pressure solution creep also develops at grain scale by diffusion-accommodated grain sliding (Fig. 3B; Ashby and Verrall, 1973) within highly sheared and foliated shale in which feldspar and quartz are depleted by the pressure solution process. This can be seen both near the southern deforming zone (sample 3, Fig. 2H) and in the middle of the central deforming zone (sample 4, Fig. 3E). Evidence of dissolution is documented at grain contacts in the SAFOD creeping zones (Schleicher et al., 2009).

KINETICS OF PRESSURE SOLUTION CREEP

A key issue is whether pressure solution kinetics are consistent with the measured permanent fault creep rates (Titus et al., 2006). To solve this issue, we propose a model (Fig. 3) where steady-state creeping occurs within a vertical shear zone as much as 10 km deep. We use a pressure solution creep law for quartz and calcite derived from laboratory indentation experiments (Gratier et al., 2009; Zubtsov et al., 2005). The strain rate $\dot{\varepsilon}$ derived from the experimental relationship is:

$$\dot{\varepsilon} = \Delta d / (d\Delta t) = 8DwcV_s \left(e^{3\Delta\sigma_n V_s/RT} - 1\right) / d^3, \quad (2)$$

where c is the solubility of the diffusing solid, V_s is the molar volume of the stressed solid, R is the gas constant, T is temperature, D is the diffusion constant along the stressed interface, w is the thickness of the trapped fluid phase along which diffusion occurs, t is time, and $\Delta\sigma_n$ is the driving stress as the difference between normal stress on a dissolution surface and the fluid pressure in the vein. In experiments, d is the diam-

[1]GSA Data Repository item 2011336, Figures DR1 and DR2, is available online at www.geosociety.org/pubs/ft2011.htm, or on request from editing@geosociety.org or Documents Secretary, GSA, P.O. Box 9140, Boulder, CO 80301, USA.

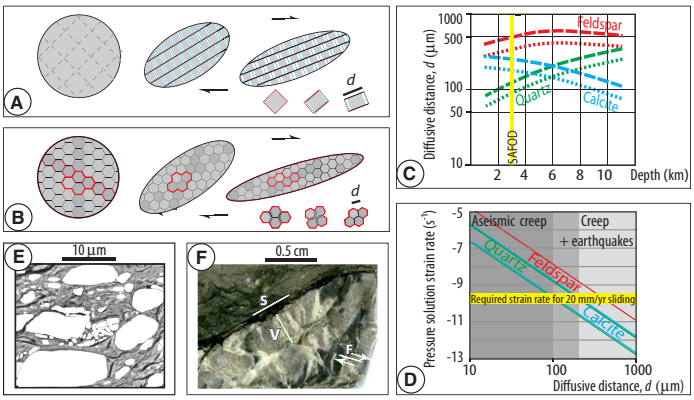

Figure 3. Pressure solution creep mechanisms. A: Mass transfer from solution cleavage (black) to veins (white) with detail of progressive mass transfer process for given element; *d* is mean diffusion distance between veins along solution cleavage; free fluid in veins is blue. B: Diffusion-accommodated grain sliding, with detail of geometry of progressive grain sliding (Ashby and Verrall, 1973); *d* is mean diffusion distance. C: Distance of diffusive mass transfer *d* versus depth for various minerals required to accommodate 20 mm/yr horizontal displacement rate by pressure solution creep in vertical shear zone of 1 m width (dotted line, strain rate of 3.3×10^{-10} s^{-1}) or 3 m width (dashed lines, strain rate of 1.1×10^{-10} s^{-1}). SAFOD—San Andreas Fault Observatory at Depth. D: Pressure solution strain rate versus distance of diffusive mass transfer through entire crust for various minerals; minimum and maximum values for quartz and calcite; yellow line is required strain rate for creeping zone. E: Scanning electron microscope image of sample 4, within creeping zone of central deforming zone (CDZ), showing mixing of phyllosilicates (soft smectite, chlorite, in various grays) and soluble-rigid minerals (quartz, feldspars, calcite, serpentine, in white); crack networks (black) are linked to dewatering of smectite during sample preparation. Deformation is accommodated by grain boundary sliding, possibly by diffusion for soluble species. F: Remnant of sandstone patch deformed by pressure solution cleavage (S)–veins (V) process embedded in CDZ creeping zone, with microfaults (F) (sample 4). (Images E and F can be seen in larger view in the Data Repository [see footnote 1].)

eter of the indenter. In nature, *d* can refer either to the spacing between fractures that corresponds to the diffusive mass transfer distance between veins along a dissolution surface (Fig. 3A), to the grain size in the case of diffusion-accommodating grain boundary sliding (Fig. 3B). Such a diffusion-controlled pressure solution creep law is likely to operate in conditions prevailing at 6–10 km, whereas for the lesser depths (2–4 km), a shift from diffusion control to reaction control is predicted (Renard et al., 1999), but only if *d* exceeds 300 µm, which is not likely here (see following). It is possible to extend the creep law for quartz obtained at 350 °C to lower temperatures within the entire upper crust by assuming an activation energy of 15 kJ/mole (Rutter and Mainprice, 1978). It is also possible to extend the creep law to other minerals such as calcite (Zubtsov et al., 2005) and feldspars by changing the solubility and molar volume parameters. Using such creep laws, with a given stress condition, we can estimate the maximum values of *d* required to accommodate a displacement rate of 20 mm/yr over a 1–3-m-thick shear zone, such as the central deforming zone (Fig. 1C). At 3 km depth, a minimum conservative value for the pressure solution driving stress is the difference between the maximum and the minimum horizontal stress (S_{hmax} and S_{hmin}, respectively). This difference was measured to be ~60 MPa, S_{hmin} being very near the overburden stress (Hickman and Zoback, 2004). The same stress value was used for the entire upper crust (Figs. 3C and 3D). With this model, we show that the maximum required distance of mass transfer at 3 km depth varies with mineral composition in the range 90–350 µm and 125–500 µm for 1 and 3 m width fault zones, respectively (Fig. 3C). These values are larger than the fracture spacing observed for samples 2 and 3 (solution cleavage–veins process; Figs. 2E–2G). They are also much larger than the observed grain sizes in the foliated zones, as in sample 3 and 4 (diffusion-accommodated grain-sliding process; Figs. 2H and 3E). Since the observed diffusion distances are smaller than a conservatively calculated *d* value, pressure solution creep can therefore easily accommodate the measured displacement rate of 20 mm/yr. The diffusion-accommodated grain-sliding process can accommodate much larger finite deformations than the solution cleavage–veins process (Ashby and Verrall, 1973). For this reason, with increasing deformation, the part of the rock deformed by the solution cleavage–veins process, which is also relevant to the most rigid part of the deformed zone, is probably progressively dilacerated and dispersed into the creeping zone (e.g., dark gray grains, Fig. 3B). Evidence of large patches of sandstone deformed by the solution cleavage–veins process can be found in the middle of the central deforming zone (sample 4, Fig. 3F). The solution cleavage–veins process appears therefore to be a transitory state of deformation, which testifies to the efficiency of the pressure solution mechanism and is probably superseded by the diffusion-accommodated grain-sliding process within the most deformed regions of creep.

DISCUSSION AND CONCLUSION

Interaction between creep and seismic (microseismic) fracturing is an important issue. Dissolution indenter experiments show that grain-scale fracturing can drastically accelerate the displacement rate accommodated by pressure solution creep (Gratier, 2011); fracturing opens new paths for solute transport along fluid-filled fractures, decreasing the distance of diffusion, *d*. However, if the fractures are progressively sealed, this effect disappears as sealing increases the distance of mass transfer (*d*), and consequently reduces the displacement rate. At grain scale in the laboratory, such a microfracture pressure solution sealing process may be observed within no less than a few months. In nature, pressure solution fracture sealing probably takes several years or decades, depending on the spacing and the width of the fractures (Gratier, 2011). This could partially explain the effect of the A.D. 2004 M6 Parkfield earthquake on the creep rate southeast of the SAFOD site: coseismic fracturing activated afterslip creep (Freed, 2007) that progressively decreased with time as the fault healed (Li et al., 2006).

The crucial role of the diffusion distance *d* is shown in Figure 3D. When *d* is small enough (10–100 µm), steady-state pressure solution creep can accommodate the observed aseismic displacement rate of 20 mm/yr through the entire upper crust. When *d* is larger (>100 µm), pressure solution creep occurs but cannot accommodate the displacement rate and relax the stress. Consequently, small seismic ruptures occur (Fig. 3F), in turn activating pressure solution creep.

Pressure solution creep is compatible with the low heat flow measurements in the creeping section (Zoback et al., 2010), since this process does not generate significant heat. Various explanations have been proposed for the apparent low friction behavior of the creeping zone. Increases in fluid pressure may reduce the frictional resistance to sliding (Scholz, 2002), but elevated fluid pressures were not measured during drilling, although transient increases of fluid pressure may have occurred episodically in the past (Mittempergher et al., 2011). Talc minerals were found in SAFOD cuttings and should have a weakening effect (Moore and Rymer, 2007), especially if they develop a foliation (Collettini et al., 2009). However, there is as yet no evidence for the presence of continuous layers of talc at SAFOD (Holdsworth et al., 2011). Alternatively, from experiment on cuttings, or laboratory-ground samples, of San Andreas fault creeping zones, Carpenter et al. (2011) and Lockner et al. (2011) found friction values as low as 0.15–0.2, due to the presence of weak phyllosilicate as saponite. It is clear from samples of the San Andreas fault creeping zone (Fig. 3E) that the deformation is accommodated by grain boundary sliding. Friction and

diffusion may compete to accommodate such grain sliding, but it is likely that, at an imposed strain rate, the less energy-consuming process will win. Pressure solution driving forces of 10 and 0.01 MPa are enough to accommodate 10^{-10} s^{-1} strain rate over 3 m width, with 100 and 10 µm grain size, respectively, for quartz and calcite at 6 km depth. Moreover, saponite becomes unstable above ~150 °C and is unlikely to be found deeper in the fault zone than 3.5–4 km. Consequently, as long as the deformation requires grain boundary sliding involving soluble minerals, pressure solution creep is an efficient mechanism of aseismic creep through the entire upper crust down to more than 10 km.

A final question is why, at a given time, pressure solution creep is localized along some segments of the fault. The answer may be that pressure solution creep needs specific conditions to develop at a significant rate. Soluble minerals such as feldspar, calcite, quartz (Gratier et al., 2003), and serpentine (Andreani et al., 2005) must be present with a reactive fluid phase. The distance of diffusive mass transfer (d) must be as small as possible. This requires very fine grained material, possibly related to intense seismic fracturing in the San Andreas fault. Soluble grains must not seal together in order to keep fast diffusive paths along solution seams (Niemeijer and Spiers, 2005). Two processes could avoid such sealing, and occur in the San Andreas fault creeping zones, i.e., passive concentration of phyllosilicates due to soluble species pressure solution depletion (Figs. 2H, 3E, and 3F) and the growth of new phyllosilicates (Holdsworth et al., 2011). In such a way, phyllosilicates get trapped around the soluble species, preventing their sealing and activating diffusive mass transfer. Under these conditions, the process is self-organized through a positive feedback process, which allows pressure solution creep process localization within some fault segments.

ACKNOWLEDGMENTS

We thank S. Hickman and B. Holdsworth for their suggestions on an early version, and F. Agosta, C. Colletini, and J. Imber for their comments on the final version that significantly improved the manuscript. The Grenoble team was partially supported by CNRS-INSU (Centre National de la Recherche Scientifique–Institut National des Sciences de l'Univers) natural hazards program and Agence Nationale de la Recherche ANR-09-JCJC-0011-1. Hadizadeh and Di Toro were partially supported by U.S. National Science Foundation grant EAR-0545472. Di Toro and Mittempergher were supported by a Progetti di Eccellenza Fondazione Cassa di Risparmio di Padova e Rovigo and by European Research Council Starting Grant Project 205175.

REFERENCES CITED

Andreani, M., Boullier, A.-M., and Gratier, J.-P., 2005, Development of schistosity by dissolution-crystallization in a Californian serpentinite gouge: Journal of Structural Geology, v. 27, p. 2256–2267, doi:10.1016/j.jsg.2005.08.004.

Ashby, M., and Verrall, R., 1973, Diffusion-accommodated flow and superplasticity: Acta Metallurgica, v. 21, p. 149–163, doi:10.1016/0001-6160(73)90057-6.

Carpenter, B.M., Marone, C., and Saffer, D.M., 2011, Weakness of the San Andrea Fault revealed by samples from the active fault zone: Nature Geoscience, v. 4, p. 251–254, doi:10.1038/ngeo1089.

Collettini, C., Niemeijer, A., Viti, C., and Marone, C., 2009, Fault zone fabric and fault weakness: Nature, v. 462, p. 907–910, doi:10.1038/nature08585.

Freed, A.M., 2007, Afterslip (and only afterslip) following the 2004 Parkfield, California, earthquake: Geophysical Research Letters, v. 34, L06312, doi:10.1029/2006GL029155.

Gratier, J.-P., 2011, Fault permeability and strength evolution related to fracturing and healing episodic processes (years to millennia): The role of pressure solution: Oil & Gas Science and Technology, v. 66, no. 3, doi:10.2516/ogst/2010014.

Gratier, J.-P., Favreau, P., and Renard, F., 2003, Modeling fluid transfer along Californian faults when integrating pressure solution crack sealing and compaction process: Journal of Geophysical Research, v. 108, no. B2, p. 28–52, doi:10.1029/2001JB000380.

Gratier, J.-P., Guiguet, R., Renard, F., Jenatton, L., and Bernard, D., 2009, A pressure solution creep law for quartz from indentation experiments: Journal of Geophysical Research, v. 114, B03403, doi:10.1029/2008JB005652.

Hickman, S., and Zoback, M., 2004, Stress orientations and magnitudes in the SAFOD pilot hole: Geophysical Research Letters, v. 31, L15S12, doi:10.1029/2004GL020043.

Holdsworth, R.E., van Diggelen, E.W.E., Spiers, C.J., de Bresser, J.H.P., Walker, R.J., and Bowen, L., 2011, Fault rocks from the SAFOD core samples: Implications for weakening at shallow depths along the San Andreas fault, California: Journal of Structural Geology, v. 33, p. 132–144, doi:10.1016/j.jsg.2010.11.010.

Li, Y.G., Chen, P., Cochran, E.S., Vidale, J.E., and Burdette, T., 2006, Seismic evidence for rock damage and healing on the San Andreas fault associated with the 2004 M 6.0 Parkfield earthquake: Seismological Society of America Bulletin, v. 96, p. S349–S363, doi:10.1785/0120050803.

Lockner, D.A., Morrow, C., Moore, D.E., and Hickman, S., 2011, Low strength of deep San Andreas fault gouge from SAFOD core: Nature, v. 472, p. 82–85, doi: 101038/Nature09927.

Mittempergher, S., Di Toro, G., Gratier, J.-P., Hadizadeh, J., Smith, S.A.F., and Spiess, R., 2011, Evidence of transient increases of fluid pressure in SAFOD phase III cores: Geophysical Research Letters, v. 38, L03301, doi:10.1029/2010GL046129.

Moore, D.E., and Rymer, M.J., 2007, Talc-bearing serpentinite and the creeping section of the San Andreas fault: Nature, v. 448, p. 795–797, doi:10.1038/nature06064.

Nadeau, R.M., and Dolenc, D., 2005, Nonvolcanic tremors deep beneath the San Andreas Fault: Science, v. 307, p. 389, doi:10.1126/science.1107142.

Niemeijer, A., and Spiers, C.-J., 2005, Influence of phyllosilicates on fault strength in the brittle-ductile transition: Insight from rock analogue experiments, *in* Bruhn, D., and Burlini, L., eds., High-strain zones: Structure and physical properties: Geological Society of London Special Publication 245, p. 303–327, doi:10.1144/GSL.SP.2005.245.01.15.

Renard, F., Park, A., Ortoleva, P., and Gratier, J.-P., 1999, An integrated model for transitional pressure solution in sandstones: Tectonophysics, v. 312, p. 97–115, doi:10.1016/S0040-1951(99)00202-4.

Rutter, E.H., and Mainprice, D.H., 1978, The effect of water on stress relaxation of faulted and unfaulted sandstones: Pure and Applied Geophysics, v. 116, p. 634–654, doi:10.1007/BF00876530.

Schleicher, A.M., Tourscher, S.N., van der Pluijm, B.A., and Warr, L.N., 2009, Constraints on mineralization, fluid-rock interaction, and mass transfer during faulting at 2–3 km depth from the SAFOD drill hole: Journal of Geophysical Research, v. 114, B04202, doi:10.1029/2008JB006092.

Scholz, C., 2002, The mechanics of earthquakes and faulting: Cambridge, Cambridge University Press, 439 p.

Solum, J.G., Hickman, S.H., Lockner, D.A., Moore, D.E., van der Pluijm, B.A., Schleicher, A.M., and Evans, J.P., 2006, Mineralogical characterization of protolith and fault rocks from the SAFOD Main Hole: Geophysical Research Letters, v. 33, L21314, doi:10.1029/2006GL027285.

Titus, S.J., DeMets, C., and Tikoff, B., 2006, Thirty-five-year creep rates for the creeping segment of the San Andreas fault and the effects of the 2004 Parkfield earthquake: Constraints from alignment arrays, continuous global positioning system, and creepmeters: Seismological Society of America Bulletin, v. 96, p. S250–S268, doi:10.1785/0120050811.

Zoback, M., Hickman, S., and Ellsworth, W., 2010, Scientific drilling into the San Andreas fault zone: Eos (Transactions, American Geophysical Union), v. 91, p. 197–199, doi:10.1029/2010EO220001.

Zubtsov, S., Renard, F., Gratier, J.-P., Dysthe, D.K., and Traskine, V., 2005, Single-contact pressure solution creep on calcite monocrystals, *in* Gapais, D., et al., eds., Deformation mechanisms, rheology and tectonics: From minerals to the lithosphere: Geological Society of London Special Publication 243, p. 81–95, doi:10.1144/GSL.SP.2005.243.01.08.

Manuscript received 14 January 2011
Revised manuscript received 31 May 2011
Manuscript accepted 9 July 2011

Printed in USA

Journal of Structural Geology 42 (2012) 246–260

Contents lists available at SciVerse ScienceDirect

Journal of Structural Geology

journal homepage: www.elsevier.com/locate/jsg

A microstructural study of fault rocks from the SAFOD: Implications for the deformation mechanisms and strength of the creeping segment of the San Andreas Fault

Jafar Hadizadeh [a,*], Silvia Mittempergher [b,c], Jean-Pierre Gratier [c], Francois Renard [c,d], Giulio Di Toro [b,e], Julie Richard [c], Hassan A. Babaie [f]

[a] 212 Lutz Hall, Department of Geography & Geosciences, University of Louisville, Louisville KY 40292, USA
[b] University of Padova, Padova, Italy
[c] ISTerre, University Joseph Fourier & CNRS, BP 53, 3804 Grenoble, France
[d] PGP, University of Oslo, Oslo, Norway
[e] Istituto Nazionale di Geofisica e Vulcanologia, Rome, Italy
[f] Geosciences, Georgia State University, Atlanta, GA, USA

ARTICLE INFO

Article history:
Received 13 June 2011
Received in revised form
23 April 2012
Accepted 24 April 2012
Available online 7 May 2012

Keywords:
San Andreas Fault
SAFOD
Foliated gouge
Shear localization
Cataclasis
Pressure solution

ABSTRACT

The San Andreas Fault zone in central California accommodates tectonic strain by stable slip and microseismic activity. We study microstructural controls of strength and deformation in the fault using core samples provided by the San Andreas Fault Observatory at Depth (SAFOD) including gouge corresponding to presently active shearing intervals in the main borehole. The methods of study include high-resolution optical and electron microscopy, X-ray fluorescence mapping, X-ray powder diffraction, energy dispersive X-ray spectroscopy, white light interferometry, and image processing.

The fault zone at the SAFOD site consists of a strongly deformed and foliated core zone that includes 2–3 m thick active shear zones, surrounded by less deformed rocks. Results suggest deformation and foliation of the core zone outside the active shear zones by alternating cataclasis and pressure solution mechanisms. The active shear zones, considered zones of large-scale shear localization, appear to be associated with an abundance of weak phases including smectite clays, serpentinite alteration products, and amorphous material. We suggest that deformation along the active shear zones is by a granular-type flow mechanism that involves frictional sliding of microlithons along phyllosilicate-rich Riedel shear surfaces as well as stress-driven diffusive mass transfer. The microstructural data may be interpreted to suggest that deformation in the active shear zones is strongly displacement-weakening. The fault creeps because the velocity strengthening weak gouge in the active shear zones is being sheared without strong restrengthening mechanisms such as cementation or fracture sealing. Possible mechanisms for the observed microseismicity in the creeping segment of the SAF include local high fluid pressure build-ups, hard asperity development by fracture-and-seal cycles, and stress build-up due to slip zone undulations.

1. Introduction

The orientation of horizontal principal stresses and data from heat flow measurements require the San Andreas Fault (SAF) in central California to deform at a low resolved shear stress (Lachenbruch and Sass, 1992; Rice, 1992; Bird and Kong, 1994; Zoback, 2000; Townend and Zoback, 2000; Hickman and Zoback, 2004; Chéry et al., 2004; Boness and Zoback, 2006). For the creeping segment of the SAF, mechanisms such as fluid overpressure and presence of intrinsically weak fault rocks have been invoked to support the weak fault model (e.g. Byerlee, 1993; Rice, 1992; Faulkner and Rutter, 2001; Lockner et al., 2011; Carpenter et al., 2011). Hydrological modeling of the SAF by Fulton and Saffer (2009), Fulton et al. (2009), and the results of Faulkner and Rutter (2001) by implication, ruled out fluid overpressure weakening by metamorphic dehydration, but did not rule out the possibility of fluid overpressure due to dehydration of mantle-derived serpentinites.

* Corresponding author. Tel.: +1 502 852 2691.
E-mail addresses: j0hadi01@louisville.edu, hadizadeh@louisville.edu (J. Hadizadeh).

0191-8141/$ – see front matter © 2012 Elsevier Ltd. All rights reserved.
doi:10.1016/j.jsg.2012.04.011

The central California segment of the SAF exhibits creep that diminishes from ~28 mm/year, in the central region of the segment, to ~20 mm/year at the San Andreas Fault Observatory at Depth (SAFOD) site near Parkfield. The creep rate diminishes almost to zero at the southeast end of the segment where transition to a locked section of the SAF occurs near Fort Tejon (Titus et al., 2006). In addition to creep, the segment shows repeating $M < 3$ earthquakes with an average recurrence time of ~3 years (Nadeau et al., 2004) on seismic patches with estimated 15–20 m radial dimensions (Nadeau and Johnson, 1998; Dreger et al., 2007). Seismic inversion studies near the observatory site show that the patches occur in roughly strike-parallel clusters that make up 1% or less of the total fault surface area (Nadeau and Johnson, 1998: Rubin et al., 1999; Waldhauser et al., 2004; Dreger et al., 2007; Chen and Lapusta, 2009). While the weak SAF is estimated to have coefficient of friction $\mu < 0.2$, the seismic asperity patches are expected to have $\mu > 0.2$, suggesting that the contrasting frictional strengths could serve as a source of mechanical instability (Townend and Zoback, 2004; Chéry et al., 2004; d'Alessio et al., 2006; Dreger et al., 2007; Imanishi and Ellsworth, 2006; McGarr et al., 2010). Nadeau et al. (1995) reported that locations of dominant repeating events appear to migrate cyclically within the clusters over several years. Establishment of the SAFOD is the latest effort to shed light on the strength model controversy and understand the nature of the creep and seismic activity in the SAF via direct observations (Fig. 1a). The discovery in 2005 of steel casing deformation within the SAFOD Main Hole revealed two distinct intervals of active shearing. The intervals (Fig. 1b) were subsequently named by Zoback et al. (2011) the Southwestern Deforming Zone (SDZ) and Central Deforming Zones (CDZ). The direct evidence of active shearing within the SAF core zone has made the microstructural features associated with the SDZ and CDZ more significant because majority of microstructural studies on fault rocks to date are from exhumed fault zones.

Zoback et al. (2011) outlined major findings of the SAFOD as: 1. Major fault strands of the SAF encountered in the drill hole consist of strongly foliated gouge, 2. The SAF acts as a barrier to fluid flow, 3. The maximum horizontal principal stress is at high angles to the SAF to within 100 m of the fault zone, 4. There are no temperature anomalies and no evidence of higher-than-hydrostatic fluid pressures in the SAFOD borehole. Recent investigations based on the SAFOD core and cuttings samples explain the fault's apparent absolute weakness mainly in terms of frictional weakness of the fault rock constituents. Solum and van der Pluijm (2004) and Solum et al. (2006, 2007) studied the authigenesis and distribution of phyllosilicate assemblages in the SAFOD cores and cuttings. These results showed concentrations of chlorite, illite, and illite-smectite along several identifiable strands of the SAF while smectite mineral saponite and serpentine mineral lizardite were found in samples from the active shear zones. Moore and Rymer (2007) suggested that their discovery of talc coating on serpentinite particles is a possible explanation for the weak fault model. Schleicher et al. (2008), however, found little or no talc associated with serpentinites in the fault gouge. Janssen et al. (2010) reported amorphous material in the foliated gouge samples close to the active shear zones. Holdsworth et al. (2011) concluded that the presence of low-friction Mg-rich smectites is a viable explanation for the creep behavior (velocity strengthening) and the absolute weakness, but suggested that the material weakness model may hold true only down to 5–6 km depths in this segment of the SAF. The latter conclusion was reached because Mg-rich smectites tend to breakdown into frictionally stronger Mg-rich chlorites at $T > 150$ °C (Inoue and Utada, 1991). Wenk et al. (2010) determined that phyllosilicates in the SAFOD gouge had a much

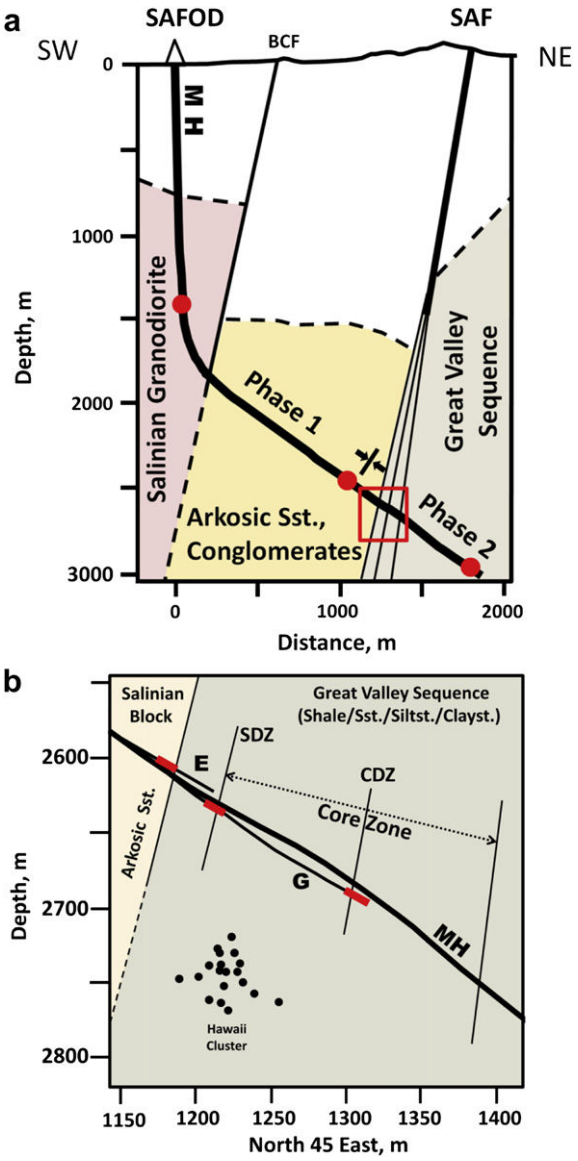

Fig. 1. Profile of the SAFOD drill holes marked with location of core intervals. (a) SAFOD main hole (MH) with location of Phase 1 and Phase 2 spot core intervals (solid red circles). Lithological units SW of SAF are collectively known as the Salinian Block. (b) Enlarged inset box showing Salinian-Great Valley Formation contact and position of the Phase 3 lateral holes E and G with respect to MH. Coring intervals in lateral holes are shown with solid red rectangles. Approximate trace of the well-casing deformation zones, SDZ and CDZ, and position of SAF core zone are shown. Note that well-casing deformation was only detected in the main hole. Hawaii cluster refers to one of the two target microseismicity clusters near the SAFOD boreholes. (For interpretation of the references to color in this figure legend, the reader is referred to the web version of this article.)

weaker crystallographic preferred orientation (CPO) fabric relative to the fabrics found in shale from North Sea sedimentary basin, and schist from metamorphic rocks in the Alps (also see Haines et al., 2009). Weak fault gouge CPO fabrics were attributed to randomization by heterogeneous deformation, as well as dissolution–precipitation reactions. A study by Schleicher et al. (2009) indicated that mineralogical transformation in the SAFOD damage zone and active shear zones are mainly due to pressure solution and diagenetic processes. Gratier et al. (2011) suggested that creep accommodated by pressure solution could explain the weakness of the SAF at depths greater than a few km.

Based on stress measurements in the SAFOD pilot hole, Chéry et al. (2004) argued that only a fault model with $\mu < 0.1$ could match both the far field and the pilot hole stress data. Based on frictional sliding experiments on reconstituted gouge (lacking in-situ fabric) at room temperature, Tembe et al. (2006) reported $\mu = 0.4$ to $\mu = 0.55$ for bulk samples of the SAFOD clay gouge and its mostly siltstone-shale protolith. Velocity-stepping sliding experiments by Lockner et al. (2011) gave $\mu = 0.19$ and $\mu = 0.16$ respectively for the SDZ and CDZ core material, and showed that the material is velocity strengthening. Extrapolating from the slowest sliding rates in the experiments to the SAF creep rate of $\leq$34 mm/year, Lockner et al. (2011) suggested that the actual friction in the active shear zones may be as low as $\mu = 0.16$ for SDZ and $\mu = 0.14$ for CDZ. Carpenter et al. (2011) reported velocity-stepping sliding experiments that provided similar strength results for the SAFOD gouge as well as showing zero frictional-contact healing rates for the active shear zone materials. These results and work by others (Wintsch et al., 1995; Moore and Lockner, 2008; Tembe et al., 2009; Ikari et al., 2009; Janssen et al., 2010) suggested that friction coefficients as low as 0.1 should be expected if slip surfaces were to be lined with small amounts of weak phases such as talc or amorphous material. Furthermore, frictional strengths lower than those found by sliding experiments should be expected due to microstructural control of gouge strength. For example, Chester and Chester (1998), Jefferies et al. (2006), Tembe et al. (2010), and Niemeijer et al. (2010) argued that development of foliation due to accumulation of weak alteration products, especially phyllosilicates, is often associated with long-term weakening of mature crustal-scale fault zones. Foliation itself as a microstructural weakening mechanism was investigated by Collettini et al. (2009) in an experimental study that showed intact foliated gouge samples had a lower frictional strength than their powdered equivalents. In view of the previous work described, this study is mainly focused on providing a better understanding of the microstructurally recognizable deformation mechanisms in the SAFOD samples, particularly in the active shear zones. In this respect, an important question centers on the strength implications of shear localization and whether this could be interpreted from microstructures and materials of the studied rocks.

2. The core samples and sections

The SAFOD main hole profile marked with spot core intervals in the phase 1 and 2 drilling and a close-up of the lateral holes E and G core intervals from the phase 3 drilling are shown in Fig. 1. The lithological unit boundaries encountered in the SAFOD main hole together with the velocity and resistivity logs are shown in Fig. 2a. A close-up of the main hole interval that includes the SAF core zone (main damage zone in Zoback et al., 2011) and location of the studied samples are shown in Fig. 2b. The drill site structural and stratigraphic units and the lithologies encountered in the SAFOD are described elsewhere (Rymer et al., 2003; Thurber et al., 2004; Darcy et al., 2004; McPhee et al., 2004; Boness and Zoback, 2006; Bradbury et al., 2007; Zoback et al., 2011). We studied 6 samples from the phase 1 and 2 spot cores and 9 samples from the phase 3 lateral holes. The study was further expanded by using a set of 6 SAFOD-provided petrographic thin sections (SAFOD, 2010) from locations other than our phase 3 core samples. Information about

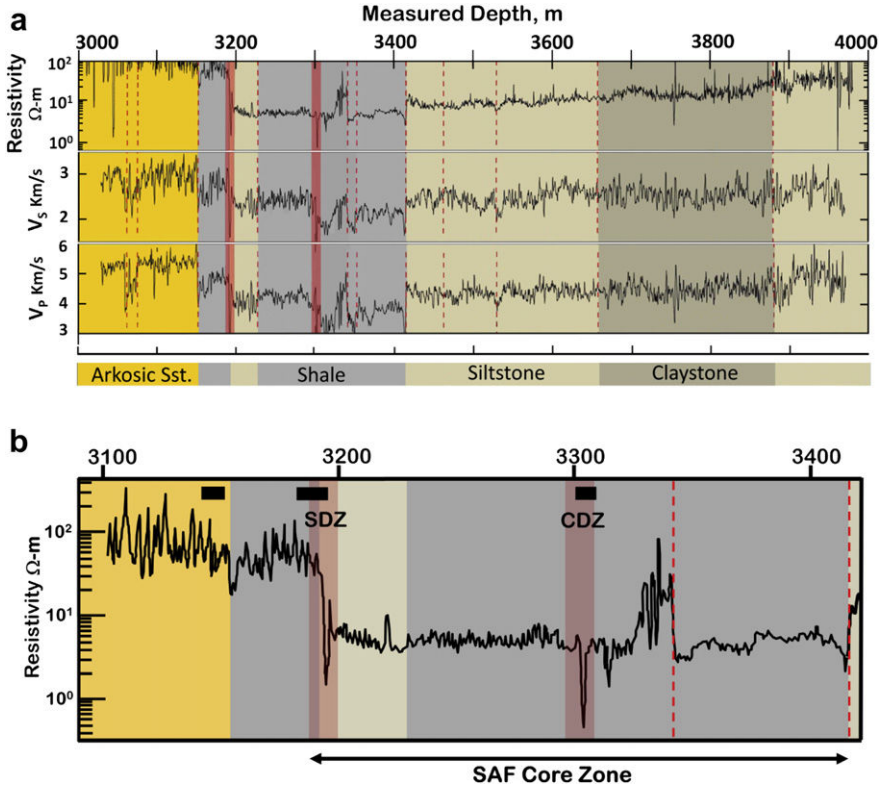

Fig. 2. The San Andreas Fault core zone including currently active shear zones represented by geophysical logs from the SAFOD main hole. See Jeppson et al. (2010) for additional information. (a) Changes in resistivity and seismic wave velocity within lithological units that host the fault rocks. Dashed red lines indicate minor faults or fracture zone while the two red bands are intervals of well-casing deformation that indicate active shearing. (b) A close-up of the 3100–3400m measured depth interval including the fault core zone. The entire core zone including well-casing deformation zones, SDZ and CDZ, are coincident with notable drops in resistivity. Depth range of samples used in this study (see Table 1) is marked by solid black rectangles. (For interpretation of the references to color in this figure legend, the reader is referred to the web version of this article.)

Table 1
The studied samples listed in order of measured depth (MD) in SAFOD boreholes. The relevant lithological and structural boundaries are marked. The depths for core sections G12–G54 (Phase 3 lateral holes) are Main Hole equivalent measured depths. Abbreviations: Box = Spot core repository box number; E and G are lateral borehole designations. For example, G25 stands for hole G, Run 2, Section 5; SAFOD TS = Petrographic thin sections provided by the SAFOD; SDZ = Southwestern Casing-Deformation Zone; CDZ = Central Casing-Deformation Zone.

	Core Section	Main Hole MD, m	Studied Sample	
	Box 14	3059.28	3A1	Salinian Block
	Box 16	3061.75	5B1	
	Box 17	3062.63	P3-01	
	E11	3141.78	1C-2	
	E13	3143.55	5A-1	
	E25	3152.24	SAFOD TS	
~3174m MD				
	G12	3183.03	SAFOD TS	Great valley
	G14	3184.70	SAFOD TS	
	G21	3186.04	SAFOD TS	
	G21	3186.53	B1XY	
~3187m To ~3414m SAF Core Zone	G24	3188.97	7B2XY and 7B4XY	
	G25	3189.94	A1	
SDZ	G27	3191.41	SAFOD TS	
SDZ	G28	3192.17	G28-01	
	G31	3193.67	SM-1	
	G42	3300.00	10B-1	
CDZ	G43	3301.04	SAFOD TS	
CDZ	G54	3308.78	G54-A1	
	Box 1	3990.32	P4	
	Box 2	3991.45	P5	
	B0x 3	3993.08	P6	

all 21 individual samples and petrographic thin sections is provided in Table 1. The set of SAFOD-provided petrographic thin sections (see SAFOD TS in Table 1) was also used in the study by Holdsworth et al. (2011). Since Table 1 provides cross-referenced sample information, here we refer to our samples by their core section designation (e.g. G25, E11).

The SDZ and CDZ active shear zone intervals are centered at 3192 m MD (~1.6 m wide) and 3302 m MD (~2.6 m wide). For technical reasons an accurate measurement of the rate of the casing deformation has not been possible except that deformation appears to be more intense in the CDZ than in the SDZ, and the deformation in each case involves some sympathetic buckling of the casing on either side of the intervals (Hickman personal communication 2010). The SAFOD geophysical logs (Fig. 2) place the CDZ and SDZ within a low-velocity zone consisting of foliated and non-foliated gouges. Our study included a thin section from G27 and a sample from G28 in the SDZ, and a thin section from G43 in the CDZ. The sample coverage, therefore, is representative of a variety of the SAF rocks encountered during the 3 phases of drilling.

Since core samples in phase 3 were acquired by lateral drilling from the SAFOD main hole, the measured depths for hole-G samples listed in Table 1 are the main hole equivalent depths rather than the actual drilling depths in the lateral hole. The purpose of this depth conversion was to correlate the phase 3 samples with the SDZ and CDZ intervals, which were identified by borehole caliper measurements only in the main hole. Offset distances of −5.03 m and 3.96 m were applied to measured depths of the hole-G core samples. The phase 3, hole-E measured depth values were left unchanged since this run was close to the main hole and did not coincide with the casing deformation intervals. The applied correction values, provided by Zoback et al. (2011), were determined mainly by matching open-hole gamma logs (not shown in Fig. 2) from phase 2 with phase 3 logs since: 1. The SDZ and CDZ were both associated with distinct low total natural

gamma counts in the open-hole logs, and 2. Both intervals of foliated gouge in the Phase 3 core yielded distinctly low total counts in post-drilling gamma scanning. The correlation suggests that samples G27, G28 and G43 used in this study (Table 1) were probably deforming at the time of coring as part of the SDZ and CDZ.

3. Methods

The samples were directly cut from repository core lengths using bench saws. To prevent swelling in clay mineral phases, a $CaCl_2$ solution with slightly higher salinity than the formation fluid was used during cutting. The solution was also used for sectioning the core samples. All petrographic sections were polished sections to allow both optical and electron microscopy. The relatively less deformed samples were cut from the core billets along 3 mutually perpendicular planes without a structural or ground reference and were not impregnated prior to sectioning. The foliated gouge samples were impregnated with clear epoxy resin and cut along 2 directions perpendicular and 1 direction parallel to foliation using visual judgment. Optical transmitted and reflected light microscopy as well as high-resolution SEM was used for viewing and imaging the fault rock microstructures. Energy dispersive X-ray (EDX) with internal standards was frequently used during SEM observations for determining mineral phases and estimating the atomic wt. % of the phases. A limited number of XRF chemical composition maps were created for sample G24 to ascertain the direct relationship between foliation microstructures and mineral phase distribution. Changes in 2D image porosity across typical foliated clay gouge (sample G24 in Table 1) were estimated using digital image processing. We used digital thresholding of image pixel intensities to isolate pore spaces on binary images, from which total pore areas were measured. The measurements were made on overlapping, 1.15 mm wide tracts of backscatter SEM images over 68.7 mm total tract length. The tracts were processed one image at a time by thresholding at the narrowest and the widest possible range of pixel intensities that could represent pore areas on the image. Each step created a pair of binary images with a range of porosity values. The low-side of the range (0–10) provided the lower-bound porosity value and was considered to be the most reliable since the pixel intervals included darker tones of gray. Further details of the method may be found in Hadizadeh et al. (2010). Errors in porosity estimates due to particle plucking or filling of pores during surface preparation were assumed negligible because the gouge samples were resin impregnated. This assumption was further justified because the results were in good agreement with the average porosity values obtained for the SAFOD gouge by porosimetry (Janssen et al., 2011). The detailed microstructural study of foliation, veins, faulting and fracturing in the samples was complemented by bulk and oriented X-ray powder diffraction (XRPD) analyses. We were primarily interested in compositional changes in a direction normal to the fault plane particularly with respect to the boundaries of the SDZ and CDZ active shear zones. A suite of 11 samples (Table 2) were selected for XRPD analysis including:

1. The fractured, but otherwise undeformed host rock (core box samples).
2. The relatively weakly deformed material such as proto-cataclasites and microbreccia (G21, G54).
3. The highly deformed material adjacent to the zones of active shear localization such as cataclasites and foliated cataclasites (G24, G25, G31).
4. Mostly foliated cataclasite and ultracataclasite gouge from the SDZ active shear zone (G28).

A total of 17 XRPD scans were carried out, 6 of which were duplicates to assure reproducibility in strongly foliated gouge materials. For bulk analyses, each sample was ground and sieved to include particles $\leq$37 μm, packed into a sample holder and scanned at 2°/minute with a Siemens D5000Matic diffractometer at 40 kV over the range 2–61° 2θ using Cu-Kα radiation. The XRD scanning of sample G25with possible presence of amorphous material was repeated 3 times, including 1 scan under the same conditions as for other runs, but using a Rigaku DMAX B diffractometer at 0.5°/minute for a more detailed scan. We found no notable difference between the three scans for sample G25. For clay phase identification, a portion of the ground samples was first washed with dilute HCl to eliminate carbonates followed by thoroughly washing and mixing the remaining mixture with distilled water. An oriented mount was made by settling the aqueous mixture onto a cellulose acetate filter and then rolling the deposited material onto a glass disk. The oriented mounts were first scanned over the range 2–30° 2θ for all phyllosilicates and then treated with glycol and re-scanned over the range 2–22° 2θ for smectite clays. Mineral concentrations were estimated using XRF-determined elemental compositions and the relative peak-height to peak-area on the XRPD scans. The X-ray results are shown in Table 2. The detection limit for an average mineral in these samples is ~1–3% and the analytical reproducibility was taken to be approximately equal to the square root of the amount of the phase in the analyzed powder. The XRPD scans for sample G31from the CDZ were analyzed by Mittempergher et al. (2011) using the Rietveld method. White light

Table 2
The X-ray powder diffraction results. Methods are explained in the text. See Table 1 for core section information.

N	Core section	Qtz.	Felds.	Cal.	Pyrite	Chl.	I & I–S	Verm.	Amor.	UnID
1	Box 14	39	54	0	0	0	5	0	0	2
1	Box 17	29	54	0	0	0	15	0	0	2
2	G21	62 ± 2	10	5 ± 2	2	7.5 ± 2.5	13.5 ± 1.5	0	0	0
2	G24	49 ± 1	9.5 ± 3.5	11.5 ± 0.5	1	2.5 ± 2.5	25.5 ± 0.5	0	0	1
3	G25	8.5 ± 2.5	5.5 ± 0.5	4.5 ± 0.5	0	0	36 ± 1	2.5 ± 2.5	40 ± 10	3
2	G28	10	7 ± 2	4 ± 1	0	0	0	77.5 ± 2.5	0	1.5
1	G31[a]	19	25	1	1	5	49	0	0	0
2	G54	31.5 ± 0.5	19.5 ± 0.5	0	0.5 ± 0.5	29 ± 1	16.5 ± 2.5	0	0	3
1	Box 1	24	32	0	0	23	18	0	0	3
1	Box 2	22	38	0	1	24	14	0	0	1
1	Box 3	32	39	5	0	18	5	0	0	1

Abbreviations: *N* = number of runs; Qtz. = quartz; Felds. = Feldspars; Cal. = calcite; Chl. = chlorite; I & I–S = illite and illite–smectite; Verm. = vermiculite; Amor. = amorphous material; UnID = unidentified.

[a] Analysis using Rietveld method.

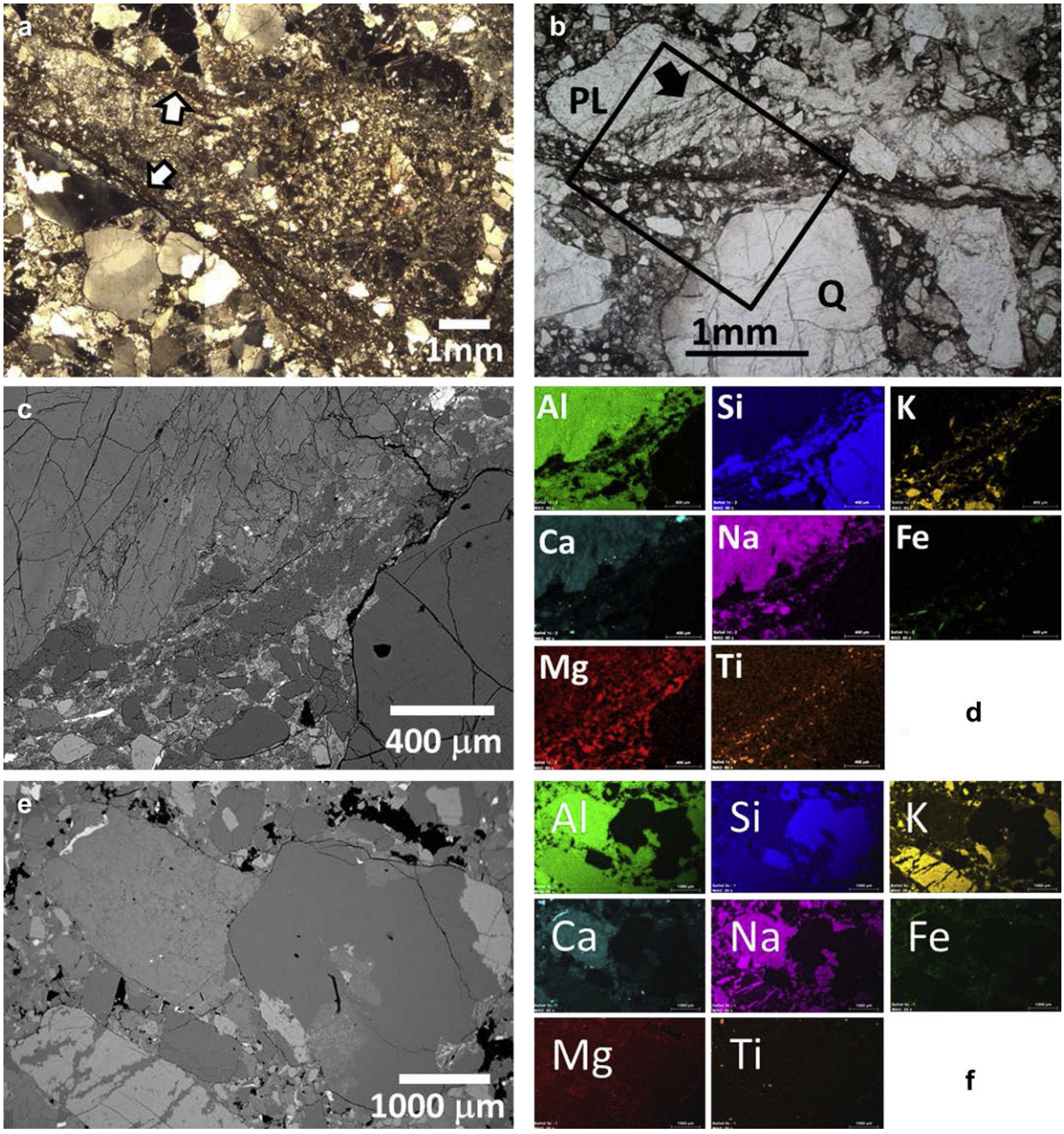

Fig. 3. Typical deformation microstructures outside the core zone. The data is in order of increasing measured depth toward SW border of the zone. (a) Thin gouge zone in Salinian arkosic sandstone/fine conglomerate. Highly comminuted dark streaks (arrowed) contain iron oxide and phyllosilicates. Cross polarized light (XPL) image; sample Box 16. (b) Imbricate plagioclase (PL) cleavage fractures (arrow) and grain-boundary attrition of quartz (Q) showing role of cataclasis in the development of minor gouge zones. Plane polarized light (PPL) image; sample E11. (c–d) Backscatter SEM image from inset box in b, and XRF elemental maps of the same area. The elemental maps are consistent with presence of iron oxides in the shear zone, probably passively concentrated where soluble mineral were removed by pressure solution, as well as sericitization of plagioclase feldspar. Note lack of calcite deposits and concentration of Ti in the gouge. Sample E11. (e–f) Pressure solution indentation of Na-feldspar by quartz (indenter) in coarse arkosic sandstone. The impingement area includes no calcite or clay deposits. Black spots are pore spaces. Backscatter SEM image; sample E13. (g) Indentation microfracturing and pressure solution of quartz by neighboring feldspar grain in arkosic sandstone cataclasite. Calcite crack-seal veins indicate creep opening of the indentation cracks. XPL image; sample E25. (h–i) Development of vein-cleavage fabric in shale-siltsone cataclasites of Great Valley Formation. Close-up view of calcite vein fillings transverse to dissolution contacts. XPL images; sample G12. (j) Calcite veins cross-cutting quartz-healed transgranular fractures (arrows) indicating an older deformation episode in shale-siltstone cataclasite. XPL image; sample G14. (k–l) Foliation in shale-siltstone cataclasite defined by large elongated siltstone clasts separated by clay gouge (PPL image). Inset box shows calcite-healed fractures transverse to foliation, typical of vein-cleavage fabric (XPL image). Sample G21.

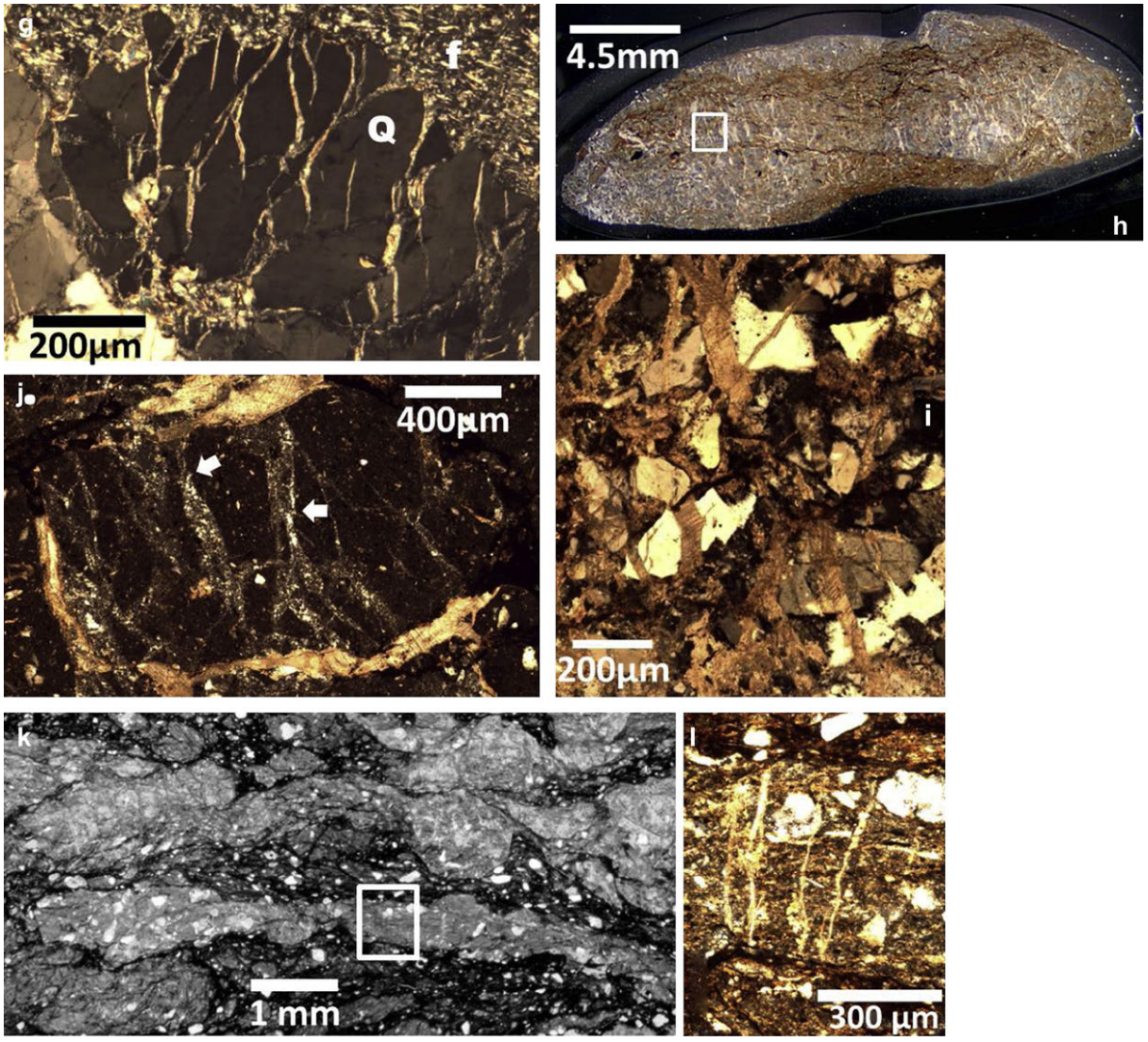

Fig. 3. (*continued*).

interferometry (WLI) scanning using a Zygo New View 6300 scanner was carried out on a ~4 × 3 × 2 mm chip from freshly exposed striated gouge surface in sample G28. The surface sample was removed from the soft and fragile core material under microscope to avoid physical damage resembling the natural striations. The sample was mounted on glass slide using a small sticky pad and was thoroughly air-brushed before scanning.

4. Microstructural and analytical observations

The SAF core zone is ~227 m wide (3187 m–3414 m MD in the main hole) as defined by significant drops in the V_p and V_s velocity, and resistivity logs (Fig. 2b). At the scale of core sections the zone appeared to be confined to shale and mudstone units of the Great Valley sequence (Rymer et al., 2003; Thurber et al., 2004). These units are interbedded with distinct siltstone layers of up to ~5 m thick (e.g. 3301–3306 m MD interval in Hole G). A mixed shale-siltstone gouge that probably developed close to the shale-siltstone contacts, but intervals of shale and mudstone cataclasite and siltstone cataclasite were also common along the core sections. In addition, visible streaks and irregularly shaped serpentinite porphyroclasts of diameters up to ~0.15 m were present in the core lengths that include SDZ and CDZ. More specific lithological description of the SAFOD core sections is provided elsewhere (see Bradbury et al., 2011; Holdsworth et al., 2011).

The deformation outside the core zone, in the Salinian arkosic sandstone, was mostly concentrated in networks of minor fault zones with mm to cm-scale apparent displacements. These features were mostly observed at distances of 126 m to 35 m from the core zone (Box 16 to E25 series, Table 1) as gouge-filled cataclastic shear zones that ranged in thickness from 1 mm to 2 cm with abundant iron oxide staining (Fig. 3a). Sliding on feldspar cleavage fractures (Fig. 3b–c) and concentration of Ti (Fig. 3d), indicating both processes of alteration and dissolution of feldspar, were frequently observed. Indentation of feldspar by quartz, with little or no local clay residual (Fig. 3e–f), and crack-seal calcite veins at the indentation sites (Fig. 3g) were also common outside and away from the core zone. Similar minor shear zones were found in the Salinian granodiorite core samples from 1464 m MD

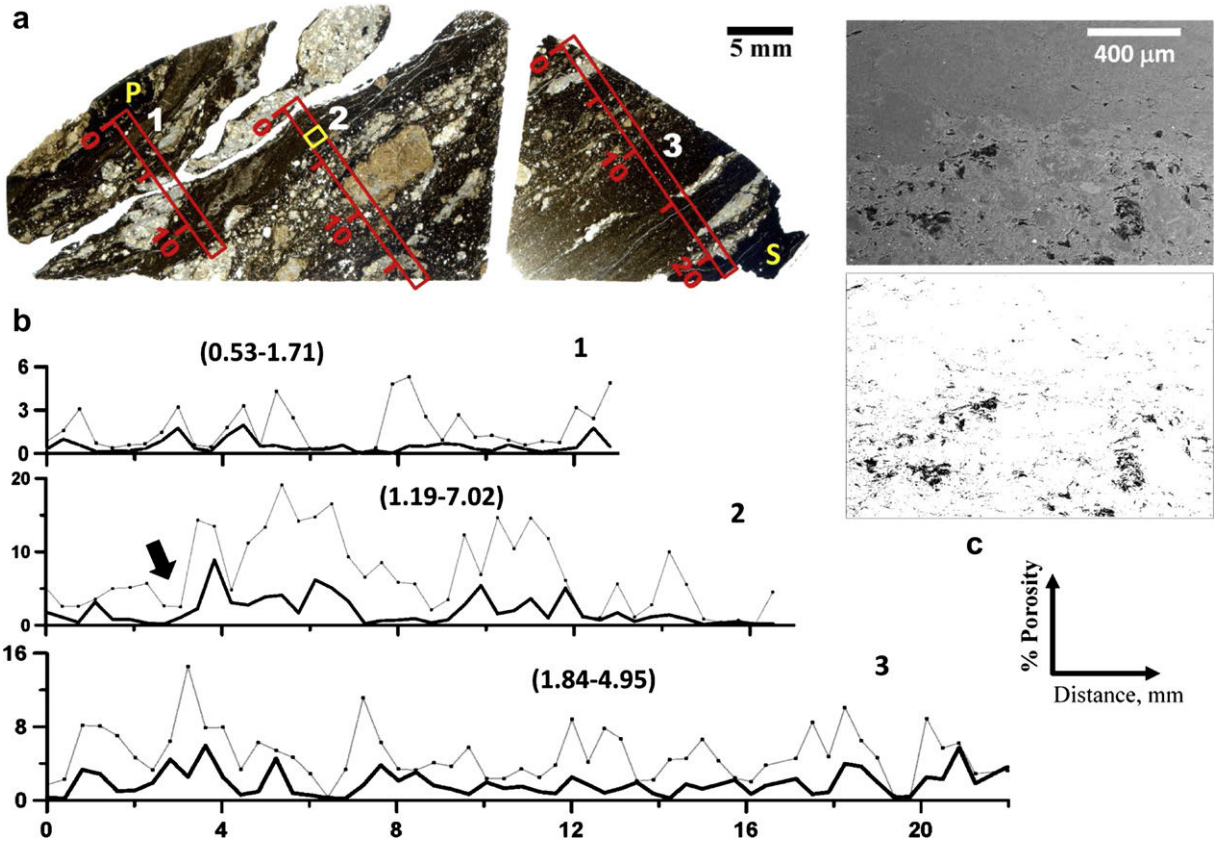

Fig. 4. Variations in porosity across foliation in typical shale-siltstone cataclasites of the core zone. (a) Whole section PPL image of petrographic thin sections of sample G24 showing exact position of tracts used for 2D image porosity measurement. The tracts, staggered for increased coverage, begin in host shale cataclasite P and end in deformed pyrite mass S. (b) Porosity–distance plots. Black and gray curves respectively show porosity values corresponding to narrowest (most certain) and widest (least certain) range of intensity that represented pore spaces on the images. Numbers in parenthesis are average porosity for the upper and lower-bound curves in each tract. (c) Top: backscatter SEM image located in tract 2 (inset box) showing a porosity contrast boundary in the gouge (arrow on plot 2). Bottom: binary frame based on widest pixel intensity range of pore areas on the same SEM image. Sample G24, 3188.97 m MD.

(Hadizadeh et al., 2007) and in the samples studied by Almeida et al. (2005).

The fault rocks within ~5 m of the core zone, in Great Valley shale and siltstone-shale units, were studied in thin sections from samples G12, G14, and G21. The deformation appeared more intense than in the previously described small-displacement faults mainly due to the development of foliation and greater evidence of systematic veining. Calcite veins running transverse to what appeared to be dissolution seams in the cataclasite gouge (Fig. 3h–i) indicated an early-stage cleavage development by pressure solution. There was evidence that earlier generation of transgranular fractures were sealed with quartz (Fig. 3j). A well-developed foliation in siltstone-shale cataclasites ~1 m away from the core zone border (G21) was defined by anastomosing bands of clay-rich and quartz-rich gouge (Fig. 3k). Fractures transverse to length of quartz-rich bands were sealed with calcite (Fig. 3l). The described microstructural deformation (Fig. 3a–l) was also associated with increased levels of illite-smectite phases toward the main damage zone (Table 2). Outside the core zone, the dominance of quartz-feldspar mineralogy in the SW side of the fault (Table 2) is probably due to shearing at the contact between arkosic sandstone units of the Salinian block and the Great valley shale-siltstone units.

The core zone, represented by samples G24 through G54 (Table 1), consisted of highly comminuted, altered, and foliated rocks. As described in the following, we found the microstructural deformation to be transitional across the geophysical border of the core zone (3187 m MD). The foliation was defined by mm to sub-mm bands of clay-rich gouge intermittent with highly veined quartz-rich cataclasites (Fig. 4a). The 2-D image porosity varied across the foliation depending on clay content, distribution of hard mineral particles, and veining intensity (Fig. 4b). The porosity approached zero in quartz-rich cataclasite bands heavily veined with calcite transverse to the length of the band. The range of average porosities derived from all lower and upper bound measurements in sample G24 was 1.18–4.56%, which is comparable to the average porosity values for the SAFOD gouge obtained by porosimetry and from TEM images by Janssen et al. (2011). The foliated gouge in Fig. 5a (enlarged left side of Fig. 4a) contained microstructural evidence of reworked cataclasites as well as banding and vein fabric that appeared to be due to pressure solution. Some quartz-rich bands were vein-saturated by multiple vein network imprints. Sheared pyrite masses and feldspar alteration products in the XRF elemental maps (Fig. 5b–c) indicated hydrothermal fluid flow and mineral alterations in the gouge. The sample G42 ~1 m from the CDZ boundary revealed clear evidence of a foliation defined by pressure solution cleavage, where dissolution seams were separated by microlithons with transverse vein fabric (Fig. 5d–e). The compositional proportion of mixed-layer illite-smectite clays and other weak phases such as chlorite and vermiculite was elevated in the core zone and close to the active

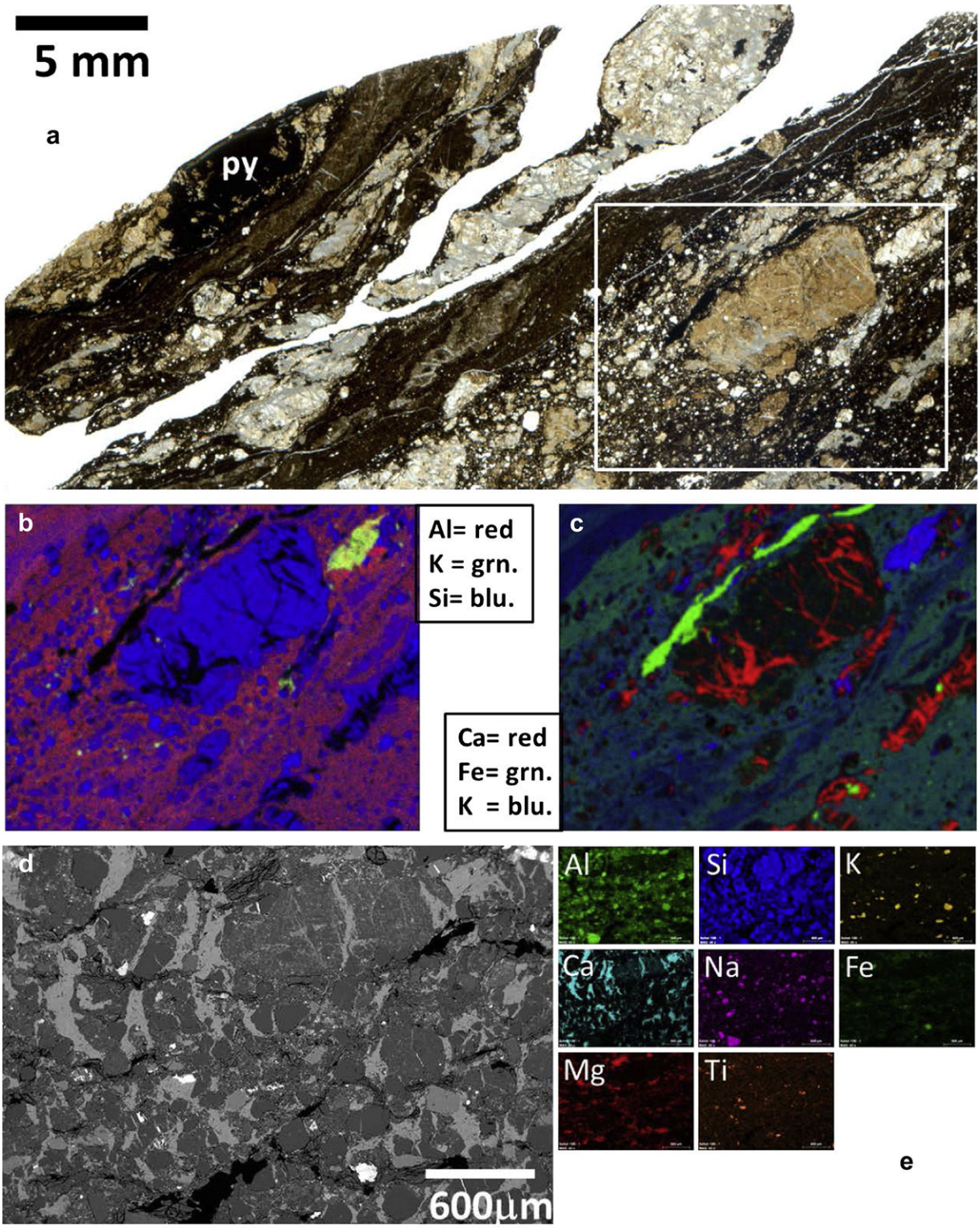

Fig. 5. Well-developed foliation in siltstone-shale cataclasites typical of the core zone rocks. (a) The foliation is defined by interlaced bands of siltstone-rich gouge and dark-colored clay-rich gouge. Siltstone clasts consist of variably healed cataclasites. A mass of deformed pyrite (py) forms an inverted sigma that indicates dextral sense of shear in the sample. (b) Distribution of Aluminum in XRF elemental map for inset area in the foliated gouge indicates pervasive clay mineralization. (c) XRF elemental map from the same area shows pattern of the transverse calcite veins in a quartz-rich band and reveals smearing of pyrite along foliation. Sample G24. (d) SEM backscatter image of fully-developed vein-cleavage pressure solution foliation in the core zone, ~1 m distance from the CDZ boundary. Sample G42. (e). XRF elemental maps of the area shown in d.

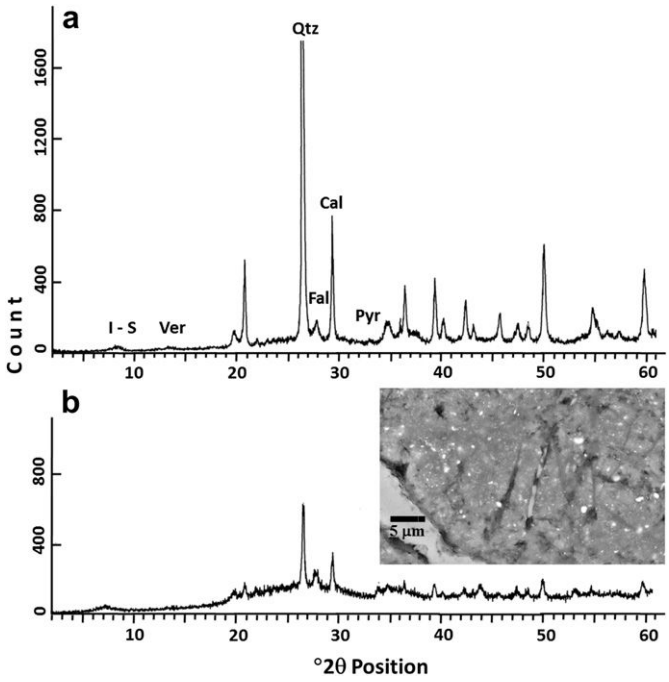

Fig. 6. Bulk XRPD scans comparing (a) G24 gouge sample composition from 3188.97 m MD with (b) G25 gouge sample composition from 3189.97 m MD. Raised baseline and broad peaks indicate presence of a significant component of amorphous material ~1.3 m outside active shear zone SDZ. The inset SEM image shows typical texture of the gouge. Large vein in foreground is calcite and well-distributed bright phases are pyrite particles. Note the blurred appearance of fractures in the gouge. I–S = mixed-layer illite–smectite; Ver = vermiculite; Qtz = quartz; Fal = albite feldspar; Cal = calcite; Pyr = pyrite.

shear zones (Table 2). It is reasonable to assume that the clays were derived from alteration of illite in the host shale as well as from alteration of feldspars in the gouge (see Schleicher et al., 2008). The XRPD spectra of sample G25 bordering the SDZ also indicated the presence of 30–50% of amorphous (non-crystalline) material (Table 2). The proportion of quartz and feldspar in sample G25 was anomalously low compared to other samples from the core zone, suggesting that the amorphous material was mainly composed of these two minerals. The reduced crystallinity of mineral components in sample G25 compared to those of sample G24 is demonstrated by showing the XRPD scans of these two samples side by side in Fig. 6. In Close-up view, backscattered SEM images of sample G25 showed an extremely fine-grained gouge with a fuzzy texture (inset in Fig. 6b). The foliation in sample G25 was disrupted by dilation jogs and microstructures that indicate rapid volume increase of a fluid phase (Fig. 7a). In the same sample we found microstructures that appeared to be reworked dilation jogs (Fig. 7c).

The samples G27, G28 and G43 represented the SDZ and CDZ active creeping zones in this study (Table 1). The XRPD data for the SDZ sample G28 (Table 2) indicated that ~75% of the material consists of Mg-rich clay vermiculite. Although these samples were as strongly foliated as other rocks in the core zone, the XRPD, SEM-EDX, WLI and optical microscopy revealed a number of features distinct from the foliated gouge elsewhere in the core zone as follows.

1. The gouge had little or no vein network structure (Fig. 8).
2. The anastomosing phyllosilicate foliation, sigmoidal porphyroclasts, strain shadows and overgrowths (Fig. 8a–b) provided clear indication of bulk ductile flow, possibly by a combination of distributed brittle deformation, diffusive

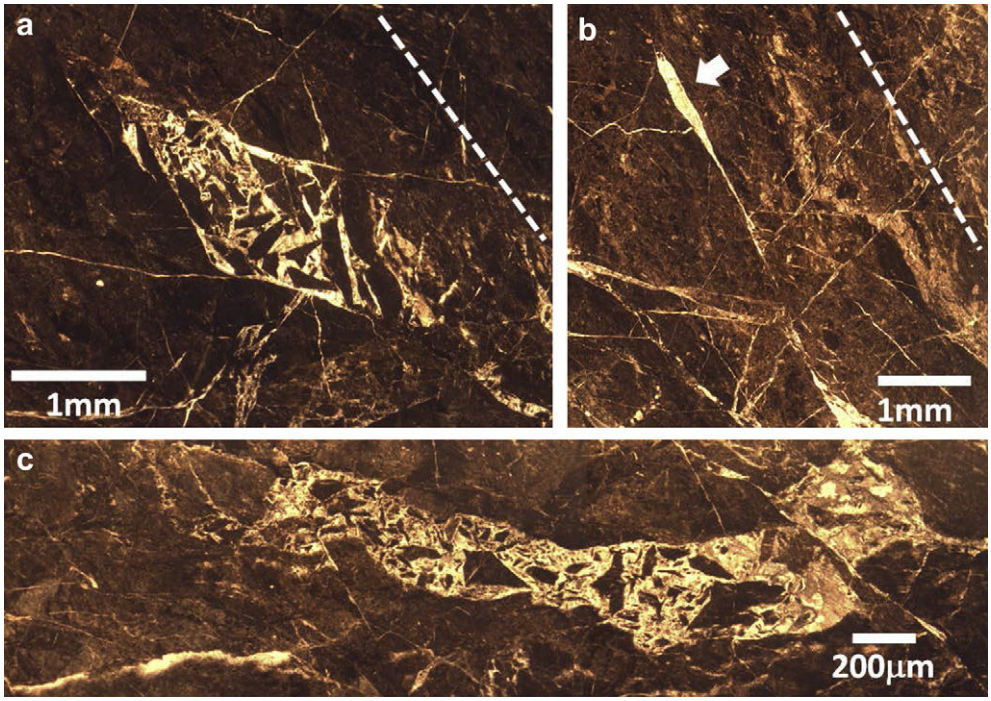

Fig. 7. Evidence of fluid pressures exceeding local normal stresses in the core zone, and multiple episodes of brittle fracture in foliated clay gouge ~1.2 m outside the active shear zone SDZ. Most fracture openings appear to have a shear displacement component. General trace of foliation is indicated by a dashed line. (a) Dilational jog with blocky calcite filling. Stranded angular fragments of gouge in blocky calcite matrix indicate rapid volume increase. (b) A network of cross-cutting calcite-filled microfractures is superimposed on older sheared veins. Blocky calcite vein filling in the large fracture opening (arrow) indicates an open vein crystallization environment. (c) A reworked dilation jog. PPL images from sample G25.

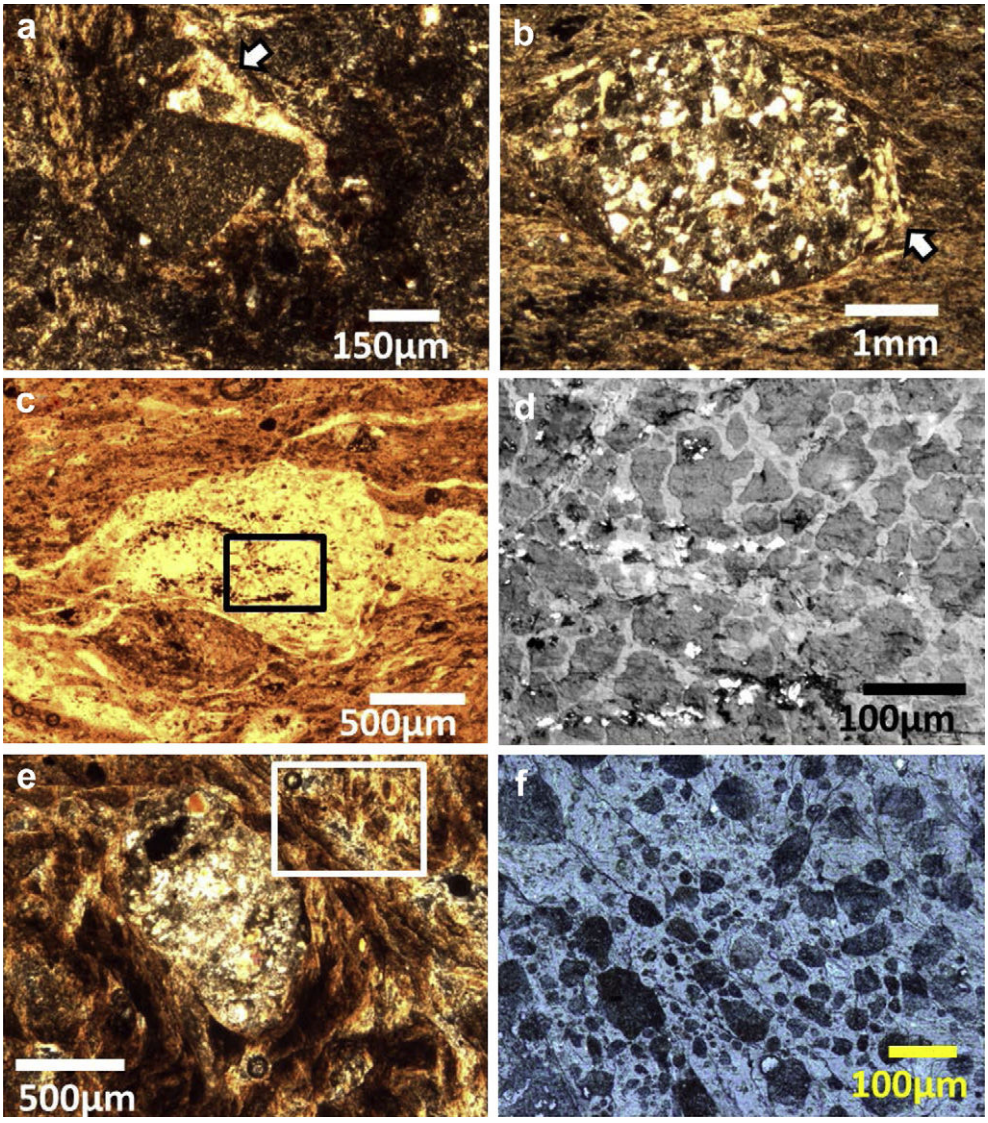

Fig. 8. Bulk ductile flow and alteration softening microstructures within the active shear zones. (a) Flow in clay gouge indicated by rotation of a rigid clast that has produced strain shadow (arrow) with elongated calcite crystals. (b) Sigmoid-shaped clast of arkosic sandstone cataclasite with calcite strain shadows (arrows) indicating left-lateral sense of shear in the clay gouge. (c) Optically continuous, stretched and boudinaged, serpentinite porphyroclast. (d) Enlarged view of inset box in previous image revealing nature of deformation in the porphyroclast. Alteration fragmentation of serpentinite porphyroclast is indicated by anhedral serpentinite grains in smectite-rich matrix. (e) A sub-rounded clast of arkosic sandstone cataclasite in clay gouge. (f) Enlarged view of inset box in previous image, showing smectite-rich clays mantling the cataclasite fragment. Sub-rounded quartz and feldspar grain (dark-colored) float in the clay matrix, some with concave boundaries indicative of dissolution by grain impingement. Microstructural similarity between d and f points to pervasive nature of the alteration softening in both active shear zones. Images a through d are from sample G27 (~0.2 m within SDZ); Images e and f, are from sample G43(~1 m within CDZ). Images a, b, and e are in XPL; c is in PPL; d and f are optical reflected light images.

mass transfer, and reaction softening (see White and Knipe, 1978 for the latter mechanism). In close-up images (Fig. 8c–f), the flow microstructures were associated with matrix-supported gouge that includes quartz and feldspar with anhedral grain boundaries.

3. Locally, serpentinite porphyroclasts made approximately 5–15% of the gouge while the rest consisted of Mg-rich smectite clays, vermiculite (Table 2), or direct alteration products of the serpentinite possibly lizardite and saponite (SEM-EDX spot checks).
4. Sample G28 as well the entire G28 core section (~0.8 m) was an incohesive foliated mass. The gouge foliation was defined by sets of anastomosing P and R1 Riedel shear surfaces (Rutter et al., 1986) separating serpentinite porphyroclasts and lithic fragments mantled by alteration products (Fig. 9a). The surfaces showed strong slickenside striations with mm to μm-scale spacing (Fig. 9b–d).

5. Discussion

We recognize three structural components of interest in the SAF near the SAFOD site: the core zone, the active shear zones (SDZ and CDZ), and features that may correspond to seismogenic asperity patch model related to the microseismic activity in the creeping segment of the SAF (see Nadeau et al., 2004; Dreger et al., 2007). The components are discussed in the above order with regard to our observations.

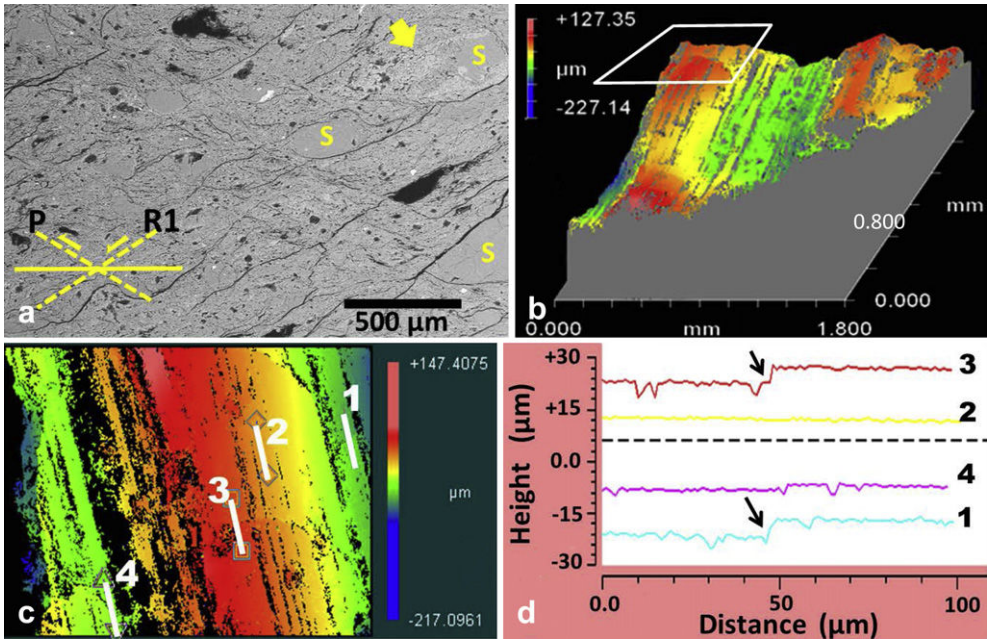

Fig. 9. Evidence of frictional granular flow in the active shear zones. (a) Typical lozenge-shaped microstructure of sample G28 (Sample G28 ~1 m within SDZ) showing microlithons separated by bands of clay-rich gouge oriented along R1 and P type Riedel shears. Clasts marked S are serpentinite porphyroclasts, some including an alteration mantle (arrow). (b) A 3-D plot of white light interferometry data revealing typical slickenside foliation surface. (c) 2-D plot of projected inset area in b showing a total relief of ~70 μm across the striations. (d) Plot of profiles 1-4 marked on c, showing slip-parallel roughness in the order of 1–3 μm. Deviations from average roughness appear to be related to hard mineral protrusions and/or microcrack steps that intersect slip surface (arrows).

5.1. Deformation mechanisms outside the active shear zones

The evidence presented here and supported by other SAFOD studies (Schleicher et al., 2009; Holdsworth et al., 2011; Gratier et al., 2011) show deformation in the core zone is taken place by both cataclasis and pressure solution (Fig. 3). The dominating role of pressure solution as a deformation mechanism, at least outside the active shear zones, is demonstrated by the development of a strong foliation (Fig. 5). Disruption of the foliated gouge by cataclastic deformation close to the active creeping zones (Fig. 7) is consistent with operation of both cataclasis and pressure solution mechanisms over the entire seismic cycle. The primary fault zone process that may be concluded from our observations is particle size reduction by cataclasis and widespread clay mineral authigenesis (enhanced by abundance of shale), both of which are conducive to establishment of pervasive pressure solution. Similar deformation processes were indicated in a study of fault rocks from the Median Tectonic Line in Japan (Jefferies et al., 2006). The enhancing effects on pressure solution of the presence of clay minerals have been known for sometimes (Weyl, 1959; Engelder and Marshak, 1985; Houseknecht and Hathon, 1987). Hickman and Evans (1995) suggested that clay minerals such as illite and smectite, which are capable of maintaining bound water under load, enhance pressure solution by providing higher diffusivities in the contact layer. In terms of particle size changes, Rutter (1976) showed that, where diffusion is the rate-limiting step, the rate of pressure solution creep in polycrystalline aggregates should follow an inverse cube dependence on grain size. However, if pressure solution is accompanied by mineral transformations (incongruent pressure solution), it is likely that reaction-rate is the rate-limiting step (e.g. de Meer et al., 2002; Niemeijer et al., 2009). Lack of alteration products as clay mineral residues at dissolution contacts (Fig. 3e) and presence of a cleavage-vein fabric (Fig. 5d) suggest that the pressure solution is not responsible for mineral alterations found in the studied samples and that diffusion is likely to be the rate-limiting step in the process. This interpretation is consistent with a study of pressure solution in the same suite of SAFOD rocks by Gratier et al. (2011).

5.2. Deformation mechanisms in the active shear zones

In agreement with recent studies (Holdsworth et al., 2011; Jeppson et al., 2010; Zoback et al., 2011) we found that the serpentinite-bearing active shear zones SDZ and CDZ consist of intensely foliated Mg-rich phyllosilicates that unlike the surrounding core zone rocks, lack pervasive vein networks. Considering both core-scale and microstructural data, we characterize these zones as sites of large-scale shear localization within the fault core. The microstructural and compositional evidence, including clast rotation, strain shadows, streamlined flow microstructures (Fig. 8), lack of cohesion and vein networks, Riedel shears, slickenside surfaces (Fig. 9), and amorphous and weak clay phases (Table 2) are associated with the active shear zones. An abundance of phyllosilicates at the site of SDZ and CDZ has contributed to a highly developed foliation, where slip occurs on a hierarchy of surfaces in the foliated gouge, producing polished slickenside surfaces. At the finest scale, the P and R1 slip surfaces shown in Fig. 9a act as clay-lined microlithon boundaries in a wavy lozenge-shaped pattern. These observations link the shear localization by a granular flow to intrinsic (absolute) material weakness. The data suggest that shear localization is mainly by a granular flow mechanism that involves frictional sliding of microlithons set in a matrix of phyllosilicates. However, the grain-boundary sliding in this mechanism may be assisted by pressure solution, which was estimated by Gratier et al. (2011) to accommodate strain values as large as 60% by solution cleavage at the boundary of the active shear zones. Such stress-driven mass transfer in fine-grained gouge is probably efficient for distances <100 μm as might be the case in Fig. 5d–e. A similar flow mechanism was shown to operate in experimental fault gouge consisting of halite and phyllosilicates (Bos and Spiers, 2000; Niemeijer and Spiers, 2006). However, as argued for the Carboneras Fault zone (Faulkner and Lewis, 2003),

the distributed nature of the deformation and thickness of the SDZ and CDZ also are consistent with strain hardening/velocity strengthening of the weak gouge material. Lockner et al. (2011) showed that some of the weakest SAFOD gouge material ($\mu < 0.2$) lies within the active shear zones. It should be noted that the stability field of smectite minerals in the active zones ($\sim$120 °C) is limited to about 150–200 °C. At temperature >200 °C, smectite clays will be replaced by Mg-Chlorites with higher friction coefficients (Frey and Robinson, 1999). To explain the creeping process at depths below the SAFOD, presence of significant proportions of stable weak phases such as talc or deformation mechanisms such as diffusive grain-boundary sliding have been invoked (Lockner et al., 2011; Holdsworth et al., 2011; Gratier et al., 2011).

5.2.1. The shear localization

Based on energy considerations alone, Beeler et al. (1996) argued that the strength of a fault tends to be minimized provided there is a path by which weakness can occur (also see Ben-Zion and Sammis, 2003). Amorphous material is found bordering both the SDZ (in this study) and CDZ (Janssen et al., 2010). The amorphous material reported by Janssen et al. (2010) was attributed to intense comminution, and considered to be significant as a friction reducing material in the creeping SAF. Whether the amorphous material is produced through comminution or by alteration processes, its spatial coincidence with the active shear zone is significant in terms of weakening and shear localization in the core zone. We note that further studies are needed to shed light on the genesis and distribution of the observed amorphous material. The results also suggest other weakening mechanisms that might have preceded the shear localization, including dissolution of strong load bearing minerals (quartz and feldspar) by pressure solution, and fluid assisted alteration of feldspars and serpentinite to phyllosilicates such as illite and illite-smectite clay minerals (also see Moore and Rymer, 2012). The existence of the active shear zones indicate that the weakening has occurred by a reduction in the effective (actively shearing) thickness of the fault zone rather than by widening or what may be termed a delocalization. If we let strain rate and strain $(\tau(\dot{\gamma},\gamma))$ be the only variables affecting shear strength of the fault with effective thickness h, we may rewrite equation (4) from Beeler et al. (1996) simply as $d\tau = -1/h^2\ (V\tau/\dot{\gamma} + \delta\tau/\gamma)dh$, where V is slip velocity, $\dot{\gamma}$ and γ are shear strain rate and shear strain respectively. As applied to the SAFOD site, $dh < 0$ (shear localization condition), and the term $V\tau/\dot{\gamma}$ is non-zero (velocity strengthening gouge). For the fault strength to be minimized through shear localization ($d\tau/dh < 0$) the relative effect of displacement dependence ($\delta\tau/\gamma$) must be greater than that of the velocity dependence $V\tau/\dot{\gamma}$, which would require a strongly displacement-weakening fault zone. A physical explanation for this mechanical behavior, as suggested by Niemeijer and Spiers (2005, 2006) experiments, is the possible role of phyllosilicates in inhibiting healing and sealing of the foliated gouge deforming by frictional granular flow assisted by stress-driven mass transfer. Lack of cohesion and vein networks in the SDZ sample support this explanation. Further support for this argument is provided by experimental results showing that the gouge material in the active shear zones is velocity strengthening (Lockner et al., 2011) and has an extremely low healing rate (Carpenter et al., 2011). It appears that the velocity strengthening gouge in the active shear zones is being sheared in the absence of pervasive restrengthening mechanisms such as cementation or fracture sealing.

5.3. Possible explanations for the microseismicity

The two active shear zones encountered in the drill hole are $\sim$110 m apart. It is reasonable to assume that the zones could vary in width and spacing and have tendency to pinch, branch, and converge along strike. Such non-planar patterns of shear localization resulting from deformation-related lithological obstructions (material contrasts), which are likely to act as local restraining and releasing bends, have been reported from other major fault zones (e.g. Faulkner and Lewis, 2003 and Imber et al., 2008). Chester et al. (2010) noted that slip on pinched regions of the active shear zones must occur on gouge material with higher frictional strengths. The primary fault rock support for the presence of meter-scale undulations of the active shear zones is vein-sealed lenses of coarse siliciclastic cataclasites interlaced with clay gouge in the core zone (e.g. 3295 m to 3296.5 m MD, and 3301.5 m to 3303.3 m MD in Hole G). Varied-size blocks of serpentinite encountered in some drill core sections (e.g. $\sim$0.36 m length section at 3196.63 m MD in hole G) may serve as nucleation spots for microseismicity in the same manner described for dolomite blocks in the Carboneras fault zone (Faulkner and Lewis, 2003).

The permeability variations due to a combination of the lithological heterogeneity and fabric development are likely to affect fluid availability for alteration reactions and, therefore, the distribution of phyllosilicate phases. Field evidence and modeling (e.g. Chester and Chester, 2000; Sagy and Brodsky, 2009; Resor and Meer, 2009; Griffith et al., 2010; Mittempergher et al., 2011) suggest that the undulations of the active shear zones embedded within the core could result in non-uniform stress distribution and pore pressure build-up in the structural boundary regions. Collettini and Barchi (2002) suggested that localized, transient fluid overpressures due to presence of structural seals generate the microseismicity along the creeping Altotiberina fault zone in northern Umbria in central Italy. The distribution and geophysical estimates of the dimensions of the repeating microearthquake source suggest that regions adjacent to lithological contrasts and geometric undulations of the SAF active shear zones may act as hard patches or asperities, and should be considered as possible sources of the observed microseismicity along the SAF creeping segment.

Holdsworth et al. (2011) suggested that the core zone foliated gouge outside the active shear zones is probably inactive, but the transitional contact between the active shear zones and the surrounding core zone rocks suggests a structural coupling and raises the possibility of strain partitioning. This argument may be supported by the fabric analysis of the SAFOD foliated cataclasites that indicates fault-normal compaction in the main damage zone (Chester et al., 2010). It is possible that while most of the shear displacement is being accommodated in the CDZ and SDZ by frictional granular flow or a combination of frictional and pressure solution mechanisms, a portion of the creep is accommodated through a pressure solution-related relaxation in the core zone. If the active shear zones tend to assume an undulating (anastomosing) geometry, the pressure solution-related stress relaxation is also likely to be non-uniformly distributed. Thus an alternative explanation for the microseismicity is repetitive local healing and hardening of the fault core as it accommodates a portion of the creep rate along the SAF. Gratier et al. (2011) argued that if creeping by pressure solution results in diffusion distance >100 μm, stresses do not relax and the observed microseismic activity may be attributed to local restrengthening of the gouge. The seismic rupture induces fracturing, which in turn promotes pressure solution (Gratier and Gueydan, 2007). A seismic cycle involving such fracture-and-seal processes is expected to result in episodic fluid pressure build-up. The non-uniform porosity distribution in the gouge resulting from the pressure solution cleavage development (see Fig. 4) tends to produce strike-parallel fluid barriers as well as local high fluid pressures. The disruption of foliation by episodes of higher-than-local normal stress fluid pressure was indicated by evidence of dilation jogs, reworked dilation jogs (Fig. 6), and

intrusion of shale into pre-existing veins (Mittempergher et al., 2011; Holdsworth et al., 2011). These microstructures appeared to be confined to certain intervals of the foliated clay gouge. The occurrence of localized high fluid pressures in the main damage zone is further supported by evidence of fluid composition variations (Mittempergher et al., 2011) and abrupt changes in real-time mud gas analysis during drilling (Wiersberg and Erzinger, 2008).

Whether the repeating microseismicity is explained by stress-releasing slip zone undulations and/or by fracture-and-seal episodes, local fluid pressures exceeding local normal stresses appears to be a mechanical requirement as seismic rupture on a hard asperity patch is likely to be prevented in a predominantly velocity strengthening fault zone (Nadeau et al., 1995; Tembe et al., 2009). An absence of higher-than-hydrostatic fluid pressures during SAFOD drilling (Zoback et al., 2011) in contrast to our microstructural evidence suggests that: 1. Intermittent high fluid pressure events must have occurred in the past, and 2. The current high fluid pressures, if any, are localized. The possible explanations for the microseismicity discussed here are consistent with the clustered and contained nature of the seismicity in the creeping segment.

6. Conclusions

The microstructural evidence suggests that cataclasis and pressure solution alternated in the core zone of the creeping segment of San Andreas Fault North of Parkfield, California. The pressure solution, assisted by alteration of feldspars to phyllosilicates and episodic particle size reduction by cataclasis, has been responsible for the development of the strongly foliated structure of the gouge in this segment of the fault.

The weakest material of the fault zone is found at the borders and within the currently active shear zones, suggesting that the zones represent large-scale shear localization within the SAF core zone. The energy considerations for shear localization require that the zones are strongly displacement-weakening. This theoretical requirement is consistent with a granular-type flow mechanism involving frictional sliding of the gouge microlithons along phyllosilicate-lined Riedel shear surfaces, possibly coupled with stress-driven diffusive mass transfer. The velocity strengthening weak gouge in the currently active shear zones is deforming in the absence of pervasive restrengthening mechanisms such as cementation or fracture sealing.

The study suggests two possible mechanisms for the repeating microearthquakes in the creeping fault zone. Seismic fracture occurs in frictionally strong regions (asperity patches) of the damage zone associated with stress-concentrating undulations and material contrast points. Alternatively, the asperity patches are fracture-and-seal regions in the fault core where the pressure solution accommodates a portion of the current creep movement. Evidence of local high fluid pressures presented in this study is relevant to both these explanations.

Acknowledgments

The authors would like to thank Dan Faulkner, Bob Holdsworth, and an anonymous reviewer whose valuable comments greatly improved the manuscript. The authors would also like to thank Steve Hickman from the USGS for his valuable comments during the entire course of this research. This research was partially supported by the U.S. National Science Foundation grant NSF-EAR-0545472 to Hadizadeh, DiToro, Mair, and Babaie. DiToro and Mittempergher were also supported by a Progetti di Eccellenza Fondazione Cassa di Risparmio di Padova e Rovigo, and by a European Research Council Starting Grant Project 205175 (USEMS). The Grenoble team was partially supported by CNRS-INSU natural hazards program and ANR-09-JCJC-0011-1.

References

Almeida, R., Chester, J.S., Chester, F.M., Kirschner, D.L., Waller, T.D., Moore, D.E., 2005. Mesoscale structure and Lithology of the SAFOD phase I and II core samples. Eos Trans. Am. Geophys. Union 86 (52) (Abstr. T21A–0454).

Beeler, N.M., Tullis, T.E., Weeks, J.D., 1996. Frictional behavior of large displacement experimental faults. J. Geophys. Res. 101, 8697–8715.

Ben-Zion, Y., Sammis, C.G., 2003. Characterization of fault zones. Pure Appl. Geophys. 160, 677–715.

Bird, P., Kong, X., 1994. Computer simulations of California tectonics confirm very low strength of major faults. Geol. Soc. Am. Bull. 106, 159–174.

Boness, N.L., Zoback, M.D., 2006. A multiscale study of the mechanisms controlling shear velocity anisotropy in the San Andreas Fault Observatory at Depth. Geophysics 71 (4), F131–F146.

Bos, B., Spiers, C.J., 2000. Effect of phyllosilicates on fluid-assisted healing of gouge-bearing faults. Earth Plan. Sci. Lett. 184, 199–210.

Bradbury, K.K., Barton, K.C., et al., 2007. Mineralogic and textural analyses of drill cuttings from the San Andreas Fault Observatory at Depth (SAFOD) boreholes: Initial interpretations of fault zone composition and constraints on geologic models. Geosphere 3, 299–318.

Bradbury, K.K., Evans, J.P., Chester, J.S., Chester, F.M., Kirschner, D.L., 2011. Lithology and internal structure of the San Andreas Fault at depth based on characterization of phase 3 whole-rock core in the San Andreas Fault Observatory at depth (SAFOD) borehole. Earth Planet. Sci. Lett. 310, 131–144.

Byerlee, J., 1993. Model for episodic flow of high-pressure water in fault zones before earthquakes. Geology 21, 303–306.

Carpenter, B.M., Marone, C., Saffer, D.M., 2011. Weakness of the San Andreas Fault revealed by samples from the active fault zones. Nat. Geosci., 1–4. doi:10.1038/NGEO1089. online publ.

Chen, T., Lapusta, N., 2009. Scaling of small repeating earthquakes explained by interaction of seismic and aseismic slip in a rate and state fault model. J. Geophys. Res. 114, B01311.

Chéry, J., Zoback, M.D., Hickman, S., 2004. A mechanical model of the San Andreas Fault and SAFOD Pilot Hole stress measurements. Geophys. Res. Lett. 31, L15S13.

Chester, F.M., Chester, J.S., 1998. Ultracataclasite structure and friction processes of the Punchbowl fault, San Andreas system, California. Tectonophysics 295, 199–221.

Chester, F.M., Chester, J.S., 2000. Stress and deformation along wavy frictional faults. J. Geophys. Res. 105 (B10). 23,421–23.

Chester, J.S., Chester, F.M., Sills, D.W., Heron, B., Almeida, R.V., Guillemette, R.N., 2010. Structure of the San Andreas Fault at SAFOD. Eos Trans. Am. Geophys. Union 91 (52) (Abstr. T52B-03).

Collettini, C., Barchi, M.R., 2002. A low-angle normal fault in the Umbria region (Central Italy): a mechanical model for the related microseismicity. Tectonophysics 359, 97–115.

Collettini, C., Niemeijer, A., Viti, C., Marone, C., 2009. Fault zone fabric and fault weakness. Nature 462, 907–910.

d'Alessio, M.A., Williams, C.F., Burgmann, R., 2006. Frictional strength heterogeneity and surface heat flow: implications for the strength of the creeping San Andreas Fault. J. Geophys. Res. 111, B05410.

Darcy, K., McPhee, R.C.J., Wentworth, C.M., 2004. Crustal structure across the San Andreas Fault at the SAFOD site from potential field and geologic studies. Geophys. Res. Lett. 31, L12S03.

de Meer, S., Spiers, C.J., Peach, C.J., Watanabe, T., 2002. Diffusive properties of fluid-filled grain boundaries measured electrically during active pressure solution. Earth Plan. Sci. 200, 147–157.

Dreger, D., Nadeau, R.M., Chung, A., 2007. Repeating earthquake finite source models: strong asperities revealed on the San Andreas Fault. Geophys. Res. Lett. 34, L23302.

Engelder, T., Marshak, S., 1985. Disjunctive cleavage formed at shallow depths in sedimentary rocks. J. Struct. Geol. 7, 327–343.

Faulkner, D.R., Rutter, E.H., 2001. Can the maintenance of over pressured fluids in large strike-slip fault zones explain their apparent weakness? Geology 29, 503–506.

Faulkner, D.R., Lewis, A.C., 2003. Rutter, E. H. On the internal structure and mechanics of large strike-slip fault zones: field observations of the Carboneras fault in southeastern Spain. Tectonophysics 367, 235–251.

Frey, M., Robinson, D., 1999. Low-grade Metamorphism. Blackwell Science, Cambridge, 313 pp.

Fulton, P.M., Saffer, D.M., 2009. Potential role of mantle-derived fluids in weakening the San Andreas Fault. J. Geophys. Res. 114, B07408.

Fulton, P.M., Saffer, D.M., Bekins, B.A., 2009. A critical evaluation of crustal dehydration as the cause of an overpressured and weak San Andreas Fault. Earth Plan. Sci. Lett. 284, 447–454.

Gratier, J.P., Gueydan, F., 2007. Deformation in the presence of fluids and mineral reactions: effect of fracturing and fluid-rocks interaction on seismic cycle. In: Handy, M.R., Hirth, G., Hovius, N. (Eds.), Tectonic Faults: Agent of Change on a Dynamic Earth. The MIT Press, Cambridge, Mass., USA, pp. 319–356.

Gratier, J.-P., Richard, J., Renard, F., Mittempergher, S., Doan, M.-L., Di Toro, G., Hadizadeh, J., Boullier, A.-M., 2011. Aseismic sliding of active faults by pressure

solution creep: evidence from the San Andreas Fault Observatory at Depth. Geology 39, 1131–1134.
Griffith, W.A., Nielsen, S., Di Toro, G., Smith, S.A.F., 2010. Rough faults, distributed weakening, and off-fault deformation. J. Geophys. Res. 115, B08409.
Hadizadeh, J., Babaie, H. A., DiToro, G., Mair, K., 2007. What is the role of minor gouge zones in the damage zone of the SAF system? Proceedings 3rd Annual Earth Scope National Meeting, Monterey, CA.
Hadizadeh, J., Sehhati, R., Tullis, T.E., 2010. Porosity and particle shape changes leading to shear localization in small-displacement faults. J. Struct. Geol. 32, 1712–1720.
Haines, S.H., van der Pluijm, B.A., Ikari, M.J., Saffer, D.J., Marone, C., 2009. Clay fabrics in natural and artificial gouge. J. Geophys. Res. 114, B05406.
Hickman, S.H., Evans, B., 1995. Kinetics of pressure solution at halite-silica interfaces and intergranular clay film. J. Geophys. Res. 100, 13113–13132.
Hickman, S., Zoback, M.D., 2004. Stress orientations and magnitudes in the SAFOD Pilot Hole. Geophys. Res. Lett. 31, L15S12.
Holdsworth, R.E., van Diggelen, E.W., Spiers, C.J., de Bresser, H., Walker, R.J., Bowen, L., 2011. Fault rocks from the SAFOD core samples: implications for weakening at shallow depths along the San Andreas Fault. California. J. Struct. Geol. 33, 132–144.
Houseknecht, D.W., Hathon, L.A., 1987. Petrographic constraints on models of intergranular pressures solution in quartzose sandstones. Appl. Geochem. 2, 507–521.
Ikari, M.J., Saffer, D.M., Marone, C., 2009. Frictional and hydrologic properties of clay-rich fault gouge. J. Geophys. Res. 114, B05409.
Imanishi, K., Ellsworth, W.L., 2006. Source scaling relationships of microearthquakes at Parkfield, CA, determined using the SAFOD pilot hole seismic array. In: Abercrombie, R., et al. (Eds.), Earthquakes: Radiated Energy and the Physics of Earthquake Faulting. AGU Geophys. Monog. Series, 170, pp. 81–90.
Inoue, A., Utada, M., 1991. Smectite-to-chlorite transformation in thermally metamorphosed volcanoclastic rocks in the Kamikita area, northern Honshu, Japan. Am. Mineral. 76, 628–640.
Imber, J., Holdsworth, R.E., Smith, S.A.F., Jeffries, S.P., Collettini, C., 2008. Frictional-viscous flow, seismicity and the geology of weak faults: a review and future directions. Geol. Soc. London Spec. Publ. 299, 151–173.
Janssen, C., Wirth, R., Rybacki, E., Naumann, R., Kemnitz, H., Wenk, H.-R., Dresen, G., 2010. Amorphous material in SAFOD core samples (San Andreas Fault): evidence for crush- origin pseudotachylytes? Geophys. Res. Lett. 37, L01303.
Janssen, C., Wirth, R., Reinicke, A., Rybacki, E., Naumann, R., Wenk, H.-R., Dresen, G., 2011. Nanoscale porosity in SAFOD core samples (San Andreas Fault). Earth Plan. Sci. Lett. 301, 179–189.
Jefferies, S.P., Holdsworth, R.E., Shimamoto, T., Takagi, H., Lloyd, G.E., Spiers, C.J., 2006. Origin and mechanical significance of foliated cataclastic rocks in the cores of crustal- scale faults: Examples from the Median Tectonic Line, Japan. J. Geophys. Res. 111, B12303.
Jeppson, T.N., Bradbury, K.K., Evans, J.P., 2010. Geophysical properties within the San Andreas Fault zone at the San Andreas Fault observatory at depth and their relationships to rock properties and fault zone structure. J. Geophys. Res. 115, B12423.
Lachenbruch, A., Sass, J., 1992. Heat flow from Cajon Pass, fault strength, and tectonic implications. J. Geophys. Res. 97, 4995–5015.
Lockner, D.A., Morrow, C., Moore, D., Hickman, S., 2011. Low strength of deep San Andreas Fault gouge from SAFOD core. Nature 472, 82–85.
McGarr, J.B., Fletcher, M., Boettcher, M., Beeler, N., Boatwright, J., 2010. Laboratory-based maximum slip rates in earthquake rupture zones and radiated energy. Bull. Seism. Soc. Am. 100 (6), 3250–3260.
McPhee, D.K., Jachens, R.C., Wentworth, C.M., 2004. Crustal structure across the San Andreas Fault at the SAFOD site from potential field and geologic studies. Geophys. Res. Lett. 31, L12S03.
Mittempergher, S., Di Toro, G., Gratier, J.-P., Hadizadeh, J., Smith, S.A., Spiess, R., 2011. Evidence of transient increases of fluid pressure in SAFOD phase III cores. Geophys. Res. Lett. 38, L03301.
Moore, D.E., Rymer, M.J., 2007. Talc-bearing serpentinite and the creeping section of the San Andreas Fault. Nature 448, 795–797.
Moore, D.E., Lockner, D.A., 2008. Talc friction in the temperature range 25 °C–400 °C: Relevance for fault zone weakening. Tectonophysics 449, 120–132.
Moore, D.E., Rymer, M.J., 2012. Correlation of clayey gouge in a surface exposure of serpentinite in the San Andreas Fault with gouge from the San Andreas Fault Observatory at Depth (SAFOD). J. Struct. Geol. 38, 51–60.
Nadeau, R.M., Foxall, W., McEvilly, T.V., 1995. Clustering and periodic recurrence of microearthquakes on the San Andreas Fault at Parkfield, California. Science 267, 503–507.
Nadeau, R.M., Johnson, L.R., 1998. Seismological studies at Parkfield VI: moment release rates and estimates of source parameters for small repeating earthquakes. Bull. Seism. Soc. Am. 88, 790–814.
Nadeau, R.M., Michelini, A., Uhrhammer, R.A., Dolenc, D., McEvilly, T.V., 2004. Detailed kinematics, structure and recurrence of micro-seismicity in the SAFOD target region. Geophys. Res. Lett. 31, L12S08.
Niemeijer, A.R., Spiers, C.J., 2005. Influence of phyllosilicates on fault strength in the brittle–ductile transition: insights from rock analogue experiments. In: Bruhn, D., Burlini, L. (Eds.), High-strain Zones: Structure and Physical Properties. Geol. Soc. London, Special Publications, vol. 245, pp. 303–327.
Niemeijer, A.R., Spiers, C.J., 2006. Velocity dependence of strength and healing behaviour in simulated phyllosilicate-bearing fault gouge. Tectonophysics 427, 231–253.
Niemeijer, A.R., Elsworth, D., Marone, C., 2009. Significant effect of grain size distribution on compaction rates in granular aggregates. Earth Plan. Sci. 284, 386–391.
Niemeijer, A.R., Marone, C., Elsworth, D., 2010. Fabric induced weakness of tectonic faults. Geophys. Res. Lett. 37, L03304.
Resor, P.G., Meer, V.E., 2009. Slip heterogeneity on a corrugated fault. Earth Plan. Sci. Lett. 288, 483–491.
Rice, J.R., 1992. Fault stress states, pore pressure distributions, and the weakness of the San Andreas Fault. In: Evans, B., Wong, T.-F. (Eds.), Fault Mechanics and Transport Properties of Rock: a Festschrift in Honor of W. F. Brace. Academic, San Diego, CA, pp. 475–503.
Rubin, A.M., Gillard, D., et al., 1999. Streaks of microearthquakes along creeping faults. Nature 400, 635–641.
Rutter, E.H., 1976. The kinetics of rock deformation by pressure solution. Phil. Trans. R. Soc. London 283, 203–219.
Rutter, E.H., Maddock, R.H., Hall, S.H., White, S.H., 1986. Comparative microstructures of natural and experimentally produced clay-bearing fault gouges. Pure Appl. Geophys. 124, 3–30.
Rymer, M.J., Catchings, R.D., Goldman, M.R., 2003. Structure of the San Andreas Fault zone as revealed by surface geologic mapping and high-resolution seismic profiling near Parkfield, California. Geophys. Res. Abstr. 5, 13523.
SAFOD, 2010. The Core Atlas (Version 4). available from: http://www.earthscope.org/es_doc/data/safod/Core%20Photo%20Atlas%20v4.pdf.
Sagy, A., Brodsky, E.E., 2009. Geometric and rheological asperities in an exposed fault zone. J. Geophys. Res. 114
Schleicher, A.M., Warr, L.N., van der Pluijm, B.A., 2008. On the origin of mixed-layered clay minerals from the San Andreas Fault at 2.5–3 km vertical depth (SAFOD drill hole at Parkfield, California). Contrib. Mineral. Petrol. 157 (2), 173–187.
Schleicher, A.M., Tourscher, S.N., van der Pluijm, Ben A., Warr, L.N., 2009. Constraints on mineralization, fluid-rock interaction, and mass transfer during faulting at 2–3 km depth from the SAFOD drill hole. J. Geophys. Res. 114, B04202.
Solum, J.G., van der Pluijm, B.A., 2004. Phyllosilicate mineral assemblages of the SAFOD pilot hole and comparison with an exhumed segment of the San Andreas Fault system. Geophys. Res. Lett. 31, L15S19.
Solum, J.G., Hickman, S., Lockner, D.A., Moore, D.E., van der Pluijm, B.E., Schleicher, A.M., Evans, J.P., 2006. Mineralogical characterization of protolith and fault rocks from the SAFOD main hole. Geophys. Res. Lett. 33, L21314.
Solum, J., Hickman, S., Lockner, D.A., Tembe, S., Evans, J.P., Draper, S.D., Barton, D.C., Kirschner, D.L., Chester, J.S., Chester, F.M., van der Pluijm, B.A., Schleicher, A.M., Moore, D.E., Morrow, C., Bradbury, K., Calvin, W.M., Wong, Teng-fong, 2007. San Andreas Fault zone mineralogy, geochemistry, and physical properties from SAFOD cuttings and core. Sci. Drill. (Special Issue No.1).
Tembe, S., Lockner, D.A., Solum, J.G., Morrow, C.A., Wong, Teng-fong, Moore, D.E., 2006. Frictional strength of cuttings and core from SAFOD drill hole phases 1 and 2. Geophys. Res. Lett. 33, L23307.
Tembe, S., Lockner, D.A., Wong, Teng-fong, 2009. Constraints on the stress state of the San Andreas Fault with analysis based on core and cuttings from San Andreas Fault Observatory at Depth (SAFOD) drilling phases 1 and 2. J. Geophys. Res. 114, B11401.
Tembe, S., Lockner, D.A., Wong, Teng-fong, 2010. Effect of clay content and mineralogy on frictional sliding behavior of simulated gouges: binary and ternary mixtures of quartz, illite, and montmorillonite. J. Geophys. Res. 115, B03416.
Thurber, C., Roecker, S., Zhang, H., Baher, S., Ellsworth, W., 2004. Fine-scale structure of the San Andreas Fault and location of the SAFOD target earthquakes. Geophys. Res. Lett. 31, L12S02.
Titus, S.J., DeMets, C., Tikoff, B., 2006. Thirty-five-year creep rates for the creeping segment of the San Andreas Fault and the effects of the 2004 Parkfield earthquake: constraints from alignment arrays, continuous global positioning system, and creepmeters. Bull. Seism. Soc. Am. 96, S250–S268.
Townend, J., Zoback, M.D., 2000. How faulting keeps the crust strong. Geology 28, 399–402.
Townend, J., Zoback, M.D., 2004. Regional tectonic stress near the San Andreas Fault in central and southern California. Geophys. Res. Lett. 31, L15S11.
Waldhauser, F., Ellsworth, W.L., et al., 2004. Streaks, multiplets, and holes: high-resolution spatiotemporal behavior of Parkfield seismicity. Geophys. Res. Lett. 31, L18608.
Wenk, H.-R., Kanitpanyacharoen, W., Voltolini, M., 2010. Preferred orientation of phyllosilicates: comparison of fault gouge, shale and schist. J. Struct. Geol. 32, 478–489.
Weyl, P.K., 1959. Pressure solution and the force of crystallization – a phenomenological theory. J. Geophys. Res. 64, 2001–2025.
White, S.H., Knipe, R.J., 1978. Transformation and reaction enhanced ductility in rocks. J. Geol. Soc. (London) 135, 513–516.
Wiersberg, T., Erzinger, J., 2008. Origin and spatial distribution of gas at seismogenic depths of the San Andreas Fault from drill-mud gas analysis. Appl. Geochem. 23, 1675–1690.
Wintsch, R.P., Christoffersen, R., Kronenberg, A.K., 1995. Fluid-rock reaction weakening of fault zones. J. Geophys. Res. 100, 13021–13032.
Zoback, M.D., 2000. Stren of the San Andreas Fault. Nature 405, 31–32.
Zoback, M., Hickman, S., Ellsworth, W., 2011. Scientific drilling into the San Andreas Fault zone – an overview of SAFOD's first five years. Sci. Drill. 11, 14–28.